Inverse Problems for Blood Perfusion Identification

Dumitru Trucu

Submitted in accordance with the requirements for the degree of

Doctor of Philosophy

The University of Leeds

Centre for Computational Fluid Dynamics

School of Mathematics

School of Process, Environmental and Materials Engineering

June 2009

The candidate confirms that the work submitted is his own, except where work which has formed part of jointly-authored publications has been included. The contribution of the candidate and the other authors to this work has been explicitly indicated overleaf. The candidate confirms that appropriate credit has been given within the thesis where reference has been made to the work of others.

Acknowledgment

I would like to express my deepest respect and gratitude for my Lead Supervisor, Professor Daniel Lesnic, from School of Mathematics, Department of Applied Mathematics, as well as for my Second Supervisor, Professor Derek B. Ingham, from Centre for Computational Fluid Dynamics and School of Process, Environmental and Materials Engineering, and to thank them for their continuous guidance and advice during my three years of PhD studies, July 2006 to June 2009, at The University of Leeds.

A special thanks is addressed to the European Union, European Research Commission, who has fully supported the entire research for my PhD by awarding me with a three-years Marie Curie EST Research Fellowship, July 2006-July 2009, in the Centre for Computational Fluid Dynamics at The University of Leeds. I want to thank the members of staff in the Centre for Computational Fluid Dynamics, Professor Mohamed Pourkashanian, Dr Kevin Hughes and Dr Lin Ma, for their very helpful comments, support and encouraging remarks over the past three years.

A warm thanks goes to my very good friends Dr. Liviu Marin, from Institute of Solid Mechanics, Romanian Academy, Dr. Radu-Bogdan Munteanu, from University of Bucharest, and Dr. Tomas B. Johansson, from School of Mathematics, University of Birmingham, who have continuously encouraged me in the specially honest, high valuable and always reliable discussions that we had during my PhD studies.

Finally, I would like to thank to my entire family, my parents Dumitru and Elena Trucu, my sister Iuliana Trucu, my brother Nicolae and my sister-in-law Mirela Trucu, as well as to my two nieces Maria Trucu and Stefania Trucu, which together

have stood by me in my hardest life challenges, giving me strength in moments of weakness, bringing me the peace of mind at times of unrest, making me feel that more than anybody else they want me to win, and always living with the most sincere happiness for every success that I had.

Abstract

In this thesis we investigate a sequence of important inverse problems associated with the bio-heat transient flow equation which models the heat transfer within the human body. Given the physical importance of the blood perfusion coefficient that appears in the bio-heat equation, attention is focused on the inverse problems concerning the accurate recovery of this information when exact and noisy measurements are considered in terms of the mass, flux, or temperature, which we sampled over the specific regions of the media under investigation.

Five different cases are considered for the retrieval of the perfusion coefficient, namely when this parameter is assumed to be either constant, or dependent on time, space, temperature, or on both space and time.

The analytical and numerical techniques that are used to investigate the existence and uniqueness of the solution for this inverse coefficient identification are embedded in an extensive computational approach for the retrieval of the perfusion coefficient. Boundary integral methods, for the constant and the time-dependent cases, or Crank-Nicolson-type global schemes or local methods based on solutions of the first-kind integral equations, in the space, temperature, or space and time cases, are used in conjunction either with Gaussian mollification or with Tikhonov regularization methods, which are coupled with optimization techniques. Analytically, a number of uniqueness and existence criteria and structural results are formulated and proved.

Information

This thesis includes the content of the following research papers:

1. Dumitru Trucu, Derek B. Ingham and Daniel Lesnic (2009), "Inverse Space- and Time-Dependent Perfusion Coefficient Reconstruction", *submitted to*: *Heat Transfer Engineering* (Taylor and Francis).

2. Dumitru Trucu, Derek B. Ingham and Daniel Lesnic (2009), "Inverse Temperature-Dependent Perfusion Coefficient Reconstruction", *submitted to*: *International Journal of Non-Linear Mechanics* (Elsevier).

3. Dumitru Trucu, Derek B. Ingham and Daniel Lesnic (2009), "Space-dependent perfusion coefficient identification in the transient bio-heat equation", *accepted for publication in*: *Journal of Engineering Mathematics* (Springer).

4. Dumitru Trucu, Derek B. Ingham and Daniel Lesnic (2009), "An inverse coefficient identification problem for the bio-heat equation", *Inverse Problems in Science and Engineering* (Taylor and Francis) **17**, pp. 65-83.

5. Dumitru Trucu, Derek B. Ingham and Daniel Lesnic (2008), "Inverse Space-Dependent Perfusion Coefficient Identification", *Journal of Physics: Conference Series* (Institute of Physics) **135**, 012098 (8pp).

6. Dumitru Trucu, Derek B. Ingham and Daniel Lesnic (2008), "Inverse Time-Dependent Perfusion Coefficient Identification", *Journal of Physics: Conference Series* (Institute of Physics) **124**, 012050 (28pp).

7. Dumitru Trucu, Derek B. Ingham and Daniel Lesnic (2007), "Direct boundary element method for the transient bio-heat transfer equation", *Advances*

in Boundary Integral Methods - Proceedings of the Sixth UK Conference on Boundary Integral Methods, (ed. J.Trevelyan), Durham University, Ch. 24, pp. 223-232 (*peer reviewed*).

8. Dumitru Trucu, Derek B. Ingham and Daniel Lesnic (2007), "The inverse coefficient identification problem in bioheat transient flow equation", *Inverse Problems, Design and Optimization (IPDO-2007)*, (eds. G.S. Dulikravich, M.J. Colaco, H.R.B. Orlande and M. Tanaka) **I**, pp. 214-221 (*peer reviewed*).

Contents

List of Figures

Nomenclature

$\mathcal{A}$	set-value function (Ch. 4)
A	the matrix of the resulting linear systems of equations (Ch. 4, Ch. 6 and Ch. 7)
B	the matrix in the linear system of equations induced by the first-kind Fredholm integral equation (Ch. 7)
$\mathbf{B}(x,r)$	ball of centre x and radius r (Ch. 2 and Ch. 6)
$\mathscr{C}^k$	the class of order$-k$ smooth (continuously $k-$times differentiable) functions (Ch. 2 - Ch. 8)
C, D, E G	nonlinear operators, which are defined on $\overline{\Omega}$ and take matrix values, *i.e.* $C, D, G : \overline{\Omega} \longrightarrow L(\mathbb{R}^{2N}, \mathbb{R}^{N})$, $E : \overline{\Omega} \longrightarrow L(\mathbb{R}^{N_0}, \mathbb{R}^{N})$ (Ch. 4)
$Card(\widetilde{\Omega})$	cardinal of the set $\widetilde{\Omega}$, for any arbitrary $\widetilde{\Omega}$ (Ch. 4)
C_j^{ξ}, D_j^{ξ}, E_k	BEM coefficients, for $\xi \in \Gamma$ (Ch. 2)
C_Γ, D_Γ, E_Γ	boundary associated linear operators (Ch. 4)
C^*, D^*, E^*, G^*	nonlinear operators, which are defined on the set of all possible paths $\{\gamma \,\vert\, \gamma : (0, t_f] \rightarrow \overline{\Omega}\}$ and take matrix values, *i.e.* $C^*, D^*, G^* : \{\gamma \,\vert\, \gamma : (0, t_f] \rightarrow \overline{\Omega}\} \rightarrow L(\mathbb{R}^{2N}, \mathbb{R}^{N})$ and $E^* : \{\gamma \,\vert\, \gamma : (0, t_f] \rightarrow \overline{\Omega}\} \rightarrow L(\mathbb{R}^{N_0}, \mathbb{R}^{N})$ (Ch. 4)
$D_k(m)$	$(m-k)\times m$ dimensional order$-k$ smoothness matrix, $k = \overline{0,2}$ (Ch. 7)
$\mathcal{E}$	mass measurement (Ch. 3 and Ch. 4) and time-average measurement (Ch. 5)

F, F_1, F_2	characterization functions (Ch. 3), and Tikhonov regularization functionals (Ch. 5 - Ch. 6)
F_λ	Morozov nonlinear functional (Ch. 5 - Ch. 7)
G	arbitrary positive function (Ch. 6)
G_1, G_2, G_1^α, G_2^α, $\widetilde{G}_2^\alpha$, $\overline{G}_2^\alpha$	temperature measurements (Ch. 7)
H	Heaviside step function (Ch. 2 - Ch. 3)
H^*, $\overline{H^*}$, $\overline{\overline{H^*}}$, $\widetilde{H}$, Q	nonlinear functionals (Ch. 3 and Ch. 4)
$\mathcal{L}$	characteristic dimension of the tissue (Ch. 1)
L_2	the class of square integrable functions (Ch. 2 - Ch. 7)
L_∞	the class of essentially bounded functions, *i.e.* contains those f such that the essential supremum norm $\| f \| := ess\sup \lvert f \rvert$ is finite (Ch. 2 - Ch. 7)
$L(\mathbb{R}^m, \mathbb{R}^n)$	the space of linear operators from $\mathbb{R}^m$ to $\mathbb{R}^n$ (Ch. 4)
M	special function in representation formula for the solution of boundary value problems with homogeneous initial conditions for heat equation (Ch. 3 and Ch. 4)
N	number of time nodes (Ch. 2 - Ch. 8)
N_0	number of space cells (Ch. 2 - Ch. 8)
$N_0(\tilde{\mathcal{E}})$	the maximum from the cardinals of the subsets of space discretization points x_is that can be included in the $\Lambda(t_j)$ at each time t_j, $j = \overline{1, N}$, *i.e.* $N_0(\tilde{\mathcal{E}}) := \max\limits_{j=\overline{1,N}} Card\left(\{\tilde{x}_i \mid \tilde{x}_i \in \Lambda(\tilde{t}_j)\}\right)$ (Ch. 4)

$P_{\overline{1,N}}$, $P_{\overline{N+1,2N}}$	projections, $P_{\overline{1,N}}, P_{\overline{N+1,2N}} : \mathbb{R}^{2N} \to \mathbb{R}^N$, on the first N and last N components, respectively (Ch. 4)
P_f	perfusion coefficient (Ch. 1 - Ch. 8)
Q_b	energy sink (Ch. 1)
S	nonlinear functional whose unique positive minimum is the constant coefficient P_f (Ch. 3)
S_v	the volumetric heat source (Ch. 1)
S_1, S_{11}, S_{12}, S_2	time and space boundaries of the space×time region (Ch. 2)
T	tissue temperature (Ch. 1 - Ch. 8)
T_a	the arterial temperature (Ch. 1)
T_{air}	temperature of the air stream (Ch. 1)
T_s	the temperature at the top surface of the probe (Ch. 1)
$W/(m^2K)$	standard unit for the heat transfer coefficient (Ch. 1)
c_b	specific heat of the blood (Ch. 1)
c_t	specific heat of the tissue (Ch. 1)
$col_i(mat)$	the $i-$th column of the matrix mat, for any arbitrary matrix mat (Ch. 4)
$colmat_{\overline{i_1,i_2}}$	for any arbitrary matrix $colmat \in L(\mathbb{R}^m, \mathbb{R}^n)$ and any $1 \leq i_1 \leq i_2 \leq m$, this represents the submatrix containing only the columns $col_i(colmat)$, $i_1 \leq i \leq i_2$ (Ch. 4)
$[colmat_1 colmat_2]$	for any arbitrary matrix $colmat_1 \in L(\mathbb{R}^{m_1}, \mathbb{R}^n)$ and $colmat_2 \in L(\mathbb{R}^{m_2}, \mathbb{R}^n)$, this represents the matrix from $L(\mathbb{R}^{m_1+m_2}, \mathbb{R}^n)$ whose columns are the reunion of the columns of $colmat_1$ and $colmat_2$, maintaining their order (Ch. 4)

$\begin{bmatrix} colmat_1 \\ colmat_2 \end{bmatrix}$	for any arbitrary matrix $colmat_1 \in L(\mathbb{R}^m, \mathbb{R}^{n_1})$ and $colmat_2 \in L(\mathbb{R}^m, \mathbb{R}^{n_2})$, this represents the matrix from $L(\mathbb{R}^m, \mathbb{R}^{n_1+n_2})$ whose lines are the reunion of the lines of $colmat_1$ and $colmat_2$, maintaining their order (Ch. 4)
$diag(vec)$	the diagonal matrix whose main diagonal contains the components of the vector vec, for any arbitrary vector vec (Ch. 4)
erf, $erfc$	error functions (Ch. 2 and Appendix)
f, $\overline{f}$, $\overline{\overline{f}}$, g, $\overline{g}$, $\overline{\overline{g}}$	Dirichlet boundary conditions (Ch. 3 - Ch. 4)
f	function of the temperature (Ch. 6)
f_1, f_2	Dirichlet boundary conditions
h, h_0, h_1, $\overline{h}$	flux measurement or Neumann boundary conditions (Ch. 3 - Ch. 7)
i, j, k, l	integer indices (Ch. 2 - Ch. 7)
k_t	thermal conductivity of the tissue (Ch. 1)
k_1, k_2	first-kind integral kernels (Ch. 7)
kPa	standard unit for gauge pressure (Ch. 1)
n, n_ξ	normal directions, for $\xi \in \Gamma$ (Ch. 2)
r	special exponential-type function used in the change of variable (Ch. 4)
$\tilde{\mathcal{E}}$, $\tilde{f}$, $\tilde{g}$, $\tilde{h}_0$, $\tilde{h}_1$, $\tilde{P}_f$, $\tilde{r}$, $\tilde{r}'$, $\tilde{u}$, $r \cdot \mathcal{E}$, $r \cdot f$, $r \cdot u$	vectors containing the discretization at the time nodes $\tilde{t}_j$'s of the functions $\mathcal{E}$, f, g, h_0, h_1, P_f, r, r', u, $r\mathcal{E}$, rf, ru, respectively (Ch. 4)

t, τ	time coordinates (Ch. 2 - Ch. 7)
t_j, $\tilde{t}_j$	time nodes (Ch. 2 - Ch. 7)
t_f	final time (Ch. 1 - Ch. 8)
u	internal temperature measurement (Ch. 3 and Ch. 4)
u_0, v_0	initial conditions (Ch. 3 - Ch. 7)
v, w	changes of variable or test solution used for numerical examples (Ch. 2 - Ch. 4)
$\tilde{v}_\Gamma$, $\tilde{v}'_\Gamma$	$2N-$dimensional vector containing the discretization of v and $\frac{\partial v}{\partial n}$ over the boundary Γ at the time nodes $\tilde{t}_j$s (Ch. 4)
$\tilde{v}_0$	N_0-dimensional vector containing the discretization of v_0 at the space points x_i
x, ξ	space coordinates (Ch. 1 - Ch. 8)
x_i, $\tilde{x}_i$, y_i	space discretization points (Ch. 1 - Ch. 8)
w_b	dimensional blood perfusion rate (Ch. 1)
Θ	$(N-1)-$dimensional vector of angles, *i.e.* $\Theta = \{\theta_k\}_{k=\overline{1,N-1}}$ (Ch. 6)
Λ	set-valued map defined by two paths, $\overline{\gamma}_1 < \overline{\gamma}_2$, *i.e.* $\Lambda(t) = [\overline{\gamma}_1(t), \overline{\gamma}_2(t)]$, $t \in [0, t_f)$ (Ch. 4)
Ξ	set of possible boundary conditions (Ch. 5)
Σ	heat source containing the heat generation due to metabolism and heat deposition (Ch. 1, Ch. 2, Ch. 5 - Ch. 8)
Φ	fundamental solution for the time-dependent bio-heat equation (Ch. 2 - Ch. 3), and fundamental solution for the heat equation (Ch. 4)

Ω	region of interest (Ch. 1 - Ch. 8)
$\partial\Omega$, Γ	the boundary of Ω (Ch. 2 - Ch. 4)
$\overline{\Omega}$	the topological closure of Ω (Ch. 2 - Ch. 4)
α	percentage of random noise η (Ch. 3 - Ch. 8)
β, ζ	parameters
γ, γ_k $\overline{\gamma}_1$, $\overline{\gamma}_2$	paths in the region $\overline{\Omega}$, *i.e.* $\gamma, \gamma_k, \overline{\gamma}_1, \overline{\gamma}_2 : [0, t_f) \rightarrow \overline{\Omega}$ (Ch. 4)
δ, δ_g	total amount of noise introduced in the data (Ch. 5 - Ch. 7)
ε	upper bound in Morozov discrepancy principle (Ch. 5 and Ch. 6)
η	random noise sampled from a uniform distribution on (-1,1) (Ch. 3 - Ch. 8)
λ, λ_0, λ_1, λ_2	regularization parameters (Ch. 5 - Ch. 7)
μ	Neumann boundary condition (Ch.5)
μ_1, μ_2, μ^*, $\overline{\mu}_1$	Dirichlet boundary conditions (Ch. 5)
μ_0, μ_1, μ_2	regularization parameters (Ch. 7)
ρ_b, ρ_t	the density of blood and the tissue, respectively (Ch. 1)
σ	boundary coefficient (Ch. 2)
ϕ, ϕ_0	solutions for associated well-posed second-order parabolic equations (Ch. 3, Ch. 4, Ch. 6)
ϕ_{y_i}, ϕ_{t_j}	functions for which we compute the second-order space and the first-order time derivatives, respectively (Ch. 7)
$\chi_{\widetilde{\Omega}_1}$	the characteristic function of the subset $\widetilde{\Omega}_1$ in the arbitrary set $\widetilde{\Omega}$, $\widetilde{\Omega}_1 \subset \widetilde{\Omega}$ (Ch. 4)
ω	Neumann boundary condition (Ch. 6)

Chapter 1

Introduction

1.1 Motivational Background:

The Process of Blood Perfusion

Blood perfusion, defined as the blood volume flow exchanged through a given volume of tissue, is absolutely essential for normal tissue physiology and plays an important part in the temperature regulatory system of the human body. Blood perfusion is concerned with the local, multidirectional blood flow through the capillary and intracellular space of the living human body tissue. Given the convoluted nature of the pathways through which it evolves, blood perfusion is considered to be a directionless quantity. Capillary and intracellular space blood flow allows the oxygen and nutrients to travel in the human body in order to sustain the life processes. In addition, in order to maintain a healthy system, blood perfusion is also responsible for removing the waste generated by the same life processes it is also fueling. Changes in blood perfusion are a significant characteristic for several pathologic processes.

As an example, tumors are well-known for having a changed perfusion with respect to the surrounding healthy tissue. This perfusion difference has a very discrepant character in the case of the cancer tumors. Therefore, the perfusion information can be used as an assisting control tool during certain clinical treatment procedures where, as in the case of the skin cancer, some parts of the affected tissue are heated above the human body temperature, $37°C$.

The ability to infer the disruption of local perfusion could help detect and evaluate the type and condition of, or the extent of integumentary tumors or other skin lesions. The quantitative evaluation of the blood perfusion would also help in the assessment of skin graft healing. Further, blood perfusion data on the peripheral skin is useful in evaluating normal and abnormal conditions in other tissues, such as the skeletal muscle, pulmonary or cardiovascular systems. Direct assessment of the perfusion of myocardial, renal, intestinal, cerebral, spinal, and other tissues during surgery could also be very significant in the decision-making of the surgical procedures and in the planning of patient prognosis. The ability to continuously and accurately measure blood perfusion in recently repaired ischaemic tissue can predetermine and help prevent the common problem of reperfusion injury.

The knowledge and control of blood is becoming extremely important in the specific situation of organ transplants. After the organs are collected from the donors, during the time of their storage, or while they are transported toward the receiving patient, the permanent knowledge and adjustment of the blood perfusion of the organ inside the temporary storage container becomes crucially important for ensuring that its vital functions are kept unaltered.

The ability to reliably measure the blood perfusion would improve many clinical

applications. Several measurement methods, based on the clearance of a thermal or chemical marker, require an invasive procedure.

1.1.1 Measurements of Local Blood Perfusion with an Invasive Character

The history of the measurement of local blood perfusion using thermal methods have been reviewed by several researchers, including Bowman et al. [8], Bowman [9], Chato [26], Eberhart et al. [48], Scott et al. [98]. Most of the methods discussed in these works are invasive, and the most common method uses a thermistor bead inserted into the tissue. A controlled power sequence is dissipated by the bead and the temperature response of the bead is recorded. The two most common heating methods that occur in practice are pulse decay and step heating, as described in Kress and Roemer [64]. Multiple probes and sinusoidal heating have also been used, see Valvano and Nho [112]. An analytical model is then used to determine the blood perfusion from the experimental temperature response. However, the critical open question regarding these procedures lies in their invasiveness character, which could cause discomfort, possibly harming the patient, and has the effect of disrupting the flow that is being measured. Moreover, when using invasive methods, the possibility of patient infection becomes an important issue.

1.1.2 Noninvasive Methods

Several noninvasive methods have been attempted for the measurement of the blood perfusion. In many of these methods, heat is supplied at the surface of the tissue,

whilst the temperature is measured at the same locations. The most common part of the measurement devices that has been used so far consists of a thermistor covered with insulation to supply heat and simultaneously record the temperature, see Patel et al. [80] and Wei et al. [116]. Castellana et al. [23], used a thin film resistor to supply heat and to measure the surface temperature.

Because of the transient heat loss to the insulation, Walsh and Bowman [113] added a second active thermistor to control the heat entering the tissue. Holti and Mitchel [57] used a thermopile between a heated copper disk and a surrounding non heated ring, which both were placed on the skin. Valvano et al. [111] used a thermal imaging technique to measure the temperature response due to a copper block placed on the skin surface, and Cui and Barbenel [33] modelled the temperature response when different types of materials were placed on the skin.

These methods exhibit a series of limitations. The first constraint consists in the difficulty encountered for determining the actual heat flux into the tissue, since the ambient losses can be relatively large for the noninvasive heating, as opposed to the invasive heating where they are small. A second problem is determined by the thermal contact resistance between the probe and the tissue, which is generally unknown and varies on use. A third important problem is that the basic premise of heating leaves the potential for thermal tissue damage if the temperature of the tissue exceeds about 42°C.

Another important class of measurement methods is the one that uses focused ultrasound as the heating source with a thermistor placed on the surface of the tissue, see Anderson and Burnside [2]. However, the ultrasound based methods are limited in their ability to measure blood perfusion in microcirculation. In order to overcome

this problem, laser light was used instead of sound, and this led to the development of laser-Doppler blood flowmetry to measure perfusion. This noninvasive technique, reviewed by Shepherd and Oberg [102], has received special attention over the last 30 years. The laser light is delivered to the tissue and returned to a detector by optic fiber light guides. Light in the tissue is diffusively scattered by stationary tissue. This light reaches the detector without being Doppler-shifted, while light intercepted by moving red blood cells experience the Doppler effect. The earliest measurements of blood flow using laser-Doppler techniques were made by Riva et al. [96]. Tissue perfusion was first measured in 1975 by Stern [104] and he continued this work with the development of an instrument to permanently monitor the blood flow, see Stern and Lappe [105] and Stern et al. [106]. The work has been continued in this field with improvements of the instrumentation, see Nilsson et al. [75] and Adrian and Borgos [3], which allowed the laser-Doppler systems to be commercialized for use in clinical blood perfusion measurements. Although successful and noninvasive, this measurement system still has drawbacks and the results are not well-quantifiable. These type of measurements are sensitive to a variety of external influences that are not necessarily correlated with the media under investigation. One important limitation is that only relative, rather than absolute, perfusion measurements can be made. Also, in this measurement method the red blood cell motion is recorded only in one direction, and this makes the obtained data dependent on the optical properties of the tissue that can vary with the location and between different patients. The high cost of the equipment should also be considered.

1.1.3 Practical Measurements Using Minimally Invasive Blood Perfusion Probes

Michener et al. [72] have described a probe based on a heat flux sensor that is used to measure directly both the heat flux and the temperature at the skin surface. This work has been further developed by Fouquet et al. [52]. In order to avoid any thermal destruction, the tissue was cooled rather than heated. Initially, the cooling process was achieved by using water channels, whose design makes them very difficult for practical use. To overcome this issue, O'Reilly et al. [90] used pressurized air, instead of water, to cool the tissue. This cooling process has produced a light weight, and easy to use, probe.

Scott et al. [98, 99] have described a method which is accurate, and enables absolute measurements to be made. The method is also cost effective and practical to use. The basic probe design is the one described by O'Reilly et al. [90]. However, in this new probe design, a mixture of heat flux and temperature sensors form the core component. The temperature is measured with a thermocouple, and the heat flux is measured with a thermopile across a thin thermal resistance layer. In the heat flux sensor, called the *Omega* $HFS-3$, a type$-K$ wire thermocouple wire is used for the temperature measurements, while a type$-K$ thermocouple foil is used as the thermopile for the heat flux measurements. The sensors, which have a small thermal capacitance, allow us to accurately follow the change in heat flux and temperature. When a heat flux sensor, in equilibrium with the tissue, is subjected to outside cooling, then the resulting temperature differential causes heat to be conducted through the sensor from the tissue. This heat feedback attempts to bring the tissue

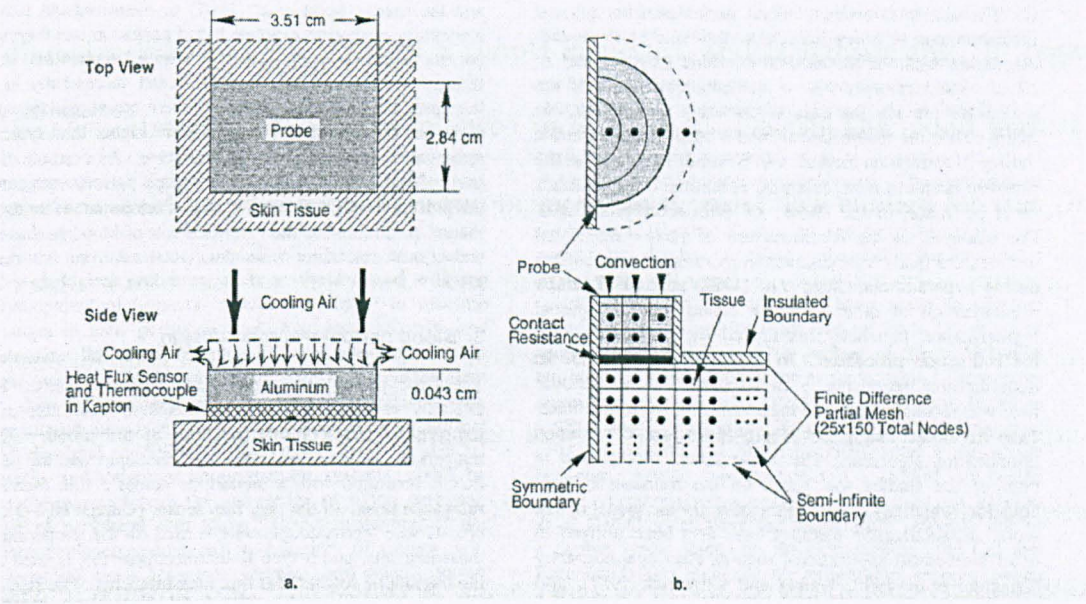

Figure 1.1: A scanned reproduction of the original *"Figure 1. Illustration of probe in contact with the skin tissue; (a) physical set-up and (b) numerical model"*, which has been published in [99].

back to equilibrium and recover any temperature loss that may enter through the sensor into the tissue. This recovery is aided by the exchange of new warmer blood within the volume of the tissue beneath the sensor to replace the blood that has lost part of its thermal energy.

The front side of the probe, used by Scott et al. [98, 99] is placed in continuous contact with the tissue, see Figure 1.1. During the short transient tests of up to $120\,s$ long, the back side of the probe, which has a thin, $0.038\,cm$, sheet of aluminum attached, is cooled with small jets of air pointed normal to the tissue surface. Velocities of less than about $100\ m/s$ from a low pressure air supply, at room temperature, are found to be sufficient to generate heat transfer coefficients in excess

of 200 $W/(m^2K)$. The probe is small, with a total area of about $20\,cm^2$, having a diameter less that $2.5\,cm$, has a simple structure and is lightweight. In regard to the experimental procedures followed in Scott et al. [98, 99] the blood perfusion probe was held steady on the forearm, being pressed with a low enough force so that the skin would not be indented. The probe was placed on the interior forearm at a spot located away from excessive hair or obvious large blood vessels. The top of the probe was attached to a $1.0\,cm$ hose and fitting, through which air was supplied at a gauge pressure of approximately $70\,kPa$. In order to allow the probe to reach thermal equilibrium, this was first placed on one of the patients forearms for $300\,s$. The probe was then transferred to the other forearm and allowed to settle briefly in order to obtain minimal thermal disruption of the tissue. Once the steady-state conditions have been achieved, namely constant heat flux and temperature profiles, the cooling process was turned on for $60\,s$. During this period, the voltage output from both the heat flux sensor and the probe thermocouple were logged at a rate of 32 measurements per second. Also, the constant temperature of the cooling air stream was recorded with a separate thermocouple sensor, while the body core temperature was recorded using a thermocouple placed under the subject's tongue. The only signal processing applied consists of the amplification in the voltage outputs prior to the recording. The voltages were then converted into heat flux and temperature using the corresponding sensor calibration coefficients described in [90]. It is very important that, before starting the actual tests, the convection heat transfer coefficient from the air jets could be determined in separate tests by placing the heat flux sensor and the thermocouple on the air side of the aluminium. The aluminium was placed on a heated piece of copper while the air jets were operating. Time traces of

voltages from the heat sensor and thermocouple were recorded at 32 measurements per second together with the temperature of the cooling air stream. After converting the voltages into heat flux and surface temperature, the convection coefficient was found as the ratio $\frac{h}{T_s - T_{air}}$, where h is the measured heat flux, T_s is the temperature at the top surface of the probe, and T_{air} is the temperature of the air stream. The convection coefficient for the probe, taken as the average of the calculated values over the $60\,s$ period, was found to be approximately $700\,W/(m^2K)$. It is important to mention here that the heat transfer coefficient will be dependent on the probe geometry, air supply, as well as on the physical connections.

1.1.4 A Water-Sponge Experiment for Testing the Blood Perfusion Measurement with a Minimally Invasive Probe

Using a probe similar to that described and used in Scott et al. [98, 99], Robinson et al. [97] have performed an experiment to simulate the thermal phenomena associated with perfusion tests, using a porous medium sponge, acting as a tissue phantom. The sponge was assumed to be homogeneous and no heat was assumed to be generated. In this experiment, water was used instead of blood as the perfusion liquid, see Figure 1.2.

The probe itself is included in the model with the appropriate thermal properties, namely having no perfusion and assuming convective boundary conditions at the probe-cooling air interface. At the probe-sponge interface, the heat flux is equal to the temperature difference in the porous media and on the probe surfaces divided

by the contact resistance. The thermal properties of the sponge, the water, and the probe, as well as the convective heat transfer coefficient, were assumed to be known in the model.

From the design point of view, although similar to the one described in Scott et al. [98, 99], the probe has several new features. A new type of sensor, based on a thermopile formed from ink-etching techniques, was used. This sensitive thermopile, in which layers of dissimilar metal junctions were placed across a layer of polymer, is deposited on a sheet of anodized aluminum substrate and then covered with a very thin piece of aluminum foil. In order to measure the surface temperature of the probe, an isolated type$-E$ thermocouple is embedded in the foil layer. The probe is very small, with an area of $2.9\,cm^2$ and $0.07\,cm$ thick, resulting in a low thermal capacity, which enables the accurate recording of the heat flux and temperature. The front side of the probe remains in continuous contact with the tissue under investigation. Jets of air at room temperature cool the back side of the probe, pointing normal to the surface of the probe.

A special setup, that provides a controlled rate of flow of liquid through a porous media, is used as a test for the blood perfusion probe described above. This consists of a small-pore sponge placed between a removable top and a metal plate within a sample box. A variable speed peristaltic pump is inserting water through the bottom of the box. A central hole in the metal plate forces the upwards flow of water to pass through the centre of the sponge before spreading out towards the sides. The skin is simulated by having the top of the sponge covered with a thin layer of plastic wrap, which prevents the flow from continuing out through the removable top. A large hole in the centre of the removable top allows the probe to be positioned directly

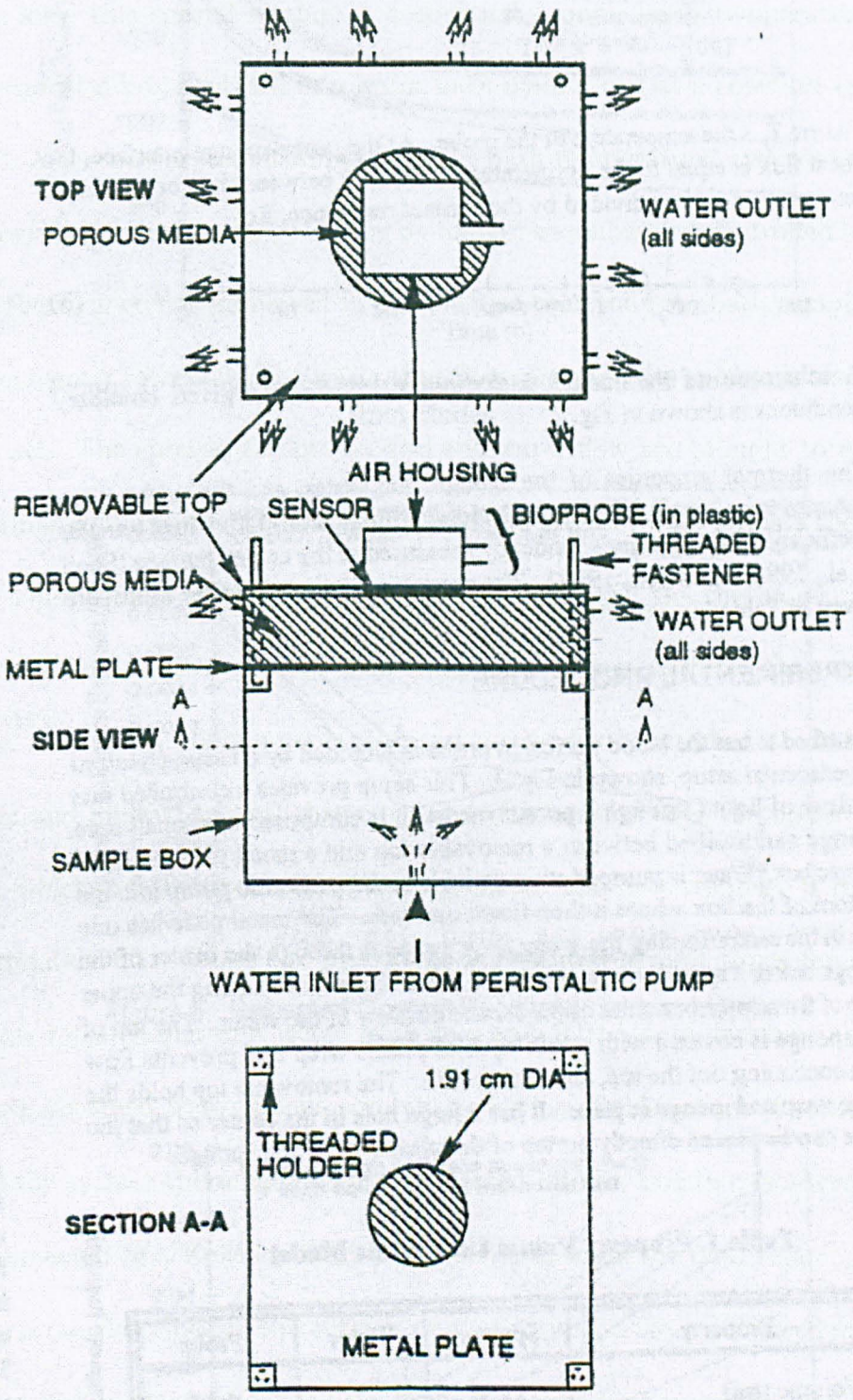

Figure 1.2: A scanned reproduction of the original *"Figure 3. Experimental Setup"*, which has been published in [97].

on the top of the plastic wrap and the sponge.

In order to keep this special setting at a constant human body temperature, the entire experimental box is placed in a water bath maintained at a constant temperature, 37°C. A thermistor, monitoring the water bath temperature, ensures that the temperature is kept constant by switching on and off an embedded controlled heating system. A thermometer is immersed in the bath so that the true bath temperature can be permanently recorded. The water that flows through the sponge is also taken from this bath. The sponge, the probe, and the water flow are brought to *a priori* known thermal equilibrium. The variable speed peristaltic pump adjusts the water flow rate. The probe is placed on the sponge so that both the thermocouple and the thermopile are in direct contact with the plastic-sponge surface. Once thermal equilibrium is reached, room temperature compressed air, supplied at $70\,kPa$, is switched on and allowed to flow through the probe housing over the upper side of the sensor, which creates a convective cooling effect. The heat response is recorded for approximately $60\,s$. Then the procedure is repeated several times for each of the four flow rates chosen in a range from zero to $2.92\,ml/s$. A number of 36 sets of data were obtained from various combination runs of this setup. The heat flux sensor and the surface thermocouple are connected into an isolated, isothermal box which is connected to a Keithley DAS-TC which transmits the data to a computer. Having the probe described in this section as a prototype, a more advanced measurement tool, called the bioprobe, has been later developed and presented by Cardinali et al. [22], which has been used to record blood perfusion data in two experiments using a canine medial saphenous fasciocutaneous free tissue flap model, that allows the experimental control of blood flow in the area of interest . The bioprobe consists

of two distinct components, namely a physical sensor that records experimental data and a *tissue-probe computer model* that determine the perfusion estimate. Also this time the sensor consists of a combination of a thermocouple and thermopile, which measures the heat flux and the temperature on the surface of the region under investigation. The information obtained from the sensors is coupled with the second component of the bioprobe, namely the tissue-probe computer model, which consists of a reliable numerical implementation of a mathematical model that governs the energy balance of the tissue.

1.2 Mathematical Model: The Bio-Heat Equation

The experimental measurements performed in all the works related to the investigation of blood perfusion have all been coupled with a data processing part in which a key role is played by a mathematical model of the energy balance in the region of interest in the human body tissue. The mathematical model is regarded as an approximation of the actual environment that it represents.

Well known and widely accepted, since it was introduced in 1948 by Harry H. Pennes [81], the bio-heat equation is the mathematical model considered and applied along with all the experimental work described in the papers concerning the blood perfusion measurement techniques that have been reviewed in the previous section.

The bio-heat equation is placed at the heart of an extensive quantitative analysis of the relationship between the arterial blood and tissue temperature. This equation has been brought to light as the conclusion of an extensively complex experiment

that took place in the laboratory of H.H. Pennes in 1948, in the Department of Neurology, College of Physicians and Surgeons, Columbia University, New York. This important experiment has been determined by *a priori* observations made in the same laboratory regarding the temperature gradient in the intact human biceps muscle and its coherent matching with the theory of heat conduction flow applied to a localized arm segment. Figure 1.3 presents a scanned reproduction of the original experimental set-up that has been published in Pennes [81]. Without entering into the very complex details of Pennes's original experiment, in essence, its first achievement consisted of a cutaneous topography of temperature in the upper extremity on the proximal forearm, revealing links with both the presence of gradients and the effects of the blood flow. Simultaneous temperature measurements in rectal, brachial arterial blood, and the deep forearm region, have been recorded. Within the setting created for this experiment, the blood flow acted as a warming agent, both for the superficial tissue and for the forearm tissue between the skin and the axis of the limb. After the steady-state tissue temperature-depth distributions have been identified, the analytical theory of heat transfer has been applied in order to determine the influence of the local heat production and circulation.

The conclusion of the experiment conducted by Pennes postulates that the effect of the temperature difference between the blood supply and the tissue acts as an energy sink term, which we denote by $Q_b := w_b \rho_b c_b (T - T_a)$, where w_b =*the blood perfusion rate*, ρ_b =*the density of blood*, c_b =*the specific heat of blood*, T =*the tissue temperature* and T_a =*the arterial blood temperature*, see Pennes [81]. Also, taking into account the other quantities that play a part in the heat transfer process within the human tissue, that is k_t =*thermal conductivity of the tissue*, ρ_t =*the density*

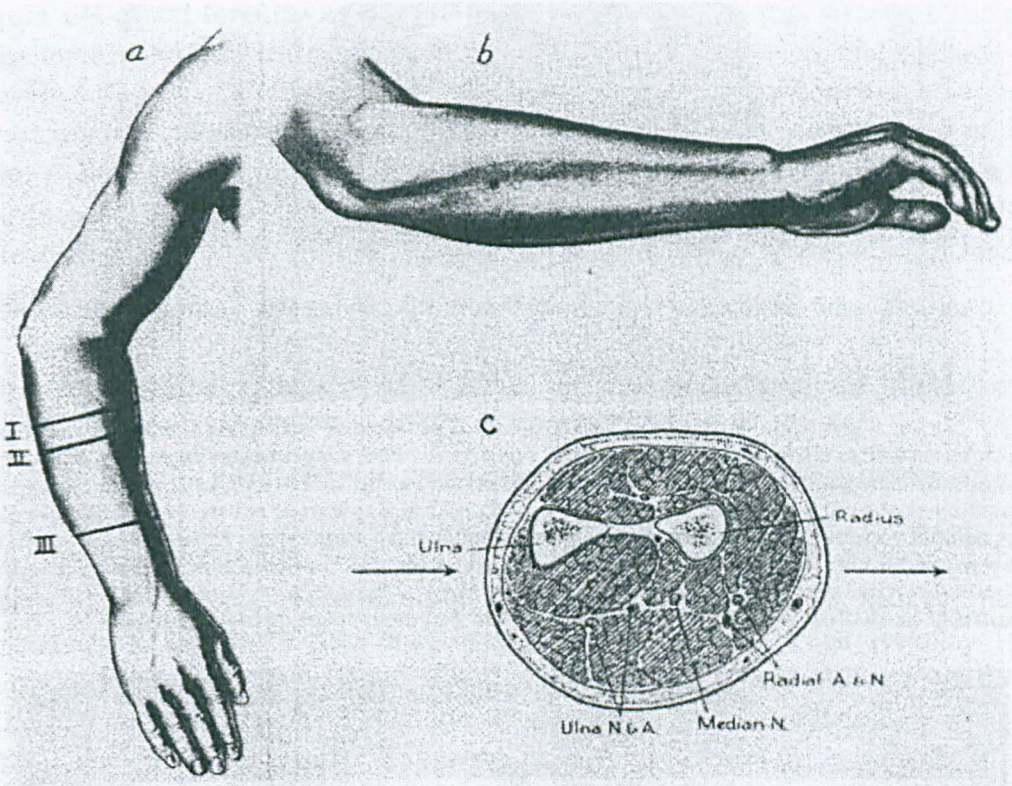

Fig. 3a. EXPERIMENTAL POSITION OF THE RIGHT ARM (superior surface). The pronated forearm was centered between the 2 vertical supports of the wire controller shown in figure 4. The elbow was supported by a soft rubber disc with a central opening just wide enough to receive the medial malleolus of the humerus. The palm of hand was supported on a flat surface of linen towels extended from the head of the metacarpals to the finger tips. Forearm and distal half of upper arm were completely in the air. Inferior aspect of the forearm 5.0 cm. above base of the wire controller (fig. 4). Horizontal *line I* indicates the plane of passage of the needle; *line II* indicates the level of figure 3c.; *line III* indicates the distal plane around the circumference of which temperature was measured in 4 subjects (see section III).

Fig. 3b. EXPERIMENTAL VIEW RIGHT FOREARM (lateral surface). Asterisk indicates point of insertion of the needle of figure 1 (*top*). This plane was always 8.0 cm. distal to tip of ulna olecranon and midway between superior and inferior surfaces of the forearm. The needle was directed perpendicularly to lateral aspect of the forearm. After penetration of the medial side of the arm, the protruding lengths of needle were measured with millimeter-graduated flexible rule. The sum of these two lengths subtracted from total needle length gave the length of the experimental transverse axis. The thermocouple was drawn into the arm by pulling the needle completely through; the needle was then discarded by clipping lead wire. At end of experiment, the thermocouple was removed by traction on 'active' wire so that the path was reversed.

Fig. 3c. CROSS-SECTIONAL ANATOMY of pronated forearm at level II. Broken arrow indicates path of *V*-model thermocouple. (Adapted from Morris's Textbook of Human Anatomy, 9th ed., p. 451, 1933.)

Figure 1.3: A scanned reproduction of the original *"Figure 3"*, which has been published in [81] by Harry H. Pennes.

of the tissue, c_t =*the specific heat of the tissue*, as well as S_v =*the volumetric heat source*, Pennes [81] formulated the bio-heat transfer equation as

$$k_t \Delta T - \mathcal{Q}_b + S_v = \rho_t c_t \frac{\partial T}{\partial t} \qquad \text{in} \quad \Omega \times (0, t_f], \tag{1.1}$$

where $t_f > 0$ is the final time of interest, Ω is the spatial solution domain, and Δ represents the Laplace operator. This equation, in essence, is very similar to the equation for the heat transfer in a fin, where the sink term represents the convective heat loss to the surrounding.

After carrying out an appropriate normalization procedure, the dimensionless formulation of the governing equation for the bio-heat flow in the bounded domain Ω, see Chan [24] and Ren et al. [94], can then be expressed as

$$\Delta T - P_f T + \Sigma = \frac{\partial T}{\partial t}, \qquad \Omega \times (0, t_f], \tag{1.2}$$

where Σ is the heat source containing the heat generation due to the metabolism and heat deposition, and the coefficient

$$P_f := \frac{w_b \rho_b c_b \mathcal{L}^2}{k_t}, \tag{1.3}$$

where $\mathcal{L}$ denotes *the characteristic dimension of the tissue*. Without confusion, in what follows, we call P_f the blood *perfusion* parameter.

Given the central role played in the quantitative characterization of the relation between the arterial blood and the tissue temperatures, it is worth mentioning that the applications of the bio-heat conduction equation range over several medical areas, such as the field of modeling hyperthermia, thrombosis and vascular sclerosis, see Liu and Xu [69]. Note that equation (1.2) arises also in other physical applications, such as optical tomography, see Klibanov et al. [63]. In what concerns the blood

perfusion evaluation, the appearance of P_f as a parameter in the bio-heat equation (1.2) has special importance, creating room for a mathematical investigation, once data are made available from practical measurements.

1.3 Inverse Problem Formulation for the Blood Perfusion Parameter Identification

The efforts presented in the experimental and analytical work of all the researchers, which were briefly introduced and reviewed in the Section 1.1, can be regarded as being all placed within the same framework of the blood perfusion coefficient identification, P_f, that shows up in equation (1.2). Through decades of intensive scientific effort, as briefly highlighted in Section 1.1, different instruments and methods to measure perfusion have been invented, developed and improved, in order to obtain a better accuracy in the blood perfusion measured data. From the way the probes, and later on the bioprobes, were designed, together with the fact that using those probes in different parts of the body is not an easy or not always a possible task, we could draw a first conclusion concerning the major difficulty that this blood perfusion identification problem inherits. All the works reviewed in Section 1.1 have considered the bio-heat equation as a working environment, making use of the powerful analytical tools it enables in assessing their measurement accuracy. However, it is exactly this environment, which characterizes the media under investigation, that is unknown. This leads to inverse problems in which the coefficients of the governing equation, together with its corresponding solution, are determined from additional information.

The inverse problem formulation places this perfusion identification problem within the following perspective. While initial and boundary conditions are specified to ensure the well-posedness of the direct problem associated with the bio-heat equation, the additional information received from the measured data, would make possible a unique simultaneous retrieval of both the perfusion coefficient P_f and of the solution of the corresponding bio-heat equation for $T(x,t)$, without *a prior* knowledge of either of them.

The inverse problem formulation underlines the importance of the various measurements, in terms of heat flux, temperature or energy, investigated by many researchers in the briefly reviewed experimental work, and highlights the difficult problem of inverting these real world data. The need for interpretation of this tomographic data is paving the way to focus more and more on developing new inversion techniques that would enable us to recover the desired information from the measurements taken in most difficult conditions on the human body. Because of the position, current technical limitations of the abilities in taking these measurements, physiological state, as well as the degree of relaxation in which the body is found at the time when the investigation is underway, a certain level of noise exists in the measured data. This can cause the inverse problem to become severely ill-posed, by which we understand that small perturbations in the measured data can determine very large inaccuracies in the final results.

A major advantage in solving this class of inverse problems in a wider and more general sense, considering various initial and boundary conditions, as well as a mixture of several types of measurements, resides in a more accurate retrieval of the perfusion coefficient, given the current practical investigation abilities. Moreover, an

equally or yet more important aspect consists in the precious information, extracted from the inverse problem solution, regarding how the future probes and bioprobes should be actually built. The existence and uniqueness of the solution in this class of inverse problems can give important design guidelines in the manufacture of the new probes and in the development of new experimental methodologies. Therefore, all this cumulated effort, together with its design guidelines spiral effect, represents an important step forward in assisting medical expertise with immediate impact, since better accuracy in more flexible, larger area covering, and eventually more relaxed measurements, used in developed inverse problems methodologies, provides a better and faster approximation of the perfusion coefficient, which finally results in an improved therapeutics for a wider class of health problems. This is the major and most important incentive for which the investigation of this class of inverse problems, both analytically, in terms of existence and uniqueness, and from the point of view of creating robust numerical computations of their solution, represents the focus of this thesis.

Chapter 2

Preliminary Considerations

2.1 Introduction

Regarded as a central part in all the theoretical and practical investigations of the biomedical heat transfer, see Chato [25], the bio-heat equation

$$\Delta T - P_f T + \Sigma = \frac{\partial T}{\partial t}, \qquad \Omega \times (0, t_f], \tag{2.1}$$

where $\Delta = \nabla^2$ denotes the Laplace operator, has to be solved subject to appropriate initial and boundary conditions. If Ω, P_f and Σ are specified, then this gives rise to a well-posed problem, see Strohbehn and Roemer [107] for a review of numerical solutions.

As stated in Chapter 1, this work is focused on inverse problems concerned with the identification the blood perfusion rate, captured by the perfusion coefficient P_f defined in equation (1.3). The identification of P_f is sought under the presence of a hostile environment, where the measurements taken on parts of the boundary $\partial\Omega$, or inside Ω are inaccurate, or they may well be inaccessible.

There are several numerical approaches for building direct solvers for the bio-heat

equation (2.1), mainly by using finite-difference or finite element methods and, in particular, for the steady state case, the Boundary Element Method (BEM), see Chan [24].

In our approach, in the non-steady state bio-heat equation with either constant or time-dependent blood perfusion coefficient P_f, during the inverse problem investigation related to the perfusion coefficient identifications from Chapters 3 and 4, in addition to the targeted theoretical aspects (such as uniqueness and existence of the solution), from the numerical stand point, in order to construct the computational solver, we will perform first a change of variable that will transform the equation (2.1) into the standard heat equation, and then apply the BEM, see Brebbia et al. [7]. For the constant coefficient non-steady state case, this change of variable has the form

$$v(x,t) = T(x,t)e^{P_f t}, \tag{2.2}$$

from which T is recovered via the inverse transformation

$$T(x,t) = v(x,t)e^{-P_f t}. \tag{2.3}$$

In our attempt to solve the forward problems that are embedded in the forthcoming inverse problem investigations related to transient bio-heat equation with constant coefficients, we formulate an alternative BEM, which is built directly for the bio-heat equation (2.1). This new BEM will be the focus of our attention throughout the rest of the current chapter.

2.2 The Boundary Element Method

The associated adjoint equation to (2.1) in an infinite domain reduces to the form

$$\Delta\Phi - P_f\Phi + \delta(x-\xi, t-\tau) = -\frac{\partial\Phi}{\partial t}$$

giving the fundamental solution, see [24]:

$$\Phi(x,\xi,t,\tau) = \frac{H(t-\tau)}{[4\pi(t-\tau)]^{\frac{d}{2}}} \exp\left[-P_f(t-\tau) - \frac{\| x-\xi \|^2}{4(t-\tau)}\right] \tag{2.4}$$

where $\| \cdot \|$ is the usual Euclidean distance, d is the dimensionality of the domain Ω, and $H(\cdot)$ is the Heaviside step function. Thus, by using the Green theorem, the integral expression for the solution of equation (2.1) is given by:

$$\begin{aligned} T(x,t) &= \int_0^t \int_\Gamma \left[\Phi(x,\xi,t,\tau)\tfrac{\partial T}{\partial n_\xi}(\xi,\tau) - \tfrac{\partial\Phi}{\partial n_\xi}(x,\xi,t,\tau)T(\xi,\tau)\right] d\Gamma_\xi d\tau \\ &\quad + \int_0^t \int_\Omega \Phi(x,\xi,t,\tau)\Sigma(\xi,\tau)d\Omega_\xi d\tau + \int_\Omega \Phi(x,\xi,t,0)T(\xi,0)d\Omega_\xi, \end{aligned} \tag{2.5}$$

for any $(x,t) \in \Omega \times (0,t_f)$, where n is the outward normal to the boundary $\Gamma = \partial\Omega$.

2.2.1 The Boundary Element Method Description

The Boundary Element Method (BEM) is an important tool that we will employ within our investigation. While a complete description of the general BEM methodology can be found in Brebbia et al. [7], we will give here the main steps and the subsequent proofs required by the case of our discussion. Let us start by recasting the integral equation (2.5) as

$$\begin{aligned} \sigma(x)T(x,t) &= \int_0^t \int_\Gamma \left[\Phi(x,\xi,t,\tau)\tfrac{\partial T}{\partial n_\xi}(\xi,\tau) - \tfrac{\partial\Phi}{\partial n_\xi}(x,\xi,t,\tau)T(\xi,\tau)\right] d\Gamma_\xi d\tau \\ &\quad + \int_0^t \int_\Omega \Phi(x,\xi,t,\tau)\Sigma(\xi,\tau)d\Omega_\xi d\tau + \int_\Omega \Phi(x,\xi,t,0)T(\xi,0)d\Omega_\xi, \end{aligned} \tag{2.6}$$

for any $x \in \overline{\Omega}$ and any $t \in (0, t_f]$, $t_f > 0$, where the coefficient

$$\begin{cases} \sigma(x) = 1 & \forall x \in \Omega \\ \sigma(x) = \frac{1}{2} & \forall x \in \Gamma(smooth) \end{cases}$$

is supplied by reasons concerning the integration inside the closed region $\overline{\Omega}$. Particularly in our case, the boundary Γ being piecewise smooth, an approximate explanation of the above values for the coefficients σ is that except the points at the corners, if we choose any other point $\xi \in \Gamma$ and we consider all the balls $\mathbf{B}(\xi, r)$, for any arbitrarily small radius r, then

$$\lim_{r \to 0} \frac{\int\limits_{\mathbf{B}(\xi,r) \cap \overline{\Omega}} 1 \, dx}{\int\limits_{\mathbf{B}(\xi,r) \cap (\mathbb{R}^d \setminus \overline{\Omega})} 1 \, dx} = 1. \tag{2.7}$$

Further details regarding this coefficient are given in Brebbia et al. [7].

Since for the moment we consider $\Sigma(x, t) = 0$, the second integral in (2.6) vanishes, so that, if we denote $S_1 = \Gamma \times (0, t_f]$ and $S_2 = \Omega \times \{0\}$, we can rewrite (2.6) as

$$\begin{aligned} \sigma(x)T(x,t) \;=\; & \int_{S_1} \left[\Phi(x,\xi,t,\tau) \tfrac{\partial T}{\partial n_\xi}(\xi,\tau) - T(\xi,\tau) \tfrac{\partial \Phi}{\partial n_\xi}(x,\xi,t,\tau) \right] dS_1(\xi,\tau) \\ & + \int_{S_2} T(\xi,\tau) \Phi(x,\xi,t,\tau) dS_2(\xi,\tau). \end{aligned} \tag{2.8}$$

From now on, the forthcoming analysis will be carried out in an one-dimensional setting. The next step in our BEM approach is the discretization of the boundary integral (2.8), which proceeds as follows:

(i) S_1 is discretized into a series of small boundary elements

$$S_{11} = \{0\} \times (0, t_f] = \bigcup_{j=1}^{N} \{0\} \times (t_{j-1}, t_j], \quad S_{12} = \{1\} \times (0, t_f] = \bigcup_{j=1}^{N} \{1\} \times (t_{j-1}, t_j]$$

and at the same time S_2 is discretized in a series of small cells

$$S_2 = [0, 1] \times \{0\} = \bigcup_{k=1}^{N_0} [x_{k-1}, x_k] \times \{0\}.$$

The temperature T and the flux $\frac{\partial T}{\partial n}$ are assumed to be constant over each boundary element $(t_{j-1}, t_j]$, taking their values at the midpoint $\tilde{t}_j = (t_{j-1} + t_j)/2$, and so we denote

$$\begin{aligned} T(0,t) &= T(0,\tilde{t}_j) =: T_{0j}, \quad \forall t \in (t_{j-1}, t_j], \\ T(1,t) &= T(1,\tilde{t}_j) =: T_{1j}, \quad \forall t \in (t_{j-1}, t_j], \\ \tfrac{\partial T}{\partial n}(0,t) &= \tfrac{\partial T}{\partial n}(0,\tilde{t}_j) =: T'_{0j}, \quad \forall t \in (t_{j-1}, t_j], \\ \tfrac{\partial T}{\partial n}(1,t) &= \tfrac{\partial T}{\partial n}(1,\tilde{t}_j) =: T'_{1j}, \quad \forall t \in (t_{j-1}, t_j]. \end{aligned} \tag{2.9}$$

Also the temperature T is assumed to be constant over each space cell $[x_{k-1}, x_k)$, taking its value at the midpoint $\tilde{x}_k = (x_{k-1} + x_k)/2$, i.e.

$$T(x,0) = T(\tilde{x}_k, 0) =: T^0_k, \quad \forall x \in [x_{k-1}, x_k). \tag{2.10}$$

(ii) The boundary integral (2.8) can now recast as

$$\begin{aligned} \sigma(x)T(x,t) &= \sum_{j=1}^{N} T'_{0j} \int_{t_{j-1}}^{t_j} \Phi(x,0,t,\tau)d\tau + \sum_{j=1}^{N} T'_{1j} \int_{j-1}^{t_j} \Phi(x,1,t,\tau)d\tau \\ &\quad - \sum_{j=1}^{N} T_{0j} \int_{t_{j-1}}^{t_j} \tfrac{\partial \Phi}{\partial n_0}(x,0,t,\tau)d\tau - \sum_{j=1}^{N} T_{1j} \int_{t_{j-1}}^{t_j} \tfrac{\partial \Phi}{\partial n_1}(x,1,t,\tau)d\tau \\ &\quad + \sum_{k=1}^{N_0} T^0_k \int_{x_{k-1}}^{x_k} \Phi(x,\xi,t,0)d\xi \end{aligned} \tag{2.11}$$

for $(x,t) \in [0,1] \times (0, t_f]$, where n_0 and n_1 represent the outward unit normals at the boundary points $\xi = 0$ and $\xi = 1$, respectively.

(iii) By denoting

$$\begin{aligned} C^{\xi}_j(x,t) &= \int_{t_{j-1}}^{t_j} \Phi(x,\xi,t,\tau)d\tau \\ D^{\xi}_j(x,t) &= \int_{t_{j-1}}^{t_j} \tfrac{\partial \Phi}{\partial n_\xi}(x,\xi,t,\tau)d\tau \\ E_k(x,t) &= \int_{x_{k-1}}^{x_k} \Phi(x,\xi,t,0)d\xi \end{aligned} \tag{2.12}$$

we can rewrite equation (2.11) as

$$\begin{aligned}\sigma(x)T(x,t) &= \sum_{j=1}^{N}\left[T'_{0_j}C_j^0(x,t)+T'_{1_j}C_j^1(x,t)-T_{0_j}D_j^0(x,t)-T_{1_j}D_j^1(x,t)\right]\\ &\quad+\sum_{k=1}^{N_0}T_k^0E_k(x,t), \qquad \forall(x,t)\in[0,1]\times(0,t_f].\end{aligned} \tag{2.13}$$

2.2.2 Analytical Expressions for the BEM Coefficients

We calculate now the analytical expressions of the coefficients involved in the computation. As a general approach, we apply the change of variables $z=\sqrt{t-\tau}$ or $z=\frac{1}{\sqrt{t-\tau}}$ for the correspondent integrals and then insert the primitive (A.1) whenever it is requested, see Appendix A.

Let us consider the following notations:

$$\begin{gathered}r=|x-\xi|,\ z_1=\sqrt{P_f(t-t_{j-1})},\ z_2=\sqrt{P_f(t-t_j)},\\ w_1=\frac{r}{2\sqrt{t-t_{j-1}}},\ w_2=\frac{r}{2\sqrt{t-t_j}}.\end{gathered} \tag{2.14}$$

For the coefficients

$$\begin{aligned}C_j^{\xi}(x,t) &= \int_{t_{j-1}}^{t_j}\Phi(x,\xi,t,\tau)d\tau\\ &= \int_{t_{j-1}}^{t_j}\frac{H(t-\tau)}{2\sqrt{\pi(t-\tau)}}\exp\left[-P_f(t-\tau)-\frac{(x-\xi)^2}{4(t-\tau)}\right]d\tau\end{aligned} \tag{2.15}$$

we have the following cases:

Case 1: for $t\le t_{j-1}$

$$C_j^{\xi}(x,t)=0.$$

Case 2: for $t_{j-1}\le t\le t_j$ and $r=0$

$$C_j^{\xi}(x,t)=\int_{t_{j-1}}^{t_j}\frac{H(t-\tau)}{2\sqrt{\pi(t-\tau)}}\exp[-P_f(t-\tau)]d\tau=\frac{1}{2\sqrt{P_f}}erf\left(\sqrt{P_f(t-t_{j-1})}\right),$$

where erf is the standard *error function*, defined by $erf(\zeta) = \frac{2}{\sqrt{\pi}} \int_0^{\zeta} e^{-\sigma^2} d\sigma$, $\forall \zeta \in \mathbb{R}_+$, see Abramowitz and Stegun [1].

Case 3: for $t_{j-1} < t \leq t_j$ and $r \neq 0$

$$\begin{aligned} C_j^{\xi}(x,t) &= \int_{t_{j-1}}^{t_j} \frac{H(t-\tau)}{2\sqrt{\pi(t-\tau)}} \exp\left[-P_f(t-\tau) - \frac{r^2}{4(t-\tau)}\right] d\tau \\ &= \frac{1}{4\sqrt{P_f}} \left[-\exp(r\sqrt{P_f}) erfc\left(\sqrt{P_f(t-t_{j-1})} + \frac{r}{2\sqrt{t-t_{j-1}}}\right) \right. \\ &\quad \left. + \exp(-r\sqrt{P_f})\left(1 + erf\left(\sqrt{P_f(t-t_{j-1})} - \frac{r}{2\sqrt{t-t_{j-1}}}\right)\right)\right], \end{aligned}$$

where $erfc = 1 - erf$ is the complement of the error function erf.

Case 4: for $t_j < t$ and $r = 0$

$$\begin{aligned} C_j^{\xi}(x,t) &= \int_{t_{j-1}}^{t_j} \frac{1}{2\sqrt{\pi(t-\tau)}} \exp(-P_f(t-\tau)) d\tau \\ &= \frac{1}{2\sqrt{P_f}} \left[erf(\sqrt{P_f(t-t_{j-1})}) - erf(\sqrt{P_f(t-t_j)}) \right]. \end{aligned}$$

Case 5: for $t_j < t$ and $r \neq 0$

$$\begin{aligned} C_j^{\xi}(x,t) &= \int_{t_{j-1}}^{t_j} \frac{1}{2\sqrt{\pi(t-\tau)}} \exp\left[-P_f(t-\tau) - \frac{r^2}{4(t-\tau)}\right] d\tau \\ &= \frac{1}{4\sqrt{P_f}} \left\{ \exp(r\sqrt{P_f}) \left[erf\left(\sqrt{P_f(t-t_{j-1})} + \frac{r}{2\sqrt{t-t_{j-1}}}\right) \right.\right. \\ &\qquad \left. - erf\left(\sqrt{P_f(t-t_j)} + \frac{r}{2\sqrt{r-t_j}}\right)\right] \\ &\quad + \exp(-r\sqrt{P_f}) \left[erf\left(\sqrt{P_f(t-t_{j-1})} - \frac{r}{2\sqrt{t-t_{j-1}}}\right) \right. \\ &\qquad \left.\left. - erf\left(\sqrt{P_f(t-t_j)} - \frac{r}{2\sqrt{r-t_j}}\right)\right]\right\}. \end{aligned}$$

Therefore, using the notation (2.14), we can summarize the coefficients $C_j^{\xi}(x,t)$ as follows:

$$C_j^{\xi}(x,t) =$$

$$\begin{cases} 0 & t \le t_{j-1} \\ \frac{1}{2\sqrt{P_f}} erf(z_1) & t_{j-1} < t \le t_j \\ & r = 0 \\ \frac{1}{4\sqrt{P_f}} \left[\exp(-r\sqrt{P_f})\,(1 + erf(z_1 - w_1)) \right. & t_{j-1} < t \le t_j \\ \quad \left. - \exp(r\sqrt{P_f}) erfc(z_1 + w_1)\right] & r \neq 0 \\ \frac{1}{2\sqrt{P_f}} \left[erf(z_1) - erf(z_2)\right] & t_j < t \\ & r = 0 \\ \frac{1}{4\sqrt{P_f}} \left[\exp(r\sqrt{P_f})\,(erf(z_1 + w_1) - erf(z_2 + w_2)) \right. & t_j < t \\ \quad \left. + \exp(-r\sqrt{P_f})\,(erf(z_1 - w_1) - erf(z_2 - w_2))\right] & r \neq 0 \end{cases} \tag{2.16}$$

We proceed in a similar manner to calculate the coefficients

$$\begin{aligned} D_j^{\xi}(x,t) &= \int_{t_{j-1}}^{t_j} \frac{\partial \Phi}{\partial n_\xi}(x,\xi,t,\tau)\,d\tau \\ &= \int_{t_{j-1}}^{t_j} \frac{H(t-\tau)|x-\xi|}{4\sqrt{\pi(t-\tau)^3}} \exp\left[-P_f(t-\tau) - \frac{(x-\xi)^2}{4(t-\tau)}\right] d\tau, \end{aligned}$$

which gives

$$D_j^{\epsilon}(x,t) =$$

$$\begin{cases} 0 & \left| t \le t_{j-1} \right. \\ \frac{1}{4}\left[\exp(r\sqrt{P_f})erfc(w_1+z_1)+\exp(-r\sqrt{P_f})erfc(w_1-z_1)\right] & \left| \begin{array}{l} t_{j-1} < t \le t_j \\ r \neq 0 \end{array} \right. \\ 0 & \left| \begin{array}{l} t_{j-1} < t \le t_j \\ r = 0 \end{array} \right. \\ \begin{array}{l} \frac{1}{4}\left[\exp(r\sqrt{P_f})\left(erf(w_2+z_2)-erf(w_1+z_1)\right)\right. \\ \left.+\exp(-r\sqrt{P_f})\left(erf(w_2-z_2)-erf(w_1-z_1)\right)\right] \end{array} & \left| t_j < t \right. \end{cases} \tag{2.17}$$

Finally, the coefficients $E_k(x,t)$ take the form

$$\begin{aligned} E_k(x,t) &= \int_{x_{k-1}}^{x_k} \Phi(x,\xi,t,0)d\xi \\ &= \int_{x_{k-1}}^{x_k} \frac{1}{2\sqrt{\pi t}} \exp\left(-P_f t - \frac{(x-\xi)^2}{4t}\right) d\xi \\ &= \frac{\exp(-P_f t)}{2}\left[erf\left(\frac{x-x_{k-1}}{2\sqrt{t}}\right) - erf\left(\frac{x-x_k}{2\sqrt{t}}\right)\right]. \end{aligned} \tag{2.18}$$

Numerically , the error functions *erf* and *erfc* are evaluated using the NAG routines S15AEF and S15ADF, respectively.

We use now these coefficients in equation (2.13) and, provided that we know both the initial condition on $T(x,t)$ for all $(x,t) \in S_2$ and the Dirichlet boundary conditions on $T(x,t)$ for all $(x,t) \in S_1$, we can compute the values of the Neumann data $\frac{\partial T}{\partial n}(x,t)$ for all $(x,t) \in S_1$.

For this purpose we apply the integral equation (2.13) at the boundary nodes $(0, \tilde{t}_i)$ and $(1, \tilde{t}_i)$ for $i = \overline{1, N}$ and obtain a $2N \times 2N$ linear system of algebraic equations in the unknowns $\{T'_{0j}, T'_{1j} | j = \overline{1, N}\}$, which is solved numerically using a Gaussian elimination method.

After obtaining the solution of this system of linear equations, we use it in equation (2.13) and obtain the solution $T(x, t)$ at any point (x, t) in the region $[0, 1] \times [0, t_f]$.

2.2.3 Numerical Results and Discussion

The BEM that we have just described will be applied directly for solving the problem:

$$\frac{\partial T}{\partial t}(x, t) = \frac{\partial^2 T}{\partial x^2}(x, t) - P_f T(x, t), \qquad (x, t) \in (0, 1) \times (0, 1], \tag{2.19}$$

$$T(x, 0) = x^2, \qquad x \in [0, 1], \tag{2.20}$$

$$T(0, t) = 2t \exp(-P_f t), \qquad t \in (0, 1], \tag{2.21}$$

$$T(1, t) = (2t + 1) \exp(-P_f t), \qquad t \in (0, 1], \tag{2.22}$$

for a range of values of the perfusion coefficient P_f, as well as for a set of numbers of boundary elements. In our attempt to investigate the power of this method, we make a comparison between the present results and those obtained using another method based on a classical BEM for heat equation that has already been tested. This second method, in brief, is using first the change of variable:

$$v(x, t) = T(x, t) e^{P_f t}, \tag{2.23}$$

so that the equations (2.19)-(2.22) are transformed into the heat equation

$$\frac{\partial v}{\partial t}(x, t) = \frac{\partial^2 v}{\partial x^2}(x, t), \qquad (x, t) \in (0, 1) \times (0, 1], \tag{2.24}$$

subject to

$$v(x,0) = x^2, \qquad x \in [0,1], \tag{2.25}$$

$$v(0,t) = 2t, \qquad t \in (0,1], \tag{2.26}$$

$$v(1,t) = 2t+1, \qquad t \in (0,1], \tag{2.27}$$

for which the BEM, as described by Lesnic [66], can be applied.

The analytical solutions of the problems (2.19)-(2.22) and (2.24)-(2.27) are given by

$$T(x,t) = (x^2 + 2t)\exp(-P_f t), \quad v(x,t) = x^2 + 2t. \tag{2.28}$$

Figures 2.1, 2.2 and 2.3 show the L_2-errors in the heat fluxes at $x = 0$ and $x = 1$, and in the interior temperature, respectively, as functions of the number of boundary elements N, for $N \in \{20, 40, 80, 160, 320, 640, 1280\}$, which are obtained by running the BEM for both equations (2.19) and (2.24). The number of space cells is taken to be $N_0 = N/2$.

In each of the Figures 2.1, 2.2 and 2.3 we have: (a) $P_f = 0.01$, (b) $P_f = 0.1$, (c) $P_f = 1$, and (d) $P_f = 10$. In each of the plots, the numbers in the legends represent the coordinates of the marked points on the corresponding graph. The $*$s annotated and interpolated with a solid line stand for the graph of the L_2-errors obtained directly by the BEM that we have proposed for the bio-heat equation (2.19), whereas the +s annotated and interpolated with a dash-dot line stand for the graph of the L_2-errors obtained when the BEM, as described in Lesnic [66], is applied to the transformed heat equation (2.24).

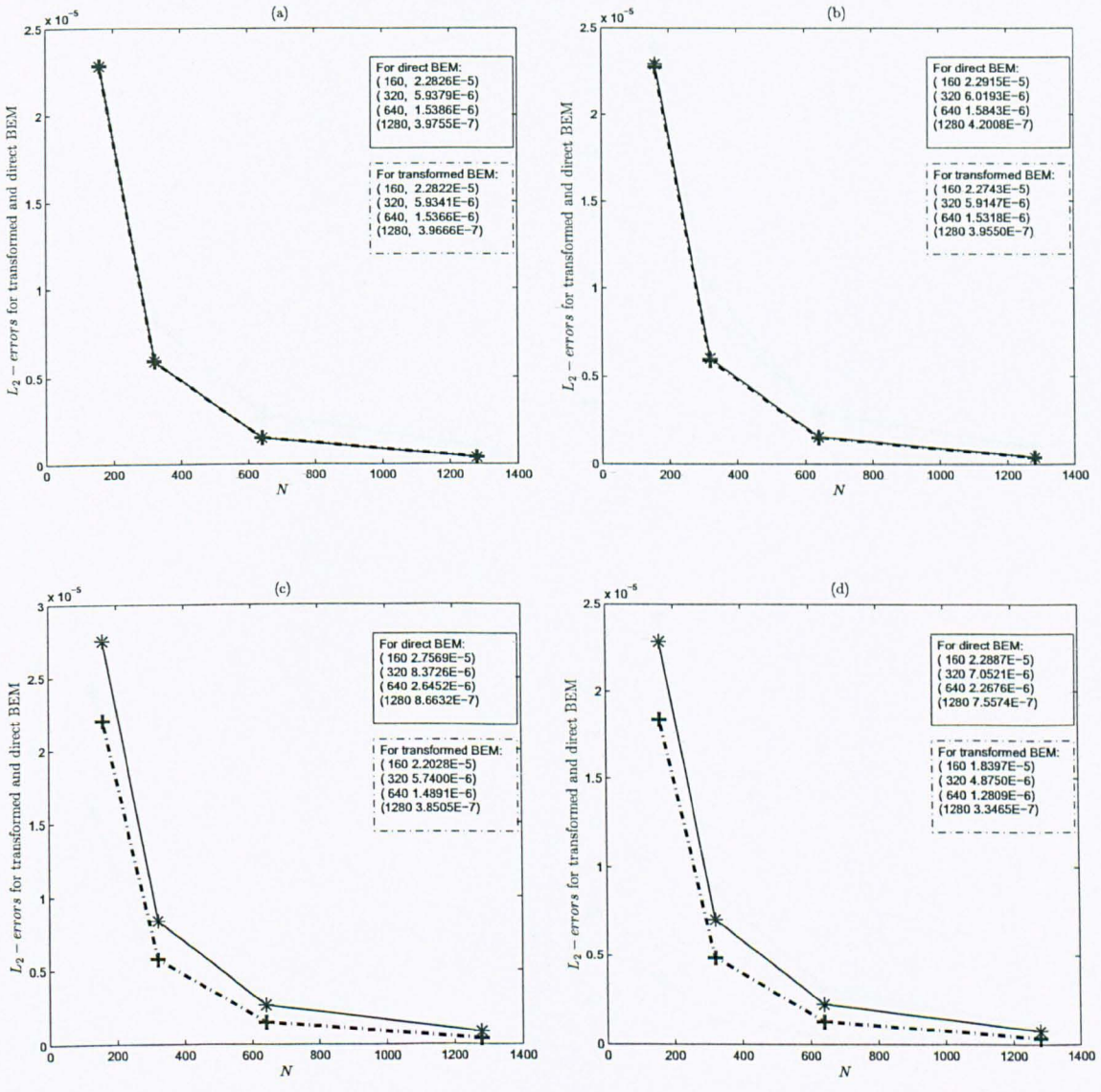

Figure 2.1: L_2-errors for the flux at $x = 0$.

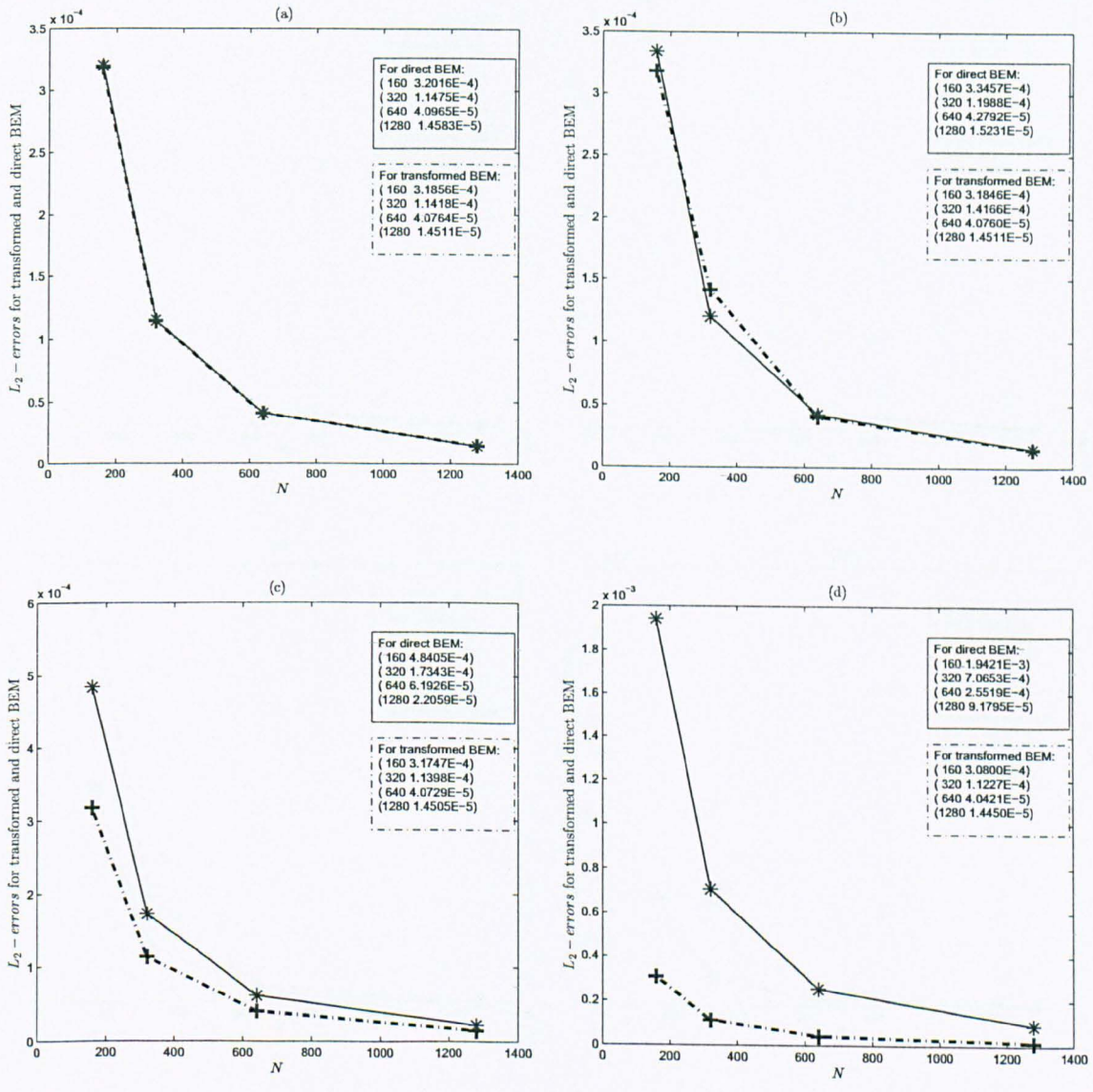

Figure 2.2: L_2-errors for the flux at $x = 1$.

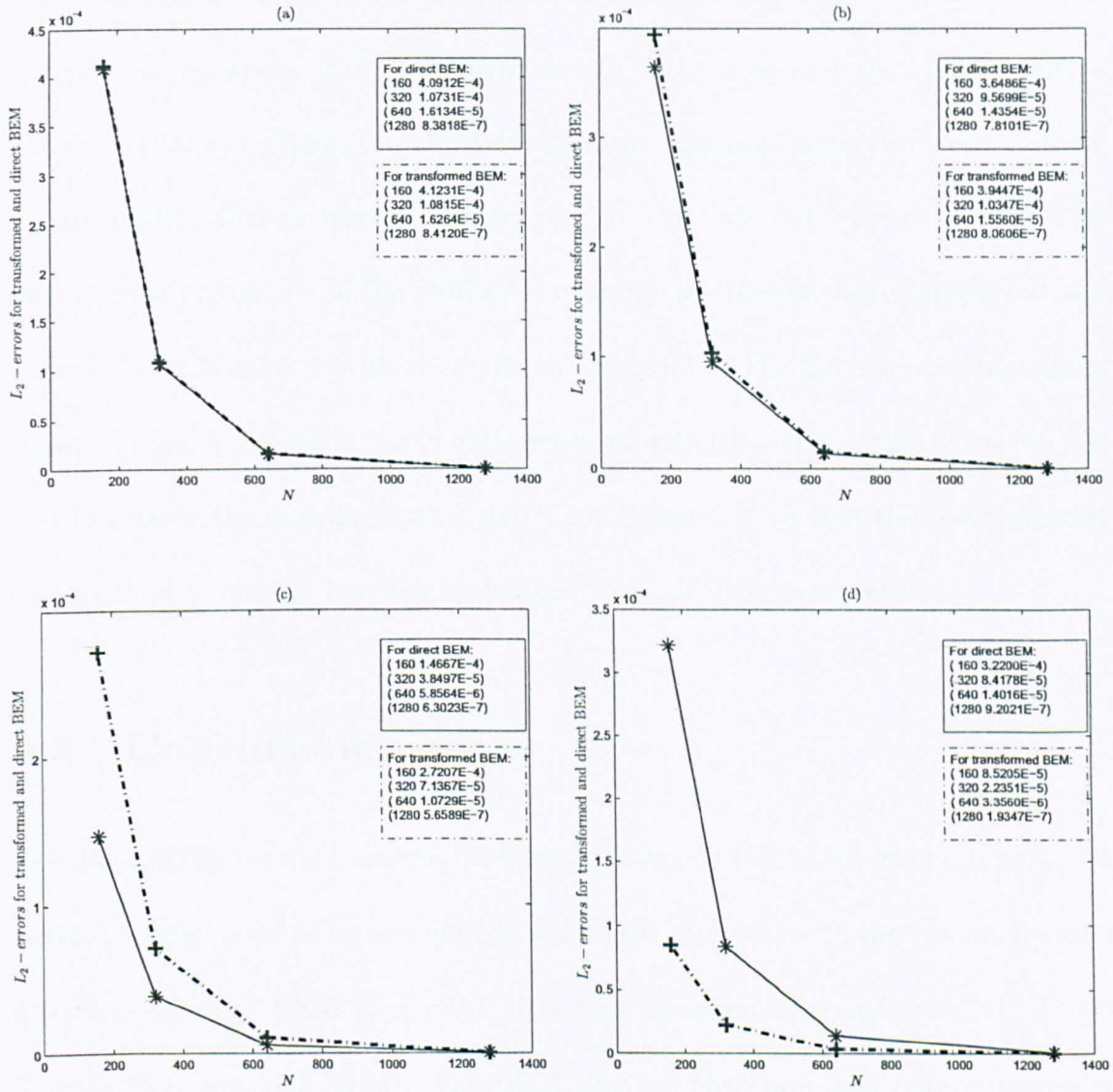

Figure 2.3: L_2-errors for the interior temperature inside the solution domain $\Omega \times (0, t_f] = (0, 1) \times (0, 1]$.

Using a fixed number N of boundary elements, we observe from the distribution of the L_2-errors in Figures 2.1, 2.2 and 2.3, for the two BEMs, as P_f ranges over the interval $(0.01, 10)$, that for $P_f < 1$ the BEM that we have proposed, applied directly to the bio-heat equation (2.19) gives a better accuracy than the BEM for the transformed heat equation (2.24). However, for $P_f \geq 1$, using first the transformation (2.23) and then applying the BEM to the heat equation gives rise to marginally better results, with an increase in accuracy, of the order 10^{-7} for $N > 640$. This behaviour is present in all the numerical experiments that we have carried out, see Figures 2.1, 2.2 and 2.3. Moreover, the computation of the flux over the boundary, shown in Figures 2.1 and 2.2, is in full agreement with the computation of the interior solution inside the domain $(0, 1) \times (0, 1)$, see Figure 2.3, so that the recommended best method to employ remains unchanged from all these perspectives.

2.3 Conclusions

The direct BEM for the transient bio-heat equation (2.19), which has been proposed in this chapter, aims to be considered as a robust alternative to the commonly used scheme where the BEM is applied after this equation is transformed via (2.23) into the heat equation (2.24). The BEM that we have proposed does numerically converge, the L_2-errors decay almost quadratically as N increases, for $N = 1280$ the error becoming less that 10^{-7} both for the flux at $x = 0$ and for the interior solution, see Figures 2.1 and 2.3, and less than 10^{-5} for the flux at $x = 1$. However, both methods perform equally well and either of them can be employed with confidence in the numerical computation of the bio-heat conduction equation (2.19).

Chapter 3

Inverse Constant Perfusion Coefficient Identification

3.1 Introduction

Projected as the main focus for the entire work, the investigation for the retrieval of the perfusion coefficient is started by first considering the case when P_f is a constant coefficient of the steady state and the transient bio-heat conduction equation (1.2). Using both analytical and numerical techniques, under the presence of initial and Dirichlet boundary conditions, in this inverse coefficient identification problem, the additional measurement necessary to render a unique solution may be a heat flux, an interior temperature, or an average temperature measurement at a single instant. We should note the nonlinear character of the resulting inverse problems, as both P_f and the temperature T are considered simultaneously unknown and are sought as a couple solution. Other inverse problems in which either the heat source Σ or parts of $\partial\Omega$ are unknown, with application in tumors detection, have been

approached already in various regards, see Kleinman and Roemer [62], Ren et al. [94], and Partridge and Wrobel [78].

As this study represents a first attempt to recover the perfusion parameter P_f entering the equation (1.2), we consider $\Omega = (0,1)$ to be a one-dimensional spatial domain and restrict the non-dimensional time variation to an interval $[0, t_f]$, with $t_f > 0$. For simplicity, we neglect the source Σ and seek a solution for the constant coefficient P_f. Then equation (1.2) simplifies as follows:

$$\frac{\partial^2 T}{\partial x^2}(x,t) - P_f T(x,t) = \frac{\partial T}{\partial t}(x,t) \quad (x,t) \in (0,1) \times (0,t_f]. \tag{3.1}$$

In the following sections we formulate and investigate the existence and uniqueness of the solution for four inverse problems that are induced by the different types of measurements considered, *i.e.* heat flux, temperature or mass, which are taken at one space point and one instance in time, in both transient and steady-state regimes. For the numerical approach, after performing the change of variable (2.2), which transforms the bio-heat equation (3.1) into the standard heat equation, the boundary element method (BEM) is used for obtaining the computational results, which are presented and discussed later in the chapter. As, in this particular case, the equation (3.1) is linear with constant coefficients, so will be the heat equation obtained after performing the change of variable (2.2), and thus a fundamental solution is available. Since the BEM requires the discretisation of the boundary only, and therefore it reduces the dimensionality of the problem by one, this method is much more advantageous to use than the traditional domain discretisation ones, e.g. the finite-difference, the finite element or the finite volume methods. The robustness of the numerical method will be challenged by allowing the measurement

data to be contaminated with random noise.

3.2 Mathematical Formulation

We consider the following inverse problems: find the temperature $T(x,t)$ in $\mathscr{C}^{2,1}((0,1)\times(0,t_f])\bigcap\mathscr{C}^{1,0}([0,1]\times[0,t_f])$, and the constant perfusion coefficient $P_f>0$ satisfying the one-dimensional bio-heat equation (3.1), subject to the initial condition

$$T(x,0)=T_0(x),\quad x\in[0,1], \tag{3.2}$$

the Dirichlet boundary conditions

$$\begin{aligned} T(0,t) &= f(t),\quad t\in[0,t_f],\ f(0)=T_0(0),\\ T(1,t) &= g(t),\quad t\in[0,t_f],\ g(0)=T_0(1), \end{aligned} \tag{3.3}$$

and one of the following additional information:

a) a heat flux measurement at $(0,t_0)\in\{0\}\times(0,t_f]$

$$-\frac{\partial T}{\partial x}(0,t_0)=h_0, \tag{3.4}$$

b) a heat flux measurement at $(1,t_0)\in\{1\}\times(0,t_f]$

$$\frac{\partial T}{\partial x}(1,t_0)=h_1, \tag{3.5}$$

c) a temperature measurement at an internal point $(x_0,t_0)\in(0,1)\times(0,t_f]$

$$T(x_0,t_0)=u, \tag{3.6}$$

d) a mass measurement at a single time $t_0\in(0,t_f]$

$$\int_0^1 T(x,t_0)dx=\mathcal{E}(t_0). \tag{3.7}$$

In what follows we assume that $T_0\in\mathscr{C}^0([0,1])$, $f,g\in\mathscr{C}^1([0,t_f])$.

3.3 A Steady-State Analysis

Before launching into examples and the numerical approach, let us assess our inverse problem in the steady-state. The inverse problems (3.1)-(3.7) in the steady-state are rewritten in the following form:

$$T''(x) - P_f T(x) = 0, \qquad x \in (0,1), \tag{3.8}$$

subject to the Dirichlet boundary conditions

$$T(0) = f, \quad T(1) = g, \qquad f, g \in \mathbb{R}, \tag{3.9}$$

with one of the following additional information:

a) flux measurement at $x = 0$, namely $-T'(0) = h_0$

b) flux measurement at $x = 1$, namely $T'(1) = h_1$,

c) internal measurement taken at $x_0 \in [0,1]$, $T(x_0) = u$,

d) mass measurement $\int_0^1 T(x)dx = \mathcal{E}$.

Let us first notice that by integrating equation (3.8) we obtain

$$P_f \mathcal{E} = h_1 - h_0. \tag{3.10}$$

Since $P_f > 0$, by solving the ODE (3.8), we obtain the general solution

$$T(x) = C_1 e^{\sqrt{P_f}x} + C_2 e^{-\sqrt{P_f}x}, \qquad C_1, C_2 \in \mathbb{R}. \tag{3.11}$$

Using the Dirichlet boundary conditions (3.9), we determine the constants C_1 and C_2, and obtain

$$T(x) = \frac{1}{\left(e^{\sqrt{P_f}}\right)^2 - 1}\left[\left(e^{\sqrt{P_f}}\right)^x \left(ge^{\sqrt{P_f}} - f\right) + \left(e^{\sqrt{P_f}}\right)^{(1-x)} \left(fe^{\sqrt{P_f}} - g\right)\right]. \tag{3.12}$$

By denoting

$$\beta := e^{\sqrt{P_f}}, \tag{3.13}$$

we obtain

$$T(x) = \frac{1}{\beta^2 - 1}\left[\beta^x (g\beta - f) + \beta^{1-x}(f\beta - g)\right]. \tag{3.14}$$

Therefore

$$T'(x) = \frac{\ln(\beta)}{\beta^2 - 1}\left[\beta^x (g\beta - f) - \beta^{1-x}(f\beta - g)\right], \tag{3.15}$$

which enables us to calculate

$$h_0 = -T'(0) = \frac{\left[\left(\beta^2 + 1\right) f - 2\beta g\right]\ln(\beta)}{\beta^2 - 1}, \quad h_1 = T'(1) = \frac{\left[\left(\beta^2 + 1\right) g - 2\beta f\right]\ln(\beta)}{\beta^2 - 1}. \tag{3.16}$$

Also, from (3.14), we obtain both the internal measurement

$$u = T\left(\frac{1}{2}\right) = \frac{\sqrt{\beta}}{\beta + 1}(f + g), \tag{3.17}$$

for the internal point chosen to be $x_0 = \frac{1}{2}$, and the mass measurement

$$\mathcal{E} = \frac{(\beta - 1)(f + g)}{(\beta + 1)\ln(\beta)}. \tag{3.18}$$

First, let us consider case c) in which the internal temperature measurement u is supplied at $x_0 = \frac{1}{2}$.

Based on equations (3.14) and (3.17), we distinguish the following conclusions:

i) If $u = 0$ and $f + g \neq 0$, then the inverse problem does not have a solution;

ii) If $u = 0$ and $f + g = 0$, then the problem has infinitely many solutions $P_f > 0$ and $T(x) = \frac{f}{\beta - 1}(\beta^{1-x} - \beta^x)$, where $\beta = e^{\sqrt{P_f}}$;

iii) If $u \neq 0$ and $(f + g)^2 - 4u^2 \leq 0$, then the problem does not have a solution;

iv) If $u \neq 0$ and $(f+g)^2 - 4u^2 > 0$, then the problem has a unique solution, as $\beta = \left[\frac{f+g+\sqrt{(f+g)^2-4u^2}}{2u}\right]^2$, thus $P_f = \left[\ln\left(\left[\frac{f+g+\sqrt{(f+g)^2-4u^2}}{2u}\right]^2\right)\right]^2$.

Another situation to consider is case d) in which the additional information supplied is the mass measurement (3.18). Since the function

$$\begin{aligned} &F : (1,\infty) \to \mathbb{R}, \\ &F(\beta) = \tfrac{\beta-1}{(\beta+1)\ln(\beta)}, \qquad \text{for any } \beta \in (1,\infty) \end{aligned} \tag{3.19}$$

is strictly decreasing and

$$\lim_{\beta\to 1} F(\beta) = \frac{1}{2} \quad \text{and} \quad \lim_{\beta\to\infty} F(\beta) = 0, \tag{3.20}$$

we obtain that the inverse problem in case d) has a unique solution if and only if

$$0 < \frac{\mathcal{E}}{f+g} < \frac{1}{2}. \tag{3.21}$$

Otherwise, it has no solution.

Finally, we analyze the cases a) and b), when the additional information supplied is either a flux measurement h_0 at $x = 0$, or a flux measurement h_1 at $x = 1$. In either of these cases the existence and uniqueness of the solution of the corresponding inverse problem is related to the number of zeros on $(1,\infty)$ of the particular functions $F_0(\beta)$, for the flux measurement at the left, or $F_1(\beta)$, for the flux measurement at the right. These two functions are defined as follows:

$$\begin{aligned} F_0(\beta) &= ((\beta^2+1)f - 2\beta g)\ln(\beta) - (\beta^2-1)h_0, \\ F_1(\beta) &= ((\beta^2+1)g - 2\beta f)\ln(\beta) - (\beta^2-1)h_1. \end{aligned} \tag{3.22}$$

Let us now consider some particular choices of the boundary conditions and measurements for which we can determine the numbers of zeroes of the functions defined in (3.22). For example, if $f = g$, then

$$F_0(\beta) = -(\beta^2-1)[f\ln(\beta) + h_0], \quad F_1(\beta) = (\beta^2-1)[f\ln(\beta) - h_1]. \tag{3.23}$$

Therefore, if $0 < -\frac{h_0}{f} < \infty$, then the inverse problem for the flux measurement at $x = 0$ (case a)) has a unique solution given by

$$P_f = \left(\frac{h_0}{f}\right)^2, \qquad T(x) = \frac{f}{\beta+1}\left[\beta^x + \beta^{1-x}\right], \tag{3.24}$$

where $\beta = e^{-\frac{h_0}{f}}$. Otherwise, the inverse problem has no solution.

Also, if $0 < \frac{h_1}{f} < \infty$, then the inverse problem for the flux measurement at $x = 1$ (case b)) has a unique solution given by

$$P_f = \left(\frac{h_1}{f}\right)^2, \qquad T(x) = \frac{f}{\beta+1}\left[\beta^x + \beta^{1-x}\right], \tag{3.25}$$

where $\beta = e^{\frac{h_1}{f}}$. Otherwise, the inverse problem has no solution.

In the rest of the chapter we consider the transient case given by the bio-heat conduction equation (3.1).

3.4 Analysis for the Flux Measurement

Let $\phi \in \mathscr{C}^{2,1}((0,1)\times(0,t_f]) \bigcap \mathscr{C}^{1,0}([0,1]\times[0,t_f])$ be the unique solution of the direct, well-posed problem (3.1) - (3.3) with $P_f = 0$, namely

$$\frac{\partial \phi}{\partial t}(x,t) = \frac{\partial^2 \phi}{\partial x^2}(x,t), \quad (x,t) \in (0,1)\times(0,t_f], \tag{3.26}$$

$$\phi(x,0) = T_0(x), \qquad x \in [0,1], \tag{3.27}$$

$$\begin{aligned} &\phi(0,t) = f(t), \quad t \in [0,t_f],\ f(0) = T_0(0), \\ &\phi(1,t) = g(t), \quad t \in [0,t_f],\ g(0) = T_0(1). \end{aligned} \tag{3.28}$$

Then the function

$$w(x,t) := e^{P_f t} T(x,t) - \phi(x,t) \tag{3.29}$$

satisfies the following problem:

$$\frac{\partial w}{\partial t}(x,t) = \frac{\partial^2 w}{\partial x^2}(x,t), \quad (x,t) \in (0,1)\times(0,t_f], \tag{3.30}$$

$$w(x,0) = 0, \qquad x \in [0,1], \tag{3.31}$$

$$\begin{aligned} w(0,t) &= f(t)(e^{P_f t} - 1) =: \overline{f}(t), \quad t \in [0,t_f],\ \overline{f}(0) = 0, \\ w(1,t) &= g(t)(e^{P_f t} - 1) =: \overline{g}(t), \quad t \in [0,t_f],\ \overline{g}(0) = 0, \end{aligned} \tag{3.32}$$

and the flux measurement (3.4), namely

$$-\frac{\partial w}{\partial x}(0,t_0) = h_0 e^{P_f t_0} + \frac{\partial \phi}{\partial x}(0,t_0). \tag{3.33}$$

Let us assume that a solution to the problem (3.30)-(3.33) exists.

Since $\overline{f}, \overline{g} \in \mathscr{C}^0([0,t_f])$, we have the representation formula

$$w(x,t) = -\int_0^t \frac{\partial M}{\partial x}(x,t-\tau)\overline{f}(\tau)d\tau + \int_0^t \frac{\partial M}{\partial x}(x-1,t-\tau)\overline{g}(\tau)d\tau, \tag{3.34}$$

where

$$M(\xi,\sigma) := \frac{H(\sigma)}{\sqrt{\pi\sigma}} \sum_{n=-\infty}^{\infty} \exp\left[-\frac{(\xi+2n)^2}{4\sigma}\right], \tag{3.35}$$

and H is the Heaviside step function, see Hartman and Wintner [55] for details.

By differentiating equation (3.34) with respect to x, we obtain

$$\frac{\partial w}{\partial x} = -\int_0^t \frac{\partial^2 M}{\partial x^2}(x,t-\tau)\overline{f}(\tau)d\tau + \int_0^t \frac{\partial^2 M}{\partial x^2}(x-1,t-1)\overline{g}(\tau)d\tau. \tag{3.36}$$

Since

$$\frac{\partial M}{\partial \tau}(x-\xi,t-\tau) = -\frac{\partial^2 M}{\partial x^2}(x-\xi,t-\tau), \quad x \neq \xi,\ t > \tau, \tag{3.37}$$

it follows that

$$\frac{\partial w}{\partial x}(x,t) = \int_0^t \frac{\partial M}{\partial \tau}(x,t-\tau)\overline{f}(\tau)d\tau - \int_0^t \frac{\partial M}{\partial \tau}(x-1,t-\tau)\overline{g}(\tau)d\tau. \tag{3.38}$$

On the other hand, let us first notice that, from equation (3.35), we obtain

$$\lim_{\tau \nearrow t} M(x-\xi,t-\tau) = 0, \quad x \neq \xi, \tag{3.39}$$

and since $\overline{f}, \overline{g} \in \mathscr{C}^1([0,t_f])$, with $\overline{f}(0) = \overline{g}(0) = 0$, by using integration by parts in (3.38), we have

$$\frac{\partial w}{\partial x}(x,t) = -\int_0^t M(x,t-\tau)\overline{f}'(\tau)d\tau + \int_0^t M(x-1,t-\tau)\overline{g}'(\tau)d\tau, \tag{3.40}$$

for all $(x,t) \in (0,1) \times (0,t_f]$. By using now the Lebesgue's Dominative Convergence Theorem, see Stroock [108], we obtain

$$\lim_{x \searrow 0} \frac{\partial w}{\partial x}(x,t) = -\int_0^t M(0,t-\tau)\overline{f}'(\tau)d\tau + \int_0^t M(1,t-\tau)\overline{g}'(\tau)d\tau \tag{3.41}$$

for all $t \in (0,t_f]$.

For $t \in (0,t_f]$ and $P_f \in (0,\infty)$, let us define

$$H^*(t,P_f) := -\int_0^t M(0,t-\tau)\overline{f}'(\tau)d\tau + \int_0^t M(-1,t-\tau)\overline{g}'(\tau)d\tau, \tag{3.42}$$

$$Q(P_f) := -\left(H^*(t_0,P_f) + \frac{\partial \phi}{\partial x}(0,t_0)\right)e^{-P_f t_0} \tag{3.43}$$

and remark that equation (3.33) implies

$$Q(P_f) = h_0. \tag{3.44}$$

Thus, if the inverse problem (3.1) - (3.4) has a solution then the coefficient P_f must satisfy equation (3.44). Moreover, the inverse problem (3.1) - (3.4) is actually equivalent to the nonlinear algebraic equation (3.44) in the following sense:

Theorem 3.4.1 *Let $f, g \in \mathscr{C}^1([0,t_f])$ and $T_0 \in \mathscr{C}^2([0,1])$. Then the inverse problem (3.1) - (3.4) has a unique solution if and only if equation (3.44) has a unique positive solution.*

Proof: The proof follows a path similar to the one used for **Theorem 2.1** in Cannon [10]. Assume that the inverse problem (3.1) - (3.4) has a unique solution

$(T(x,t)\,;P_f)$. Therefore, from the above analysis, we find that equation (3.44) has a positive solution P_f.

Let us suppose, by reduction to absurd, that P_f is not the only positive constant that satisfies equation (3.44). Thus there exists $P_{f1} > 0$ and $P_{f2} > 0$, $P_{f1} \neq P_{f2}$, such that both P_{f1} and P_{f2} are solutions of equation (3.44). If we consider

$$T_i(x,t) = e^{-P_{fi}t}\left[\phi(x,t) - \int_0^t \frac{\partial^2 M}{\partial x^2}(x,t-\tau)\overline{f}_i(\tau)d\tau + \int_0^t \frac{\partial^2 M}{\partial x^2}(x-1,t-\tau)\overline{g}_i(\tau)d\tau\right], \tag{3.45}$$

where $\overline{f}_i(\tau) = f(\tau)(e^{P_{fi}\tau}-1)$ and $\overline{g}_i(\tau) = g(\tau)(e^{P_{fi}\tau}-1)$, for $i \in \{1,2\}$, using both the change of variable equation (3.29) and the representation formula (3.34), we obtain that $(T_1(x,t)\,;P_{f1})$ and $(T_2(x,t)\,;P_{f2})$ are both solutions of (3.1) - (3.4). Therefore, since $P_{f1} \neq P_{f2}$ immediately implies $(T_1(x,t)\,;P_{f1}) \neq (T_2(x,t)\,;P_{f2})$, which contradicts the uniqueness assumption for the inverse problem (3.1) - (3.4) that we have considered, we obtain that equation (3.44) has a unique positive solution P_f.

Conversely, let us assume now that equation (3.44) has a unique positive solution P_f. If we suppose by reduction to absurd that there exists two different couples $(T_1(x,t)\,;P_{f1})$ and $(T_2(x,t)\,;P_{f2})$ that are both solutions of (3.1) - (3.4), then by using again the change of variables equation (3.29) and following for each of the solutions all the argument described from equation (3.44) onward, before the statement of our theorem, we obtain that both P_{f1} and P_{f2} are solutions of equation (3.44). However, since equation (3.44) is assumed to have a unique solution, we obtain $P_{f1} = P_{f2} = P_f$. Therefore, the two functions

$$w_i(x,t) = e^{P_f t}T_i(x,t) - \phi(x,t), \quad i \in \{1,2\}, \tag{3.46}$$

satisfy the same problem (3.30)-(3.33) and so, using the representation formula (3.34), we obtain that $w_1(x,t) = w_2(x,t)$, which finally implies that

$$T_1(x,t) = T_2(x,t). \tag{3.47}$$

Thus we can conclude that the inverse problem (3.1) - (3.4) has a unique solution.

□

Remark 3.4.2 *We notice that, using the definition (3.43) and equation (3.44), the construction of the graph of $Q(P_f)$ is sufficient to yield the numerical solution for P_f. A similar analysis holds for the heat flux measurement (3.5) instead of (3.4).*

3.5 Analysis for the Internal Temperature Measurement

Let ϕ_0 be the unique solution of the problem (3.26) - (3.28) with $T_0 = 0$.

Theorem 3.5.1 *Let $f, g \in \mathscr{C}^0([0,t_f])$, $f(0) = g(0) = 0$, $T = 0$, $f \geq 0$, $g \geq 0$, $f^2 + g^2 \not\equiv 0$. Then the inverse problem (3.1) - (3.3) and (3.6) has at most one solution. Moreover, if $u \in (0, \phi_0(x_0,t_0))$ then the solution also exists.*

Proof: The transformation

$$w(x,t) := e^{P_f t} T(x,t) \tag{3.48}$$

recasts the problem (3.1) - (3.3) into

$$\frac{\partial w}{\partial t}(x,t) = \frac{\partial^2 w}{\partial x^2}(x,t), \qquad (x,t) \in (0,1) \times (0,t_f], \tag{3.49}$$

$$w(x,0) = 0, \qquad x \in [0,1], \tag{3.50}$$

$$w(0,t) = f(t)e^{P_f t}, \quad w(1,t) = g(t)e^{P_f t}, \qquad t \in [0,t_f]. \tag{3.51}$$

The internal temperature measurement (3.6) becomes

$$w(x_0,t_0) = ue^{P_f t_0}. \tag{3.52}$$

Since $f, g \in \mathscr{C}^0([0,t_f])$, we have the representation formula (3.34) which, when applied at (x_0,t_0), gives

$$u = \overline{H^*}(P_f), \tag{3.53}$$

where $\overline{H^*}(P_f)$ is defined as

$$\overline{H^*}(P_f) := -\int_0^{t_0} \frac{\partial M}{\partial x}(x_0,t_0-\tau)f(\tau)e^{P_f(\tau-t_0)}d\tau + \int_0^{t_0} \frac{\partial M}{\partial x}(x_0-1,t_0-\tau)g(\tau)e^{P_f(\tau-t_0)}d\tau. \tag{3.54}$$

By taking the derivative of $\overline{H^*}$ with respect to P_f and then using that $f \geq 0$, $g \geq 0$, $\frac{\partial M}{\partial x}(x_0,t_0-\tau) < 0$, $\frac{\partial M}{\partial x}(x_0-1,t_0-\tau) > 0$, $(x_0,\tau) \in (0,1)\times[0,t_0]$, and $f^2+g^2 \not\equiv 0$, we obtain

$$\overline{H^*}'(P_f) < 0. \tag{3.55}$$

This means that the function $\overline{H^*} : (0,\infty) \to \mathbb{R}$ is strictly monotonic decreasing. Hence, $\overline{H^*}$ is injective and therefore equation (3.53) has at most one solution.

By using that $\lim_{\tau \nearrow t_0} \frac{\partial M}{\partial x}(x_0,t_0-\tau) = 0$ and $f(0) = g(0) = 0$, as well as the representation formula (3.34) for ϕ_0, we have

$$0 = \lim_{P_f \to \infty} \overline{H^*}(P_f) < \lim_{P_f \to 0} \overline{H^*}(P_f) = \phi_0(x_0,t_0). \tag{3.56}$$

Let us also note that from the maximum principle we obtain $\phi_0(x_0,t_0) > 0$. Thus we can conclude that the function

$$\overline{H^*} : (0,\infty) \to (0,\phi_0(x_0,t_0)) \tag{3.57}$$

is bijective and hence equation (3.53) has a unique solution if

$$u \in \text{Range}(\overline{H^*}) = (0, \phi_0(x_0, t_0)). \tag{3.58}$$

Finally, the last part of our argument is identical to the proof of the Theorem 3.4.1. Therefore, we obtain the targeted conclusion that the inverse problem (3.1) - (3.3) and (3.6) has at most one solution, which, moreover, does exist if $u \in (0, \phi_0(x_0, t_0))$.

□

3.6 Analysis for the Mass Measurement

Let $T_0 \equiv 0$. If we consider the mass measurement (3.7), then the representation formula (3.34) and the change of variable (3.48) imply

$$\begin{aligned} \mathcal{E}(t_0) &= -\int_0^1 \int_0^{t_0} \frac{\partial M}{\partial x}(x, t_0 - \tau) f(\tau) e^{P_f(\tau - t_0)} d\tau dx \\ &\quad + \int_0^1 \int_0^{t_0} \frac{\partial M}{\partial x}(x - 1, t_0 - \tau) g(\tau) e^{P_f(\tau - t_0)} d\tau dx. \end{aligned} \tag{3.59}$$

After carrying out the integration by invoking Fubini's theorem and then taking advantage of the fact that M is an even function with respect to x, we obtain

$$\mathcal{E}(t_0) = \overline{\overline{H^*}}(P_f), \tag{3.60}$$

where $\overline{\overline{H^*}}(P_f)$ is defined as

$$\overline{\overline{H^*}}(P_f) = \int_0^{t_0} (M(0, t_0 - \tau) - M(1, t_0 - \tau))(f(\tau) + g(\tau)) e^{P_f(\tau - t_0)} d\tau. \tag{3.61}$$

By making use of the fact that $M(0, t_0 - \tau) < M(1, t_0 - \tau)$, we obtain:

Theorem 3.6.1 *Let $f, g \in \mathscr{C}^0([0, t_f])$, $f(0) = g(0)$, $f + g \leq 0$ and $f^2 + g^2 \not\equiv 0$. Then the inverse problem (3.1) - (3.3) and (3.7) has at most one solution. Moreover, if $\mathcal{E}(t_0) \in \left(0, \int_0^1 \phi_0(x, t_0) dx\right)$, then the solution also exists.*

Proof: Under these hypotheses we obtain immediately that $\overline{\overline{H^*}}'(P_f) < 0$. Thus the function $\overline{\overline{H^*}} : (0, \infty) \to \mathbb{R}$ is strictly monotonic decreasing and since the range of $\overline{\overline{H^*}}$ is $\left(0, \int_0^1 \phi_0(x, t_0)dx\right)$, the theorem follows.

□

3.7 Examples and Numerical Results

3.7.1 Homogeneous Boundary Conditions

Let us first find the solution of the inverse problem (3.1) - (3.4) considering the particular data for the initial condition

$$T(x, 0) = sin(\pi x), \quad x \in [0, 1], \tag{3.62}$$

and the boundary conditions

$$T(0, t) = T(1, t) = 0, \quad t \in (0, t_f], \tag{3.63}$$

while the flux measurement (3.4) is taken at a fixed point $t_0 \in (0, t_f]$ as

$$-\frac{\partial T}{\partial x}(0, t_0) = -\pi e^{-(\pi^2+1)t_0}. \tag{3.64}$$

By using the change of variable (2.23), we obtain the governing equation

$$\frac{\partial v}{\partial t}(x, t) = \frac{\partial^2 v}{\partial x^2}(x, t), \quad (x, t) \in (0, 1) \times (0, 1] \tag{3.65}$$

with the corresponding initial condition

$$v(x, 0) = \sin(\pi x), \quad x \in [0, 1], \tag{3.66}$$

and the boundary conditions

$$v(0, t) = v(1, t) = 0, \quad t \in (0, t_f]. \tag{3.67}$$

The flux measurement (3.64) transforms into

$$-\frac{\partial v}{\partial x}(0,t_0) = -\pi e^{-(\pi^2+1)t_0} e^{P_f t_0}. \tag{3.68}$$

However, by solving the heat equation (3.65) with the initial condition (3.66) and boundary conditions (3.67), we obtain

$$v(x,t) = \sin(\pi x) e^{-\pi^2 t}, \quad (x,t) \in [0,1] \times (0,t_f]. \tag{3.69}$$

Thus from (3.68) and (3.69) we infer that

$$-\pi e^{-(\pi^2+1)t_0} e^{P_f t_0} = -\frac{\partial v}{\partial x}(0,t_0) = -\pi e^{-\pi^2 t_0}. \tag{3.70}$$

Therefore $e^{(P_f-1)t_0} = 1$ and so $P_f = 1$. Using the solution (3.69), and going backwards through the transformation (2.23), we obtain $T(x,t) = \sin(\pi x) e^{-(\pi^2+1)t}$ as the corresponding solution for equations (3.1) - (3.3) and so

$$T(x,t) = \sin(\pi x) e^{-(\pi^2+1)t} \quad ; \quad P_f = 1 \tag{3.71}$$

is the unique solution for our inverse problem (3.1) and (3.62)-(3.64).

If instead of the flux measurement (3.64), we have the internal temperature measurement (3.6), this recasts our case as

$$T(x_0,t_0) = \sin(\pi x_0) e^{-t_0(\pi^2+1)}. \tag{3.72}$$

Then the transformation (2.23) gives

$$v(x_0,t_0) = \sin(\pi x_0) e^{-t_0(\pi^2+1)} e^{P_f t_0}. \tag{3.73}$$

Since $\sin(\pi x_0) \neq 0$, from (3.69) we obtain both $P_f = 1$ and the unique solution (3.71).

Also, if instead of the flux measurement (3.64) we have the mass measurement (3.7)

$$\mathcal{E}(t_0) = \int_0^1 T(x,t_0)dx = \frac{2e^{-t_0(\pi^2+1)}}{\pi}, \tag{3.74}$$

then the transformation (2.23) gives

$$\int_0^1 v(x,t_0) = \frac{2e^{-t_0(\pi^2+1)}e^{P_f t_0}}{\pi}. \tag{3.75}$$

Using (3.69) we obtain again both $P_f = 1$ and the unique solution (3.71).

Provided that the boundary conditions (3.3) are homogeneous, as in (3.63), the above analysis can be generalized to an arbitrary integrable function T_0 with $T_0(0) = T_1(1) = 0$.

By considering $T_0 \in \mathscr{C}^2([0,1])$, the solution of the problem (3.1)-(3.2) and (3.63), may be obtained by separation of variables and is given as follows,

$$T(x,t) = e^{-P_f t}\sum_{l=1}^{\infty}\zeta_l e^{-l^2\pi^2 t}\sin(l\pi x), \tag{3.76}$$

where $\zeta_l = 2\int_0^1 T_0(\xi)\sin(l\pi\xi)d\xi$, $l = 1,2...$, see Horvath [58] and Tikhonov and Samarskii [110]. By differentiating the Fourier series (3.76) with respect to x, we obtain a uniform convergent series. Thus the derivative

$$\frac{\partial T}{\partial x}(x,t) = \pi e^{-P_f t}\sum_{l=1}^{\infty} l\zeta e^{-l^2\pi t}\cos(l\pi x) \tag{3.77}$$

is continuous on $[0,1]\times[0,t_f]$.

Let us also introduce the mass function

$$\mathcal{E}(t) = \int_0^1 T(x,t)dx, \qquad t \geq 0. \tag{3.78}$$

From (3.76) we obtain

$$\mathcal{E}(t) = \frac{e^{-P_f t}}{\pi}\sum_{l=1}^{\infty}\frac{\zeta_l}{l}[1-(-1)^l]e^{-l^2\pi^2 t}. \tag{3.79}$$

We remark that the particular case of $T_0(x) = \sin(\pi x)$ falls within our current general analysis, since $\zeta_1 = 2\int_0^1 sin^2(\pi\xi)dx = 1$ and $\zeta_l = 0$ for all $l \geq 2$.

Considering now the analytical expression (3.76) within the specific context of each type of measurements (3.4)-(3.7), we obtain:

$$h_0 = -\frac{\partial T}{\partial x}(0,t_0) = -\pi e^{-P_f t_0} \sum_{l=1}^{\infty} l\zeta_l e^{-l^2\pi^2 t_0}, \tag{3.80}$$

$$h_1 = \frac{\partial T}{\partial x}(1,t_0) = \pi e^{-P_f t_0} \sum_{l=1}^{\infty} (-1)^l l\zeta_l e^{-l^2\pi^2 t_0}, \tag{3.81}$$

$$u = T(x_0,t_0) = e^{-P_f t_0} \sum_{l=1}^{\infty} \zeta_l e^{-l^2\pi^2 t_0} \sin(l\pi x_0), \tag{3.82}$$

$$\mathcal{E}(t_0) = \int_0^1 T(x,t_0)dx = \frac{e^{-P_f t_0}}{\pi} \sum_{l=1}^{\infty} \frac{\zeta_l}{l}[1-(-1)^l]e^{-l^2\pi^2 t_0}. \tag{3.83}$$

From these expressions, using the existence and uniqueness theorems from the previous sections, we obtain the necessary and sufficient conditions for the existence and uniqueness of the perfusion coefficient P_f in each of the four additional measurement cases, namely

Case 1: for the flux measurement (3.4):

$$0 < A := -\frac{h_0}{\pi \sum_{l=1}^{\infty} l\zeta_l e^{-l^2\pi^2 t_0}} < 1, \tag{3.84}$$

Case 2: for the flux measurement (3.5):

$$0 < A := \frac{h_1}{\pi \sum_{l=1}^{\infty} (-1)^l l\zeta_l e^{-l^2\pi^2 t_0}} < 1, \tag{3.85}$$

Case 3: for the internal temperature measurement (3.6):

$$0 < A := \frac{u}{\sum_{l=1}^{\infty} \zeta_l e^{-l^2\pi^2 t_0} \sin(l\pi x_0)} < 1, \tag{3.86}$$

Case 4: for the mass measurement (3.7):

$$0 < A := \frac{\pi \mathcal{E}(t_0)}{2\sum_{l=0}^{\infty} \frac{\zeta_{2l+1}}{2l+1} e^{-(2l+1)^2\pi^2 t_0}} < 1. \tag{3.87}$$

From (3.81)-(3.83) we obtain P_f explicitly given by

$$P_f = -\frac{\ln(A)}{t_0}. \tag{3.88}$$

Equation (3.88) shows that the stability of P_f is of logarithmic type, and decreases as t_0 decreases.

Once P_f has been determined, equation (3.76) provides the temperature solution $T(x,t)$.

3.7.2 A Numerical Example

While the above examples have embraced an analytical treatment, in the following example an important numerical method comes into play. Taking for simplicity $t_f = 1$, we consider the exact solution

$$T(x,t) = (x^2 + 2t)e^{-t} \; ; \quad P_f = 1 \tag{3.89}$$

for the inverse coefficient identification problem (ICIP) given by equations (3.1) - (3.4), which in the case considered, recast as follows:

$$\frac{\partial^2 T}{\partial x^2}(x,t) - P_f T(x,t) = \frac{\partial T}{\partial t}(x,t), \quad (x,t) \in (0,1) \times (0,1], \tag{3.90}$$

$$T(x,0) = x^2, \qquad x \in [0,1], \tag{3.91}$$

$$\begin{aligned} T(0,t) &= 2te^{-t}, \qquad t \in [0,1], \\ T(1,t) &= (1+2t)e^{-t}, \quad t \in [0,1]. \end{aligned} \tag{3.92}$$

Further, the flux measurement (3.4) is taken as

$$-\frac{\partial T}{\partial x}(0,t_0) = h_0 = 0. \tag{3.93}$$

Employing the transformation (2.23), we obtain

$$v(x,t) = x^2 + 2t, \quad P_f = 1 \tag{3.94}$$

which is the corresponding exact solution for the transformed problem given by

$$\frac{\partial v}{\partial t}(x,t) = \frac{\partial^2 v}{\partial x^2}(x,t), \quad (x,t) \in (0,1) \times (0,1] \tag{3.95}$$

$$v(x,0) = x^2, \qquad x \in [0,1], \tag{3.96}$$

$$\begin{aligned} v(0,t) &= 2te^{(P_f-1)t}, \qquad t \in [0,1], \\ v(1,t) &= (2t+1)e^{(P_f-1)t}, \quad t \in [0,1], \end{aligned} \tag{3.97}$$

$$-\frac{\partial v}{\partial x}(0,t_0) = 0. \tag{3.98}$$

Using the BEM for solving (3.95) - (3.97), we obtain $-\frac{\partial v}{\partial x}(0,t_0;P_f)$. Here, as well as in all the other numerical experiments throughout this subsection, we apply the BEM with $N = 320$ constant boundary elements and the number of space cells used to discretise the space domain $(0,1)$ is taken to be $N_0 = 160$. This number of discretisations was found sufficiently large such that, in all the numerical tests considered in this subsection, any further increase does not significantly affect the accuracy of the numerical results for the direct problem (3.95) - (3.97), with P_f known. By plotting the function

$$\begin{aligned} &S : (0,\infty) \longrightarrow \mathbb{R}_+, \\ &S(P_f) = \left| -\tfrac{\partial v}{\partial x}(0,t_0;P_f) \right| \end{aligned} \tag{3.99}$$

we determine its global minimum which should be located at $P_f = 1$. Figures 3.1 and 3.2 illustrate the variation of S, as a function of $P_f \in (0,2]$, when $t_0 \in \{\tilde{t}_1, \tilde{t}_2, \tilde{t}_{\frac{N}{2}}, \tilde{t}_N\}$, where $\tilde{t}_j$, $j = \overline{1,N}$, denote the element midpoint nodes of a uniform discretisation of the time interval $[0, t_f = 1]$. As one may notice, in Figure 3.1(b), the computation for the plot associated with $\tilde{t}_1$ would have been facing "a corner effect", thus heavily affected by round-off errors and so very badly behaving. However, we treat this issue by solving the problem again for a new

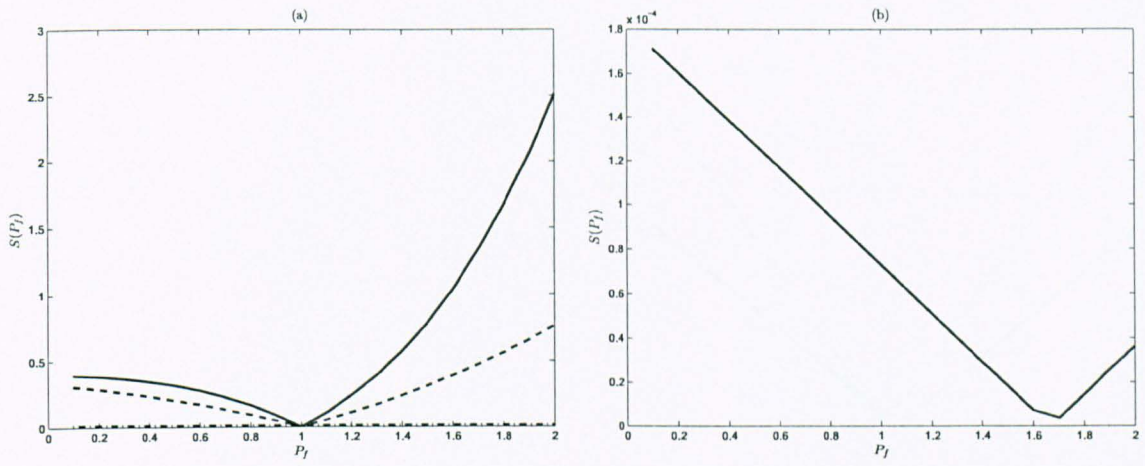

Figure 3.1: Variation of S with P_f when (a) the flux measurement is taken at $(0, \tilde{t}_2)$, $(0, \tilde{t}_{\frac{N}{2}})$, $(0, \tilde{t}_N)$, and (b) the flux measurement is taken only at $(0, \tilde{t}_1)$. In case (a) we have: solid line for $\tilde{t}_N$, dashed line is for $\tilde{t}_{\frac{N}{2}}$ and dash-dot line for $\tilde{t}_2$. In case (b) solid line is for $\tilde{t}_1$.

final time $t_f := \tilde{t}_1$, and in this way the time boundary element node $\tilde{t}_1$, from the initial computation, becomes the new $\tilde{t}_N$, see Figure 3.2(b), so that the corner effect encountered before has now vanished and thus, for the Figures 3.2(a) and 3.2(b), the plotted data have been obtained by using the code modified accordingly. Because of the large difference in scales between the plots corresponding to $\tilde{t}_1$ and $\tilde{t}_2$, which are of the order of 10^{-3}, relative to the ones corresponding to $\tilde{t}_{\frac{N}{2}}$ and $\tilde{t}_N$, which are of the order of 10, we recast the first two ones separately in Figure 3.2(b).

We consider now the ICIP given by (3.90)-(3.92) for the case of the flux measurement (3.5) at the right boundary $x = 1$, namely

$$\frac{\partial T}{\partial x}(1, t_0) = h_1 = 2e^{-t_0}. \tag{3.100}$$

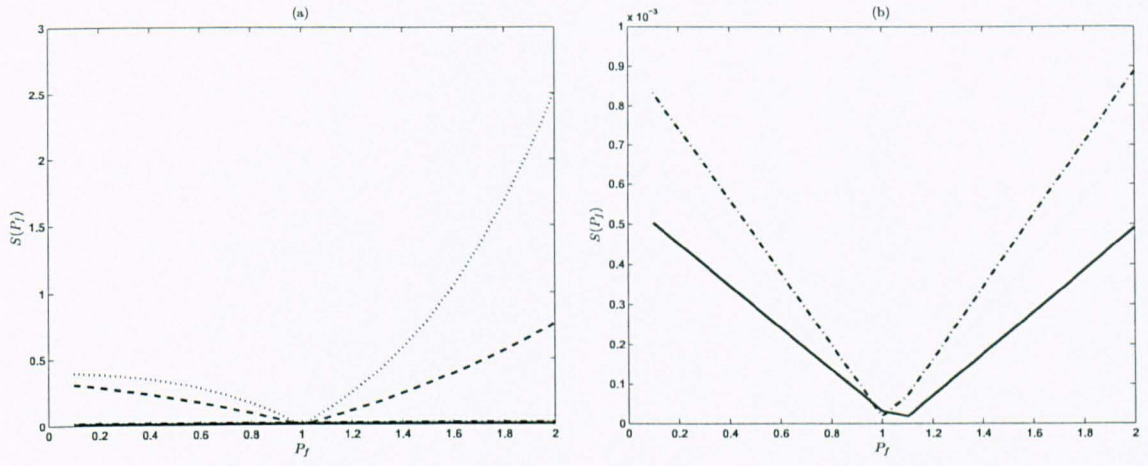

Figure 3.2: Variation of S with P_f when (a) the flux measurement is taken at $(0, \tilde{t}_1)$, $(0, \tilde{t}_2)$, $(0, \tilde{t}_{\frac{N}{2}})$ or $(0, \tilde{t}_N)$, and (b) the flux measurements is taken at $(0, \tilde{t}_1)$ and $(0, \tilde{t}_2)$. In both cases we have: dotted line for $\tilde{t}_N$, dashed line for $\tilde{t}_{\frac{N}{2}}$, dash-dot line for $\tilde{t}_2$ and solid line for $\tilde{t}_1$.

Using the transformation (2.23), the converted problem (3.95)-(3.97) receives the flux measurement

$$\frac{\partial v}{\partial x}(1, t_0) = 2e^{(P_f - 1)t_0} . \tag{3.101}$$

Using again the BEM for (3.95) - (3.97) we obtain $\frac{\partial v}{\partial x}(1, t_0; P_f)$. By plotting the function

$$\begin{aligned} &S : (0, \infty) \longrightarrow \mathbb{R}_+, \\ &S(P_f) = \left| \tfrac{\partial v}{\partial x}(1, t_0; P_f) - 2e^{(P_f - 1)t_0} \right| \end{aligned} \tag{3.102}$$

we determine the global minimum which should be located at $P_f = 1$. The corner effect is again avoided by using the technique described in the case of the flux measurement at $x = 0$. Figure 3.3 illustrates the variation of S, as a function of $P_f \in (0, 2]$, when $t_0 \in \{\tilde{t}_1, \tilde{t}_2, \tilde{t}_{\frac{N}{2}}, \tilde{t}_N\}$. Again, because of the difference in scales between the plots corresponding to $\tilde{t}_1$ and $\tilde{t}_2$, which are of the order 10^{-2}, relative

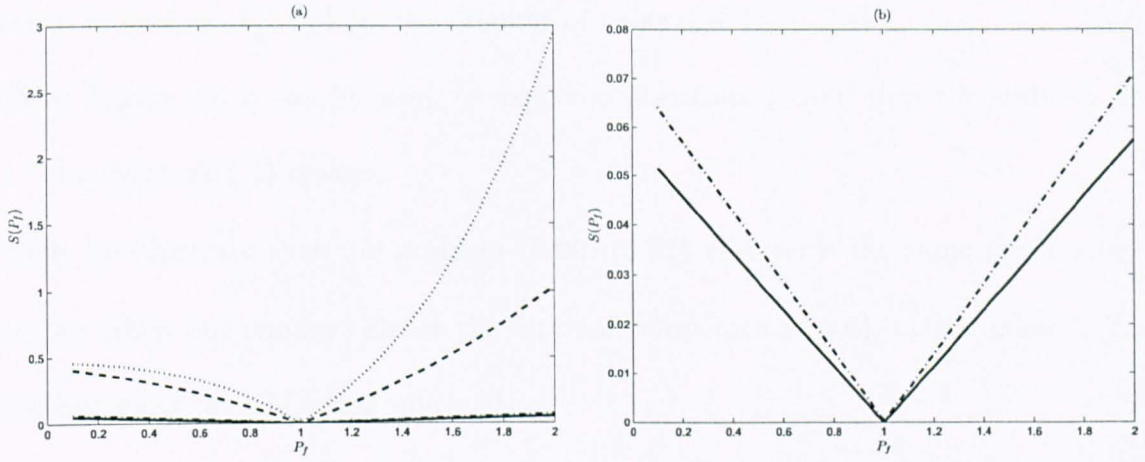

Figure 3.3: Variation of S with P_f when (a) the flux measurement is taken at $(1, \tilde{t}_1)$, $(1, \tilde{t}_2)$, $(1, \tilde{t}_{\frac{N}{2}})$ or $(1, \tilde{t}_N)$, and (b) the flux measurement is taken at $(1, \tilde{t}_1)$ or $(1, \tilde{t}_2)$. In both (a) and (b) we have: dotted line for $\tilde{t}_N$, dashed line for $\tilde{t}_{\frac{N}{2}}$, dash-dot line for $\tilde{t}_2$ and solid line for $\tilde{t}_1$.

to the ones corresponding to $\tilde{t}_{\frac{N}{2}}$ and $\tilde{t}_N$, which are of the order 10, we recast the former ones separately in Figure 3.3(b).

By comparing Figures 3.2 and 3.3, we notice that the numerical results have a very similar structure for the two types of flux measurements at $x = 0$ and $x = 1$.

Another important aspect is the effect of noisy data in the flux measurement (3.100). Here we take

$$\frac{\partial T}{\partial x}(1, t_0) = 2e^{-t_0}(1 + \alpha), \tag{3.103}$$

or

$$\frac{\partial v}{\partial x}(1, t_0) = 2e^{(P_f - 1)t_0}(1 + \alpha), \tag{3.104}$$

where, throughout the subsection, α is considered the percentage of noise up to 4%.

Figure 3.4 shows the variation of S given by (3.102), as a function of $P_f \in (0, 2]$,

when $t_0 \in \{\tilde{t}_1, \tilde{t}_2, \tilde{t}_{\frac{N}{2}}, \tilde{t}_N\}$ for the amount of noise $\alpha \in \{1,2,3,4\}\%$.

From Figure 3.4 it can be seen, as expected also from (3.88), that the stability of P_f decreases as t_0 decreases.

Next we illustrate that the problem (3.90)-(3.92) maintains the same general behavior when one employs either the internal temperature (3.6), or the mass (3.7), measurement, as additional information.

Considering first the internal temperature measurement (3.6), namely

$$T(x_0, t_0) = (x_0^2 + 2t_0)e^{-t_0}, \tag{3.105}$$

the change of variable (2.23) transforms (3.105) into the internal measurement

$$v(x_0, t_0) = (x_0^2 + 2t_0)e^{(P_f-1)t_0} \tag{3.106}$$

associated with the converted problem (3.95)-(3.97).

In order to illustrate the typical numerical results obtained using the BEM for solving (3.95)-(3.97), we compute $v(x_0, t_0; P_f)$, for internal temperatures taken at $(0.5, \tilde{t}_N)$, $(0.5, \tilde{t}_{\frac{N}{2}})$, $(0.5, \tilde{t}_{\frac{N}{4}})$ and $(0.5, \tilde{t}_{\frac{N}{8}})$. We plot the function

$$\begin{aligned} &S : (0, \infty) \longrightarrow \mathbb{R}_+, \\ &S(P_f) = \left| v(x_0, t_0; P_f) - (x_0^2 + 2t_0)e^{(P_f-1)t_0} \right|, \end{aligned} \tag{3.107}$$

expecting to obtain a curve with the global minimum located close to the point $P_f = 1$. Figure 3.5 illustrates the variation of S given by (3.107), as a function of $P_f \in (0,2]$, when $x_0 = 0.5$, $t_0 \in \left\{\tilde{t}_{\frac{N}{8}}, \tilde{t}_{\frac{N}{4}}, \tilde{t}_{\frac{N}{2}}, \tilde{t}_N\right\}$ and $\alpha \in \{0,1,2,3,4\}\%$ noise included in the measurements (3.105), as

$$T(x_0, t_0) = (x_0^2 + 2t_0)e^{-t_0}(1 + \alpha), \tag{3.108}$$

or

$$v(x_0, t_0) = (x_0^2 + 2t_0)e^{(P_f-1)t_0}(1 + \alpha). \tag{3.109}$$

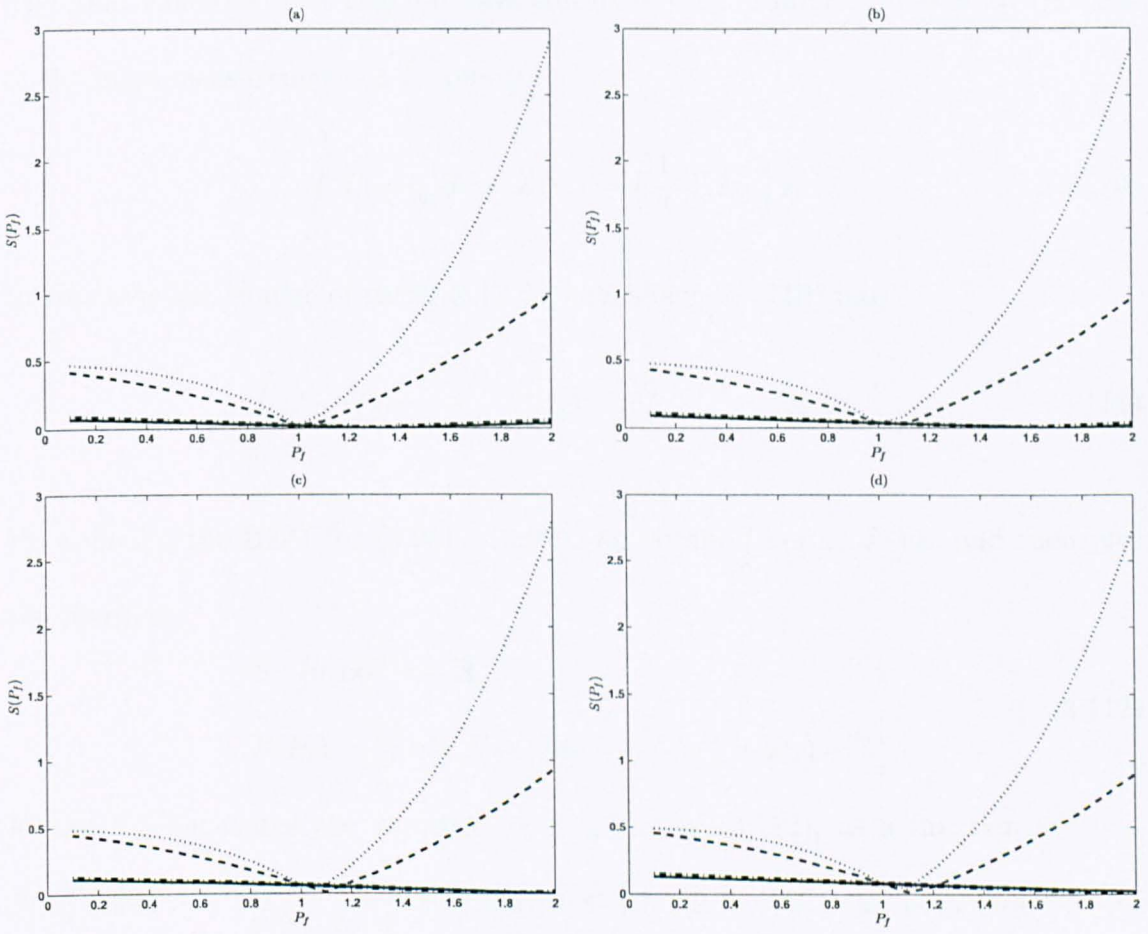

Figure 3.4: Variation of S with P_f when the flux measurements are taken at $(1, \tilde{t}_1)$, $(1, \tilde{t}_2)$, $(1, \tilde{t}_{\frac{N}{2}})$ and $(1, \tilde{t}_N)$ for cases: (a) 1% noise, (b) 2% noise, (c) 3% noise and (d) 4% noise. In all cases we have: dotted line for $\tilde{t}_N$, dashed line for $\tilde{t}_{\frac{N}{2}}$, dash-dot line for $\tilde{t}_2$ and solid line for $\tilde{t}_1$.

From Figure 3.5 it can be seen that the minimum of S is indeed achieved close to $P_f \approx 1$, Figure 3.5(a), showing also the good stability of the numerical results when the noisy data (3.108) are inverted, see Figures 3.5(b)-3.5(c).

The final numerical test that we have considered for example (3.89) is for the case of the mass measurement (3.7), namely

$$\int_0^1 T(x,t_0)dx = \mathcal{E}(t_0) = \left(\frac{1}{3} + 2t_0\right) e^{-t_0}. \tag{3.110}$$

In this case the change of variable (2.23) transforms (3.110) into

$$\int_0^1 v(x,t_0)dx = e^{P_f t_0}\mathcal{E}(t_0) = e^{P_f t_0}\left(\frac{1}{3} + 2t_0\right) e^{-t_0}. \tag{3.111}$$

By applying the BEM for (3.95) - (3.97), we obtain $\int_0^1 v(x,t_0;P_f)dx$ and then plot the function

$$\begin{aligned} &S : (0,\infty) \longrightarrow \mathbb{R}_+, \\ &S(P_f) = \left| \int_0^1 v(x,t_0;P_f)dx - e^{P_f t_0}\left(\tfrac{1}{3} + 2t_0\right) e^{-t_0} \right|. \end{aligned} \tag{3.112}$$

Figure 3.6 illustrates the variation of S given by (3.112), as a function of $P_f \in (0,2]$ when $t_0 \in \left\{\tilde{t}_{\frac{N}{8}}, \tilde{t}_{\frac{N}{4}}, \tilde{t}_{\frac{N}{2}}, \tilde{t}_N\right\}$ and $\alpha \in \{0,1,2,3,4\}\%$ noise is included in the measurement (3.110), as

$$\int_0^1 T(x,t_0)dx = \left(\frac{1}{3} + 2t_0\right) e^{-t_0}(1+\alpha), \tag{3.113}$$

or

$$\int_0^1 v(x,t_0)dx = e^{P_f t_0}\left(\frac{1}{3} + 2t_0\right) e^{-t_0}(1+\alpha). \tag{3.114}$$

Again, the same conclusions as those drawn from Figure 3.5 are obtained.

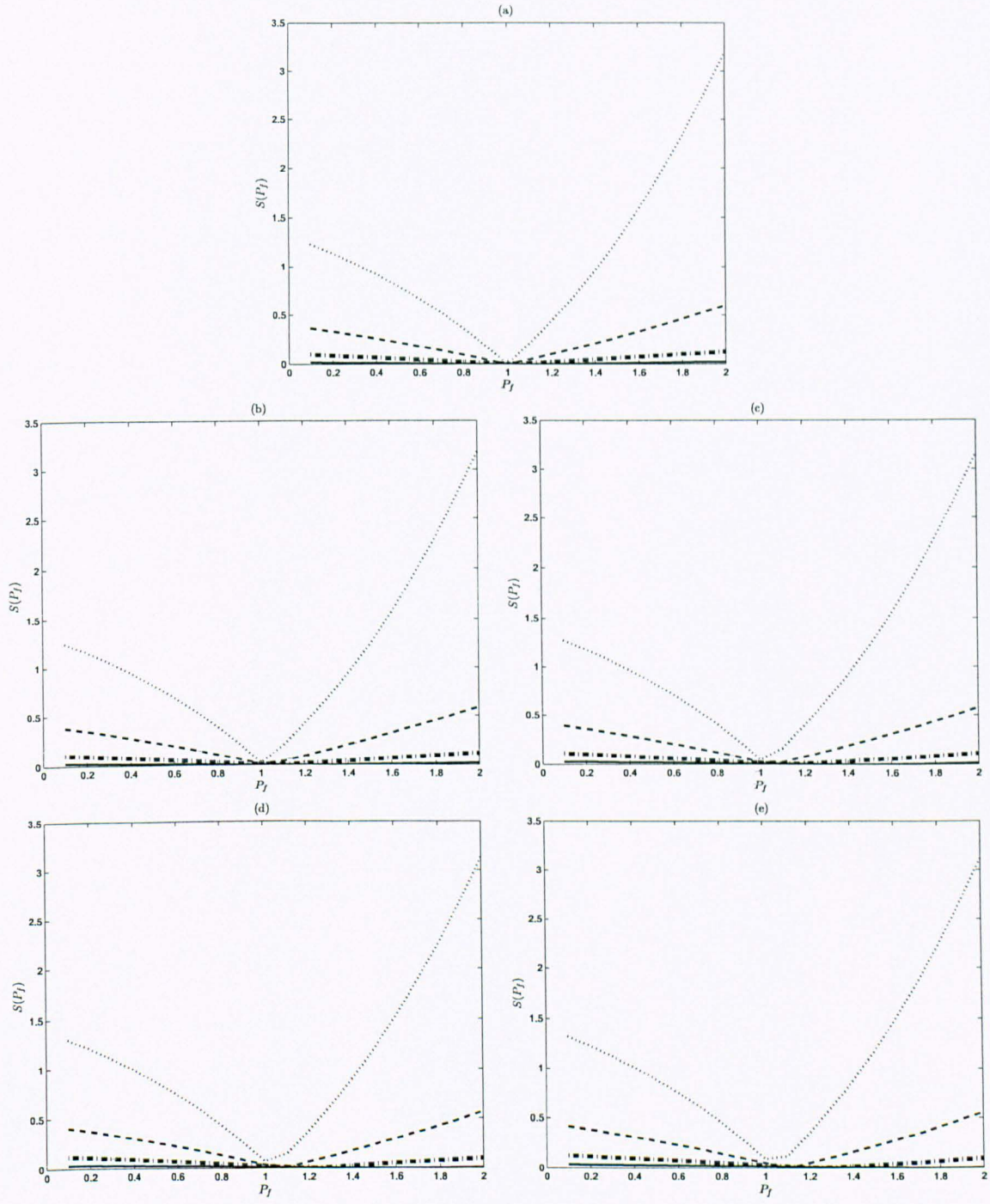

Figure 3.5: Variation of S with P_f when the temperature measurement data is taken at the interior points $(0.5, \tilde{t}_{\frac{N}{8}})$, $(0.5, \tilde{t}_{\frac{N}{4}})$, $(0.5, \tilde{t}_{\frac{N}{2}})$ and $(0.5, \tilde{t}_{N})$ for: (a) exact data, (b) 1% noise, (c) 2% noise, (d) 3% noise, and (e) 4% noise. In all the cases we have: dotted line for $\tilde{t}_{N}$, dashed line for $\tilde{t}_{\frac{N}{2}}$, dash-dot line for $\tilde{t}_{\frac{N}{4}}$ and solid line for $\tilde{t}_{\frac{N}{8}}$.

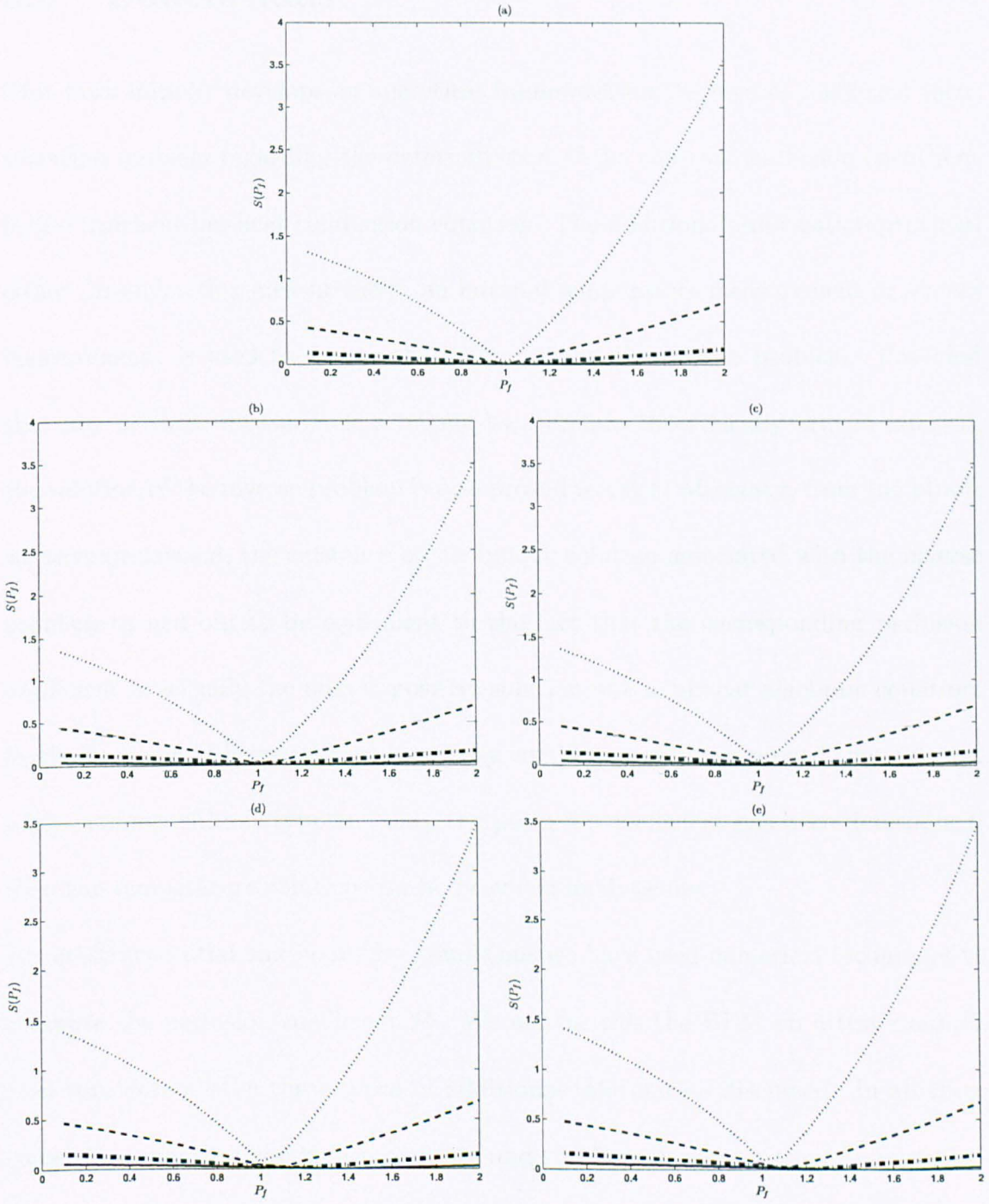

Figure 3.6: Variation of S with P_f when the mass measurement data is taken at $\tilde{t}_{\frac{N}{8}}$, $\tilde{t}_{\frac{N}{4}}$, $\tilde{t}_{\frac{N}{2}}$ and $\tilde{t}_N$, for: (a) exact data, (b) 1% noise, (c) 2% noise, (d) 3% noise, and (e) 4% noise. In all cases we have: dotted line for $\tilde{t}_N$, dashed line for $\tilde{t}_{\frac{N}{2}}$, dash-dot line for $\tilde{t}_{\frac{N}{4}}$ and solid line for $\tilde{t}_{\frac{N}{8}}$.

3.8 Conclusions

This work initially develops an analytical framework for the inverse coefficient identification problem regarding the determination of the constant perfusion coefficient in the transient bio-heat conduction equation. The additional information provided either through a flux measurement, an internal temperature measurement or a mass measurement, is used to ensure the uniqueness of the inverse problem. Provided that any of these measurements belong to a certain theoretically argued interval, the solution of the inverse problem is also proved to exist. Moreover, from the proofs we have performed, the existence of the unique solution associated with the inverse problem turned out to be equivalent to the fact that the corresponding perfusion coefficient is actually the unique positive solution of a nonlinear algebraic equation. In the presence of homogeneous boundary conditions, we have proved that the stability is of logarithmic type and once the perfusion coefficient has been determined, then the temperature solution can be provided analytically.

For arbitrary initial and boundary conditions we have used numerical techniques to compute the perfusion coefficient P_f. We use for this the BEM on a test example that considers all the three types of additional information discussed. In all three cases, the numerical results are accurate and stable with respect to noisy perturbations of the input data. Further, it was noticed that the stability of the solution increases with respect to increasing the non-dimensional time instant t_0 at which the additional measurement is recorded.

In the next chapter we will extend this analysis to the inverse problem of recovering a time-dependent perfusion coefficient.

Chapter 4

The Inverse Time-Dependent Perfusion Coefficient Identification

4.1 Introduction

The investigation opened in Chapter 3 with the constant coefficient case is now naturally extended to the case when the perfusion coefficient P_f is dependent on time.

Since, in the inverse problems under investigation, both the temperature $T(x,t)$ and the time-dependent perfusion coefficient $P_f(t)$ are unknown, the nonlinear inverse problems that are generated by the second-order parabolic equation (1.2) will be solved under the prescription of initial and boundary conditions on the boundary $\Gamma = \partial\Omega$, when additional information is provided from one of various types of measurements that can be taken. As described in the experimental work reviewed in Chapter 1, see Cardinali et al. [22], Deng and Liu [45], Loulou and Scott [71], Robinson et al. [97] and Scott et al. [98, 99], the measurements accuracy, their

invasiveness character or the extent of practical use, as well as the ability to take continuous measurements, create constraints over the range of types of possible additional information that can be considered. In a first approach described in the previous chapter, the case where P_f is constant has been discussed from both analytical and numerical stand points. However, the blood perfusion need not be constant in time in all the regions of the body.

This chapter discusses the retrieval of the time-dependent coefficient $P_f(t)$ along with the temperature $T(x,t)$ from various types of measured noisy and exact data. The one-dimensional version of equation (1.2) is given by

$$\frac{\partial^2 T}{\partial x^2}(x,t) - P_f(t)T(x,t) = \frac{\partial T}{\partial t}(x,t), \quad (x,t) \in (0,1) \times (0,t_f]. \tag{4.1}$$

Since the technique described in this chapter can be easily extended to higher dimensions, we focus our discussion on the one-dimensional problem, when Dirichlet or mixed boundary conditions are considered. As additional information, either time-dependent internal temperature measurements at fixed or moving points inside the region $(0,1)$ are taken, or total mass or partial mass measurements are supplied, or alternatively we have heat flux measurements on a part of the boundary $\Gamma = \{0,1\}$. All the measurement data are assumed to exhibit both exact and noisy characteristics.

Using an appropriate change of variable, which is of a similar nature with (2.2), the equation (4.1) will be transformed into the standard heat equation form and then the BEM will be employed. As we will see in the forthcoming sections, by performing this change of variable, the unknown time-dependent coefficient $P_f(t)$ will cause the resulting boundary conditions, as well as the measurements, to become unknown

for the obtained heat equation problem. However, in both the induced boundary conditions and the measurements for the transformed equation, the inherited structure determined by the original equation (4.1) and by the change of variable will be exploited in our attempt for the simultaneous retrieval of the unknowns $P_f(t)$ and $T(x,t)$.

Although the inverse problems considered in this chapter may have a unique solution, they are still ill-posed, since the solution does not depend continuously on the measured data (4.4), (4.5) or (4.6). In other words, this means that small errors introduced in the measured data can cause large errors in the solution $(T(x,t), P_f(t))$. In dealing with such a situation, regularization techniques based on the mollification method will be employed.

4.2 Mathematical Formulation

In this chapter we consider the following inverse problems:

Find $T(x,t)$ in $\mathscr{C}^{2,1}((0,1)\times(0,t_f]) \bigcap \mathscr{C}^{1,0}([0,1]\times[0,t_f])$ and the time-dependent perfusion coefficient $P_f(t)$ in $\mathscr{C}^0([0,t_f])$ satisfying the one-dimensional time-dependent bio-heat equation (4.1) subject to the initial condition

$$T(x,0) = T_0(x), \quad x \in [0,1], \tag{4.2}$$

the Dirichlet boundary conditions

$$\begin{aligned} T(0,t) &= f(t), \quad t \in [0,t_f], \ f(0) = T_0(0), \\ T(1,t) &= g(t), \quad t \in [0,t_f], \ g(0) = T_0(1), \end{aligned} \tag{4.3}$$

and, for the time being, one of the following types of additional information:

a) a interior temperature measurement at a given space point $x_0 \in (0,1)$

$$T(x_0,t) = u(t), \qquad t \in (0,t_f),\ u(0) = T_0(x_0), \tag{4.4}$$

b) a mass measurement

$$\int_0^1 T(x,t)dx = \mathcal{E}(t), \qquad t \in (0,t_f),\ \mathcal{E}(0) = \int_0^1 T_0(x)dx, \tag{4.5}$$

c) a flux measurement

$$\frac{\partial T}{\partial x}(1,t) = h_1(t), \qquad t \in (0,t_f),\ h_1(0) = T_0'(1). \tag{4.6}$$

The heat flux measurement (4.6) at $x = 1$ can be replaced, with no modification, by a heat flux measurement at $x = 0$.

The non-local mass specification (4.5) arises in many important applications in heat transfer in which the source control parameter $P_f(t)$ needs to be determined so that a desired thermal energy (4.5) can be obtained over the spatial domain.

More general types of measurements will be considered at the end of the chapter, in Sections 4.7 and 4.8. Further, as we will see after Section 4.6, the Dirichlet boundary conditions may also be replaced with *mixed boundary conditions*, i.e. where on a part of the boundary $\Gamma_0 \subset \Gamma$, we know only the temperature, while on $\Gamma \setminus \Gamma_0$ we know only the heat flux.

Defining

$$r(t) := \exp\left(\int_0^t P_f(\tau)d\tau\right), \qquad t \in [0,t_f], \tag{4.7}$$

the change of variable

$$v(x,t) = r(t)T(x,t) \tag{4.8}$$

transforms the time-dependent coefficient heat problem (4.1)-(4.3) into a constant coefficient heat equation problem, namely

$$\frac{\partial^2 v}{\partial x^2}(x,t) = \frac{\partial v}{\partial t}(x,t), \qquad (x,t) \in [0,1] \times (0,t_f], \tag{4.9}$$

$$v(x,0) = T_0(x) =: v_0(x), \quad x \in [0,1], \tag{4.10}$$

$$\begin{aligned} v(0,t) &= \overline{f}(t) := r(t)f(t), \quad t \in [0,t_f],\ \overline{f}(0) = T_0(0), \\ v(1,t) &= \overline{g}(t) := r(t)g(t), \quad t \in [0,t_f],\ \overline{g}(0) = T_0(1). \end{aligned} \tag{4.11}$$

4.3 The Internal Temperature Measurement at a Fixed Space Point

In this section we investigate the inverse problem given by equations (4.1)-(4.4). In (4.3) and (4.4), the conditions

$$f(0) = T_0(0),\ g(0) = T_0(1),\ u(0) = T_0(x_0) \tag{4.12}$$

are called compatibility conditions of order zero. Further, we need compatibility conditions up to first-order which require the conditions (4.12) be satisfied and in addition

$$\begin{aligned} f'(0) &= T_0''(0) + \tfrac{T_0(0)(u'(0) - T_0''(x_0))}{T_0(x_0)}, \\ g'(0) &= T_1''(1) + \tfrac{T_0(1)(u'(0) - T_0''(x_0))}{T_0(x_0)}, \quad T_0(x_0) > 0. \end{aligned} \tag{4.13}$$

The solvability of the inverse problem (4.1)-(4.4) in the spaces $\mathscr{C}^{k+\alpha}$, with α fixed in $(0,1)$ and $k \in \mathbb{N}$, of continuous functions with Hölder continuous derivatives, see Friedman [53] and Ladyzhenskaya et al. [65], has been established in Cannon et al. [18] and Prilepko and Solov'ev [88], as follows:

Theorem 4.3.1 *If* $T_0 \in \mathscr{C}^{2+\alpha}([0,1])$, $f, g, u \in \mathscr{C}^{1+\alpha/2}([0,t_f])$, $T_0 \geq 0$, $f \geq 0$, $g \geq 0$, $u > 0$, *and the compatibility conditions up to first order are satisfied, then there*

exists a unique solution ($T \in \mathscr{C}^{2+\alpha,\,1+\alpha/2}([0,1]\times[0,t_f])$, $P_f \in \mathscr{C}^{\alpha/2}([0,t_f])$) *of the inverse problem (4.1)-(4.4) which is continuously dependent upon data.*

Remark that the theorem does not guarantee that the solution for P_f is positive, hence only the uniqueness of the solution ($T(x,t)$, $P_f(t) > 0$) can be concluded. Prior to this study, numerical methods based on finite differences, see Baran [5], and Dehghan [40, 42], and radial basis functions (RBF), see Dehghan and Tatari [43], have been developed for solving (4.1)-(4.4), with extensions to two-dimensional rectangular domains given in Baran and Fatullayev [6], Cannon et al. [19], and Dehghan [36, 37, 39]. However, the finite-difference method is not easy to implement in higher dimensional irregular domains, whilst the RBF method is only an approximate meshless method which lacks rigour. Therefore, in order to overcome some of these difficulties, in this section we propose the BEM for solving the inverse problem of finding the solution ($v(x,t)$, $r(t)$) with $v \in \mathscr{C}^{2,1}((0,1)\times(0,t_f]) \bigcap \mathscr{C}^{1,0}([0,1]\times[0,t_f])$, $r \in \mathscr{C}^{1}([0,t_f])$, $r'(t) > 0$ for $t \in (0,t_f]$, $r(0) = 1$, which is satisfying (4.9)-(4.11) and the transformed interior measurement

$$v(x_0,t) = r(t)u(t), \qquad t \in [0,t_f],\ u(0) = T_0(x_0). \tag{4.14}$$

Even though both the boundary conditions and the measured data for (4.10)-(4.14) are unknown, an essential assistance in our approach comes from the integral representation formula for the heat equation (4.9), namely

$$\begin{aligned} \sigma(x)v(x,t) \;=\; & \int_0^t \int_\Gamma \left[\Phi(x,t;\xi,\tau)\tfrac{\partial v}{\partial n_\xi}(\xi,\tau) - \tfrac{\partial \Phi}{\partial n_\xi}(x,t;\xi,\tau)v(\xi,\tau)\right] d\Gamma_\xi d\tau \\ & + \int_\Omega \Phi(x,t;\xi,0)v(\xi,0)d\Omega_\xi, \qquad (x,t) \in [0,1]\times(0,t_f], \end{aligned} \tag{4.15}$$

where $\Omega = (0,1)$, $\Gamma = \{0,1\}$, $\sigma(0) = \sigma(1) = \frac{1}{2}$ and $\sigma(x) = 1$ for $x \in (0,1)$, and

$$\Phi(x,t;\xi,\tau) = \frac{H(t-\tau)}{\sqrt{4\pi(t-\tau)}} \exp\left(-\frac{(x-\xi)^2}{4(t-\tau)}\right) \tag{4.16}$$

is the fundamental solution for the one-dimensional time-dependent heat equation. For the heat equation (4.9), maintaining the same notations used for the general BEM described in Section 2.2.1, but using the appropriate fundamental solution (4.16), for $j = \overline{1,N}$, $k = \overline{1,N_0}$, $x \in [0,1]$, $\xi \in \{0,1\}$, $t \in (0,t_f]$, the BEM coefficients

$$\begin{gathered} C_j^{\xi}(x,t) = \int\limits_{t_{j-1}}^{t_j} G(x,t;\xi,\tau)d\tau, \quad D_j^{\xi}(x,t) = \int\limits_{t_{j-1}}^{t_j} \frac{\partial G}{\partial n_\xi}(x,t;\xi,\tau)d\tau, \\ E_k(x,t) = \int\limits_{x_{k-1}}^{x_k} G(x,t;\xi,0)d\xi, \end{gathered} \tag{4.17}$$

can be evaluated analytically as described in Lesnic [66]. Denoting $\tilde{t}_j = \frac{t_{j-1}+t_j}{2}$, $j = \overline{1,N}$, let us now define the three nonlinear discretization-dependent maps:

$$C, D : [0,1] \longrightarrow L(\mathbb{R}^{2N}, \mathbb{R}^N), \qquad E : [0,1] \longrightarrow L(\mathbb{R}^{N_0}, \mathbb{R}^N), \tag{4.18}$$

given by:

a) for C and D:

$$\begin{aligned} C(x)(i,j) &:= C_j^0(x,\tilde{t}_i), \quad i = \overline{1,N},\ j = \overline{1,N}, \\ C(x)(i,j) &:= C_j^1(x,\tilde{t}_i), \quad i = \overline{1,N},\ j = \overline{N+1,2N}, \\ D(x)(i,j) &:= D_j^0(x,\tilde{t}_i), \quad i = \overline{1,N},\ j = \overline{1,N}, \\ D(x)(i,j) &:= D_j^1(x,\tilde{t}_i), \quad i = \overline{1,N},\ j = \overline{N+1,2N}, \end{aligned} \tag{4.19}$$

b) for E:

$$E(x)(j,k) := E_k(x,\tilde{t}_j), \qquad j = \overline{1,N},\ k = \overline{1,N_0}, \tag{4.20}$$

for all $x \in [0,1]$, where throughout this work, for any $m, n \geq 1$, by $L(\mathbb{R}^m, \mathbb{R}^n)$ we denote the spaces of linear operators defined on R^m and taking values in R^n, which

can be represented as matrices of dimension $(n \times m)$. Using a BEM with constant boundary elements, see Brebbia et al. [7], from (4.15) we obtain that, for any space point $x \in [0,1]$, the solution vector satisfies

$$\sigma(x)\left[v(x,\tilde{t}_1),...,v(x,\tilde{t}_N)\right]^{tr} = C(x)\tilde{v}_\Gamma^{'} - D(x)\tilde{v}_\Gamma + E(x)\tilde{v}_0, \tag{4.21}$$

where the superscript ^{tr} denotes the transpose of a vector, the $2N-$dimensional vector $\tilde{v}_\Gamma$ captures the Dirichlet temperature boundary conditions (4.3), the N_0- dimensional vector $\tilde{v}_0$ gives the discretized initial condition (4.2), and the $2N-$dimensional vector $\tilde{v}_\Gamma^{'}$ represents the flux $\frac{\partial v}{\partial n}$ over the boundary $\Gamma = \{0,1\}$. These vectors are configured as follows:

$$\tilde{v}_\Gamma := \left[r(\tilde{t}_1)f(\tilde{t}_1),...,r(\tilde{t}_N)f(\tilde{t}_N),r(\tilde{t}_1)g(\tilde{t}_1),...,r(\tilde{t}_N)g(\tilde{t}_N)\right]^{tr}, \tag{4.22}$$

$$\tilde{v}_\Gamma^{'} := \left[\frac{\partial v}{\partial n_0}(0,\tilde{t}_1),...,\frac{\partial v}{\partial n_0}(0,\tilde{t}_N),\frac{\partial v}{\partial n_1}(1,\tilde{t}_1),...,\frac{\partial v}{\partial n_1}(1,\tilde{t}_N)\right]^{tr}, \tag{4.23}$$

$$\tilde{v}_0 := \left[T_0(\tilde{x}_1),...,T_0(\tilde{x}_{N_0})\right]^{tr}, \tag{4.24}$$

where n_ξ, $\xi \in \Gamma = \{0,1\}$, are the outward normal directions and $\tilde{x}_k = (x_{k-1} + x_k)/2$, $k = \overline{1,\ N_0}$.

Moreover, the boundary associated linear operators $C_\Gamma, D_\Gamma \in L(\mathbb{R}^{2N}, \mathbb{R}^{2N})$ and $E_\Gamma \in L(\mathbb{R}^{N_0}, \mathbb{R}^{2N})$, defined by

$$C_\Gamma = \begin{bmatrix} C(0) \\ C(1) \end{bmatrix},\quad D_\Gamma = \begin{bmatrix} D(0) + [\frac{1}{2}I_N \quad 0_N] \\ D(1) + [0_N \quad \frac{1}{2}I_N] \end{bmatrix},\quad E_\Gamma = \begin{bmatrix} E(0) \\ E(1) \end{bmatrix}, \tag{4.25}$$

where $I_N \in L(\mathbb{R}^N, \mathbb{R}^N)$ is the usual identity operator and $0_N \in L(\mathbb{R}^N, \mathbb{R}^N)$ is the null operator, allow us to write the following $2N \times 2N$ system of equations

$$C_\Gamma\tilde{v}_\Gamma^{'} - D_\Gamma\tilde{v}_\Gamma + E_\Gamma\tilde{v}_0 = 0, \tag{4.26}$$

which is derived from equation (4.21), for $x \in \{0,1\}$. Equation (4.26) implies

$$\tilde{v}_\Gamma^{'} = C_\Gamma^{-1} D_\Gamma \tilde{v}_\Gamma - C_\Gamma^{-1} E_\Gamma \tilde{v}_0. \tag{4.27}$$

Having chosen $x_0 \in (0,1)$, the measurement (4.14) evaluated at the time nodes $\tilde{t}_j$, $j = \overline{1, N}$, supplies us with the vector

$$r \cdot u := \left[r(\tilde{t}_1)u(\tilde{t}_1), ..., r(\tilde{t}_N)u(\tilde{t}_N)\right]^{tr}, \tag{4.28}$$

which, via the equation (4.21), can be expressed as

$$r \cdot u = C(x_0)\tilde{v}_\Gamma^{'} - D(x_0)\tilde{v}_\Gamma + E(x_0)\tilde{v}_0. \tag{4.29}$$

Let us now denote with

$$\tilde{r} := \left[r(\tilde{t}_1), ..., r(\tilde{t}_N)\right]^{tr}, \quad \tilde{u} := \left[u(\tilde{t}_1), ..., u(\tilde{t}_N)\right]^{tr}, \tag{4.30}$$

$$\tilde{f} := \left[f(\tilde{t}_1), ..., f(\tilde{t}_N)\right]^{tr}, \quad \tilde{g} := \left[g(\tilde{t}_1), ..., g(\tilde{t}_N)\right]^{tr}, \tag{4.31}$$

the vectors induced by r, u, f and g evaluated at the nodes $\tilde{t}_j$, $j = \overline{1, N}$. Also, throughout the entire chapter, by $diag(vec)$ we will understand the diagonal matrix whose main diagonal is composed from the components of the vector vec, while preserving their order. Therefore, we observe that the vector $r \cdot u$ can formally be written in diagonal matrix terms as

$$r \cdot u = diag(\tilde{u})\tilde{r}. \tag{4.32}$$

Then, using (4.27), equation (4.29) can be expressed as

$$diag(\tilde{u})\tilde{r} = (C(x_0)C_\Gamma^{-1}D_\Gamma - D(x_0))\tilde{v}_\Gamma + (-C(x_0)C_\Gamma^{-1}E_\Gamma + E(x_0))\tilde{v}_0. \tag{4.33}$$

Using the mapping $G : (0,1) \to L(\mathbb{R}^{2N}, \mathbb{R}^N)$ defined by

$$G(x) := C(x)C_\Gamma^{-1}D_\Gamma - D(x), \qquad x \in (0,1), \tag{4.34}$$

and observing that the vector $\tilde{v}_\Gamma$ can be expressed as

$$\tilde{v}_\Gamma = \begin{bmatrix} diag(\tilde{f}) \\ diag(\tilde{g}) \end{bmatrix} \tilde{r}, \tag{4.35}$$

from the equation (4.33) we obtain the following $N \times N$ linear system of equations

$$A\tilde{r} = (-C(x_0)C_\Gamma^{-1}E_\Gamma + E(x_0))\tilde{v}_0, \tag{4.36}$$

where

$$A := diag(\tilde{u}) - G(x_0) \begin{bmatrix} diag(\tilde{f}) \\ diag(\tilde{g}) \end{bmatrix}. \tag{4.37}$$

The solution $\tilde{r}$ of the system of equations (4.36) is then used, via equation (4.7), to obtain the time-dependent coefficient $P_f(t)$ in its discretized form as

$$\tilde{P}_f = diag(\frac{1}{\tilde{r}})\tilde{r}', \tag{4.38}$$

where we denoted

$$\tilde{r}' = \left[r'(\tilde{t}_1), ..., r'(\tilde{t}_N)\right]^{tr}. \tag{4.39}$$

Once the values of $\tilde{r}$ have been found accurately, the flux vector $\tilde{v}_\Gamma'$ and the interior temperature $\tilde{v}$ can be obtained from equations (4.27) and (4.21), respectively. The corresponding heat flux $\frac{\partial T}{\partial n} = \frac{\frac{\partial v}{\partial n}}{r(t)}$ and the interior temperature solution $T(x,t) = \frac{v(x,t)}{r(t)}$ are finally obtained from (4.8).

A test solution for our inverse problem (4.1)-(4.4) given by

$$T(x,t) = (x^2 + 2t)\exp\left(-t - \frac{t^2}{2}\right); \qquad P_f(t) = 1 + t, \tag{4.40}$$

provide us with experimental information and is further on used as a validation tool for the computed results. Then, chosing for $(0,1) \times (0,t_f)$ an appropriate discretization, with N constant boundary elements and $N_0 = \frac{N}{2}$ space cells, we

solve the system of equations (4.36) by using Gaussian elimination.

Throughout the chapter, we will consider a discretization with $N = 320$ boundary nodes and $N_0 = 160$ space cells. Also, we will assume that the measured data (4.4) are perturbed by a percentage $\alpha \in \{0, 1\}\%$ of random noise $\eta(t)$, which is sampled from a uniform distribution on the interval $[-1, 1]$, for each time $\tilde{t}_j$, $j = \overline{1, N}$, and is supplied by the NAG routine G05DAF.

Taking $x_0 = 0.5$, from (4.40) we obtain the measured data

$$u(t) = T(0.5, t) = \left(\frac{1}{4} + 2t\right) \exp\left(-t - \frac{t^2}{2}\right) (1 + \alpha\eta(t)). \tag{4.41}$$

In the no noise case, $\alpha = 0$, the computational results for $\tilde{r}$ and $P_f(\tilde{t})$ are compared with their analytical values and are illustrated in Figures 4.1(a) and 4.1(b), respectively. Both here, and in all the other forthcoming comparative figures included in this chapter, we use a solid line for the computed values and a dash-dot line for the analytical ones.

In Figure 4.1(a) we can see almost a perfect agreement between the values of r. This agreement further extends for P_f, as seen in Figure 4.1(b).

When there is $\alpha = 1\%$ of random noise in (4.41), Figure 4.2(a) shows that the computed $\tilde{r}$ agrees reasonably well with $r(t) = e^{t+\frac{t^2}{2}}$ obtained analytically from (4.8) and (4.40). However, Figure 4.2(b) shows that in the case of $P_f(t)$ the computed data and the analytical one are in a big disagreement. Moreover, the numerical results for $P_f(t)$ are highly unstable and this is due to the differentiation of the noisy function in $\tilde{r}$ which is then used in (4.38) to obtain the perfusion function coefficient. One way to overcame this ill-posed problem is to use a Gaussian mollification scheme, see Murio [73], for obtaining the discrete derivative $\tilde{r}'$. In short, this scheme consists

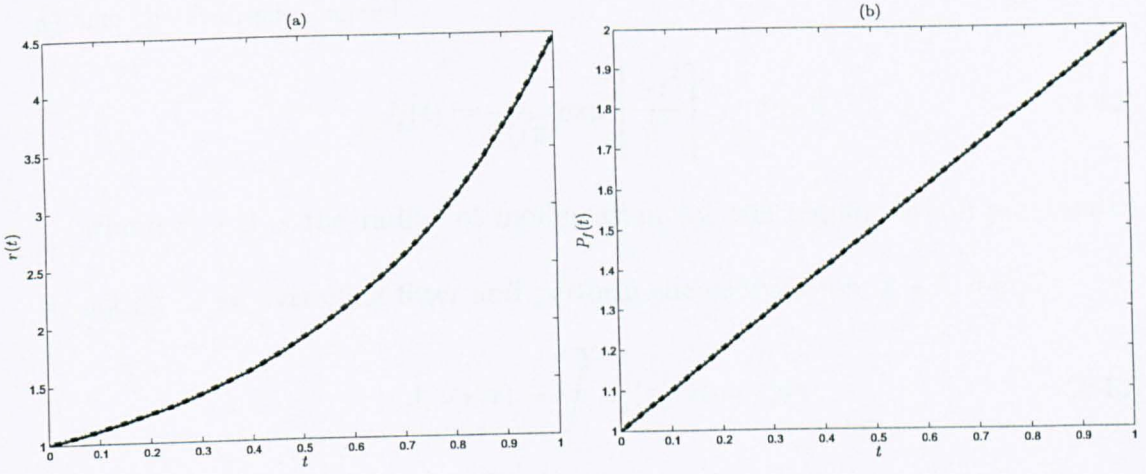

Figure 4.1: The computed and analytical values: (a) for $\tilde{r}$ and (b) for $P_f(t)$, when there is no noise in the data (4.41).

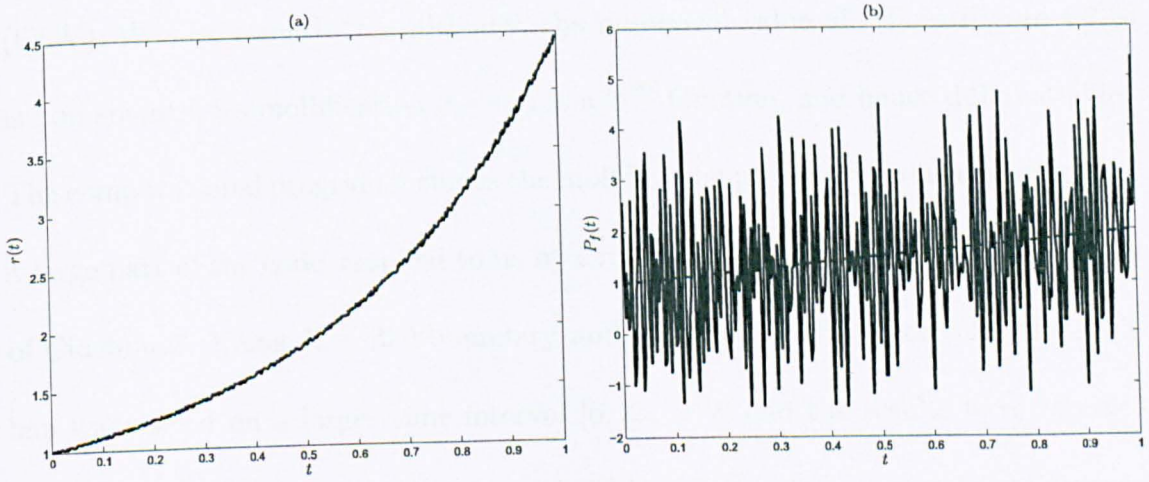

Figure 4.2: Computed and analytical values of (a) $r(t)$ and (b) $P_f(t)$, when there is $\alpha = 1\%$ of noise in the data (4.41) .

of two steps:

a) use the Gaussian kernel

$$J_\delta(t) = \frac{1}{\delta\sqrt{\pi}} \exp\left[\frac{-t^2}{\delta^2}\right], \quad \delta > 0, \tag{4.42}$$

where $\delta > 0$ is the radius of mollification (or the regularization parameter) acting as an averaging filter and perform the convolution $J_\delta * \tilde{r}$, namely

$$J_\delta * r(t) = \int_{-\infty}^{\infty} J_\delta(\tau) r(t-\tau) d\tau; \tag{4.43}$$

b) differentiate $J_\delta * \tilde{r}$ to obtain $J_\delta * r' = J_\delta' * r$.

We should notice that the mollifier J_δ is always positive and becomes very close to zero outside the interval centred at the origin and of radius 3δ. Therefore, good results for $r'(t)$ are expected in the interval $[3\delta, 1-3\delta]$. In our algorithm, the radius of mollification δ is computed automatically by Generalized Cross-Validation (GCV). We also remark that although the numerical value of $r(t)$ in Figure 4.2(a) is non-smooth, its mollification $J * r(t)$ is a $\mathscr{C}^\infty$ function, and hence differentiable. The computational program includes the mollification procedure, which encompasses a large part of the code supplied to us by Professor D.A. Murio from the University of Cincinnati. Using $N = 320$ boundary nodes and $N_0 = 160$ space cells, the problem was solved on a larger time interval $[0, 2t_f = 2]$ and the results were retained only on the restricted interval $[0, t_f = 1]$. This was found necessary due to the end effects of the mollification (4.43). This end effect could actually be seen near $t = 0$, where we could not solve the problem for negative times.

Figures 4.3(a) and 4.3(b) show the corresponding numerical mollified results in comparison with the exact values for r' and P_f, respectively. Unlike the results of Figure

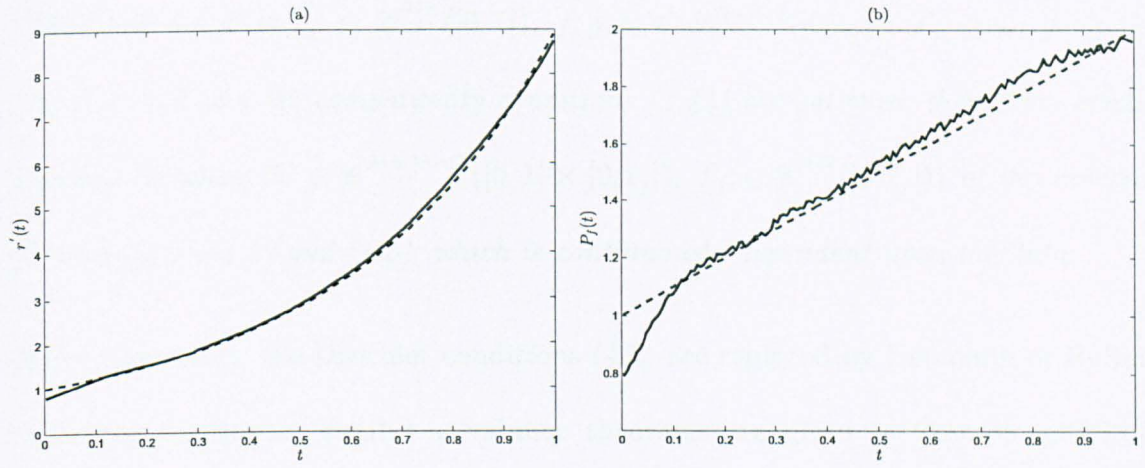

Figure 4.3: Computed and analytical values of (a) $r'(t)$ and (b) $P_f(t)$, when there is $\alpha = 1\%$ of noise in the data (4.41), after mollification.

4.2(b), from Figure 4.3(b) it can be seen that a stable solution is obtained after performing the data mollification.

4.4 The Total Mass Measurement

In this section we investigate the inverse problem given by equations (4.1)-(4.3) and (4.5). For the data in equations (4.2)-(4.3) and (4.5) we assume the following compatibility conditions:

$$\begin{aligned} &f(0) = T_0(0), \quad g(0) = T_0(1), \quad \mathcal{E}(0) = \int_0^1 T_0(x)dx, \\ &f'(0) = T_0''(0) + \frac{T_0(0)(\mathcal{E}'(0) - T_0'(1) + T_0'(0))}{\mathcal{E}(0)} \\ &g'(0) = T_0''(1) + \frac{T_0(1)(\mathcal{E}'(0) - T_0'(1) + T_0'(0))}{\mathcal{E}(0)}, \quad \mathcal{E}(0) > 0. \end{aligned} \tag{4.44}$$

Then we have the following solvability theorem established in Cannon et al. [18] and Lin [68].

Theorem 4.4.1 *If* $T_0 \in \mathscr{C}^{2+\alpha}([0,1])$, $f, g, \mathcal{E} \in \mathscr{C}^{1+\alpha/2}([0,t_f])$, $T_0 \geq 0$, $f \geq 0$, $g \geq 0$, $\mathcal{E} > 0$ *and the compatibility conditions (4.44) are satisfied, then there exists a unique solution* ($T \in \mathscr{C}^{2+\alpha,1+\alpha/2}([0,1] \times [0,t_f])$, $P_f \in \mathscr{C}^{\alpha/2}([0,t_f])$) *of the inverse problem (4.1)-(4.3) and (4.5), which is continuously dependent upon the data.*

In the case where the Dirichlet conditions (4.3) are replaced by Neumann or Robin boundary conditions, similar solvability theorems are given in Cannon and Lin [14, 15, 16] or Cannon et al. [17], respectively.

Prior to this study, numerical methods based on finite differences, see Azari [4], Cannon et al. [18], Cannon and Yin [21], Dehghan [35] and Wang and Lin [115], have been developed for solving (4.1)-(4.3) and (4.5) with extensions to two and three-dimensional rectangular and cuboidal domains given in Dehghan [38, 41]. However, as the FDM is not easy to extend to higher dimensional irregular domains, in this section we adopt the BEM.

First, recalling the definition (4.7), the change of variable (4.8) transforms the problem (4.1)-(4.3) into (4.9)-(4.11) and the total mass measurement (4.5) becomes

$$\int_0^1 v(x,t)dx = r(t)\mathcal{E}(t), \qquad t \in [0,t_f], \quad \mathcal{E}(0) = \int_0^1 T_0(x)dx. \tag{4.45}$$

Our approach for the inverse problem (4.9)-(4.11) and (4.45) follows a path that is similar to the one developed for (4.1)-(4.4). The BEM for the heat equation (4.9)-(4.11) provides us a space discretization for the mass formula, namely

$$r(t)\mathcal{E}(t) \simeq \sum_{i=0}^{N_0-1} (x_{i+1} - x_i)v(\tilde{x}_{i+1}, t) = \frac{1}{N_0}\sum_{i=1}^{N_0} v(\tilde{x}_i, t). \tag{4.46}$$

Therefore, the vector

$$r \cdot \mathcal{E} := \left[r(\tilde{t}_1)\mathcal{E}(\tilde{t}_1), ..., r(\tilde{t}_N)\mathcal{E}(\tilde{t}_N)\right]^{tr} \tag{4.47}$$

satisfies

$$r \cdot \mathcal{E} = \frac{1}{N_0} \sum_{i=1}^{N_0} \left[v(\tilde{x}_i, \tilde{t}_1), ..., v(\tilde{x}_i, \tilde{t}_N) \right]^{tr}. \tag{4.48}$$

Thus, via the equation (4.21), for $i = \overline{1, N}$, we obtain

$$r \cdot \mathcal{E} = \frac{1}{N_0} \left(\sum_{i=1}^{N_0} C(\tilde{x}_i) \tilde{v}_\Gamma^{'} - \sum_{i=1}^{N_0} D(\tilde{x}_i) \tilde{v}_\Gamma + \sum_{i=1}^{N_0} E(\tilde{x}_i) \tilde{v}_0 \right). \tag{4.49}$$

Using (4.27), equation (4.49) can be expressed as

$$r \cdot \mathcal{E} = \frac{1}{N_0} \sum_{i=1}^{N_0} \left(C(\tilde{x}_i) C_\Gamma^{-1} D_\Gamma - D(\tilde{x}_i) \right) \tilde{v}_\Gamma + \frac{1}{N_0} \sum_{i=1}^{N_0} \left(-C(\tilde{x}_i) C_\Gamma^{-1} E_\Gamma + E(\tilde{x}_i) \right) \tilde{v}_0. \tag{4.50}$$

By denoting

$$\tilde{\mathcal{E}} := \left[\mathcal{E}(\tilde{t}_1), ..., \mathcal{E}(\tilde{t}_1) \right]^{tr}, \tag{4.51}$$

we notice that the vector $r \cdot \mathcal{E}$ can formally be expressed as

$$r \cdot \mathcal{E} = diag(\tilde{\mathcal{E}}) \tilde{r}. \tag{4.52}$$

Using (4.35), and the mapping G defined in (4.34), equation (4.50) becomes

$$diag(\tilde{\mathcal{E}}) \tilde{r} = \frac{1}{N_0} \sum_{i=1}^{N_0} G(\tilde{x}_i) \begin{bmatrix} diag(\tilde{f}) \\ \\ diag(\tilde{g}) \end{bmatrix} \tilde{r} + \frac{1}{N_0} \sum_{i=1}^{N_0} \left(-C(\tilde{x}_i) C_\Gamma^{-1} E_\Gamma + E(\tilde{x}_i) \right) \tilde{v}_0. \tag{4.53}$$

Therefore, by denoting

$$A := diag(\tilde{\mathcal{E}}) - \frac{1}{N_0} \sum_{i=1}^{N_0} G(\tilde{x}_i) \begin{bmatrix} diag(\tilde{f}) \\ \\ diag(\tilde{g}) \end{bmatrix} \in L(\mathbb{R}^N, \mathbb{R}^N), \tag{4.54}$$

we obtain the following $N \times N$ linear system of equations

$$A\tilde{r} = \frac{1}{N_0} \sum_{i=1}^{N_0} \left(-C(\tilde{x}_i) C_\Gamma^{-1} E_\Gamma + E(\tilde{x}_i) \right) \tilde{v}_0. \tag{4.55}$$

Once the system (4.55) has been solved, equation (4.38) is used to obtain the discretized time-dependent coefficient $P_f(t)$.

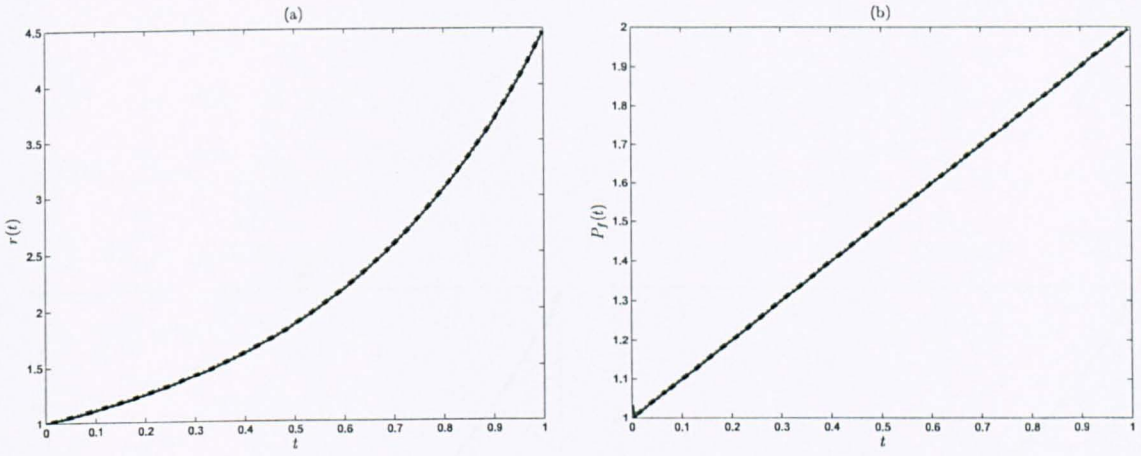

Figure 4.4: Computed and analytical values of (a) $r(t)$, and (b)$P_f(t)$, when there is no noise in the data (4.56).

The test solution (4.40) provides us with the mass measurement

$$\mathcal{E}(t) = \int_0^1 T(x,t)dx = \left(\frac{1}{3} + 2t\right) \exp\left(-t - \frac{t^2}{2}\right)(1 + \alpha\eta(t)) \qquad (4.56)$$

where the percentage $\alpha \in \{0, 1\}\%$ of noise $\eta(t)$ is involved.

Figure 4.4 illustrates the situation when there is no noise, $\alpha = 0$. In Figure 4.4(a) we can see almost perfect agreement between the values of $\tilde{r}$ deduced analytically and the computed ones. This agreement is further extended for P_f, as it is shown in Figure 4.4(b).

In Figure 4.5 we illustrate the computed and analytical values for r, r' and P_f, when the data (4.56) is affected by 1% noise. From Figure 4.5(a) it can be seen that the noise from the additional information $\mathcal{E}(t)$ determines the results for the computed $\tilde{r}$ to be noisy as well. Although these computed values of r are localized around the exact values, their instability becomes a major problem for computing the numerical derivative $r'(t)$ of the noisy function $r(t)$ shown in Figure 4.5(a). However, a solution

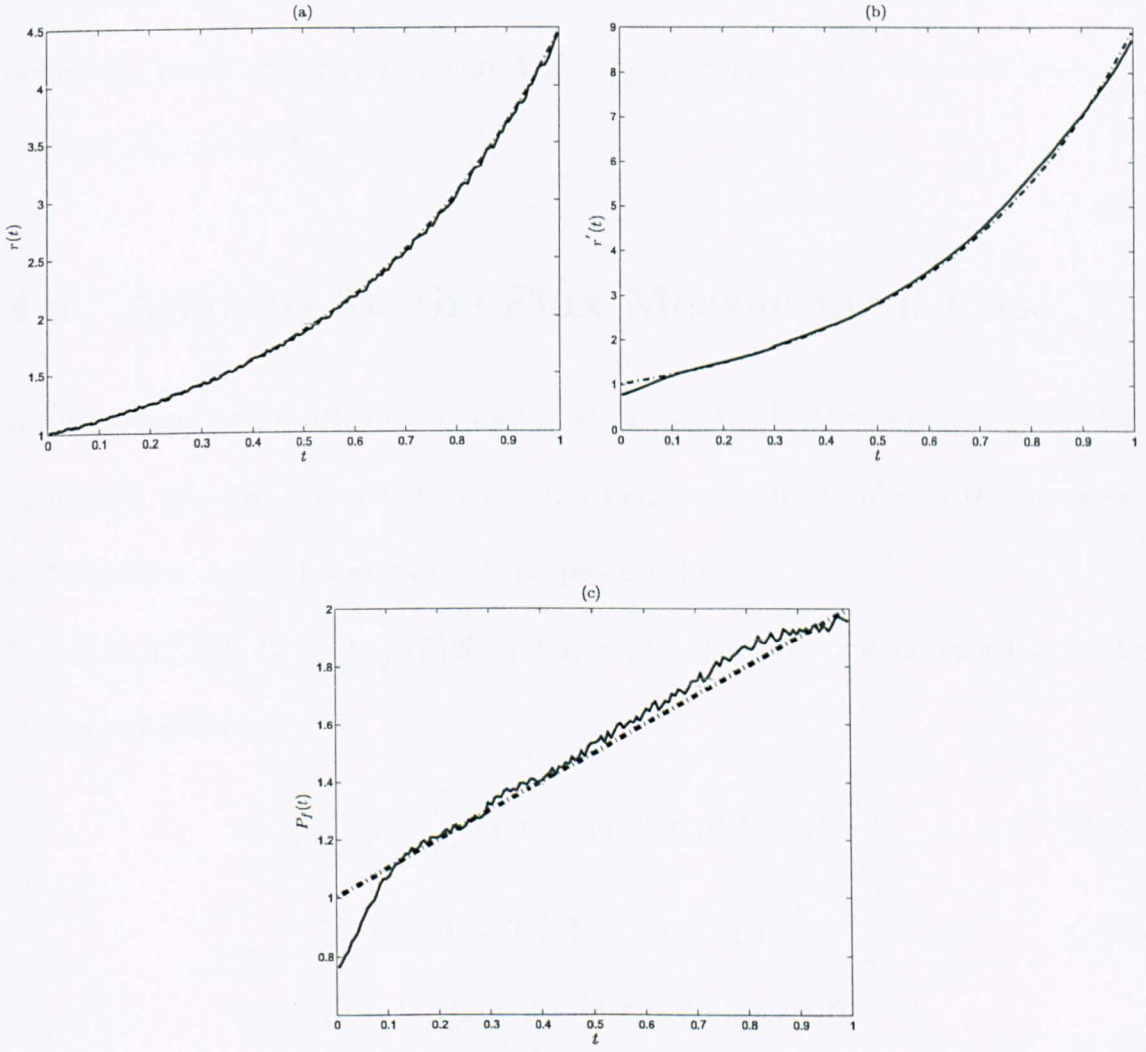

Figure 4.5: Computed and analytical values of: (a) $r(t)$, (b) $r'(t)$, and (c) $P_f(t)$, when there is $\alpha = 1\%$ of noise in the data (4.56).

for this problem is possible by using the mollification scheme in a manner similar to that described in Section 4.3. The mollified results for the derivative of $\tilde{r}$, as shown in Figure 4.5(b), agree with the analytical $r'(t) = (1+t)e^{t+\frac{t^2}{2}}$. After this, the computed results shown in Figures 4.5(a) and 4.5(b) are used in equation (4.38) to obtain P_f, which, as shown in Figure 4.5(c), approximates reasonably well the exact solution $P_f(t) = 1 + t$.

4.5 Analysis for the Flux Measurement Case

In this section we investigate the inverse problem given by the equations (4.1)-(4.3) and (4.6). For this problem we could not find solvability results in the literature and therefore, a first investigation is proposed below.

Let $\Phi \in \mathscr{C}^{2,1}((0,1) \times (0,t_f]) \bigcap \mathscr{C}^{1,0}([0,1] \times [0,t_f])$ be the unique solution of the well-posed problem:

$$\frac{\partial \phi}{\partial t}(x,t) = \frac{\partial^2 \phi}{\partial x^2}(x,t), \quad (x,t) \in (0,1) \times (0,t_f], \tag{4.57}$$

$$\Phi(x,0) = T_0(x), \qquad x \in [0,1], \tag{4.58}$$

$$\begin{aligned} &\phi(0,t) = f(t), \quad t \in [0,t_f],\ f(0) = T_0(0), \\ &\phi(1,t) = g(t), \quad t \in [0,t_f],\ g(0) = T_0(1). \end{aligned} \tag{4.59}$$

The change of variable

$$w(x,t) := r(t)T(x,t) - \phi(x,t) \tag{4.60}$$

transforms (4.1)-(4.3) into

$$\frac{\partial w}{\partial t}(x,t) = \frac{\partial^2 w}{\partial x^2}(x,t), \qquad (x,t) \in (0,1) \times (0,t_f], \tag{4.61}$$

$$w(x,0) = 0, \qquad x \in [0,1], \tag{4.62}$$

$$
\begin{aligned}
w(0,t) &= f(t)(r(t)-1) =: \overline{\overline{f}}(t), \qquad t \in [0,t_f],\ \overline{\overline{f}}(0) = 0, \\
w(1,t) &= g(t)(r(t)-1) =: \overline{\overline{g}}(t), \qquad t \in [0,t_f],\ \overline{\overline{g}}(0) = 0.
\end{aligned}
\tag{4.63}
$$

Let us first notice that, with no changes in analysis, the additional information (4.6) may well be replaced by a heat flux measurement at $x = 0$, namely

$$
-\frac{\partial T}{\partial x}(0,t) = h_0(t), \qquad \text{for any } t \in (0,t_f]. \tag{4.64}
$$

The change of variable (4.60) transforms (4.6) or (4.64) into an additional information for the problem (4.61)-(4.63), namely:

i) a left boundary flux measurement:

$$
-\frac{\partial w}{\partial x}(0,t) = h_0(t)r(t) + \frac{\partial \phi}{\partial x}(0,t) \tag{4.65}
$$

or

ii) a right boundary flux measurement:

$$
\frac{\partial w}{\partial x}(1,t) = h_1(t)r(t) + \frac{\partial \phi}{\partial x}(1,t), \tag{4.66}
$$

respectively.

However, the two cases can be treated similarly and in the following we focus our attention on the left boundary flux measurement (4.64). Let us assume that a solution to the problem (4.61)-(4.63) and (4.65) exists.

Since $\overline{\overline{f}}, \overline{\overline{g}} \in \mathscr{C}^0([0,t_f])$, we have the representation formula, see [55],

$$
w(x,t) = -\int_0^t \frac{\partial M}{\partial x}(x, t-\tau)\overline{\overline{f}}(\tau)d\tau + \int_0^t \frac{\partial M}{\partial x}(x-1, t-\tau)\overline{\overline{g}}(\tau)d\tau, \tag{4.67}
$$

where

$$
M(\xi,\sigma) := \frac{H(\sigma)}{\sqrt{\pi\sigma}} \sum_{n=-\infty}^{\infty} \exp\left[-\frac{(\xi+2n)^2}{4\sigma}\right]. \tag{4.68}
$$

By differentiating equation (4.67) with respect to x, we obtain

$$\frac{\partial w}{\partial x} = -\int_0^t \frac{\partial^2 M}{\partial x^2}(x, t-\tau)\overline{\overline{f}}(\tau)d\tau + \int_0^t \frac{\partial^2 M}{\partial x^2}(x-1, t-1)\overline{\overline{g}}(\tau)d\tau. \tag{4.69}$$

Since

$$\frac{\partial M}{\partial \tau}(x-\xi, t-\tau) = -\frac{\partial^2 M}{\partial x^2}(x-\xi, t-\tau), \quad x \neq \xi,\ t > \tau, \tag{4.70}$$

it follows that

$$\frac{\partial w}{\partial x}(x,t) = \int_0^t \frac{\partial M}{\partial \tau}(x, t-\tau)\overline{\overline{f}}(\tau)d\tau - \int_0^t \frac{\partial M}{\partial \tau}(x-1, t-\tau)\overline{\overline{g}}(\tau)d\tau. \tag{4.71}$$

On the other hand, let us first notice, from equation (4.68), that we obtain

$$\lim_{\tau \nearrow t} M(x-\xi, t-\tau) = 0, \quad x \neq \xi, \tag{4.72}$$

and since $\overline{\overline{f}}, \overline{\overline{g}} \in \mathscr{C}^1([0, t_f])$, with $\overline{\overline{f}}(0) = \overline{\overline{g}}(0) = 0$, by using integration by parts in (3.38), we have

$$\frac{\partial w}{\partial x}(x,t) = -\int_0^t M(x, t-\tau)\overline{\overline{f}}'(\tau)d\tau + \int_0^t M(x-1, t-\tau)\overline{\overline{g}}'(\tau)d\tau, \tag{4.73}$$

for all $(x,t) \in (0,1) \times (0, t_f]$. By using now the Lebesgue's Dominative convergence theorem, see Stroock [108], we obtain

$$\lim_{x \searrow 0} \frac{\partial w}{\partial x}(x,t) = -\int_0^t M(0, t-\tau)\overline{\overline{f}}'(\tau)d\tau + \int_0^t M(1, t-\tau)\overline{\overline{g}}'(\tau)d\tau \tag{4.74}$$

for all $t \in (0, t_f]$.

For $t \in (0, t_f]$ and $P_f(t) > 0$, let us define:

$$\widetilde{H}(t, P_f(t)) := -\int_0^t M(0, t-\tau)\overline{\overline{f}}'(\tau)d\tau + \int_0^t M(-1, t-\tau)\overline{\overline{g}}'(\tau)d\tau, \tag{4.75}$$

and

$$Q(P_f(t)) := -\frac{\widetilde{H}(t, P_f(t)) + \frac{\partial \phi}{\partial x}(0,t)}{r(t)}, \tag{4.76}$$

From the analysis (4.67)-(3.41) and the equation (4.65), we obtain that

$$Q(P_f(t)) = h_0(t) \qquad \text{for all } t \in (0, t_f]. \tag{4.77}$$

Thus, we arrive at the following remark:

Remark 4.5.1 *If the inverse problem (4.1)-(4.3) and (4.64) has a solution then the function $P_f(t)$ needs to satisfy equation (4.77).*

A direct consequence can be stated as follows:

Theorem 4.5.2 *If equation (4.77) has a unique positive solution, then the inverse problem (4.1)-(4.3) and (4.64) has a unique solution $(T(x,t); P_f(t))$.*

4.5.1 BEM Treatment for the Flux Measurement at $x = 1$

Let us start by recalling that equation (4.27) supplies us with a formula for $\tilde{v}_\Gamma^{'}$, where, from (4.23),

$$\tilde{v}_\Gamma^{'} = \left[r(\tilde{t}_1)h_0(\tilde{t}_1), ..., r(\tilde{t}_N)h_0(\tilde{t}_N), r(\tilde{t}_1)h_1(\tilde{t}_1), ..., r(\tilde{t}_N)h_0(\tilde{t}_N)\right]^{tr}. \tag{4.78}$$

If we further consider the vector and matrix notations

$$\tilde{h}_i := \left[h_i(\tilde{t}_1), ..., h_i(\tilde{t}_N)\right]^{tr}, \qquad i \in \{0, 1\}, \tag{4.79}$$

then equation (4.26) can be rewritten as

$$\begin{bmatrix} diag(\tilde{h}_0) \\ diag(\tilde{h}_1) \end{bmatrix} \tilde{r} - C_\Gamma^{-1} D_\Gamma \begin{bmatrix} diag(\tilde{f}) \\ diag(\tilde{g}) \end{bmatrix} \tilde{r} = -C_\Gamma^{-1} E_\Gamma \tilde{v}_0 \tag{4.80}$$

which is a $2N \times 2N$ nonlinear system with the vectors $\tilde{r}$ and $\tilde{h}_0$ as the unknowns. However, we will show that, in order to obtain the unknown vector $\tilde{r}$, we only need

N linear equations of the system (4.80).

Let us define the orthogonal projection

$$\begin{aligned} &P_{\overline{N+1,2N}} : \mathbb{R}^{2N} \to R^N, \\ &P_{\overline{N+1,2N}}([x_1, ..., x_N, x_{N+1}, ..., x_{2N}]^{tr}) = [x_{N+1}, ..., x_{2N}]^{tr}, \end{aligned} \tag{4.81}$$

for all $[x_1, ..., x_N, x_{N+1}, ..., x_{2N}]^{tr} \in \mathbb{R}^{2N}$. In order to disregard the unknown flux information $h_0(t)$, by applying $P_{\overline{N+1,2N}}$ to the system of equations (4.80), we obtain

$$P_{\overline{N+1,2N}} \begin{bmatrix} diag(\tilde{h}_0) \\ diag(\tilde{h}_1) \end{bmatrix} \tilde{r} - P_{\overline{N+1,2N}} C_\Gamma^{-1} D_\Gamma \begin{bmatrix} diag(\tilde{f}) \\ diag(\tilde{g}) \end{bmatrix} \tilde{r} = -P_{\overline{N+1,2N}} C_\Gamma^{-1} E_\Gamma \tilde{v}_0, \tag{4.82}$$

which is equivalent to the following $N \times N$ system of linear equations

$$diag(\tilde{h}_1)\tilde{r} - P_{\overline{N+1,2N}} C_\Gamma^{-1} D_\Gamma \begin{bmatrix} diag(\tilde{f}) \\ diag(\tilde{g}) \end{bmatrix} \tilde{r} = -P_{\overline{N+1,2N}} C_\Gamma^{-1} E_\Gamma \tilde{v}_0. \tag{4.83}$$

Thus, if we are only supplied with the flux measurement at $x = 1$, $h_1(t)$ for all $t \in (0, t_f]$, just by solving the linear system (4.83), we are able to obtain $\tilde{r}$, which is the BEM discretized version of $r(t)$.

We remark here that the steps proposed so far are symmetric in the sense that if the flux information at $x = 0$, $h_0(t)$ is available, and the flux information at $x = 1$, $h_1(t)$, is not known, then defining the complementary projection $P_{\overline{1,N}}$ which takes a $2N$-dimensional vector into its first N coordinates, a similar system is obtained and, thus, $r(t)$ can be retrieved again.

The test solution (4.40) provides us with the following heat flux measurement at $x = 1$:

$$h_1(t) = \frac{\partial T}{\partial x}(1, t) = 2 \exp\left(-t - \frac{t^2}{2}\right)(1 + \alpha\eta(t)). \tag{4.84}$$

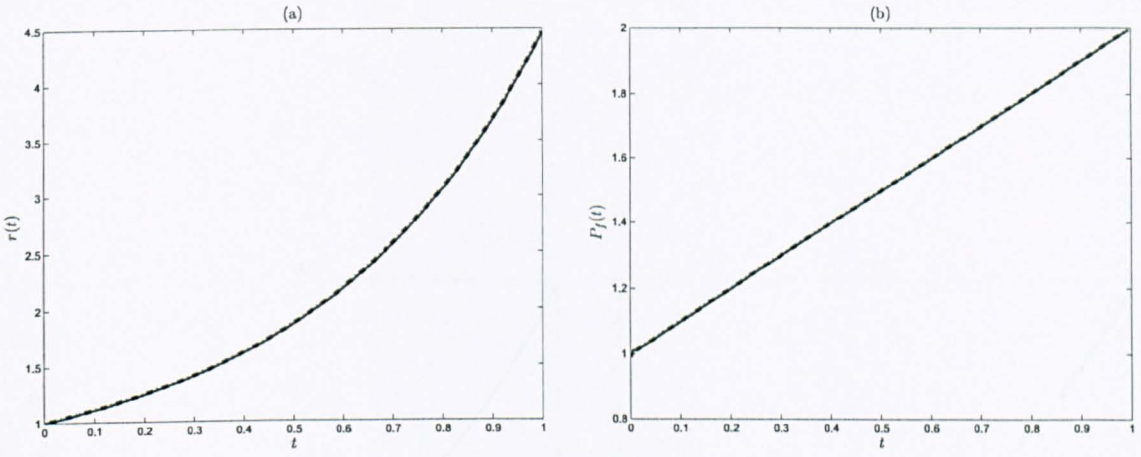

Figure 4.6: Computed and analytical values of: (a) $r(t)$ and (b) for $P_f(t)$, when there is no noise in the data (4.84) .

For the no noise case, $\alpha = 0$, as shown in Figures 4.6(a) and 4.6(b), the computed results are in a good agreement with the analytical values.

When 1% noise is included in the flux data $h_1(t)$, as in (4.84), the problem becomes again dificult, since the computed $\tilde{r}$ becomes noisy, so that the numerical derivative $\tilde{r}'$ needs special attention. However, by pursuing the same steps as in the case of noisy mass or internal measurements, we solve the system of equations (4.83) obtained for a discretization with $N = 320$ boundary nodes and $N_0 = 160$ space cells for $(0, 1) \times [0, 2]$, and perform the Gaussian mollification of the obtained results. Then we restrict our problem to the domain of interest $(0, 1) \times [0, t_f = 1]$ and, from the results obtained in the previous step, we retain only the values corresponding to this restriction. In Figure 4.7(a), the comparison between the results computed and the analytical values for $\tilde{r}$ unveil the fact that the noise from the flux measurements have been propagated through the computation and have determined $\tilde{r}$ to be noisy. However, as shown in Figure 4.7(b), after mollification, the computed derivative

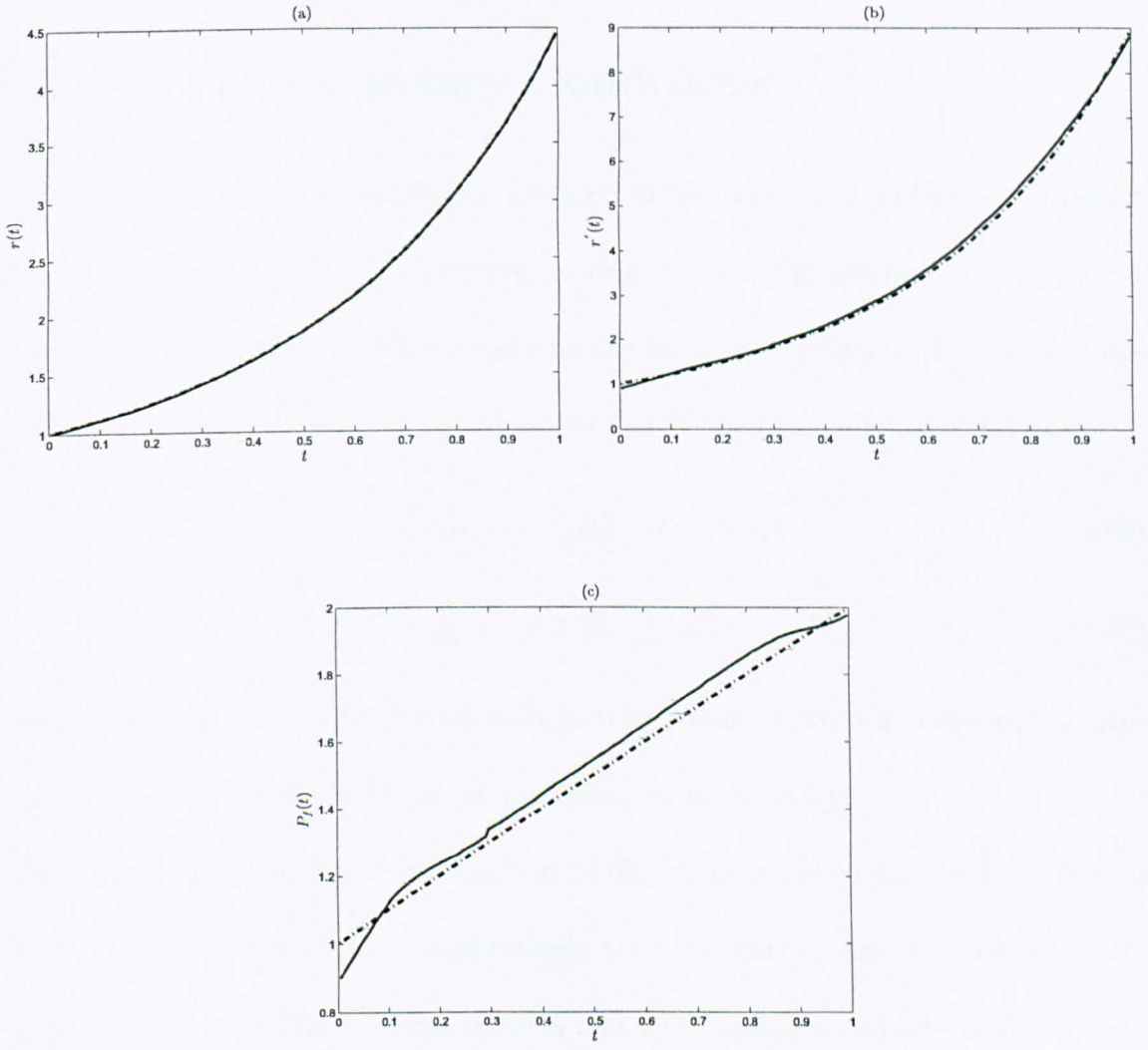

Figure 4.7: Computed and analytical values of: (a) $r(t)$, (b) $r'(t)$, and (c) $P_f(t)$, when there is 1% noise in the heat flux data (4.84).

becomes very close to its analytical value. Finally, as shown in Figure 4.7(c), the perfusion coefficient $P_f(t)$ is retrieved reasonably stable and fairly close to its true value.

4.6 Mixed Boundary Conditions

A set of mixed boundary conditions are used in this section to replace the Dirichlet boundary conditions (4.3). Therefore, in this context, the inverse time-dependent perfusion identification problem satisfying the bio-heat equation (4.1), with the initial condition (4.2), has to be solved subject to the mixed boundary conditions

$$-\frac{\partial T}{\partial x}(0,t) = h_0(t), \quad t \in [0, t_f], \tag{4.85}$$

$$T(1,t) = g(t), \quad t \in [0, t_f], \; g(0) = T_0(1), \tag{4.86}$$

while preserving the same kind of additional information given by the internal temperature measurement (4.4), or the mass measurement (4.5).

The case of the additional information (4.6), being supplied by the heat flux at $x = 1$, is expected to produce qualitatively the same conclusions as those of subsection 4.5.1 and, in addition, since there is no theory on the solvability of this inverse problem, we do not insist on this investigation. Instead, we concentrate on the analysis of Sections 4.3 and 4.4 in which the mixed boundary conditions (4.85) and (4.86) replace the boundary conditions (4.3). Similar solvability theorems to those of Sections 4.3 and 4.4 can be established, see Cannon et al. [17] and Prilepko and Solov'ev [88], for the inverse problem (4.1), (4.2), (4.85), (4.86) and (4.4) or (4.5). The change of variable defined in (4.7)-(4.8) transforms the inverse problems (4.1), (4.2), (4.85), (4.86) and (4.4), and (4.1), (4.2), (4.85), (4.86) and (4.5) into mixed

boundary condition problems for the standard heat equation (4.9) subject to the initial condition (4.10) and the mixed boundary conditions

$$-\frac{\partial v}{\partial x}(0,t) = r(t)h_0(t), \qquad t \in [0, t_f], \tag{4.87}$$

$$v(1,t) = r(t)g(t), \qquad t \in [0, t_f],\ g(0) = v_0(1). \tag{4.88}$$

and (4.14) or (4.45), respectively.

4.6.1 Internal Temperature Measurement

Recalling (4.22)-(4.25), (4.30)-(4.31), (4.35) and (4.79), the equations (4.26) and (4.29) recast as follows:

$$C_\Gamma \begin{bmatrix} diag(\tilde{h}_0) \\ diag(\tilde{h}_1) \end{bmatrix} \tilde{r} - D_\Gamma \begin{bmatrix} diag(\tilde{f}) \\ diag(\tilde{g}) \end{bmatrix} \tilde{r} + E_\Gamma \tilde{v}_0 = 0, \tag{4.89}$$

$$diag(\tilde{u})\tilde{r} = C(x_0) \begin{bmatrix} diag(\tilde{h}_0) \\ diag(\tilde{h}_1) \end{bmatrix} \tilde{r} - D(x_0) \begin{bmatrix} diag(\tilde{f}) \\ diag(\tilde{g}) \end{bmatrix} \tilde{r} + E(x_0)\tilde{v}_0. \tag{4.90}$$

From (4.89), equation (4.90) can be expressed as

$$\begin{aligned} diag(\tilde{u})\tilde{r} \;=\; & C(x_0) \left[C_\Gamma^{-1} D_\Gamma \begin{bmatrix} diag(\tilde{f}) \\ diag(\tilde{g}) \end{bmatrix} \tilde{r} - C_\Gamma^{-1} E_\Gamma \tilde{v}_0 \right] \\ & - D(x_0) \begin{bmatrix} diag(\tilde{f}) \\ diag(\tilde{g}) \end{bmatrix} \tilde{r} + E(x_0)\tilde{v}_0. \end{aligned} \tag{4.91}$$

Let us define the linear projection

$$\begin{aligned} & P_{\overline{1,N}} : \mathbb{R}^{2N} \to R^N, \\ & P_{\overline{1,N}}([x_1, ...x_N, x_{N+1}, ...x_{2N}]^T) = [x_1, ...x_N]^T, \end{aligned} \tag{4.92}$$

for all $[x_1, ..x_N, x_{N+1}, ...x_{2N}]^T \in \mathbb{R}^{2N}$. By applying $P_{\overline{1,N}} C_\Gamma^{-1}$ to the $2N$-dimensional operator equation (4.89), we can discard from our analysis the unknown N-dimensional

vector $\tilde{h}_1$, containing the unknown boundary flux at $x = 1$, and we arrive at the N-dimensional operator equation

$$diag(\tilde{h}_0)\tilde{r} - P_{\overline{1,N}} C_\Gamma^{-1} D_\Gamma \begin{bmatrix} diag(\tilde{f})\tilde{r} \\ diag(\tilde{g})\tilde{r} \end{bmatrix} + P_{\overline{1,N}} C_\Gamma^{-1} E_\Gamma \tilde{v}_0 = 0. \tag{4.93}$$

Let us denote

$$r \cdot f := [r(\tilde{t}_1)f(\tilde{t}_1), ..., r(\tilde{t}_N)f(\tilde{t}_N)]^T, \tag{4.94}$$

the BEM-discretized version of $r(t)f(t)$. We can now remark that equations (4.91) and (4.93) form the following $2N \times 2N$ linear system of equations

$$\begin{cases} diag(\tilde{h}_0)\tilde{r} - P_{\overline{1,N}} C_\Gamma^{-1} D_\Gamma \begin{bmatrix} r \cdot f \\ diag(\tilde{g})\tilde{r} \end{bmatrix} + P_{\overline{1,N}} C_\Gamma^{-1} E_\Gamma \tilde{v}_0 = 0 \\ diag(\tilde{u})\tilde{r} = C(x_0) \left[C_\Gamma^{-1} D_\Gamma \begin{bmatrix} r \cdot f \\ diag(\tilde{g})\tilde{r} \end{bmatrix} - C_\Gamma^{-1} E_\Gamma \tilde{v}_0 \right] \\ \qquad\qquad -D(x_0) \begin{bmatrix} r \cdot f \\ diag(\tilde{g})\tilde{r} \end{bmatrix} + E(x_0)\tilde{v}_0 \end{cases} \tag{4.95}$$

in the $2N$-dimensional vector of unknowns:

$$\begin{bmatrix} \tilde{r} \\ r \cdot f \end{bmatrix}. \tag{4.96}$$

Throughout the entire work, for an arbitrary matrix A, by $col_i(A)$ we understand the $i-$th column of the matrix A. Let us define now the finite dimensional operators

$$D_{\Gamma_{\overline{1,N}}} := [col_1(D_\Gamma), ..., col_N(D_\Gamma)] \in L(\mathbb{R}^N, \mathbb{R}^{2N}), \tag{4.97}$$

$$D_{\Gamma_{\overline{N+1,2N}}} := [col_{N+1}(D_\Gamma), ..., col_{2N}(D_\Gamma)] \in L(\mathbb{R}^N, \mathbb{R}^{2N}), \tag{4.98}$$

$$D(x)_{\overline{1,N}} := [col_1(D(x)), ..., col_N(D(x))] \in L(\mathbb{R}^N, \mathbb{R}^N), \quad x \in (0,1), \tag{4.99}$$

$$D(x)_{\overline{N+1,2N}} := [col_{N+1}(D(x)), ..., col_{2N}(D(x))] \in L(\mathbb{R}^N, \mathbb{R}^N), \quad x \in (0,1), \quad (4.100)$$

and remark that the system (4.95) can be equivalently expressed as

$$\begin{cases} \left\{ diag(\tilde{h}_0) - P_{\overline{1,N}} C_\Gamma^{-1} D_{\Gamma_{\overline{N+1,2N}}} diag(\tilde{g}) \right\} \tilde{r} - P_{\overline{1,N}} C_\Gamma^{-1} D_{\Gamma_{\overline{1,N}}} r \cdot f = -P_{\overline{1,N}} C_\Gamma^{-1} E_\Gamma \tilde{v}_0, \\ \\ \left\{ diag(\tilde{u}) - C(x_0) C_\Gamma^{-1} D_{\Gamma_{\overline{N+1,2N}}} diag(\tilde{g}) + D(x_0)_{\overline{N+1,2N}} diag(\tilde{g}) \right\} \tilde{r} \\ \\ + \left\{ -C(x_0) C_\Gamma^{-1} D_{\Gamma_{\overline{1,N}}} + D(x_0)_{\overline{1,N}} \right\} r \cdot f = E(x_0)\tilde{v}_0 - C(x_0) C_\Gamma^{-1} E_\Gamma \tilde{v}_0. \end{cases} \quad (4.101)$$

Thus, the linear operators $A_{\overline{1,N}}$, $A_{\overline{N+1,2N}} \in L(R^N, R^{2N})$, defined by

$$A_{\overline{1,N}} := \begin{bmatrix} diag(\tilde{h}_0) - P_{\overline{1,N}} C_\Gamma^{-1} D_{\Gamma_{\overline{N+1,2N}}} diag(\tilde{g}) \\ diag(\tilde{u}_{x_0}) - C(x_0) C_\Gamma^{-1} D_{\Gamma_{\overline{N+1,2N}}} diag(\tilde{g}) + D(x_0)_{\overline{N+1,2N}} diag(\tilde{g}) \end{bmatrix} \quad (4.102)$$

and

$$A_{\overline{N+1,2N}} := \begin{bmatrix} -P_{\overline{1,N}} C_\Gamma^{-1} D_{\Gamma_{\overline{1,N}}} \\ -C(x_0) C_\Gamma^{-1} D_{\Gamma_{\overline{1,N}}} + D(x_0)_{\overline{1,N}} \end{bmatrix} \quad (4.103)$$

enable us to rewrite the system of equations (4.101) as

$$A_{\overline{1,N}} \tilde{r} + A_{\overline{N+1,2N}} r \cdot f = \begin{bmatrix} -P_{\overline{1,N}} C_\Gamma^{-1} E_\Gamma \tilde{v}_0 \\ E(x_0)\tilde{v}_0 - C(x_0) C_\Gamma^{-1} E_\Gamma \tilde{v}_0 \end{bmatrix}. \quad (4.104)$$

Defining the linear operator

$$A := \begin{bmatrix} A_{\overline{1,N}} & A_{\overline{N+1,2N}} \end{bmatrix} \in L(\mathbb{R}^{2N}, \mathbb{R}^{2N}), \quad (4.105)$$

we can finally write the $2N \times 2N$ linear system of equations (4.104) as

$$A \begin{bmatrix} \tilde{r} \\ r \cdot f \end{bmatrix} = \begin{bmatrix} -P_{\overline{1,N}} C_\Gamma^{-1} E_\Gamma \tilde{v}_0 \\ E(x_0)\tilde{v}_0 - C(x_0) C_\Gamma^{-1} E_\Gamma \tilde{v}_0 \end{bmatrix}. \quad (4.106)$$

Since, we are only interested in the retrieval of the vector $\tilde{r}$, we are going to disregard from our considerations the other half of the solution vector, which is summarized

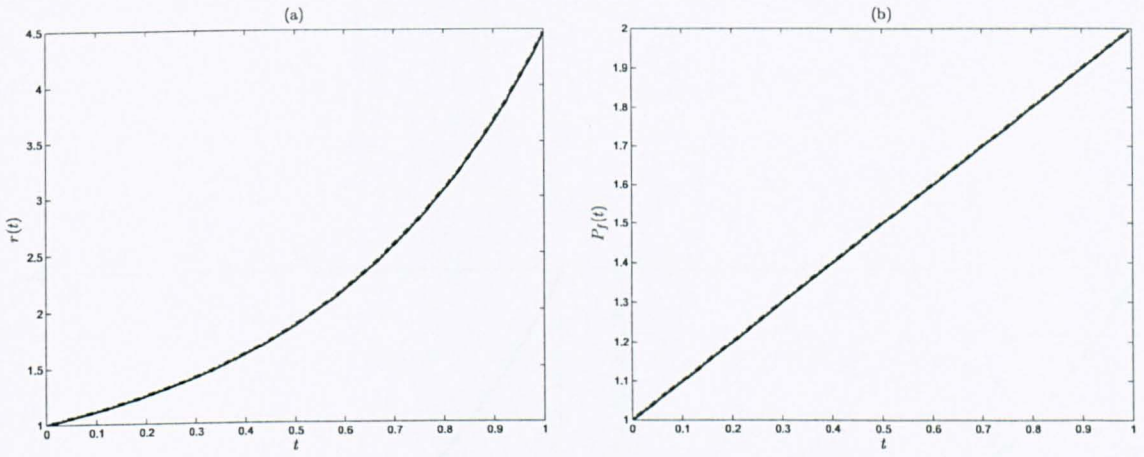

Figure 4.8: Computed and analytical values of: (a) $r(t)$, and (b) $P_f(t)$, when there is no noise in the data (4.41) .

in the components of $r \cdot f$.

The test solution considered in (4.40) supplies us with the internal measurement (4.41). In the case of exact data, $\alpha = 0\%$, the computed results agree very well with the analytical values, as shown in Figures 4.8(a) and 4.8(b).

On the other hand, in the case when $\alpha = 1\%$ noise is included in the internal measurement, we encounter the same difficulty as in the case of the Dirichlet boundary conditions, namely, that the noise from the additional information is heavily reflected in the computation of $\tilde{r}$, which becomes both noisy and unstable. This causes major difficulties in obtaining the numerical derivative $\frac{\partial \tilde{r}}{\partial t}$ which is involved in the retrieval of $P_f(t)$. However, for the retrieval of both the derivative of $\tilde{r}$ and the coefficient $P_f(t)$, applying precisely the same mollification steps as the one used and described in Sections 4.3-4.5, we similarly obtain good results that agree very well with the analytical values, as shown in Figures 4.9(a), 4.9(b) and 4.9(c).

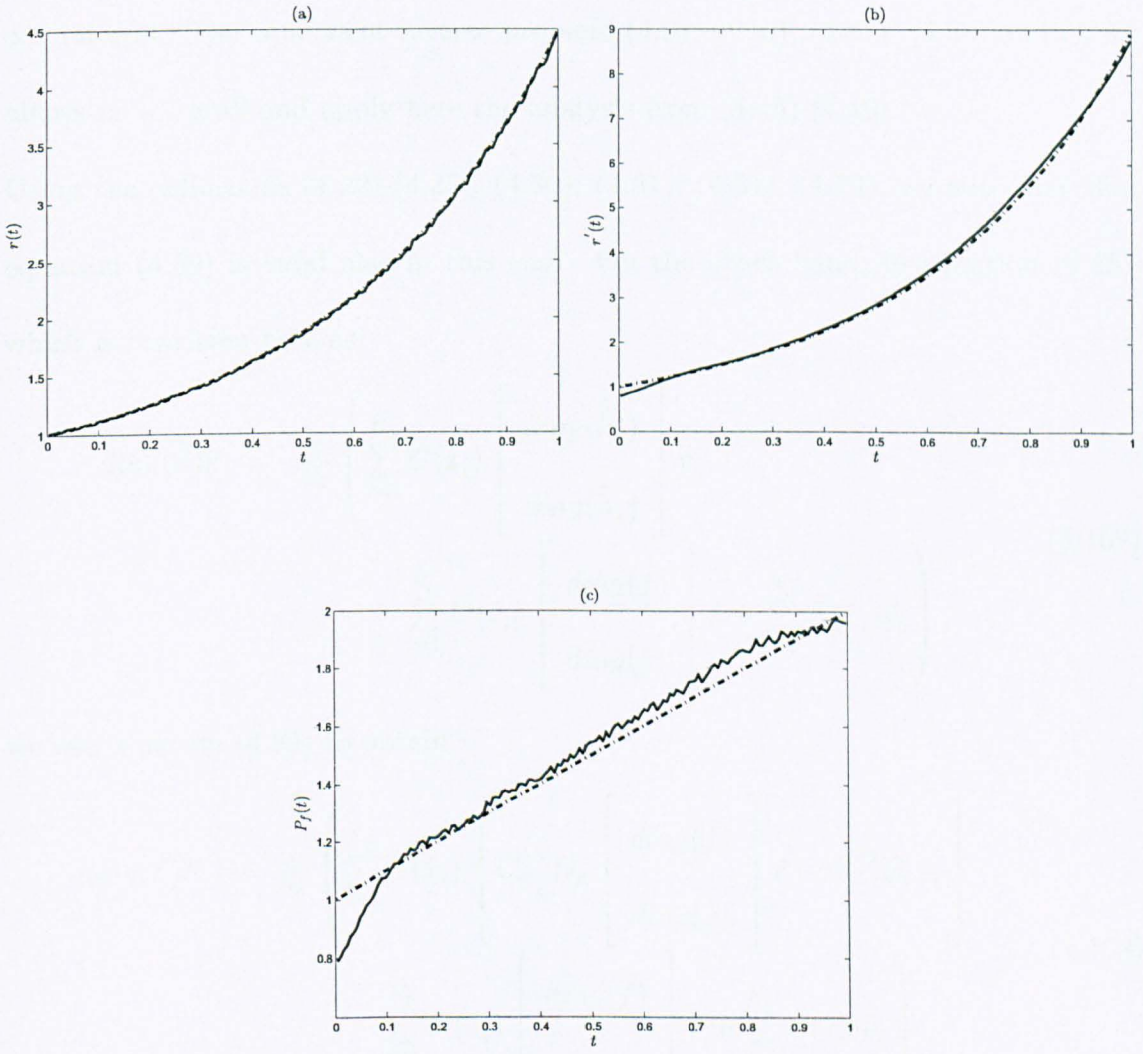

Figure 4.9: Computed and analytical values of: (a) $r(t)$, (b) $r'(t)$, and (c) $P_f(t)$, when there is $\alpha = 1\%$ of noise in the data (4.41) .

4.6.2 Total Mass Measurement Case

When the additional information considered is the mass measurement (4.5), the mixed boundary value inverse problem (4.1), (4.2), (4.85), (4.86) and (4.5) focuses our interest. The equivalent inverse problem (4.9), (4.10), (4.87), (4.88) and (4.45) allows us to recall and apply here the analysis from (4.45)-(4.49).

Using the definitions (4.22)-(4.25), (4.30), (4.31), (4.51), (4.79), we note first that equation (4.89) is valid also in this case. On the other hand, in equation (4.49), which is rewritten here as

$$\begin{aligned} diag(\tilde{\mathcal{E}})\tilde{r} \;=\; \tfrac{1}{N_0}\Bigg(&\sum_{i=1}^{N_0} C(\tilde{x}_i)\begin{bmatrix} diag(\tilde{h}_0) \\ diag(\tilde{h}_1) \end{bmatrix}\tilde{r} \\ &- \sum_{i=1}^{N_0} D(\tilde{x}_i)\begin{bmatrix} diag(\tilde{f}) \\ diag(\tilde{g}) \end{bmatrix}\tilde{r} + \sum_{i=1}^{N_0} E(\tilde{x}_i)\tilde{v}_0\Bigg), \end{aligned} \tag{4.107}$$

we use equation (4.89) to obtain

$$\begin{aligned} diag(\tilde{\mathcal{E}})\tilde{r} \;=\; \tfrac{1}{N_0}\Bigg(&\sum_{i=1}^{N_0} C(\tilde{x}_i)\left\{C_\Gamma^{-1}D_\Gamma\begin{bmatrix} diag(\tilde{f}) \\ diag(\tilde{g}) \end{bmatrix}\tilde{r} - C_\Gamma^{-1}E_\Gamma\tilde{v}_0\right\} \\ &- \sum_{i=1}^{N_0} D(\tilde{x}_i)\begin{bmatrix} diag(\tilde{f}) \\ diag(\tilde{g}) \end{bmatrix}\tilde{r} + \sum_{i=1}^{N_0} E(\tilde{x}_i)\tilde{v}_0\Bigg). \end{aligned} \tag{4.108}$$

Using the projection (4.92) in (4.89), we arrive again at the N-dimensional operator equation (4.93). Therefore, equations (4.93) and (4.108) supply us the $2N \times 2N$-

dimensional system

$$\left\{\begin{array}{l} diag(\tilde{h}_0)\tilde{r} - P_{\overline{1,N}} C_\Gamma^{-1} D_\Gamma \begin{bmatrix} diag(\tilde{f})\tilde{r} \\ diag(\tilde{g})\tilde{r} \end{bmatrix} + P_{\overline{1,N}} C_\Gamma^{-1} E_\Gamma \tilde{v}_0 = 0, \\ diag(\tilde{\mathcal{E}})\tilde{r} = \frac{1}{N_0}\sum_{i=1}^{N_0} \left(C(\tilde{x}_i) C_\Gamma^{-1} D_\Gamma \begin{bmatrix} diag(\tilde{f})\tilde{r} \\ diag(\tilde{g})\tilde{r} \end{bmatrix} - D(\tilde{x}_i) \begin{bmatrix} diag(\tilde{f})\tilde{r} \\ diag(\tilde{g})\tilde{r} \end{bmatrix} \right) \\ \qquad + \frac{1}{N_0}\sum_{i=1}^{N_0} \left(-C(\tilde{x}_i) C_\Gamma^{-1} E_\Gamma + E(\tilde{x}_i) \right) \tilde{v}_0, \end{array}\right. \tag{4.109}$$

with the $2N$-dimensional vector of unknowns

$$\begin{bmatrix} \tilde{r} \\ r \cdot f \end{bmatrix} = \begin{bmatrix} \tilde{r} \\ diag(\tilde{f})\tilde{r} \end{bmatrix}, \tag{4.110}$$

according to the definition (4.94) of the vector $r \cdot f$. Using the linear operators defined in (4.97)-(4.100), the system (4.109) is equivalently expressed as

$$\left\{\begin{array}{l} diag(\tilde{h}_0)\tilde{r} - P_{\overline{1,N}} C_\Gamma^{-1} \left\{ D_{\Gamma_{\overline{1,N}}} r \cdot f + D_{\Gamma_{\overline{N+1,2N}}} diag(\tilde{g})\tilde{r} \right\} + P_{\overline{1,N}} C_\Gamma^{-1} E_\Gamma \tilde{v}_0 = 0, \\ diag(\tilde{\mathcal{E}})\tilde{r} = \frac{1}{N_0}\sum_{i=1}^{N_0} C(\tilde{x}_i) C_\Gamma^{-1} \left\{ D_{\Gamma_{\overline{1,N}}} r \cdot f + D_{\Gamma_{\overline{N+1,2N}}} diag(\tilde{g})\tilde{r} \right\} \\ \qquad - \frac{1}{N_0}\sum_{i=1}^{N_0} \left\{ D(\tilde{x}_i)_{\overline{1,N}} r \cdot f + D(\tilde{x}_i)_{\overline{N+1,2N}} diag(\tilde{g})\tilde{r} \right\} \\ \qquad + \frac{1}{N_0}\sum_{i=1}^{N_0} \left(-C(\tilde{x}_i) C_\Gamma^{-1} E_\Gamma + E(\tilde{x}_i) \right) \tilde{v}_0. \end{array}\right. \tag{4.111}$$

Thus, using again the linear operator notations $A_{\overline{1,N}}, A_{\overline{N+1,2N}} \in L(\mathbb{R}^N, \mathbb{R}^{2N})$ to describe the matrices

$$A_{\overline{1,N}} := \begin{bmatrix} diag(\tilde{h}_0) - P_{\overline{1,N}} C_\Gamma^{-1} D_{\Gamma_{\overline{N+1,2N}}} diag(\tilde{g}) \\ diag(\tilde{\mathcal{E}}) - \frac{1}{N_0}\sum_{i=1}^{N_0} C(\tilde{x}_i) C_\Gamma^{-1} D_{\Gamma_{\overline{N+1,2N}}} diag(\tilde{g}) + \frac{1}{N_0}\sum_{i=1}^{N_0} D(\tilde{x}_i)_{\overline{N+1,2N}} diag(\tilde{g}) \end{bmatrix} \tag{4.112}$$

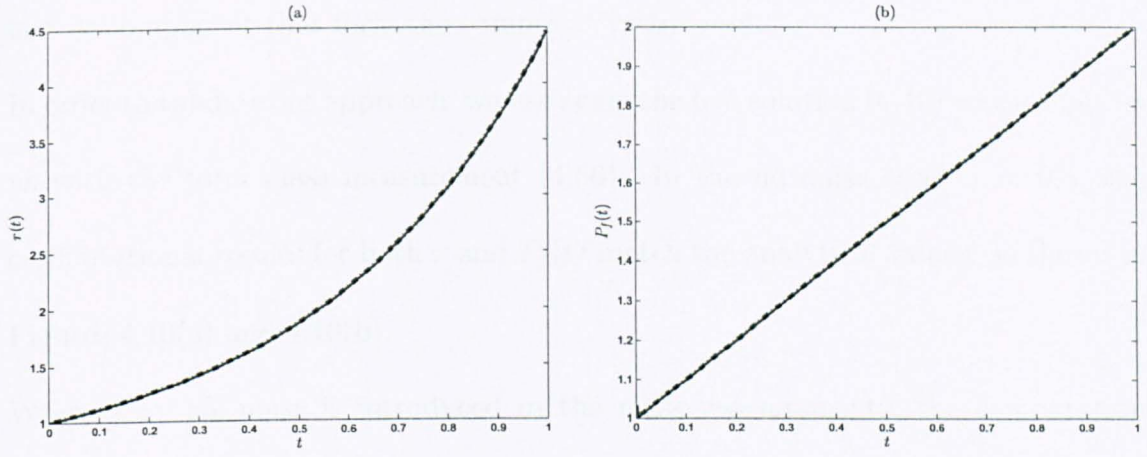

Figure 4.10: Computed and analytical values of: (a) $r(t)$ and (b) $P_f(t)$, when there is no noise in the data (4.56).

and

$$A_{\overline{N+1,\,2N}} := \begin{bmatrix} -P_{\overline{1,\,N}} C_\Gamma^{-1} D_{\Gamma_{\overline{1,\,N}}} \\ \\ \frac{1}{N_0} \sum_{i=1}^{N_0} \left(-C(\tilde{x}_i) C_\Gamma^{-1} D_{\Gamma_{\overline{1,\,N}}} + D(\tilde{x}_i)_{\overline{1,\,N}} \right) \end{bmatrix}, \tag{4.113}$$

the system of equations (4.111) recasts as

$$A_{\overline{1,\,N}} \tilde{r} + A_{\overline{N+1,\,2N}} r \cdot f = \begin{bmatrix} -P_{\overline{1,\,N}} C_\Gamma^{-1} E_\Gamma \tilde{v}_0 \\ \\ \frac{1}{N_0} \sum_{i=1}^{N_0} \left(E(\tilde{x}_i) \tilde{v}_0 - C(\tilde{x}_i) C_\Gamma^{-1} E_\Gamma \tilde{v}_0 \right) \end{bmatrix}. \tag{4.114}$$

By defining the matrix $A \in L(\mathbb{R}^{2N}, \mathbb{R}^{2N})$ as in (4.105), the system (4.114) can be written as

$$A \begin{bmatrix} \tilde{r} \\ \\ r \cdot f \end{bmatrix} = \begin{bmatrix} -P_{\overline{1,\,N}} C_\Gamma^{-1} E_\Gamma \tilde{v}_0 \\ \\ \frac{1}{N_0} \sum_{i=1}^{N_0} \left(E(\tilde{x}_i) \tilde{v}_0 - C(\tilde{x}_i) C_\Gamma^{-1} E_\Gamma \tilde{v}_0 \right) \end{bmatrix}. \tag{4.115}$$

The system (4.115) is to be solved as a whole, however, of interest for us are only the first N components of the solution vector, namely, $\tilde{r}$, and we disregard here its

last N component that form the computed vector $r \cdot f$.

In order to validate our approach, we use again the test solution (4.40) which supplies us with the total mass measurement (4.56). In the no noise case, $\alpha = 0\%$, the computational results for both r and $P_f(t)$ match the analytical values, as shown in Figures 4.10(a) and 4.10(b).

When $\alpha = 1\%$ noise is introduced in the mass measurements, the computation carried out for solving the linear system (4.115) is again heavily affected by the propagated noise. However, the quantities $\tilde{r}$, and $\frac{\partial \tilde{r}}{\partial t}$, and finally $P_f(t)$ are retrieved following the same discretization scheme and steps described in the noisy case for the Dirichlet boundary value problem, from Section 4.3. Figures 4.11(a),4.11(b) and 4.11(c) show that the computed values for $\tilde{r}$, $\frac{\partial \tilde{r}}{\partial t}$ and $P_f(t)$ agree well with the analytical values.

4.7 Internal Measurements on Arbitrarily Non-Constant Time-Dependent Paths

So far in this chapter, all the internal measurements considered were set to remain constant at one single point $x_0 \in (0,1)$, which in the $(0,1)\times(0,t_f]$ domain represents the measured value of the temperature $T(x,t)$ considered along the straight path given by the function $\gamma_0 : (0,t_f] \rightarrow (0,1)$, $\gamma_0(t) :\equiv x_0$. However, as we will see in the following, the function γ_0 need not be constant. We devote this section to investigate both the Dirichlet and the mixed boundary conditions problem, when the internal temperature measurement is taken on arbitrarily non constant paths $\gamma : (0,t_f] \rightarrow [0,1]$. Therefore, the Dirichlet inverse problem (4.1)-(4.3), or the mixed

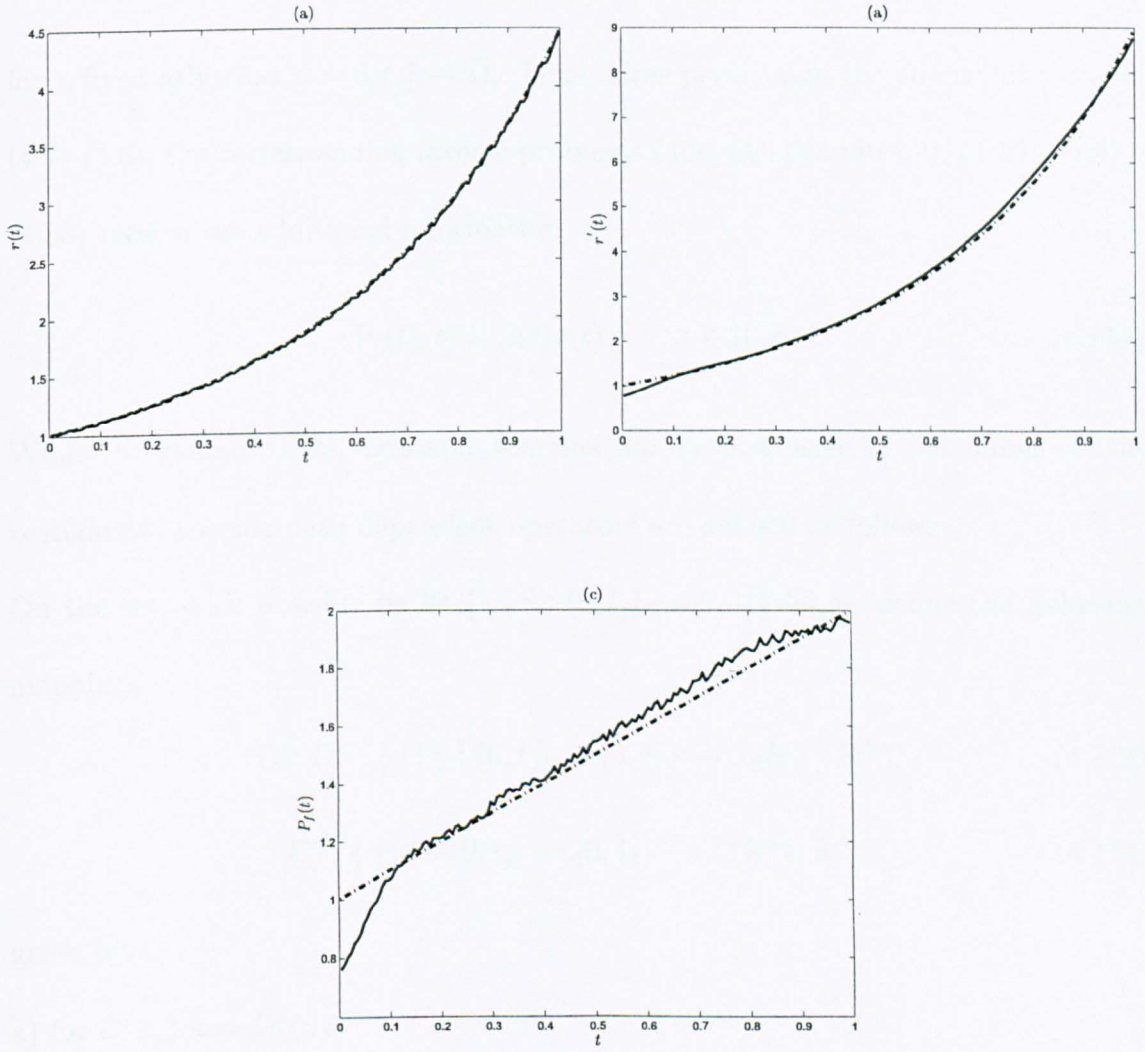

Figure 4.11: Computed and analytical values of: (a) for $r(t)$, (b) $r'(t)$, (c) $P_f(t)$, when there is $\alpha = 1\%$ of noise in the data (4.56).

boundary value inverse problem (4.1), (4.2), (4.85), (4.86), receives in this section the following internal temperature measurement:

$$T(\gamma(t),t) = u(t), \qquad t \in (0,t_f] \tag{4.116}$$

for a fixed arbitrary $\gamma : (0,t_f] \to \overline{\Omega}$. Thus, after performing the change of variable (4.7)-(4.8), the corresponding inverse problems (4.9)-(4.11) and (4.9), (4.10), (4.87), (4.88) receive the additional information

$$v(\gamma(t),t) = u(t)r(t), \qquad t \in (0,t_f]. \tag{4.117}$$

While the general BEM technique remains the method used for our numerical investigation, specific path dependent operators are defined as follows.

On the set of all possible paths $\{\gamma \,|\, \gamma : (0,t_f] \to [0,1]\}$ let us define the following mappings:

$$C^*, D^* : \{\gamma \,|\, \gamma : (0,t_f] \to [0,1]\} \to L(\mathbb{R}^{2N}, \mathbb{R}^N), \tag{4.118}$$

$$E^* : \{\gamma \,|\, \gamma : (0,t_f] \to [0,1]\} \to L(\mathbb{R}^{N_0}, \mathbb{R}^N), \tag{4.119}$$

given by:

a) for $C^*(\gamma)$ and $D^*(\gamma)$

$$\begin{aligned}
C^*(\gamma)(i,j) &:= C_j^0(\gamma(\tilde{t}_i),\tilde{t}_i), \qquad i = \overline{1,\,N},\ j = \overline{1,\,N} \\
C^*(\gamma)(i,j) &:= C_j^1(\gamma(\tilde{t}_i),\tilde{t}_i), \qquad i = \overline{1,\,N},\ j = \overline{N+1,\,2N}, \\
D^*(\gamma)(i,j) &:= D_j^0(\gamma(\tilde{t}_i),\tilde{t}_i), \qquad i = \overline{1,\,N},\ j = \overline{1,\,N}, \\
D^*(\gamma)(i,j) &:= D_j^1(\gamma(\tilde{t}_i),\tilde{t}_i), \qquad i = \overline{1,\,N},\ j = \overline{N+1,\,2N},
\end{aligned} \tag{4.120}$$

b) for $E^*(\gamma)$

$$E^*(\gamma)(k,j) := E_j(\gamma(t),\tilde{t}_k), \qquad k = \overline{1,\,N},\ j = \overline{1,\,N_0}, \tag{4.121}$$

for all γ.

Then the BEM solution vector along γ of the heat equation (4.9) satisfies

$$\left[v(\gamma(\tilde{t}_1),\tilde{t}_1),...v(\gamma(\tilde{t}_N),\tilde{t}_N)\right]^T = C^*(\gamma)\tilde{v}_\Gamma^{'} - D^*(\gamma)\tilde{v}_\Gamma + E^*(\gamma)\tilde{v}_0. \tag{4.122}$$

We notice that the operators (4.120) are compatible with the ones defined in Section 4.3 and we will use them in the subsections that follow. It is worthwhile to remark that equations (4.26) and (4.27) are valid for the Dirichlet inverse problem (4.9)-(4.11) and (4.117) and for the mixed boundary condition inverse problem (4.9), (4.10), (4.87), (4.88) and (4.117).

4.7.1 The Dirichlet Inverse Problem Revisited

Using the notation (4.28), from (4.27) and (4.122) we obtain

$$r \cdot u = (C^*(\gamma)C_\Gamma^{-1}D_\Gamma - D^*(\gamma))\tilde{v}_\Gamma + (-C^*(\gamma)C_\Gamma^{-1}E_\Gamma + E^*(\gamma))\tilde{v}_0. \tag{4.123}$$

After defining

$$G^*(\gamma) := C^*(\gamma)C_\Gamma^{-1}D_\Gamma - D^*(\gamma) \ \in L(\mathbb{R}^{2N},\mathbb{R}^N), \tag{4.124}$$

from equation (4.123), proceeding in a similar manner as in the case of a fixed internal point measurement, we obtain the $N \times N$ linear system

$$A\tilde{r} = (-C^*(\gamma)C_\Gamma^{-1}E_\Gamma + E^*(\gamma))\tilde{v}_0, \tag{4.125}$$

where

$$A := diag(\tilde{u}) - G^*(\gamma)\begin{bmatrix} diag(\tilde{f}) \\ \\ diag(\tilde{g}) \end{bmatrix}, \tag{4.126}$$

which clearly is similar in structure with the system of equations (4.36). Moreover, if γ is chosen to be the constant path $\gamma_0(t) \equiv x_0$, for all $t \in [0,t_f]$, we immediately

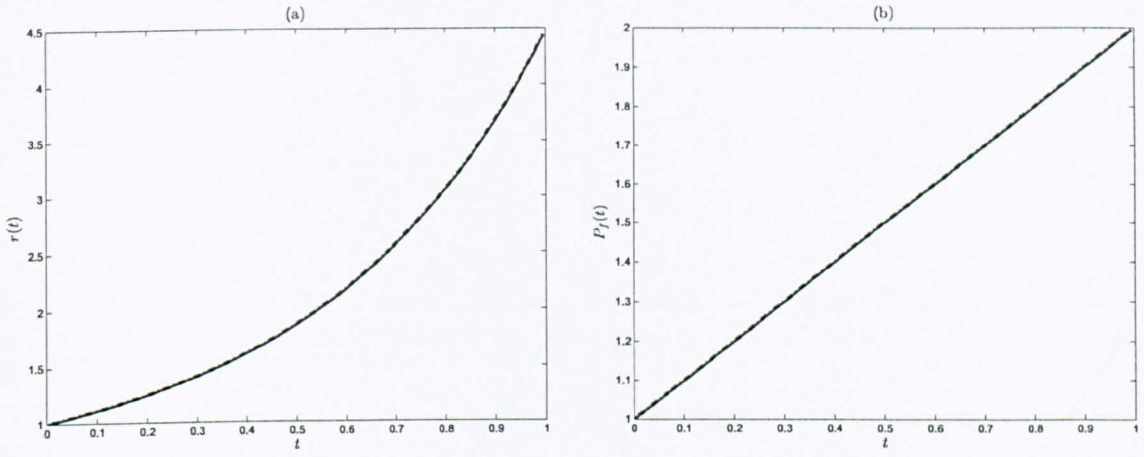

Figure 4.12: Computed and analytical values of: (a) $r(t)$, and (b) $P_f(t)$, when there is no noise in the data (4.128).

recognise that the systems (4.126) and (4.36) coincide, as was expected, since the two inverse problems become the same. Let us consider the following path γ : $[0, t_f] \to (0, 1)$

$$\gamma(t) = \frac{1}{2} + \frac{\sin t}{4}, \qquad t \in [0, t_f]. \tag{4.127}$$

Then, the test solution (4.40) gives us the path measurement

$$T(\gamma(t), t) = \left(\left(\frac{1}{2} + \frac{\sin t}{4} \right)^2 + 2t \right) \exp\left(-t - \frac{t^2}{2} \right) (1 + \alpha\eta(t))). \tag{4.128}$$

In the no noise case, $\alpha = 0\%$, after obtaining the solution of the system (4.125), as shown in Figures 4.12(a) and 4.12(b), the computed results for $\tilde{r}$ and $P_f(t)$, again agree very well with the analytical values.

When $\alpha = 1\%$ noise is introduced in the path measurement (4.128), the same types of dificulties as those in the fixed point measurement case are encounterd, namely the noise is strongly propagated through the system (4.125) in the computation of the solution $\tilde{r}$, which then causes major problems, especially for obtaining the

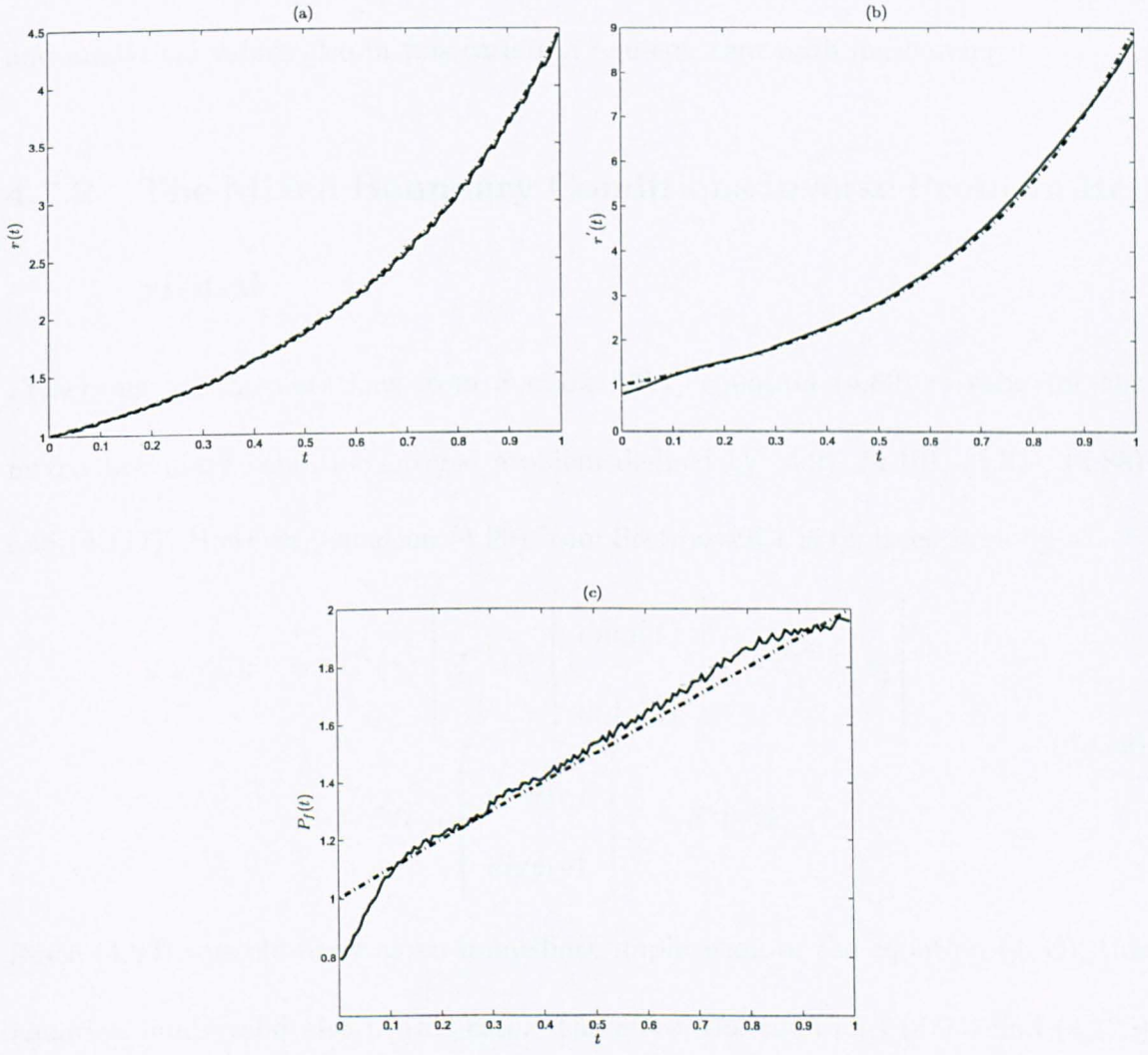

Figure 4.13: Computed and analytical values of: (a) $r(t)$, (b) for $r'(t)$, and (c) $P_f(t)$, when there is $\alpha = 1\%$ of noise in the data (4.128).

numerical derivative $\frac{\partial \tilde{r}}{\partial t}$. However, following precisely the same steps as the ones described in Section 4.3, we obtain good results both for the computation of $\tilde{r}$ and $\frac{\partial \tilde{r}}{\partial t}$ which resort in a retrieval very close to the analytical values of the coefficient $P_f(t)$. Figures 4.13(a), 4.13(b) and 4.13(c) illustrate the agreement of the computed and analytical values also in this case of a non-constant path measurement.

4.7.2 The Mixed Boundary Conditions Inverse Problem Revisited

Preserving all the notations from Section 4.6.1, equation (4.89) is valid for the mixed boundary condition inverse problem defined by (4.9), (4.10), (4.87), (4.88) and (4.117). However, equation (4.90) from Section 4.6.1 is replaced here by

$$\begin{aligned} diag(\tilde{u})\tilde{r} \;=\; & C^*(\gamma)\left[C_\Gamma^{-1}D_\Gamma\begin{bmatrix} diag(\tilde{f}) \\ diag(\tilde{g}) \end{bmatrix}\tilde{r} - C_\Gamma^{-1}E_\Gamma\tilde{v}_0\right] \\ & -D^*(\gamma)\begin{bmatrix} diag(\tilde{f}) \\ diag(\tilde{g}) \end{bmatrix}\tilde{r} + E^*(\gamma)\tilde{v}_0. \end{aligned} \tag{4.129}$$

Since (4.93) was obtained as an immediate implication of the equation (4.89), this equation holds valid also in this case. Therefore, the equations (4.93) and (4.129) form the $2N \times 2N$ system

$$\begin{cases} diag(\tilde{h}_0)\tilde{r} - P_{\overline{1,N}} C_\Gamma^{-1} D_\Gamma \begin{bmatrix} r \cdot f \\ diag(\tilde{g})\tilde{r} \end{bmatrix} + P_{\overline{1,N}} C_\Gamma^{-1} E_\Gamma \tilde{v}_0 = 0, \\ diag(\tilde{u})\tilde{r} = C^*(\gamma) \left[C_\Gamma^{-1} D_\Gamma \begin{bmatrix} r \cdot f \\ diag(\tilde{g})\tilde{r} \end{bmatrix} - C_\Gamma^{-1} E_\Gamma \tilde{v}_0 \right] \\ \qquad -D^*(\gamma) \begin{bmatrix} r \cdot f \\ diag(\tilde{g})\tilde{r} \end{bmatrix} + E^*(\gamma)\tilde{v}_0, \end{cases} \tag{4.130}$$

in the $2N$-dimensional vector of unknowns (4.96).

Let us define the finite dimensional operators

$$D^*(\gamma)_{\overline{1,N}} := [col_1(D^*(\gamma)), ..., col_N(D^*(\gamma))] \in L(\mathbb{R}^N, \mathbb{R}^N), \tag{4.131}$$

$$D^*(\gamma)_{\overline{N+1,2N}} := [col_{N+1}(D^*(\gamma)), ..., col_{2N}(D^*(\gamma))] \in L(\mathbb{R}^N, \mathbb{R}^N). \tag{4.132}$$

By continuing now with an analysis that is identical with the one performed in (4.97)-(4.103), we obtain the corresponding sub-matrices $A_{\overline{1,N}}$, $A_{\overline{N+1,2N}} \in L(R^N, R^{2N})$, which are defined as follows:

$$A_{\overline{1,N}} := \begin{bmatrix} diag(\tilde{h}_0) - P_{\overline{1,N}} C_\Gamma^{-1} D_{\Gamma_{\overline{N+1,2N}}} diag(\tilde{g}) \\ diag(\tilde{u}) - C^*(\gamma) C_\Gamma^{-1} D_{\Gamma_{\overline{N+1,2N}}} diag(\tilde{g}) + D^*(\gamma)_{\overline{N+1,2N}} diag(\tilde{g}) \end{bmatrix} \tag{4.133}$$

and

$$A_{\overline{N+1,2N}} := \begin{bmatrix} -P_{\overline{1,N}} C_\Gamma^{-1} D_{\Gamma_{\overline{1,N}}} \\ -C^*(\gamma) C_\Gamma^{-1} D_{\Gamma_{\overline{1,N}}} + D^*(\gamma)_{\overline{1,N}} \end{bmatrix}, \tag{4.134}$$

in addition to the right hand side part of the system

$$\begin{bmatrix} -P_{\overline{1,N}} C_\Gamma^{-1} E_\Gamma \tilde{v}_0 \\ E^*(\gamma)\tilde{v}_0 - C^*(\gamma) C_\Gamma^{-1} E_\Gamma \tilde{v}_0 \end{bmatrix}. \tag{4.135}$$

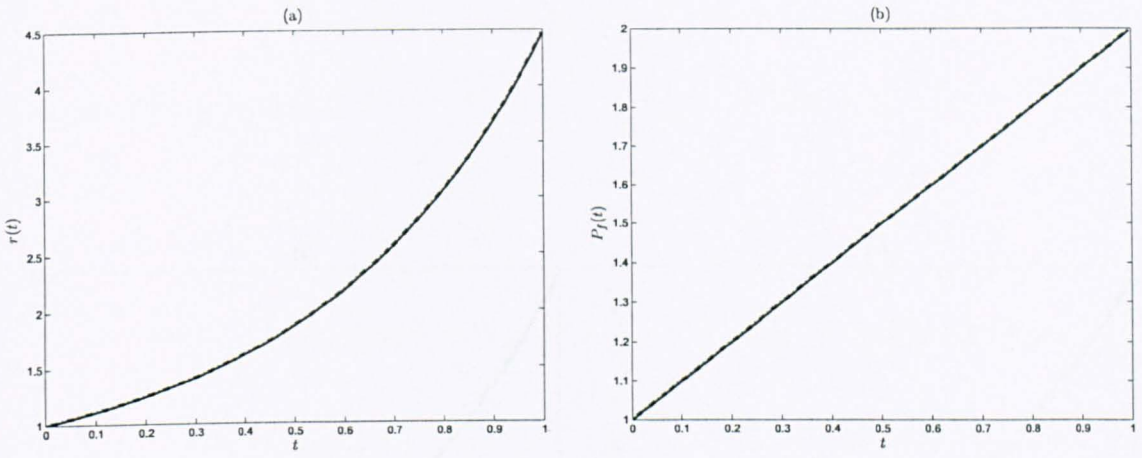

Figure 4.14: Computed and analytical values of: (a) for $r(t)$, and (b) $P_f(t)$, when there is no noise involved in the data (4.128).

Therefore, creating again the linear operator $A := \begin{bmatrix} A_{\overline{1,N}} & A_{\overline{N+1,2N}} \end{bmatrix} \in L(\mathbb{R}^{2N}, \mathbb{R}^{2N})$, we obtain the desired system

$$A \begin{bmatrix} \tilde{r} \\ r \cdot f \end{bmatrix} = \begin{bmatrix} -P_{\overline{1,N}} C_\Gamma^{-1} E_\Gamma \tilde{v}_0 \\ E^*(\gamma)\tilde{v}_0 - C^*(\gamma) C_\Gamma^{-1} E_\Gamma \tilde{v}_0 \end{bmatrix}. \tag{4.136}$$

Since we are only interested in computing $\tilde{r}$, even though we solve the entire system (4.136), we are going to disregard $r \cdot f$, which is the second half of the solution vector. To validate our approach, we consider again the test solution (4.40) and the path measurement prescribed in (4.127)-(4.128).

In the no noise case, $\alpha = 0\%$, as shown in Figures 4.14(a) and 4.14(b), the computed results agree both for $\tilde{r}$ and for $P_f(t)$ with their analytical values.

When $\alpha = 1\%$ noise is introduced in the path measurements, the computed solution of the system of equations (4.136) is heavily affected by the noise. However, applying the same aproach as in the noisy case for path measurements in the Dirichlet

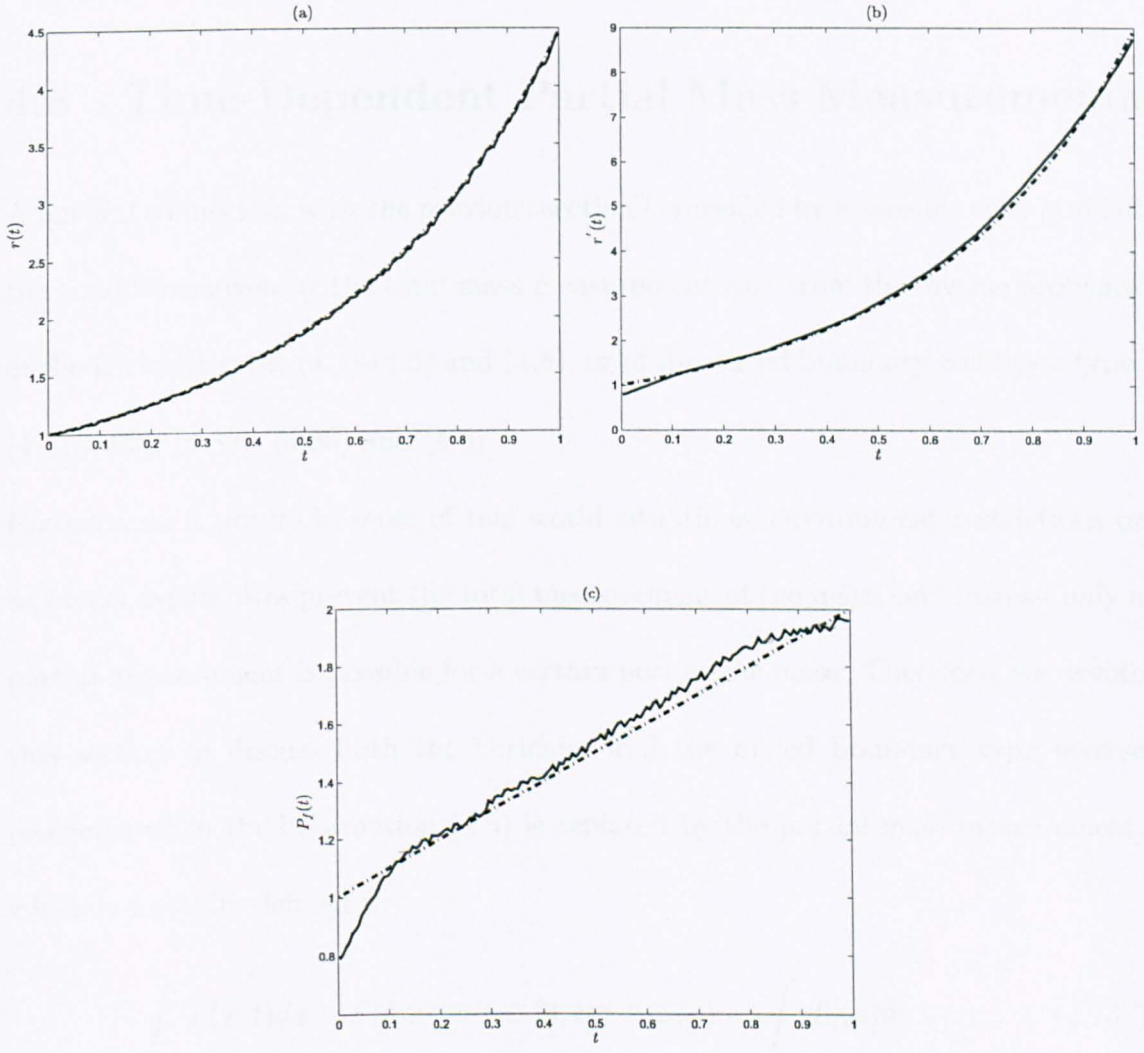

Figure 4.15: Computed and analytical values of: (a) $r(t)$, (b) $r'(t)$, and (c) $P_f(t)$, when there is $\alpha = 1\%$ of noise involved in the data (4.128).

boundary conditions, we obtain yet again good agreement between the computed and analytical values of $\tilde{r}$, $\tilde{r}'$ and $P_f(t)$, as illustrated in Figures 4.15(a), 4.15(b) and 4.15(c).

4.8 Time-Dependent Partial Mass Measurements

A natural connection with the previous section is revealed by a sensible relaxation of the conditions given by the total mass measurement case from the inverse problems of the Dirichlet type, (4.1)-(4.3) and (4.5), or of the mixed boundary condition type, (4.1), (4.2), (4.85), (4.86) and (4.5).

However, as it occurs in most of real world situations, environment restrictions or technical capabilities prevent the total measurement of the mass, and instead only a partial measurement is possible for a certain part of the mass. Therefore, we devote this section to discuss both the Dirichlet and the mixed boundary type inverse problems when the information (4.5) is replaced by the partial mass measurement, which is formally defined by

$$\int_{\Lambda(t)} T(x,t)dx = \mathcal{E}(t), \qquad t \in [0,t_f), \quad \mathcal{E}(0) = \int_{\Lambda(0)} T_0(x)dx, \tag{4.137}$$

where the set-valued map $\Lambda : [0,1] \to \{[\overline{\gamma}_1(t), \overline{\gamma}_2(t)] \,|\, t \in (0,t_f]\}$, given by

$$\Lambda(t) := [\overline{\gamma}_1(t), \overline{\gamma}_2(t)], \quad t \in [0,t_f], \tag{4.138}$$

is supplied by the *a priori* given paths $\overline{\gamma}_1, \overline{\gamma}_2 : [0,t_f] \to [0,1]$, $\overline{\gamma}_1, \overline{\gamma}_2 \in \mathscr{C}^1$. We should observe here that the Lebesque measure of both $\Lambda(t)$ and the frontier $\partial\Lambda(t)$ are smooth functions with respect to t.

The solvability of the inverse problem (4.1)-(4.3) and (4.137) has been established

in Cannon et al. [17, 18], Cannon and Yin [20] and Lin [68], as follows.

Theorem 4.8.1 *If* $T_0 \in \mathscr{C}^1([0,1])$, $f, g \in \mathscr{C}([0,t_f])$, $T_0 \geq 0$, $f \geq 0$, $g \geq 0$, $\gamma_2, \mathcal{E} \in \mathscr{C}^1$, $\mathcal{E} > 0$, $\gamma_1 \equiv 0$, *then there exists a unique solution* $(T \in \mathscr{C}^{2,1}((0,1) \times (0,t_f]) \bigcap \mathscr{C}([0,1] \times [0,t_f])$, $P_f \in \mathscr{C}([0,t_f]))$ *of the inverse problem (4.1)-(4.3) and (4.137) which is continuously dependent upon data.*

After performing the change of variable (4.7)-(4.8), the corresponding inverse problems (4.9)-(4.11) and (4.9), (4.10), (4.87), (4.88) will receive the additional information

$$\int_{\Lambda(t)} v(x,t)dx = r(t)\mathcal{E}(t), \qquad t \in (0,t_f], \quad \mathcal{E}(0) = \int_{\Lambda(0)} T_0(x)dx. \tag{4.139}$$

Thus, in terms of the BEM, using a large enough number N_0 of space cells to discretize the entire space interval $(0,1)$, we obtain

$$r(t)\mathcal{E}(t) \simeq \frac{1}{N_0}\sum_{i=1}^{N_0} r(t)T(\tilde{x}_i,t)\chi_{\Lambda(t)}(\tilde{x}_i), \tag{4.140}$$

where, for any non-empty arbitrary set $\widetilde{\Omega}$ and any subset $\widetilde{\Omega}_1 \subset \widetilde{\Omega}$, the function

$$\begin{aligned} &\chi_{\widetilde{\Omega}_1} : \widetilde{\Omega} \to \{0,1\} \\ &\chi_{\widetilde{\Omega}_1}(\sigma) = \begin{cases} 1, & \sigma \in \widetilde{\Omega}_1 \\ 0, & \sigma \in \widetilde{\Omega} \setminus \widetilde{\Omega}_1 \end{cases} \end{aligned} \tag{4.141}$$

will be called the characteristic function of $\widetilde{\Omega}_1$ in $\widetilde{\Omega}$. Using N time nodes to discretize $[0,t_f]$, from (4.140) we obtain the following N-dimensional equation

$$diag(\tilde{\mathcal{E}})\tilde{r} = \frac{1}{N_0}\sum_{i=1}^{N_0} diag\left(\left[T(\tilde{x}_i,\tilde{t}_1)\chi_{\Lambda(\tilde{t}_1)}(\tilde{x}_i), \ldots T(\tilde{x}_i,\tilde{t}_N)\chi_{\Lambda(\tilde{t}_N)}(\tilde{x}_i)\right]^{tr}\right)\tilde{r}. \tag{4.142}$$

Let us now define the integer

$$N_0(\tilde{\mathcal{E}}) := \max_{j=\overline{1,N}} Card\left(\{\tilde{x}_i \mid \tilde{x}_i \in \Lambda(\tilde{t}_j)\}\right), \tag{4.143}$$

where, in general, for any arbitrary set $\widetilde{\Omega}$, $Card(\widetilde{\Omega})$ is the cardinal of $\widetilde{\Omega}$. Clearly,

$$N_0(\tilde{\mathcal{E}}) \leq N_0. \tag{4.144}$$

Denoting $\mathcal{A}(\tilde{t}_j) := \Lambda(\tilde{t}_j) \bigcap \{\tilde{x}_k\}_{k=\overline{1,N_0}}$, $j = \overline{1,N}$, for $1 \leq i \leq N_0(\tilde{\mathcal{E}})$, for any $l \in \{0, ..., N_0(\tilde{\mathcal{E}})\}$, we consider the linear interpolating paths $\gamma_i : [0, t_f] \to [0,1]$ given by $\gamma_0(t) \equiv 0$, and iteratively we define

$$\gamma_i(\tilde{t}_j) := \begin{cases} min\left(\mathcal{A}(\tilde{t}_j) \setminus \bigcup_{l=0}^{i-1} \gamma_l(\tilde{t}_j)\right), & \text{if} \quad \mathcal{A}(\tilde{t}_j) \setminus \bigcup_{l=0}^{i-1} \gamma_l(\tilde{t}_j) \neq \varnothing, \\ max\left(\mathcal{A}(\tilde{t}_j)\right), & \text{otherwise,} \end{cases}$$

$$\gamma_i(\tilde{t}_j\lambda + (1-\lambda)\tilde{t}_{j-1}) := \gamma_i(\tilde{t}_j)\lambda + (1-\lambda)\gamma_i(\tilde{t}_{j-1}), \qquad \lambda \in (0,1). \tag{4.145}$$

Then, equation (4.142) becomes

$$\begin{aligned} diag(\tilde{\mathcal{E}})\tilde{r} &= \tfrac{1}{N_0} \sum_{i=1}^{N_0(\tilde{\mathcal{E}})} diag\left(\left[T(\gamma_i(\tilde{t}_1), \tilde{t}_1), ...T(\gamma_i(\tilde{t}_N), \tilde{t}_N)\right]^{tr}\right)\tilde{r} \\ &= \tfrac{1}{N_0} \sum_{i=1}^{N_0(\tilde{\mathcal{E}})} \left[C^*(\gamma_i)C_\Gamma^{-1}D_\Gamma - D^*(\gamma_i)\right]\tilde{v}_\Gamma \\ &\quad + \tfrac{1}{N_0} \sum_{i=1}^{N_0(\tilde{\mathcal{E}})} \left[-C^*(\gamma_i)C_\Gamma^{-1}E_\Gamma + E^*(\gamma_i)\right]\tilde{v}_0. \end{aligned} \tag{4.146}$$

4.8.1 Discussion of the Dirichlet Case

When the Dirichlet boundary conditions (4.3) are supplied, equation (4.146) becomes

$$\begin{aligned} diag(\tilde{\mathcal{E}})\tilde{r} &= \tfrac{1}{N_0} \sum_{i=1}^{N_0(\tilde{\mathcal{E}})} \left[C^*(\gamma_i)C_\Gamma^{-1}D_\Gamma - D^*(\gamma_i)\right] \begin{bmatrix} diag(\tilde{f}) \\ diag(\tilde{g}) \end{bmatrix} \tilde{r} \\ &\quad + \tfrac{1}{N_0} \sum_{i=1}^{N_0(\tilde{\mathcal{E}})} \left[-C^*(\gamma_i)C_\Gamma^{-1}E_\Gamma + E^*(\gamma_i)\right]\tilde{v}_0. \end{aligned} \tag{4.147}$$

Thus, by defining the left hand side matrix $A \in L(\mathbb{R}^N, \mathbb{R}^N)$ as

$$A := diag(\tilde{\mathcal{E}}) - \frac{1}{N_0} \sum_{i=1}^{N_0(\tilde{\mathcal{E}})} \left[C^*(\gamma_i)C_\Gamma^{-1}D_\Gamma - D^*(\gamma_i)\right] \begin{bmatrix} diag(\tilde{f}) \\ diag(\tilde{g}) \end{bmatrix}, \tag{4.148}$$

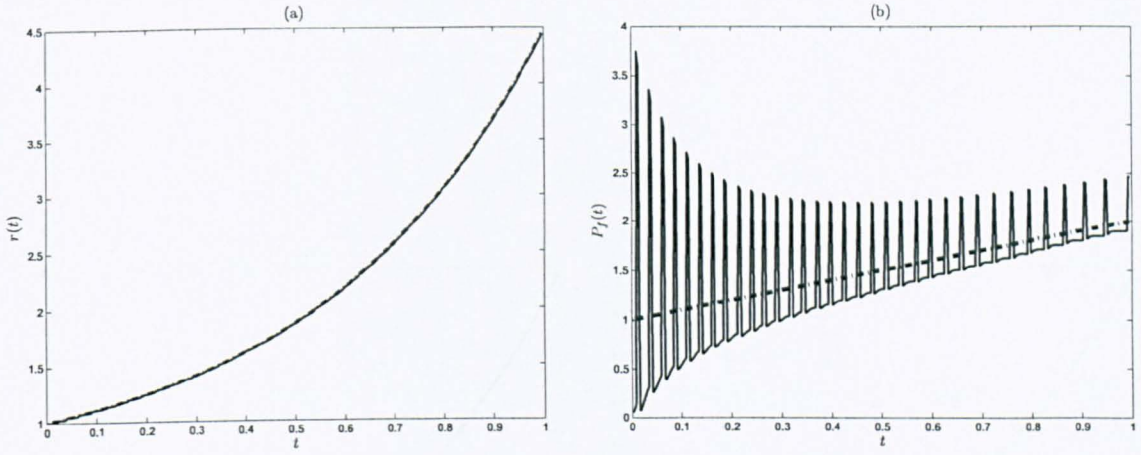

Figure 4.16: Computed and analytical values of: (a) $r(t)$ and (b) $P_f(t)$, when there is no noise in the data (4.151).

we obtain the N-dimensional linear system

$$A\tilde{r} = \frac{1}{N_0} \sum_{i=1}^{N_0(\tilde{\mathcal{E}})} \left[-C^*(\gamma_i) C_\Gamma^{-1} E_\Gamma + E^*(\gamma_i) \right] \tilde{v}_0. \tag{4.149}$$

Let us now consider the following particular set-valued map Λ given by

$$\Lambda(t) = \left\{ x \in \Omega \;\middle|\; x \in \left[0.4 + \frac{\sin t}{4}, \, 0.6 + \frac{\sin t}{4} \right] \right\}, \qquad t \in [0,1]. \tag{4.150}$$

Using the set-valued map Λ, the test solution (4.40) gives us the following time-dependent partial mass measurement

$$\int_{\Lambda(t)} T(x,t)dx = \left(\frac{x^3}{3} + 2tx \right) \exp\left(-t - \frac{t^2}{2} \right) \Bigg|_{0.4+\frac{\sin t}{4}}^{0.6+\frac{\sin t}{4}}, \qquad t \in [0,1]. \tag{4.151}$$

As we can observe in the Figures 4.16(a) and 4.16(b), by solving the system (4.149), given the shape of the measurement, even though we have considered exact data and the computation of $\tilde{r}$ behaves satisfactory, the results obtained for $P_f(t)$ are highly unstable. The instability shown in Figure 4.16(b) is caused by the direct

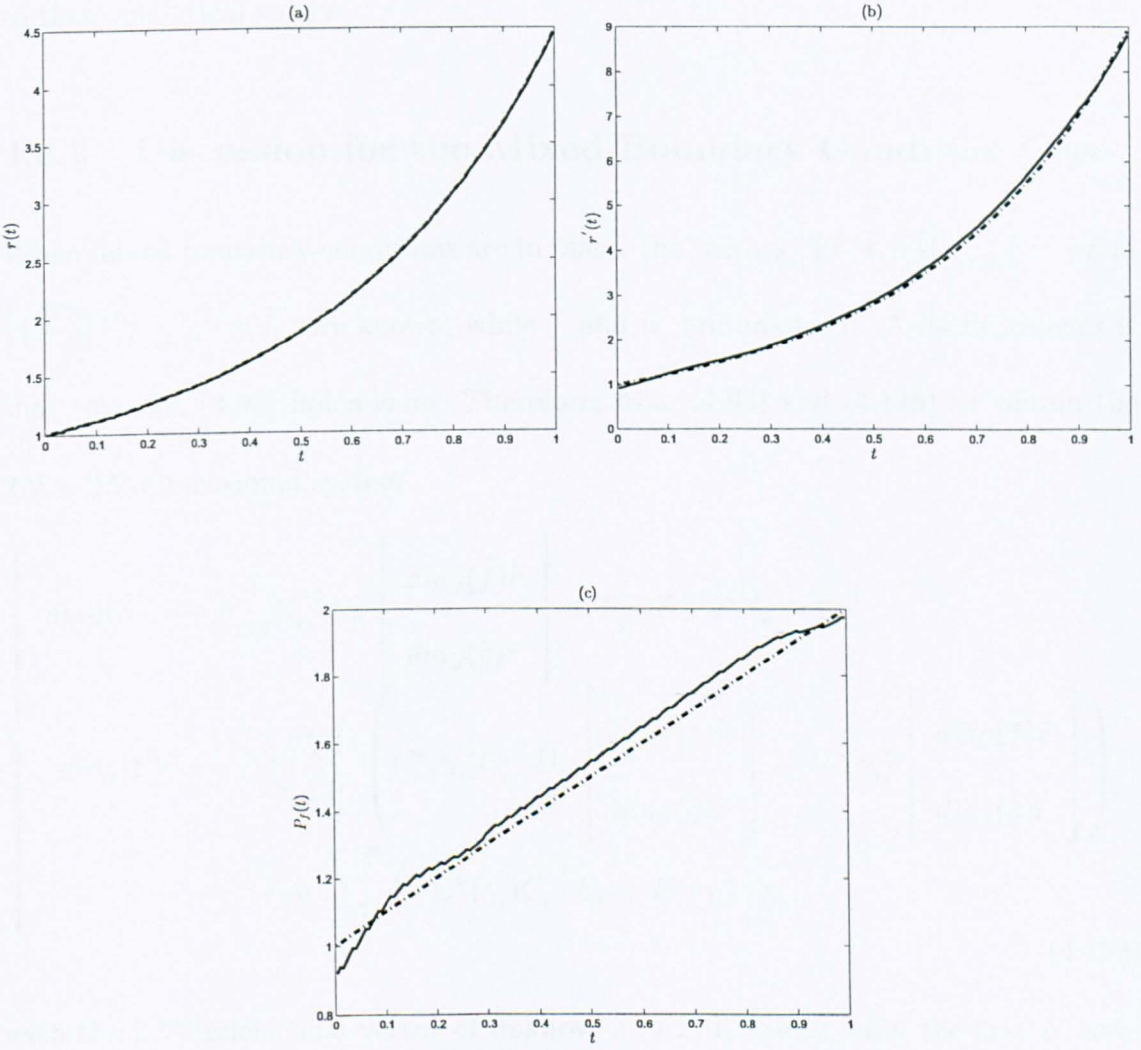

Figure 4.17: Computed and analytical values of: (a) $r(t)$, (b) $r'(t)$, and (c) $P_f(t)$, when there is no noise in the data (4.151), after mollification.

computation of the derivative $\frac{\partial \tilde{r}}{\partial t}$ using central differences. However, if we apply the mollification steps described in Section 4.3, the results stabilize and, as illustrated in Figures 4.17(a), 4.17(b) and 4.17(c), the retrieval of both $\tilde{r}$, $\frac{\partial \tilde{r}}{\partial t}$ and $P_f(t)$ is close to their analytical values.

4.8.2 Discussion for the Mixed Boundary Condition Case

When mixed boundary conditions are in place, the vectors $\left[\{T(1,\tilde{t}_j)\}_{j=\overline{1,N}}\right] = \tilde{g}$ and $\left[\{\frac{\partial T(0,\tilde{t}_j)}{\partial n}\}_{j=\overline{1,N}}\right] = \tilde{h}_0$ are known, while $\tilde{f}$ and $\tilde{h}_1$ are unknown. A useful remark is that equation (4.93) holds valid. Therefore, from (4.93) and (4.146) we obtain the $2N \times 2N$-dimensional system

$$\begin{cases} diag(\tilde{h}_0)\tilde{r} - P_{\overline{1,N}} C_\Gamma^{-1} D_\Gamma \begin{bmatrix} diag(\tilde{f})\tilde{r} \\ diag(\tilde{g})\tilde{r} \end{bmatrix} + P_{\overline{1,N}} C_\Gamma^{-1} E_\Gamma \tilde{v}_0 = 0, \\ diag(\tilde{\mathcal{E}})\tilde{r} = \frac{1}{N_0} \sum_{i=1}^{N_0(\tilde{\mathcal{E}})} \left(C^*(\gamma_i) C_\Gamma^{-1} D_\Gamma \begin{bmatrix} diag(\tilde{f})\tilde{r} \\ diag(\tilde{g})\tilde{r} \end{bmatrix} - D^*(\gamma_i) \begin{bmatrix} diag(\tilde{f})\tilde{r} \\ diag(\tilde{g})\tilde{r} \end{bmatrix} \right) \\ \qquad + \frac{1}{N_0} \sum_{i=1}^{N_0(\tilde{\mathcal{E}})} \left(-C^*(\gamma_i) C_\Gamma^{-1} E_\Gamma + E^*(\gamma_i) \right) \tilde{v}_0, \end{cases} \tag{4.152}$$

with the $2N$-dimensional vector of unknowns (4.110). Since, only the first N components of the solution for the system (4.152) are of interest to us, the second half of the components, namely $r \cdot f$, are disregarded.

By solving the system (4.152), we arrive to exactly the same difficulties as the ones encountered in the Dirichlet case, see Figures 4.18(a) and 4.18(b). The instability of direct numerical differentiation of $\tilde{r}$ using central difference, offer us again a highly unstable $P_f(t)$. This issue is solved following a similar mollification method with the one used in the Dirichlet case, and finally, as shown in Figures 4.19(a), 4.19(b)

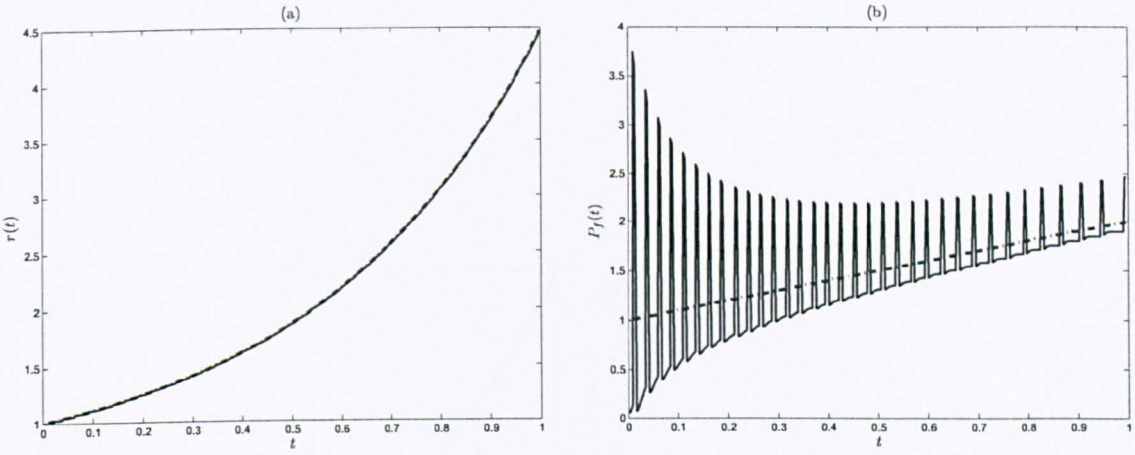

Figure 4.18: Computed and analytical values of: (a) $r(t)$ and (b) $P_f(t)$, when there is no noise in the data (4.151) .

and 4.19(c), the results obtained agree well with the analytical values.

4.9 Conclusions

The inverse problem regarding the identification of the time-dependent perfusion coefficient in the bio-heat equation has been investigated. Both exact and noisy measurements were taken into consideration. For the cases of internal and total mass measurements in the presence of Dirichlet or mixed boundary conditions, the hypotheses of the solvability theorems results were satisfied. In the heat flux measurement case, since there were no uniqueness results previously proved, we have stated and proved a uniqueness criterion which translates the uniqueness issue to the existence of a unique zero for a constructed functional. Natural generalizations to path measurements and partial mass measurements were also approached in our investigation both for the Dirichlet and for the mixed boundary conditions.

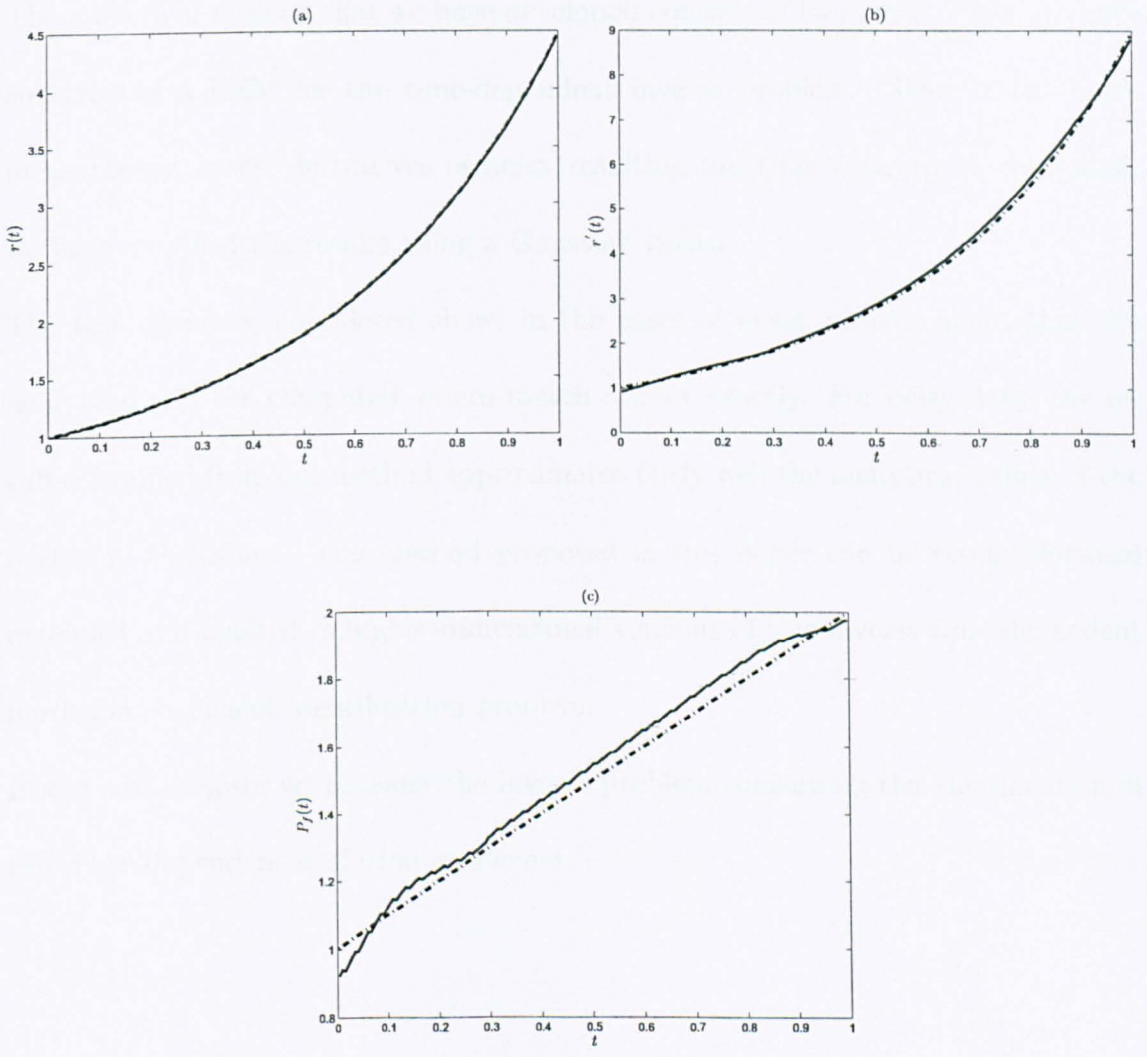

Figure 4.19: Computed and analytical values of: (a) $r(t)$, (b) $r^{'}(t)$, and (c) $P_f(t)$, when there is no noise in the data (4.151), after mollification.

However, our main effort was focused on developing a general numerical method that allows us to retrieve of the solution $(T(x,t); P_f(t))$ globally, in a unified manner, for all the types of boundary conditions and measurements considered.

The numerical method that we have developed consists of two parts. First, we have constructed a BEM for the time-dependent inverse problem. Since in the noisy measurement cases, derivatives of noisy resulting functions have to be computed, we have mollified the results using a Gaussian kernel.

The test examples considered show, in the cases of exact measurement, that the analytical and the computed values match almost exactly. For noisy data, the results obtained from our method approximates fairly well the analytical values of the perfusion coefficient. The method proposed in this paper can be straightforward extended and applied to higher-dimensional versions of this inverse time-dependent perfusion coefficient identification problem.

In the next chapter we consider the inverse problem concerning the identification of the space-dependent perfusion coefficient.

Chapter 5

Inverse Space-Dependent Perfusion Coefficient Identification

5.1 Introduction

After discussing the retrieval of the constant and time-dependent perfusion coefficient cases, in this chapter we will focus on the situation when P_f is dependent on space. Given the heterogeneity of the human body tissue, the blood perfusion will vary between different regions of the body. However, since the perfusion $P_f(x)$ will be a function of the position x, equation (1.2) will not have a fundamental solution, and this constitutes a major difficulty in approaching the subsequent class of nonlinear inverse problems.

For the space-dependent case, we investigate two classes of inverse problems. In the first instance, the bio-heat equation

$$\Delta T - P_f(x)T + \Sigma = \frac{\partial T}{\partial t}, \qquad (0, L) \times (0, t_f], \tag{5.1}$$

will be subject to Neumann boundary conditions, whereas in the last part of the chapter Dirichlet boundary conditions will be considered.

In the Neumann case, we seek the retrieval of the space-dependent coefficient $P_f(x) > 0$ along with the temperature $T(x,t)$ from exact and noisy boundary temperature measurements.

In the Dirichlet case, we discuss two inverse problems, namely IP1 and IP2, concerning the identification of the space-dependent coefficient $P_f(x) > 0$ along with the temperature $T(x,t)$ where, in the case of IP1, the additional information consists of a heat flux measurement on a part of the boundary, and in the case of IP2, a time-average temperature measurement is taken at every space point in $(0, L)$.

For both the Neumann and the Dirichlet cases, the numerical investigation will employ a Crank-Nicolson-type finite difference scheme coupled with an optimisation algorithm, which minimizes a least-squares functional that evaluates the difference between the measured data and the computed values.

However, although, subject to certain imposed hypotheses, some uniqueness results may be satisfied, the ill-posed character of all the inverse problems considered is revealed by the stability issues encountered in the numerical investigation. In dealing with these aspects, regularization techniques, such as order-0 or order-1 Tikhonov methods, together with the subsequent strategies that are used for choosing their regularization parameters, need to be employed.

5.2 The Neumann Inverse Problem

In this section, the considered space-dependent perfusion coefficient identification inverse problem is stated as follows:

Find the temperature $T(x,t)$ such that T, $T_x \in \mathscr{C}([0,\pi]\times[0,\infty))$, T_t, $T_{xx} \in \mathscr{C}((0,\pi)\times(0,\infty))$ and the space-dependent perfusion coefficient $P_f(x) \in \mathscr{C}([0,\pi])$, $P_f > 0$, satisfying the one-dimensional time-dependent bio-heat equation (5.1) subject to the initial condition

$$T(x,0) = 0, \quad x \in [0,\pi], \tag{5.2}$$

the Neuman boundary conditions

$$\frac{\partial T}{\partial x}(0,t) = 0, \qquad t \geq 0, \tag{5.3}$$

$$\frac{\partial T}{\partial x}(\pi,t) = \mu(t), \quad t \geq 0, \tag{5.4}$$

where μ satisfies the following properties:

$$\begin{cases} \mu \in \mathscr{C}^2([0,\infty)),\ \mu(0) = \mu'(0) = 0,\ \mu \not\equiv 0, \\ \text{and there exists } t_0 > 0 \text{ such that } \mu(t) = 0 \text{ for all } t \geq t_0, \end{cases} \tag{5.5}$$

and the additional boundary temperature measurement:

$$T(\pi,t) = g(t), \quad t > 0. \tag{5.6}$$

The uniqueness of solution for this inverse problem has been established in Denisov [46], pp.139-146, and is stated as follows:

Theorem 5.2.1 *Let $\Sigma = 0$ and $\mu(t)$ satisfy conditions (5.5). If $P_{fi}(x)$, $T_i(x,t)$, $i = 1,2$ are solutions, in the above regularity classes, of the inverse problem (5.1), (5.2)-(5.4) and (5.6), then $P_{f1}(x) = P_{f2}(x)$ for $x \in [0,\pi]$ and $T_1(x,t) = T_2(x,t)$ for $(x,t) \in [0,\pi]\times[0,\infty)$.*

Note that if, instead of the boundary temperature measurement (5.6) at the active end $x = \pi$, where a non-zero heat flux is applied, we supply the additional boundary temperature measurement

$$T(0,t) = g_0(t), \quad t > 0, \tag{5.7}$$

at the inactive end $x = 0$, where no heat flux occurs, then, in order to obtain a unique solution for the inverse problem (5.1),(5.2)-(5.4) and (5.7), we further need to impose the condition

$$P_f(x) = P_f(\pi - x) \quad \text{for } x \in [0,\pi], \tag{5.8}$$

see Denisov [46], p.144. This is because the additional condition (5.6) provides more information on $P_f(x)$ than condition (5.7). Furthermore, it is also possible to uniquely determine the triplet $(T(x,t), P_f(x), \mu(t))$, satisfying (5.1),(5.2)-(5.6), under the assumption that μ is non-negative, see Denisov [46], p.145.

Note that instead of the Neumann boundary conditions (5.3) and (5.4) one can prescribe the Dirichlet boundary temperature conditions

$$T(0,t) = 0, \quad t \geq 0 \tag{5.9}$$

and (5.6). In this case, the additional measurement can be the heat flux (5.4). Then, if $g \not\equiv 0$ and there exists $t_0 > 0$ such that $\int_0^{t_0} g(t)dt < \infty$, $g(t) = 0$ for all $t > t_0$, then the inverse problem given by equation (5.1),(5.2), (5.4), (5.6) and (5.9) has a unique solution, see Pierce [83] and Ramm [92].

The uniqueness of the solution of the problem given by equations (5.1), (5.2), (5.6) and (5.9) also holds under the additional final temperature measurement, see Choulli [28] and Isakov [59],

$$T(x,t_0) = e(x), \quad x \in [0,\pi]. \tag{5.10}$$

5.3 Numerical Approach

As a first step, a finite-difference algorithm based on the Crank-Nicolson scheme, see Dahlquist and Bjorck [34], pp.387-389, is developed in order to solve the direct problem for the parabolic equation (5.1), in which the coefficient P_f is considered known, subject to the initial and boundary conditions (5.2)-(5.4). At this particular stage we only wish to retrieve the temperature $T(x,t)$ given the assumed knowledge of the positive entry $P_f(x)$. Let us denote this particular computed solution by $T^{comp}(P_f;(x,t))$.

A second step involves a gradient based optimisation procedure, supplied by the NAG routine E04FCF, which minimizes the order-0 and order-1 Tikhonov regularizations: F_0, $F_1 : \{P_f \mid P_f \in \mathscr{C}([0,\pi]),\ P_f > 0\} \rightarrow \mathbb{R}_+$ defined by

$$F_0(P_f) := \| T^{comp}(P_f;(x,t)) - g(t) \|_2^2 + \lambda \| P_f \|_2^2, \tag{5.11}$$

$$F_1(P_f) := \| T^{comp}(P_f;(x,t)) - g(t) \|_2^2 + \lambda \| P_f' \|_2^2, \tag{5.12}$$

respectively, where $\lambda > 0$ is a regularization parameter to be prescribed. Remark that when $\lambda = 0$, expressions (5.11) and (5.12) coincide with the classical least-squares functional which produces an unstable solution.

The NAG routine E04FCF is a comprehensive algorithm for finding an unconstrained minimum of a sum of squares of m nonlinear functions in n variables ($m \geq n$). Further, no derivatives are required to be supplied by the user, these being calculated internally by the routine using finite differences.

The minimization algorithm is initialized with a positive continuous function P_f, which in our case is set to 1, i.e. $P_f^{initial}(x) = 1$. The constraint $P_f > 0$ cannot be imposed directly in the NAG routine, but, if in the iteration process some compo-

nents of the discretized P_f happen to become negative, they are replaced by 1 at the next iteration level. Let us consider the following test example. Let us choose

$$\mu(t) = \begin{cases} 0 & \text{for } t = 0, \\ e^{\left[-\frac{1}{\frac{1}{4}-(t-\frac{1}{2})^2}\right]} & \text{for } t \in (0,1), \\ 0 & \text{for } t \geq t_0 = 1, \end{cases} \tag{5.13}$$

which satisfies conditions (5.5) and seek to retrieve a positive continuous perfusion coefficient given by

$$P_f(x) = 1 + x^2, \quad \text{for } x \in [0, \pi]. \tag{5.14}$$

The space interval $[0, \pi]$ is discretized into $N_0 = 90$ uniform cells and we discretise a finite time interval $[0, t_f]$ into $N = 100t_f$ uniform time intervals, where $t_f \in \{1, 2, 4\}$. Thorough this section, all the computations are performed on a 64-bit $\times$86-Linux cluster architecture, with all the operations carried out in extended precision.

Figure 5.1 illustrates the results obtained with order-0 Tikhonov regularization for exact measurement data (5.6) used in each of the three time length intervals, where the appropriate choices for the values of the regularization parameter λ are considered, namely: $\lambda = 10^{-20}$ for $t_f = 1$, $\lambda = 10^{-19}$ for $t_f = 2$, and $\lambda = 10^{-19}$ for $t_f = 4$. In Figure 5.1(a), the natural logarithm of the functional given in (5.11), $\ln(F_0)$, is represented as a function of the number of iterations obtained for $(t_f, \lambda) \in \{(1, 10^{-20}), (2, 10^{-19}), (4, 10^{-19})\}$. Figures 5.1(b)-(d) show the computed P_f in comparison to the exact solution given in (5.14) for $(t_f, \lambda) = (1, 10^{-20})$, $(t_f, \lambda) = (2, 10^{-19})$, and $(t_f, \lambda) = (4, 10^{-19})$, respectively. It should be noted that as we increase the time interval, i.e. from $t_f = 1$ to $t_f = 2$ and then to $t_f = 4$, the results obtained improve, becoming more stable and at the same time increasing the

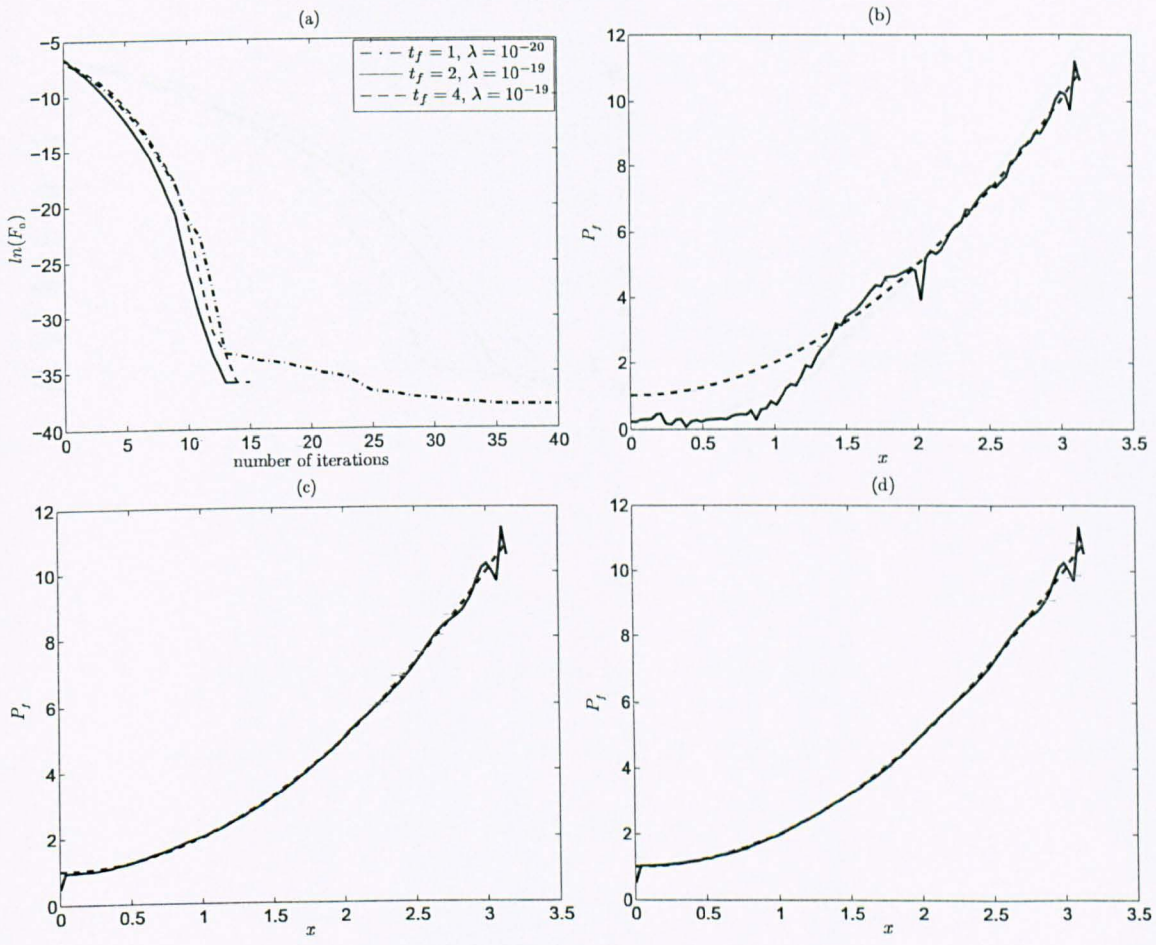

Figure 5.1: (a) Logarithm of the objective functional F_0, for order-0 regularization, as a function of the number of iterations, and the numerically obtained $P_f(x)$ for (b) $t_f = 1$, (c) $t_f = 2$, and (d) $t_f = 4$, for exact data. In figures (b)-(d) the exact solution (5.14) is shown with dashed line.

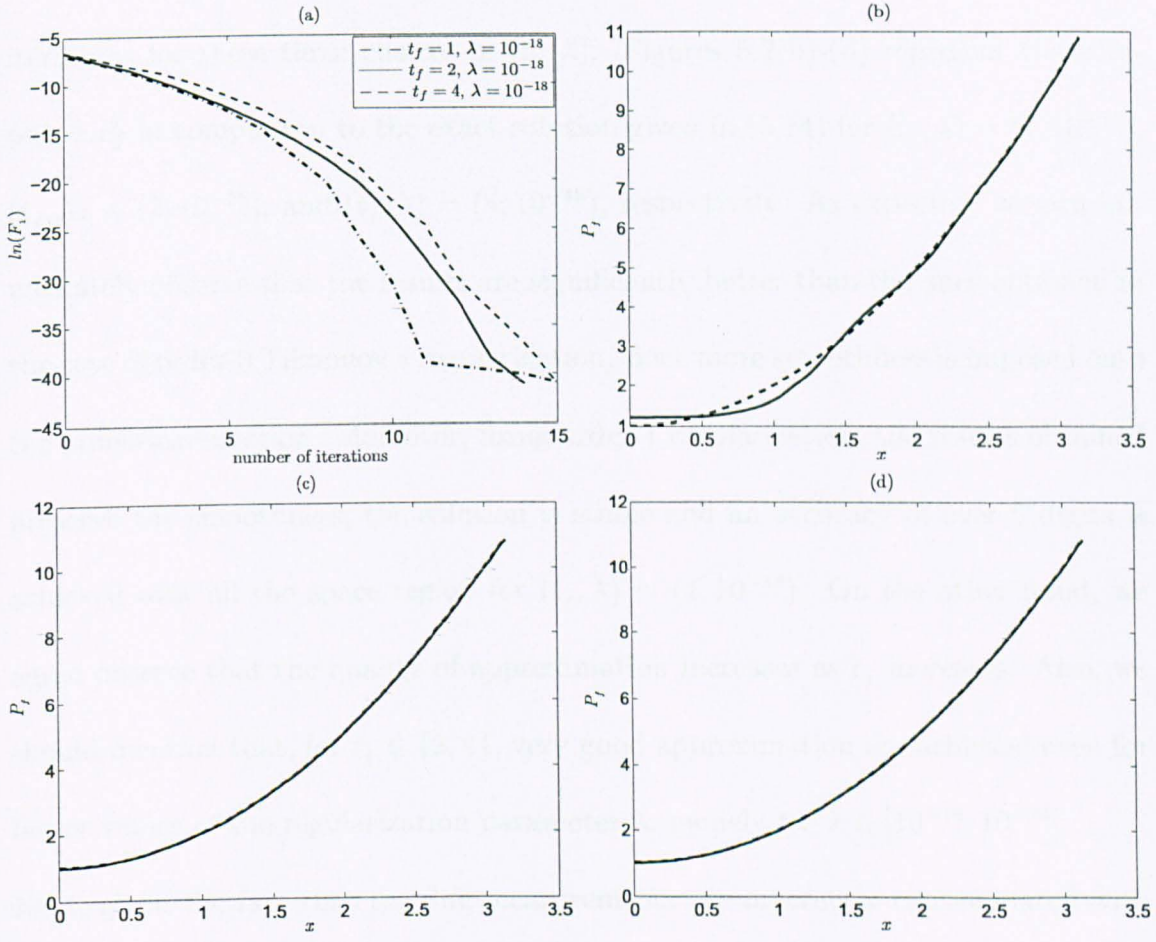

Figure 5.2: (a) Logarithm of the objective functional F_1, for order-1 regularization, as a function of the number of iterations, and the numerically obtained $P_f(x)$ for (b) $t_f = 1$, (c) $t_f = 2$, and (d) $t_f = 4$, for exact data. In figures (b)-(d) the exact solution (5.14) is shown with a dashed line.

accuracy, since more measurement information is added.

Figure 5.2 shows the results obtained for exact data when order-1 Tikhonov regularization is employed for each choice of the parameters $(t_f, \lambda) \in \{(1, 10^{-18}), (2, 10^{-18}), (4, 10^{-18})\}$. In Figure 5.2(a), $\ln(F_1)$ is represented as a function of the number of iterations for these three choices of (t_f, λ). Figures 5.2(b)-(d) represent the computed P_f in comparison to the exact solution given in (5.14) for $(t_f, \lambda) = (1, 10^{-18})$, $(t_f, \lambda) = (2, 10^{-18})$, and $(t_f, \lambda) = (4, 10^{-18})$, respectively. As expected, we can immediately observe that the results are significantly better than the ones obtained in the case of order-0 Tikhonov's regularization, since more smoothness is imposed onto the numerical solution. Moreover, using order-1 regularization, the results obtained preserve the smoothness, the solution is stable and an accuracy of over 5 digits is achieved over all the space region for $(t_f, \lambda) = (4, 10^{-18})$. On the other hand, we again observe that the quality of approximation increases as t_f increases. Also, we should mention that, for $t_f \in \{2, 4\}$, very good approximation are achieved even for larger values of the regularization parameter λ, namely for $\lambda \in [10^{-18}, 10^{-14}]$.

Next, given the fact that real life measurements are inherently contaminated with errors, we test now the proposed algorithm on noisy data. Let us consider that the measurement $g(t)$ is perturbed by 1% of random multiplicative noise that is generated by a uniform distribution on the interval $[-1, 1]$, for each time node t_j, $j = \{1, ..., \frac{t_f}{N}\}$, and this noise is supplied by the NAG routine G05DAF.

Figure 5.3 shows the results obtained with order-0 Tikhonov regularization, when the input measurement data g in (5.6) is corrupted by 1% multiplicative noise, for each choice of the parameters couple $(t_f, \lambda) \in \{(1, 10^{-11}), (2, 10^{-11}), (4, 10^{-12})\}$. The functional $\ln(F_0)$ shown in Figure 5.3(a), as a function of the number of it-

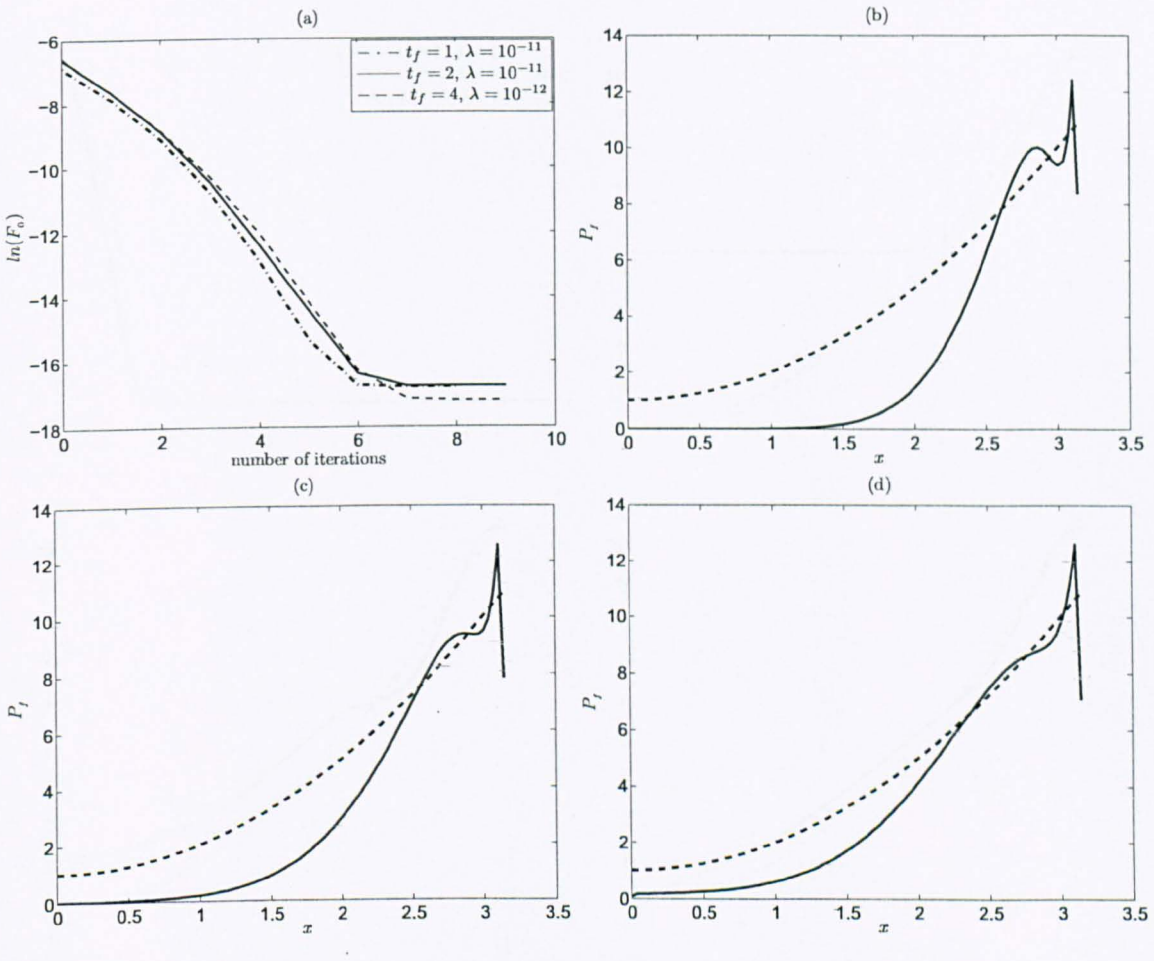

Figure 5.3: (a) Logarithm of the objective functional F_0, for order-0 regularization, as a function of the number of iterations, and the numerically obtained $P_f(x)$ for (b) $t_f = 1$, (c) $t_f = 2$, and (d) $t_f = 4$, for 1% noisy data. In figures (b)-(d) the exact solution (5.14) is shown with a dashed line.

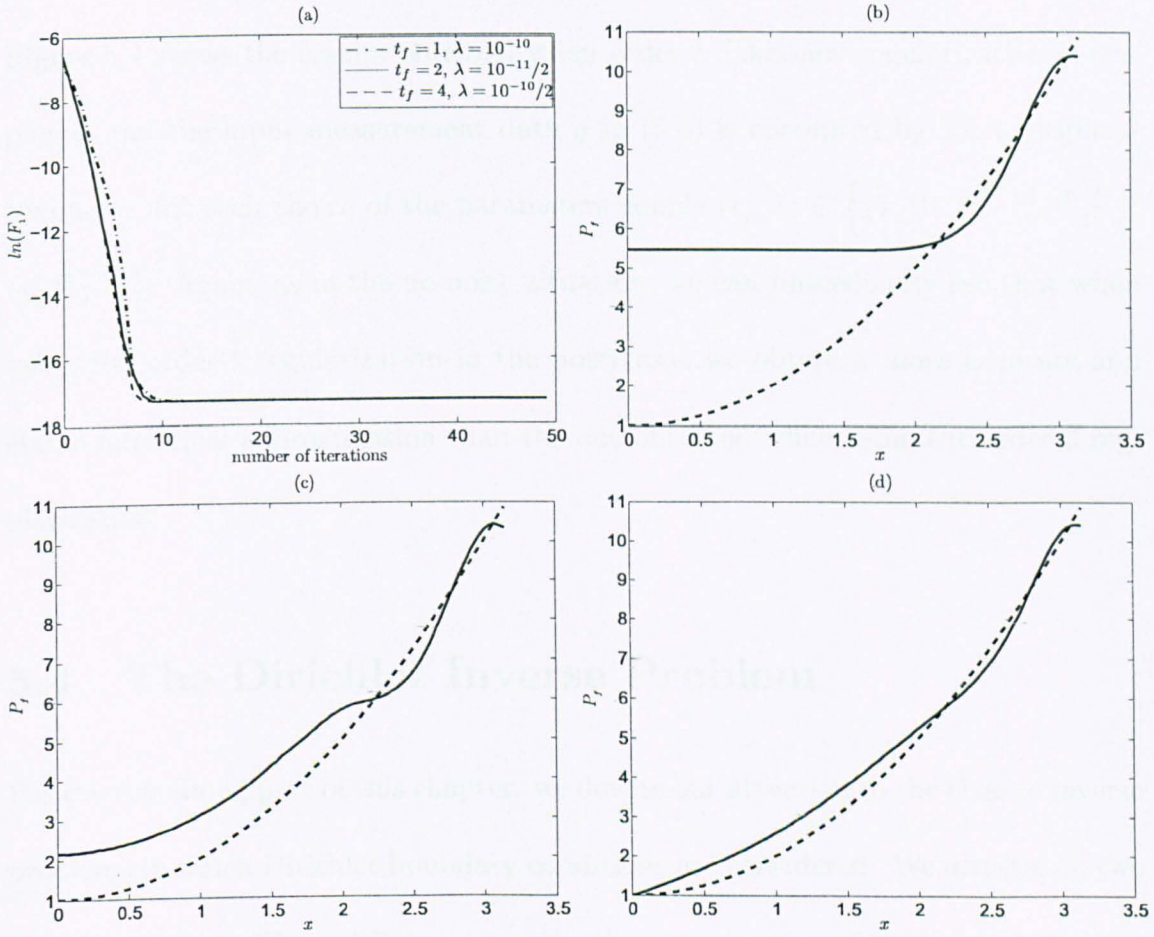

Figure 5.4: (a) Logarithm of the objective functional F_1, for order-1 regularization, as a function of the number of iterations, and the numerically obtained $P_f(x)$ for (b) $t_f = 1$, (c) $t_f = 2$, and (d) $t_f = 4$, for 1% noisy data. In figures (b)-(d) the exact solution (5.14) is shown with a dashed line.

erations, is monotonically decaying in this noisy case, for all couples (t_f, λ). The results obtained for P_f are highly sensitive to the level of noise in the data, as shown in the Figures 5.3(b)-(d) for $(t_f, \lambda) = (1, 10^{-11})$, $(t_f, \lambda) = (2, 10^{-11})$, and $(t_f, \lambda) = (4, 10^{-12})$, respectively.

Figure 5.4 shows the results obtained when order-1 Tikhonov regularization is employed and the input measurement data g in (5.6) is corrupted by 1% multiplicative noise, for each choice of the parameters couple $(t_f, \lambda) \in \left\{(1, 10^{-10}), (2, \frac{10^{-11}}{2}), (4, \frac{10^{-10}}{2})\right\}$. Again, as in the no noise situation, we can immediately see that when using the order-1 regularization in the noisy case we obtain a more accurate and stable numerical approximation than the one obtained when using the order-0 regularization.

5.4 The Dirichlet Inverse Problem

For the remaining part of this chapter, we devote our attention to the class of inverse problems in which Dirichlet boundary conditions are considered. We investigate two inverse problems, IP1 and IP2, concerning the identification of the space-dependent coefficient $P_f(x) > 0$ along with the temperature $T(x,t)$, under prescribed initial and Dirichlet boundary conditions, when, in the case of IP1, the additional information considered consists of either a heat flux measurement on a part of the boundary or, for IP2, a time-average measurement is taken at every space point $(0, L)$.

The two space-dependent perfusion coefficient identification inverse problems, IP1 and IP2, are seeking the couple $(P_f(x),\ T(x,t))$, when the following common ground is assumed:

The temperature $T(x,t)$, with $T,\ T_x \in \mathscr{C}([0,1]\times[0,\infty),\ T_t,\ T_{xx} \in \mathscr{C}((0,1)\times(0,\infty)$, and the space-dependent perfusion coefficient $P_f(x) \in \mathscr{C}([0,1])$, $P_f > 0$, are satisfying the one-dimensional space-dependent transient bio-heat equation (5.1), subject to the initial condition

$$T(x,0) = u_0(x), \quad x \in [0,1], \tag{5.15}$$

and the Dirichlet boundary conditions

$$T(0,t) = \mu_1(t), \quad t \geq 0, \tag{5.16}$$

$$T(1,t) = \mu_2(t), \quad t \geq 0. \tag{5.17}$$

For each of the inverse problems the additional information, stated individually, is defined as follows:

- for IP1 the flux at $x = 1$ is measured as:

$$h(t) = \frac{\partial T}{\partial x}(1,t), \qquad t \in (0,\infty], \tag{5.18}$$

- for IP2 the time-average measurement is taken across the space region $(0,1)$ as:

$$\mathcal{E}(x) = \int_0^{t_f} T(x,t), \qquad x \in (0,1). \tag{5.19}$$

where $t_f > 0$ is an arbitrary given time.

Remark 5.4.1 *An inverse problem similar to IP1, as given by equations (5.1), (5.15), (5.17), (5.18) and the Neumann condition*

$$\overline{h}(t) = \frac{\partial T}{\partial x}(0,t), \qquad t \in (0,\infty), \tag{5.20}$$

has been investigated theoretically, Denisov [46], pp. 139-146, and numerically in the previous section and in Rodrigues et al. [100]. Moreover, an overdetermined inverse

problem, as given by equations (5.1), (5.15)-(5.18) and (5.20), has been investigated numerically in Tadi et al. [109].

Remark 5.4.2 *An inverse problem similar to IP2, as given by the equations (5.1), (5.15), and (5.16), (5.17) or (5.18), (5.20), and the final temperature measurement*

$$\overline{e}(x) = T(x, t_f), \qquad x \in (0,1) \tag{5.21}$$

has been investigated theoretically in Choulli [28], Choulli and Yamamoto [29, 30], Isakov [59, 60], Prilepko and Kostin [89], Prilepko and Solov'ev [88], Rundell [101] and Yu [118], and numerically in Chen and Liu [27], Deng et al. [44], Yang et al. [117].

The following theorems ensure the uniqueness of the perfusion coefficient $P_f(x)$.

Theorem 5.4.3 (Ramm [91, 92]) *Let $u_0 = \mu_1 = \Sigma \equiv 0$, and assume that $\mu_2 \not\equiv 0$ is compactly supported and integrable. Further, we assume that equation (5.1) is satisfied at the boundary, $x \in \{0, 1\}$, for $t > 0$. Then the IP1 has at most one solution $P_f \in \mathcal{L}_1([0,1])$.*

Theorem 5.4.4 (Isakov [61], Sect. 9.2) *Let $\Sigma \equiv 0$, $u_0 \in \mathscr{C}^4([0,1])$, $u_0 > 0$ and*

$$\mu_1, \mu_2 \in \left\{ \frac{1}{\sqrt{\pi t}} \int_0^\infty e^{-\tau^2/(4t)} \mu^*(\tau) d\tau \;\middle|\; \mu^* \in \mathscr{C}^4([0,\infty)) \right\}. \tag{5.22}$$

Then the IP1 has at most one solution $P_f \in \mathcal{L}_\infty((0,1))$.

Theorem 5.4.5 (Prilepko and Kostin [89]) *Let $u_0 = \mu_1 = \mu_2 \equiv 0$, $\Sigma, \Sigma_t \in L_2((0,1) \times (0,t_f))$, $\Sigma \geq 0$, $\Sigma_t \geq 0$, and assume that $\mathcal{E} \in \mathcal{W}_2^2((0,1))$, with $\mathcal{E}(x) > \int_0^{t_f} T^0(x,t)dt$, $x \in (0,1)$, where T^0 is the solution of the direct problem given by equation (5.1) with $P_f = 0$ and with homogeneous conditions (5.15)-(5.17). Then the IP2 has at most one solution $P_f \in \mathcal{L}_\infty((0,1))$, $P_f \geq 0$, $T \in \mathcal{W}_2^{2,1}((0,1) \times (0,t_f))$.*

In Theorem 5.4.5, the Sobolev spaces $\mathcal{W}_2^2((0,1))$ and $\mathcal{W}_2^{2,1}((0,1)\times(0,t_f))$ are defined in the standard way, see Ladyzhenskaya [65].

5.5 Numerical Approach

The numerical approach is the same as that described in Section 5.3 except that we minimize the order-one Tikhonov regularization functional $F_1 : \{P_f \mid P_f \in \mathscr{C}^1([0,1])$ $P_f > 0\} \rightarrow \mathbb{R}_+$ defined by

$$F_1(P_f) := \lambda \parallel P_f' \parallel^2_{\mathcal{L}_2((0,1))} + \begin{cases} \parallel \frac{\partial T^{comp}}{\partial x}(P_f;(1,t)) - h(t) \parallel^2_{\mathcal{L}_2((0,\infty))} & \text{for IP1,} \\ \parallel \int_0^{t_f} T^{comp}(P_f;(x,t))dt - E(x) \parallel^2_{\mathcal{L}_2((0,1))} & \text{for IP2,} \end{cases} \tag{5.23}$$

where $\lambda > 0$ is a regularization parameter to be prescribed.

The problem is solved subject to both exact and noisy measurements

$$\widetilde{h}(t) = h(t)(1+\alpha\eta), \qquad t \in (0,\infty), \tag{5.24}$$

$$\widetilde{\mathcal{E}}(x) = \mathcal{E}(x)(1+\alpha\eta), \qquad x \in (0,1), \tag{5.25}$$

where α is the percentage of noise (typically 1%) and η are random variables generated from a uniform distribution in the interval $[-1,1]$, using the NAG routine G05DAF. Suppose that we know an upper bound $\gamma > 0$ such that

$$\delta_h(\alpha) := \parallel h - \widetilde{h} \parallel_{\mathcal{L}_2((0,\infty))} \leq \gamma, \tag{5.26}$$

$$\delta_E(\alpha) := \parallel \mathcal{E} - \widetilde{\mathcal{E}} \parallel_{\mathcal{L}_2((0,1))} \leq \gamma. \tag{5.27}$$

Then the regularization parameter λ is chosen according to the discrepancy principle as follows. Considering the functional $F : [0,\infty) \rightarrow \mathbb{R}_+$, defined by

$$F(\lambda) := \sqrt{F_1(P_f) - \lambda \parallel P_f' \parallel^2_{\mathcal{L}_2((0,1))}}, \tag{5.28}$$

the Morozov discrepancy principle suggests choosing the regularization parameter as being the largest value $\lambda > 0$ for which

$$F(\lambda) \leq \gamma. \tag{5.29}$$

5.6 Numerical Results and Discussions

Except otherwise specified, the space interval $[0,1]$ is discretized into $N_0 = 90k$ uniform cells, while the time interval $[0, t_f]$ is discretized into $N = 100kt_f$ uniform time intervals, where, for convenience, we take $t_f = 1$ and the mesh tunning factor $k = 1, 2$. We also take, for simplicity, $\Sigma \equiv 0$ in equation (5.1).

5.6.1 Numerical Example for IP1 with Homogeneous Initial Condition

Let us choose $u_0 \equiv 0$, $\mu_1 \equiv 0$, and

$$\mu_2(t) = \begin{cases} 0 & \text{for } t = 0, \\ e^{\left[-\frac{1}{\frac{1}{4}-(t-\frac{1}{2})^2}\right]} & \text{for } t \in (0,1), \\ 0 & \text{for } t \geq t_0 = 1, \end{cases} \tag{5.30}$$

which satisfies the conditions of Theorem 5.4.3 for the uniqueness of solution of problem IP1. We seek to retrieve a positive continuous perfusion coefficient given by

$$P_f(x) = 1 + x^2, \quad \text{for } x \in [0,1]. \tag{5.31}$$

Since an analytical solution for the bio-heat equation (5.1) with $\Sigma = 0$, subject to the above initial and boundary conditions, could not be determined, the measured

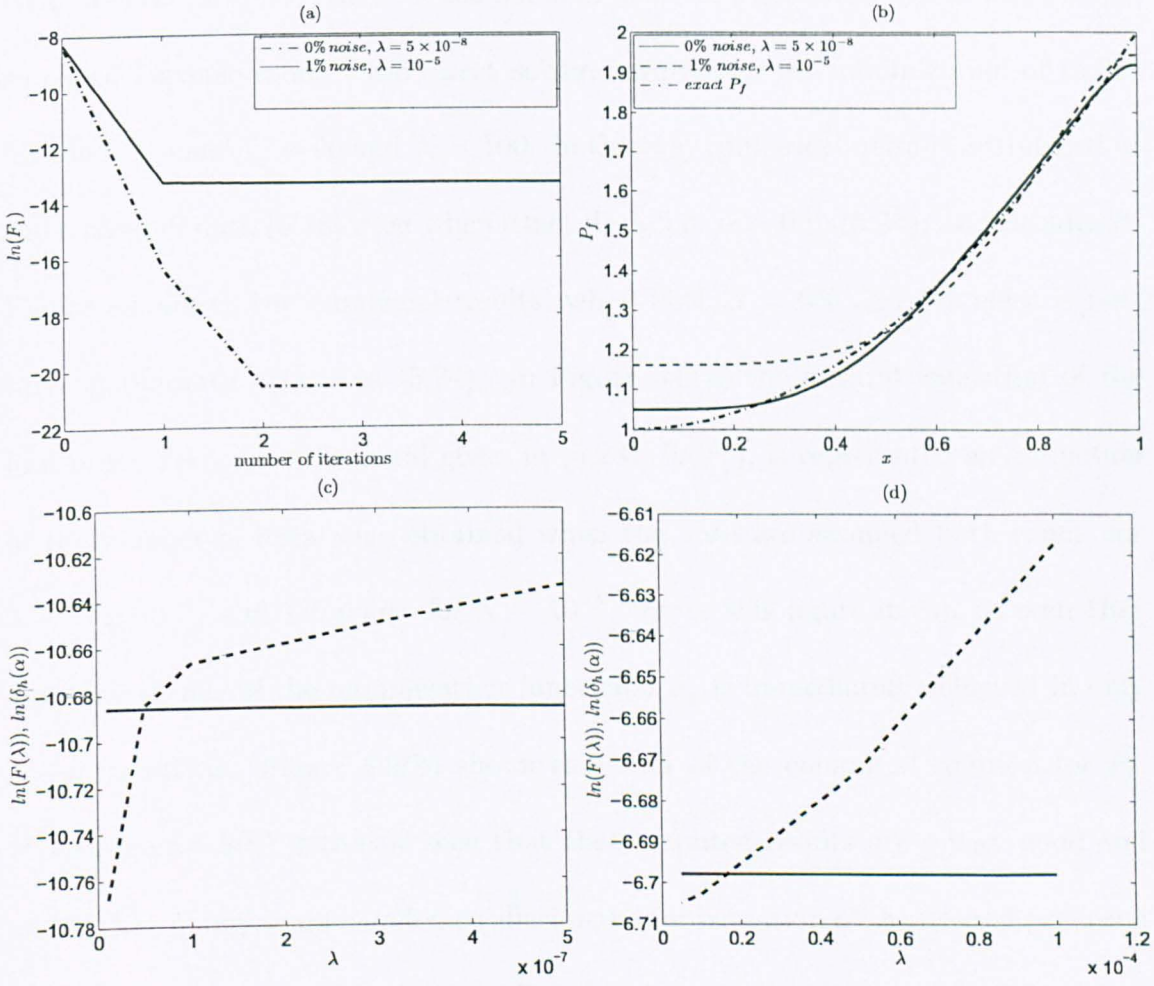

Figure 5.5: (a) Logarithm of the objective functional F_1, as a function of the number of iterations, (b) the numerically obtained $P_f(x)$, (c) the discrepancy principle for exact data, $\alpha = 0$, and (d) the discrepancy principle for $\alpha = 1\%$ noisy data. The amount of noise γ is shown with continuous line (——) in figures (c) and (d).

heat flux data (5.18) is generated numerically by solving the direct problem with P_f given by equation (5.14) using the Crank-Nicolson finite-difference method, with a mesh that uniformly discretises both the space interval $[0, 1]$ in $N_0 = 90$ cells and the time interval $[0, t_f = 1]$ in $N = 200$ subintervals. In order to avoid committing the so called "inverse crime", the direct solver, involved in the minimization of (5.23) for the IP1, uses $N_0 = 90$ and $N = 100$. In this way numerical noise is introduced in the measured data (5.18) even when exact data, i.e. $\alpha = 0$ in (5.24), are considered. Figure 5.5 shows the numerical results, when both $\alpha = 0\%$ and 1% noise is perturbing the data $h(t)$ as in (5.24). In Figure 5.5(a) the natural logarithm of the first-order Tikhonov functional given in (5.23), $ln(F_1)$, is represented as a function of the number of iterations, obtained when the data are assumed both exact, for $\lambda = 5 \times 10^{-8}$, and 1% noisy, for $\lambda = 10^{-5}$. From this figure it can be seen that the convergence of the minimization functional F_1 is immediately achieved in only $3 - 5$ iterations. Figure 5.5(b) shows the plots of the computed solution for P_f. From Figure 5.5(b) it can be seen that the computed results are a very good and stable (free of highly unbounded oscillations) approximation of the desired perfusion coefficient given in equation (5.14). For the exact data, the maximum 4% relative error to the exact solution (5.14), that occurs in the numerical solution, is justified by the numerical noise introduced when the measured data are obtained by solving the direct problem, as mentioned above. When 1% noise is included an error of maximum 16% is encountered in the numerical solution; however, the numerical solution is reasonably stable.

Figures 5.5(c) and 5.5(d) show the discrepancy principle (5.29) for $\alpha = 0\%$ and $\alpha = 1\%$, respectively. From these figures it can be seen that the discrepancy prin-

ciple enables us to locate the regularization parameter λ, when both exact and perturbed noisy measurements are considered.

5.6.2 Numerical Example for IP1 with Non-homogeneous Initial Condition

Throughout this section, the initial condition (5.15), u_0, as well as the Dirichlet boundary conditions (5.16)-(5.17), μ_1 and μ_2, are taken to be non-zero and are given by

$$u_0(x) = e^{x^2}, \quad x \in [0,1], \tag{5.32}$$

$$\mu_1(t) = e^t, \quad \mu_2(t) = e^{t+1}, \quad t \in [0,\infty). \tag{5.33}$$

If the additional heat flux measurement $h(t)$ is given by

$$h(t) = 2e^{t+1}, \qquad t \in (0,\infty), \tag{5.34}$$

then, with the input data (5.32)-(5.34), the IP1, given by equations (5.1) with $Q = 0$, (5.15)-(5.18), has the analytical solution:

$$T(x,t) = e^{x^2+t}, \qquad P_f(x) = 4x^2 + 1. \tag{5.35}$$

The direct solver involved in the minimization of (5.23) for IP1 uses a mesh of $N_0 = 180$ and $N = 100$ that is discretising uniformly both the space interval $[0,1]$ and the time interval $[0, t_f = 1]$.

Figure 5.6 shows the numerical results when both exact and 1% noisy errors are considered in the measurement $h(t)$ given by (5.34). In Figure 5.6(a), $ln(F_1)$ is presented, as a function of the number of iterations, for both exact and noisy data,

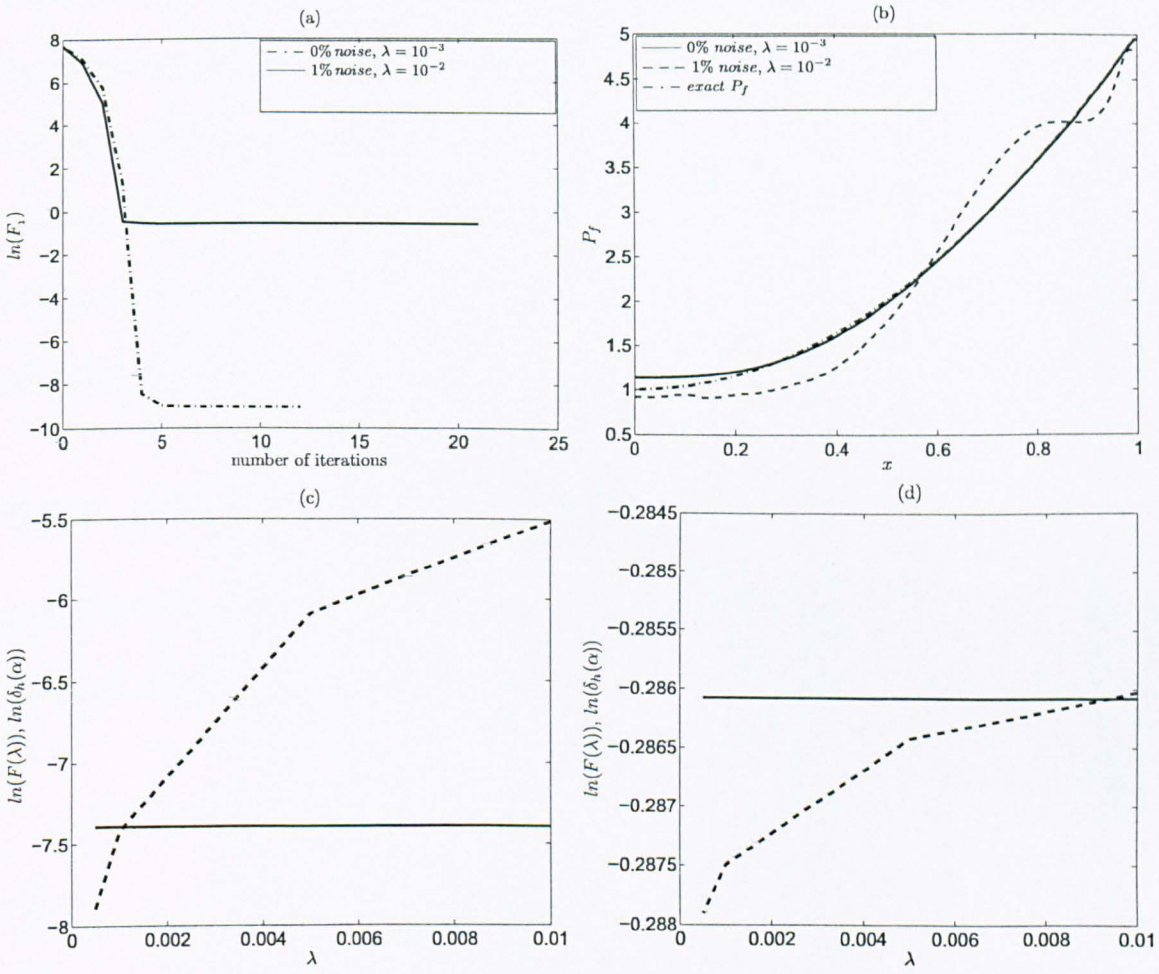

Figure 5.6: (a) Logarithm of the objective functional F_1, as a function of the number of iterations, (b) the numerically obtained $P_f(x)$, (c) the discrepancy principle for exact data, $\alpha = 0$, and (d) the discrepancy principle for $\alpha = 1\%$ noisy data. The amount of noise γ is shown with a continuous line (——) in figures (c) and (d).

with the regularization parameter chosen as follows: $\lambda = 10^{-3}$ for exact measurements, and $\lambda = 10^{-2}$ for the case when $h(t)$ is perturbed by $\alpha = 1\%$ noise. From this figure it can be seen that the convergence of the minimization functional F_1 is rapidly achieved in $10 - 15$ iterations. Figure 5.6(b) presents the computed $P_f(x)$ in comparison to the exact solution given in (5.35), showing that the numerically obtained solution is stable (free of highly unbounded oscillations). The particular choices for the regularization parameter λ have been found by applying the discrepancy principle (5.29), as shown in Figures 5.6(c) and 5.6(d) for exact and 1% noisy measurements, respectively.

5.6.3 Numerical Example for IP2

In this section the initial condition (5.15), u_0, and the Dirichlet boundary conditions (5.16)-(5.17), μ_1 and μ_2, are chosen as follows:

$$u_0(x) = (x - x^2)^2 + 20, \qquad x \in [0, 1], \tag{5.36}$$

$$\mu_1(t) = 20e^{-t}, \qquad \mu_2(t) = 20e^{-t}, \qquad t \in [0, \infty). \tag{5.37}$$

Also, considering $t_f = 1$ and taking the time-average temperature measurement (5.19) as being

$$\mathcal{E}(x) = (1 - e^{-1})((x - x^2)^2 + 20), \qquad x \in (0, 1), \tag{5.38}$$

for the IP2, given by (5.1) with $\Sigma = 0$, (5.15)-(5.17), (5.19), we obtain the following analytical solution:

$$T(x, t) = e^{-t}((x - x^2)^2 + 20), \qquad P_f(x) = \frac{x^4 - 2x^3 + 13x^2 - 12x + 22}{(x - x^2)^2 + 20}. \tag{5.39}$$

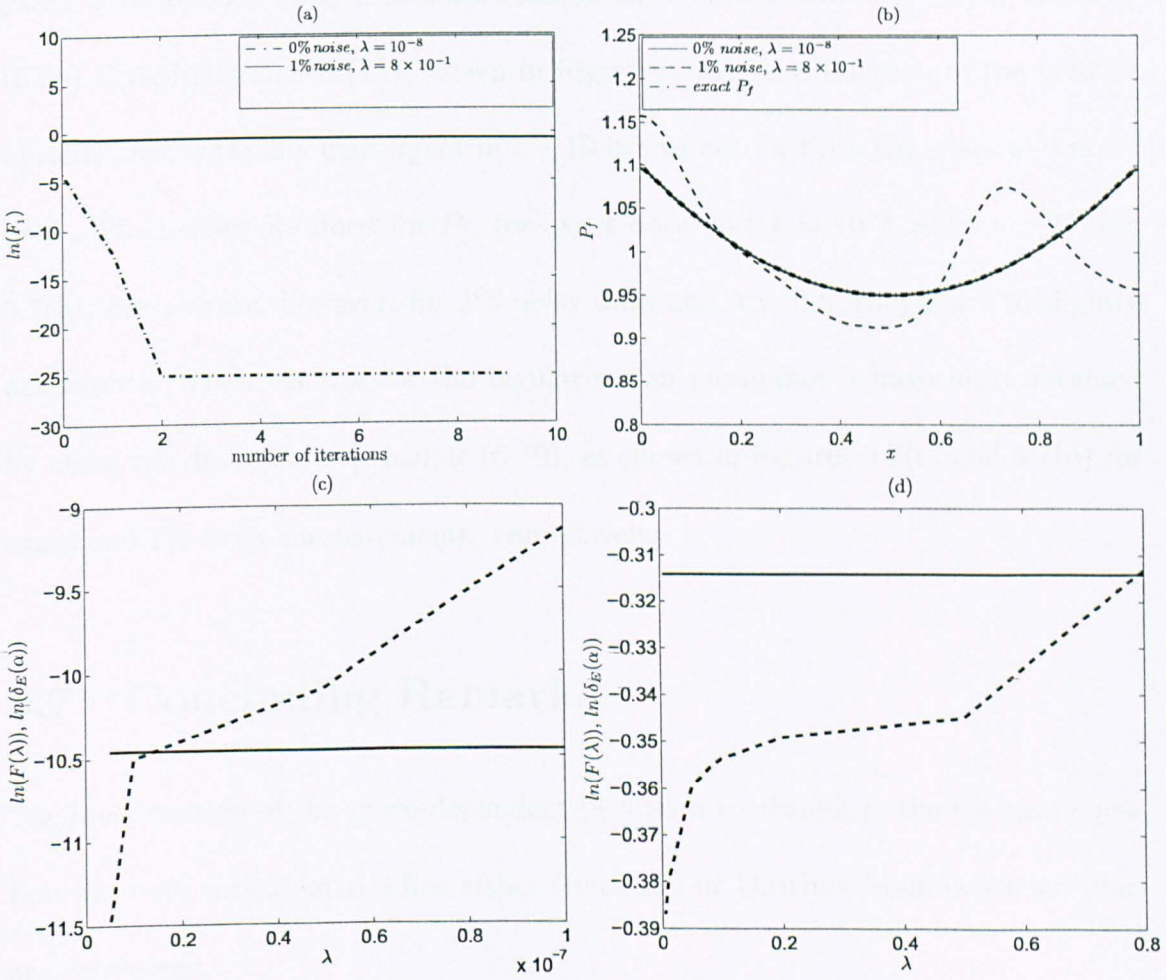

Figure 5.7: (a) Logarithm of the objective functional F_1, as a function of the number of iterations, (b) the numerically obtained $P_f(x)$, (c) the discrepancy principle for exact data, $\alpha = 0$, and (d) the discrepancy principle for $\alpha = 1\%$ noisy data. The amount of noise γ is shown with a continuous line (——) in figures (c) and (d).

The direct solver involved in the minimization of (5.23) for IP2 uses a mesh of $N_0 = 90$ and $N = 100$ that is uniformly discretising both the space interval $[0, 1]$ and the time interval $[0, t_f = 1]$. Figure 5.7 shows the numerical results when both exact data and 1% noisy errors are considered in the measurement $E(x)$ given by (5.38). The functional $ln(F_1)$, shown in Figure 5.7(a), as a function of the number of iterations, is rapidly convergent in $8 - 10$ iterations, for both the exact and noisy data. The results obtained for P_f, for exact data and $\lambda = 10^{-8}$, shown in Figure 5.7(b), are acurate; however, for 1% noisy data and $\lambda = 0.8$, they start to slightly deteriorate. These choices for the regularization parameter λ have been obtained by using the discrepancy principle (5.29), as shown in Figures 5.7(c) and 5.7(d) for exact and 1% noisy measurements, respectively.

5.7 Concluding Remarks

The identification of the space-dependent perfusion coefficient in the bio-heat equation has been investigated when either Neumann or Dirichlet boundary conditions are considered.

In the presence of initial and Neumann boundary conditions, with exact and noisy boundary temperature measurements taken into consideration, the inverse and ill-posed bio-heat conduction problem has been solved numerically. The numerical method that we have developed consists of two parts. In the first step we develop a direct solver based on the Crank-Nicolson finite-difference method, which is then coupled with the second step given by an optimization routine. In effect, the algorithm carries out a search over a class of continuous positive functions P_f in order

to find a global minimum point for the nonlinear Tikhonov regularizing functional. The Tikhonov zeroth- and first-order regularization procedures have been applied. Both in the case of exact and noisy boundary temperature measurements, the results obtained have shown that the first-order regularization is both stable and accurate and performs better that the zeroth-order regularization for all the values of the parameter λ that were considered by inspection.

The numerical results presented are obtained for the measurement data g taken on the restricted time intervals $[0, t_f]$, for $t_f \in \{1, 2, 4\}$. As expected, more accurate and stable results can be obtained if a larger time interval of measurements is considered.

The second part of this chapter is devoted to the Dirichlet inverse problem. In the presence of the Dirichlet boundary conditions, two types of measurements are considered as additional information, namely a flux measurement for $IP1$ and a time-averaged measurement across the region of interest for $IP2$. These two inverse ill-posed problems are solved numerically. For each of them we have developed algorithms that, in essence, are structured similarly and consist of two parts. In a first part a direct solver based on Crank-Nicolson is developed. This part is then coupled with a second one given by an optimization routine in which the perfusion coefficient is found as a global minimizer of the first-order Tikhonov regularization functional, over a class of positive $\mathscr{C}^1$ functions. For all the examples considered, the results obtained represent a good and stable approximation of the target space-dependent perfusion coefficient P_f. The discrepancy principle is used to identify the appropriate regularization parameter λ, in the presence of both exact and noisy measurements.

Chapter 6

Inverse Temperature-Dependent Perfusion Coefficient Reconstruction

6.1 Introduction

In this chapter we investigate the identification of the temperature-dependent perfusion coefficient, $P_f(T)$, which appears in the bio-heat conduction equation

$$\frac{\partial^2 T}{\partial x^2}(x,t) - P_f(T(x,t))T(x,t) + \Sigma(x,t) = \frac{\partial T}{\partial t}(x,t), \quad (x,t) \in (0,1) \times (0,t_f]. \quad (6.1)$$

Given that the coefficient P_f depends on the temperature, we immediately observe the nonlinear character of the equation (6.1). This situation adds up to the difficulty already created by the nonlinear character of the induced inverse problem determined by the fact that both $P_f(T)$ and T are simultaneously unknown.

Our investigation is focused on two inverse problems, namely IP1 when the source

term $\Sigma \not\equiv 0$ is present, and IP2 when the source term is absent, *i.e.* $\Sigma \equiv 0$. In both IP1 and IP2 we aim to identify the temperature-dependent coefficient $P_f(T) > 0$ along with the temperature $T(x,t)$, under prescribed initial and Neumann boundary conditions, when an additional temperature measurement is taken on a part of the boundary along the time interval. It is noticed in the development of the numerical algorithm that it is important to analytically discuss the conditions which ensure that the function $P_f(T)T$ takes its maximum range on the measurement path, namely, in the case of our discussion, on that part of the boundary where the temperature measurement is taken.

In the development of the numerical scheme for the direct solver, when attempting to design a Crank-Nicolson-type scheme, a major difficulty is induced by the nonlinearity of the system, which is caused by the solution dependence. One way to overcome this situation is to introduce a time stepping extrapolation scheme for approximating the value of the function $P_f(T)T$ given its computed values at the previous time steps. Then, a linear system is obtained for computing the solution T at the current time step. Further, this direct problem solver is coupled with an optimisation scheme that is designed to obtain the minimum of a least-squares functional which evaluates the difference between the measured data and the computed solution at the measurement *space*$\times$*time* coordinates, when the space search is a class of polygonal lines that approximates the unknown $P_f(T)$.

In order to obtain a stable solution, the ill-posed character of the inverse problems under investigation require us to apply regularization methods.

6.2 Mathematical Formulation

The two temperature-dependent perfusion coefficient identification inverse problems, namely

- IP1 when $\Sigma \not\equiv 0$,
- IP2 when $\Sigma \equiv 0$,

seek the couple $(P_f(T), T(x,t))$, satisfying the bio-heat equation (6.1), subject to the homogeneous initial condition

$$T(x,0) = 0, \quad x \in [0,1], \tag{6.2}$$

and the Neumann boundary conditions

$$\frac{\partial T}{\partial x}(0,t) = \omega(t), \quad t \in (0,t_f], \tag{6.3}$$

$$\frac{\partial T}{\partial x}(1,t) = 0, \quad t \in (0,t_f], \tag{6.4}$$

when additional information is given as a temperature measurement at the boundary point $x = 0$, along the time interval, namely

$$g(t) = T(0,t), \quad t \in [0,t_f]. \tag{6.5}$$

Let us denote

$$f(T) := P_f(T)T. \tag{6.6}$$

Then equation (6.1) becomes

$$\frac{\partial^2 T}{\partial x^2}(x,t) - f(T(x,t)) + \Sigma(x,t) = \frac{\partial T}{\partial t}(x,t), \quad (x,t) \in (0,1) \times (0,t_f). \tag{6.7}$$

Moreover, IP1 and IP2 can equivalently be recast as inverse problems $\overline{IP1}$ and $\overline{IP2}$ for finding the unknown quantity $f(T)$. This is performed immediately just

by replacing equation (6.1) with equation (6.7), where f is subject to the following constraint:

$$f(0) = 0. \tag{6.8}$$

As soon as f is identified, the temperature-dependent perfusion coefficient P_f is found as the ratio

$$P_f(T) = \frac{f(T)}{T}, \tag{6.9}$$

provided that T is bounded away from zero, except perhaps where f itself vanishes. Prior to this study, the determination of the reaction function $f(T)$ in the $\overline{IP2}$, given by equations (6.2)-(6.5) and (6.7) with $\Sigma \equiv 0$, has been investigated in Cannon and DuChateau [13] and Fatullayev [50] in one-space dimension, and in DuChateau and Rundell [47] and Fatullayev [51] in multi-space dimensions, whilst the $\overline{IP1}$ with $\Sigma \not\equiv 0$ has been investigated in Pilant and Rundell [84, 85, 86, 87]. For other inverse formulations of parabolic equations for determining a semilinear term we refer to Cannon and DuChateau [12], Choulli and Yamamoto [31], Li [67], Lorenzi [70], Orlande and Özisik [76] and Zeghal [119].

Let us define $\mathscr{C}^\alpha$, $\alpha \in (0, 1]$, as the space of Hölder continuous functions with exponent α, which is equipped with the usual norm

$$\| u \|_\alpha = \sup_{P \in Dom(u)} |u(P)| + \sup_{P,Q \in Dom(u)} \frac{|u(P) - u(Q)|}{d(P,Q)^\alpha}, \tag{6.10}$$

and let us denote by $\mathscr{C}^{k+\alpha}$ the space of functions whose k-th derivative belongs to $\mathscr{C}^\alpha$. In particular, for $k = 0$, $\alpha = 1$, the space $\mathscr{C}^{0+1}$ coincides with the space of Lipschitz functions. We denote by $\mathscr{C}$ the space of continuous functions and by $\mathscr{C}^1$ the space of smooth functions.

When f is known and belongs to the set of Lipschitz functions with uniform Lipschitz

constant, *i.e.*

$$f \in \left\{ \tilde{f} \in \mathscr{C}^{0+1}(\mathbb{R}) |\ \tilde{f}(0) = 0,\ \| \tilde{f} \|_1 \leq C \right\}, \tag{6.11}$$

one can establish the existence and uniqueness of the temperature solution T of the direct problem given by equations (6.2)-(6.4) and (6.7), see Friedman [53].

The following theorem describes the properties of the solution for the direct problem given by equations (6.2)-(6.4) and (6.7).

Theorem 6.2.1 *Let us assume that $f \in \mathscr{C}^1(\mathbb{R})$, and consider the data*

$$\begin{aligned} &\omega \in \left\{ \tilde{\omega} \in \mathscr{C}([0,t_f]) |\ \tilde{\omega}(0) = 0,\ \tilde{\omega}(t) < 0,\ t \in (0,t_f) \right\}, \\ &\Sigma \in \left\{ \tilde{\Sigma} \in \mathscr{C}^{1+1}([0,1] \times [0,t_f]) |\ \tfrac{\partial \tilde{\Sigma}}{\partial x}(x,t) \leq 0,\ (x,t) \in (0,1) \times (0,t_f) \right\}, \end{aligned} \tag{6.12}$$

In addition, we suppose that there exists $C > 0$ such that $|T(x,t)| \leq C$, for all $(x,t) \in [0,1] \times [0,t_f]$.

Then the solution of the direct problem (6.2)-(6.4) and (6.7) has the following property:

a)

$$\frac{\partial T}{\partial x}(x,t) \leq 0, \qquad (x,t) \in [0,1] \times [0,t_f]. \tag{6.13}$$

In particular, this implies that for any fixed $t \in (0,t_f)$, $T(1,t) \leq T(x,t) \leq T(0,t) = g(t)$, for all $x \in [0,1]$.

b) If, in addition, we suppose that $\Sigma - \max_{\xi \in [-C,C]} f(\xi) \geq 0$, then $T(x,t) \geq 0$ for all $(x,t) \in [0,1] \times [0,t_f]$.

Proof: The proof of part *a)* follows a path similar to the one made for Theorem 1.1 from Cannon and DuChateau [13]. Let us consider $G(\cdot,\cdot) : [0,1] \times [0,t_f] \to \mathbb{R}$ an

arbitrary non-negative continuous function $G \not\equiv 0$, and let us suppose that $\phi(\cdot,\cdot)$: $[0,1] \times [0,t_f] \to \mathbb{R}$ is the solution of the following problem:

$$\begin{cases} \frac{\partial \phi}{\partial t}(x,t) + \frac{\partial^2 \phi}{\partial x^2}(x,t) - f'(T(x,t))\phi(x,t) = G(x,t), & (x,t) \in (0,1) \times (0,t_f), \\ \phi(x,t_f) = 0, & x \in (0,1), \\ \phi(0,t) = 0, \quad \phi(1,t) = 0, & t \in (0,t_f). \end{cases} \tag{6.14}$$

We note that the system (6.14) is backward in time but is well-posed due to the reverse parabolic character of the partial differential equation.

Since $f \in \mathscr{C}^1(\mathbb{R})$ and $\max\limits_{[0,1]\times[0,t_f]} |T| \leq C$, we obtain that $f'(T(x,t))$ is bounded in $(0,1) \times (0,t_f)$. Therefore, since $G \geq 0$, $G \not\equiv 0$, using a maximum-minimum principle argument, we obtain that

$$\phi(x,t) < 0, \qquad (x,t) \in (0,1) \times (0,t_f), \tag{6.15}$$

which implies that

$$\frac{\partial \phi}{\partial x}(0,t) < 0, \qquad t \in (0,t_f). \tag{6.16}$$

Let us now evaluate the integral

$$\int_0^{t_f} \int_0^1 \frac{\partial T}{\partial x}(x,t) G(x,t) dx\, dt. \tag{6.17}$$

Using integration by parts and invoking Fubini's theorem, we obtain

$$\int_0^{t_f} \int_0^1 \frac{\partial T}{\partial x} G dx\, dt$$
$$= \int_0^{t_f} \int_0^1 \frac{\partial T}{\partial x} \left[\frac{\partial \phi}{\partial t} + \frac{\partial^2 \phi}{\partial x^2} - f'(T)\phi \right] dx\, dt = \int_0^{t_f} \int_0^1 \left[\frac{\partial T}{\partial x} \frac{\partial \phi}{\partial t} + \frac{\partial T}{\partial x} \frac{\partial^2 \phi}{\partial x^2} - \frac{\partial}{\partial x} [f(T)]\, \phi \right] dx\, dt$$

$$= \int_0^{t_f} \left[T\frac{\partial\phi}{\partial t} + \frac{\partial T}{\partial x}\frac{\partial\phi}{\partial x} - f(T)\phi\right]\Big|_{x=0}^{x=1} dt - \int_0^{t_f}\int_0^1 \left[\frac{\partial^2 T}{\partial x^2}\frac{\partial\phi}{\partial x} - f(T)\frac{\partial\phi}{\partial x}\right] dx\,dt - \int_0^1\int_0^{t_f} T\frac{\partial^2\phi}{\partial x\partial t} dt\,dx$$

$$= \int_0^{t_f} \left[T\frac{\partial\phi}{\partial t} + \frac{\partial T}{\partial x}\frac{\partial\phi}{\partial x} - f(T)\phi\right]\Big|_{x=0}^{x=1} dt - \int_0^{t_f}\int_0^1 \left[\frac{\partial^2 T}{\partial x^2}\frac{\partial\phi}{\partial x} - f(T)\frac{\partial\phi}{\partial x}\right] dx\,dt - \int_0^1 T\frac{\partial\phi}{\partial x}\Big|_{t=0}^{t=t_f} dx +$$
$$\int_0^1\int_0^{t_f} \frac{\partial T}{\partial t}\frac{\partial\phi}{\partial x} dt\,dx$$

$$= \int_0^{t_f} \left[T\frac{\partial\phi}{\partial t} + \frac{\partial T}{\partial x}\frac{\partial\phi}{\partial x} - f(T)\phi\right]\Big|_{x=0}^{x=1} dt - \int_0^1 T\frac{\partial\phi}{\partial x}\Big|_{t=0}^{t=t_f} dx + \int_0^{t_f}\int_0^1 \frac{\partial\phi}{\partial x}\left[\frac{\partial T}{\partial t} - \left(\frac{\partial^2 T}{\partial x^2} - f(T)\right)\right] dx\,dt.$$

Therefore, since equation (6.7) implies

$$\int_0^{t_f}\int_0^1 \frac{\partial\phi}{\partial x}\left[\frac{\partial T}{\partial t} - \left(\frac{\partial^2 T}{\partial x^2} - f(T)\right)\right] dx\,dt = \int_0^{t_f}\int_0^1 \frac{\partial\phi}{\partial x}\Sigma dx\,dt, \tag{6.18}$$

we obtain that

$$\int_0^{t_f}\int_0^1 \frac{\partial T}{\partial x} G dx\,dt$$

$$= \int_0^{t_f} \left[T\frac{\partial\phi}{\partial t} + \frac{\partial T}{\partial x}\frac{\partial\phi}{\partial x} - f(T)\phi\right]\Big|_{x=0}^{x=1} dt - \int_0^1 T\frac{\partial\phi}{\partial x}\Big|_{t=0}^{t=t_f} dx + \int_0^{t_f}\int_0^1 \frac{\partial\phi}{\partial x}\Sigma dx\,dt$$

$$= \int_0^{t_f} \left[T\frac{\partial\phi}{\partial t} + \frac{\partial T}{\partial x}\frac{\partial\phi}{\partial x} - f(T)\phi\right]\Big|_{x=0}^{x=1} dt - \int_0^1 T\frac{\partial\phi}{\partial x}\Big|_{t=0}^{t=t_f} dx + \int_0^{t_f} \phi\Sigma\Big|_{x=0}^{x=1} dt - \int_0^{t_f}\int_0^1 \frac{\partial\Sigma}{\partial x}\phi dx\,dt \tag{6.19}$$

Let us note that $\phi(x,t_f) = 0$, for all $0 \le x \le 1$, implies that $\frac{\partial\phi}{\partial x}(x,t_f) = 0$, for all $0 \le x \le 1$, and recall that $T(x,0) = 0$. Therefore

$$\int_0^1 T\frac{\partial\phi}{\partial x}\Big|_{t=0}^{t=t_f} dx = 0. \tag{6.20}$$

Similarly, from $\phi(0,t) = \phi(1,t) = 0$, for all $0 < t < t_f$ we obtain that $\frac{\partial\phi}{\partial t}(0,t) = \frac{\partial\phi}{\partial t}(1,t) = 0$. This implies that

$$\int_0^{t_f} \left[T\frac{\partial\phi}{\partial t} - f(T)\phi\right]\Big|_{x=0}^{x=1} dt = 0. \tag{6.21}$$

From $\phi(0,t) = \phi(1,t) = 0$ we also obtain that

$$\int_0^{t_f} \phi\Sigma \Big|_{x=0}^{x=1} dt = 0. \tag{6.22}$$

Finally, using the boundary conditions (6.3)-(6.4) we obtain that

$$\int_0^{t_f} \frac{\partial T}{\partial x}(x,t)\frac{\partial \phi}{\partial x}(x,t) \Big|_{x=0}^{x=1} dt = -\int_0^{t_f} \omega(t)\frac{\partial \phi}{\partial x}(0,t)dt \tag{6.23}$$

Using equations (6.20)-(6.23), equation (6.19) recasts as

$$\int_0^{t_f}\int_0^1 \frac{\partial T}{\partial x}(x,t)G(x,t)dx\,dt = -\int_0^{t_f} \omega(t)\frac{\partial \phi}{\partial x}(0,t)dt - \int_0^{t_f}\int_0^1 \frac{\partial \Sigma}{\partial x}(x,t)\phi(x,t)dx\,dt. \tag{6.24}$$

Thus, from equations (6.15)-(6.16) and the hypotheses that $\omega(t) < 0$, $t \in (0,t_f)$, and $\frac{\partial \Sigma}{\partial x}(x,t) \leq 0$, $(x,t) \in (0,1) \times (0,t_f)$, we obtain

$$\int_0^{t_f}\int_0^1 \frac{\partial T}{\partial x}(x,t)G(x,t)dx\,dt < 0. \tag{6.25}$$

Therefore, given the fact that G was chosen as an arbitrary non-negative continuous function, we conclude that

$$\frac{\partial T}{\partial x}(x,t) \leq 0, \qquad (x,t) \in [0,1] \times [0,t_f]. \tag{6.26}$$

This follows immediately since, if we suppose by absurd that there exists a ball $B((x_0,t_0),r)$ such that the continuous function $\frac{\partial T}{\partial x}|_{B((x_0,t_0),r)}$ remains strictly positive, *i.e.* $\frac{\partial T}{\partial x}(x,t) > 0$, $(x,t) \in B((x_0,t_0),r)$, then by choosing a non-negative continuous function $G_{(B(x_0,t_0),r)} \not\equiv 0$ so that its support is included in $B((x_0,t_0),r)$, we obtain that

$$\int_0^{t_f}\int_0^1 \frac{\partial T}{\partial x}(x,t)G_{(B(x_0,t_0),r)}(x,t)dx\,dt > 0 \tag{6.27}$$

and this contradicts (6.25). This proves (6.26) and part *a)* of the theorem.

Let un now prove part *b)* of the theorem. Since here we assume $\Sigma - \max_{\xi\in[-C,C]} f(\xi) \geq 0$, from (6.7) we obtain that

$$\frac{\partial T}{\partial t}(x,t) - \frac{\partial^2 T}{\partial x^2}(x,t) \geq 0, \qquad (x,t) \in [0,1] \times [0,t_f]. \tag{6.28}$$

Then the desired conclusion that $T(x,t) \geq 0$ for all $(x,t) \in [0,1] \times [0,t_f]$ follows from the argument involved at the end of the proof of Theorem 1.1 of Cannon and DuChateau [13], via the use of the max-min Hopf principle, see Cannon [11], p.261. This completes the proof of the entire theorem.

□

The following theorem ensures the local solvability of the inverse problem $\overline{IP1}$, given by equations (6.2)-(6.8).

Theorem 6.2.2 (Pilant and Rundell [84]) *Let us consider the data*

$$\begin{cases} \omega \in \left\{\tilde{\omega} \in \mathscr{C}^{1+1}([0,t_f])|\ \tilde{\omega}(0) = 0,\ \tilde{\omega}'(t) < 0,\ t \in [0,t_f]\right\}, \\ \Sigma \in \left\{\widetilde{\Sigma} \in \mathscr{C}^{0+1}((0,1) \times (0,t_f))|\ \widetilde{\Sigma}(x,t) > 0,\ (x,t) \in (0,1) \times (0,t_f)\right\}, \\ g \in \left\{\tilde{g} \in \mathscr{C}^{1+1}([0,t_f))|\ \tilde{g}(0) = 0,\ \tilde{g}'(0) = \Sigma(0,0),\ \tilde{g}'(t) > 0,\ t \in (0,t_f)\right\}. \end{cases} \tag{6.29}$$

Further, by taking ψ to be the solution of the problem

$$\begin{cases} \frac{\partial \psi}{\partial t}(x,t) - \frac{\partial^2 \psi}{\partial x^2}(x,t) = \Sigma(x,t), & (x,t) \in (0,1) \times (0,t_f), \\ \psi(x,0) = 0, & x \in [0,1], \\ \frac{\partial \psi}{\partial x}(0,t) = \omega(t), \quad \frac{\partial \psi}{\partial x}(1,t) = 0, & t \in [0,t_f], \end{cases} \tag{6.30}$$

we assume that there exists $C > 0$ such that $\| g'(\cdot) - \frac{\partial \psi}{\partial t}(0,\cdot) \|_1 < C$.

Then, for the inverse problem $\overline{IP1}$ given by equations (6.2)-(6.8), there exists a

unique local solution $(T, f(T))$ *in the class of functions:*

$$(i) \quad T(\cdot,t) \in \mathscr{C}^{2+1}([0,1]), \qquad t \in (0,t_f),$$

$$(ii) \quad T(x,\cdot) \in \mathscr{C}^{1+1}([0,t_f]), \qquad x \in (0,1),$$

$$(iii) \quad f \in \mathscr{C}^{0+1}(\mathbb{R}).$$

Remark that the first two conditions in (6.29) are required in order to ensure that $T(0,t) = g(t)$ is monotonic increasing for all $t \in [0,t_f]$, and, by the maximum principle, that

$$T(x,t) \leq T(0,t), \qquad (x,t) \in [0,1] \times [0,t_f], \tag{6.31}$$

when f is given and satisfies (6.11).

Alternatively, these properties can also be ensured, see Pilant and Rundell [86], if one assumes the first condition in (6.29) and that

$$\Sigma \in \{\widetilde{\Sigma} \in \mathscr{C}^{1+1}((0,1) \times (0,t_f))|\ \widetilde{\Sigma}(x,t) > 0,\ \frac{\partial \widetilde{\Sigma}}{\partial x}(x,t) \leq 0,\ \ (x,t) \in (0,1) \times (0,t_f)\}. \tag{6.32}$$

In order to be able to recover $f(T)$ over the entire range of the values of $T(x,t)$ that appear in equations (6.2)-(6.8), it is necessary to have the function $T(x,t)$ take on its maximum range at the boundary $x = 0$, where the additional (overposed) data (6.5) is prescribed. From (6.31) we obtain that the maximum of T is obtained at $x = 0$. In order to ensure that the minimum of T is attained also at $x = 0$, the additional hypothesis of part *b)* of Theorem 6.2.1 needs to be satisfied, namely that

$$\Sigma - \sup_{\xi \in \mathbb{R}} f(\xi) \geq 0.$$

The next theorem describes the properties of the solution for the direct problem given by equations (6.2)-(6.4) and (6.7) with $\Sigma \equiv 0$.

Theorem 6.2.3 (Cannon and DuChateau [13]) *In the direct problem given by (6.2)-(6.4) and (6.7) with $\Sigma \equiv 0$, let $f \in \mathscr{C}(\mathbb{R})$ and piecewise differentiable,*

$$\omega \in \left\{\tilde{\omega} \in \mathscr{C}([0,t_f))|\ \tilde{\omega}(0) = 0,\ \tilde{\omega}(t) < 0,\ t \in (0,t_f)\right\},$$

and assume that there exists $C > 0$ such that $|T(x,t)| \leq C$, for all $(x,t) \in [0,1] \times [0,t_f]$.

Then we have

$$\frac{\partial T}{\partial x}(x,t) < 0, \qquad (x,t) \in [0,1] \times [0,t_f]. \tag{6.33}$$

In particular, for any fixed $t \in (0,t_f)$, $g(t) = T(0,t) > T(x,t) > T(1,t)$, $x \in (0,1)$.

Remark that the parts *b)* of Theorem 1.1 and Corollary 1.1 from [13] do not apply to our equation (6.1) since $-f(T)T = -P_f(T)T^2 \leq 0$, as we have $P_f(T) > 0$.

Finally, the following theorem ensures the uniqueness for the solution of the inverse problem $\overline{IP2}$.

Theorem 6.2.4 (Cannon and DuChateau [13]) *Let*

$$\omega \in \left\{\tilde{\omega} \in \mathscr{C}([0,t_f])|\ \tilde{\omega}(0) = 0,\ \tilde{\omega}(t) < 0,\ t \in (0,t_f)\right\}.$$

Suppose f_1, $f_2 \in \mathscr{C}(\mathbb{R})$ are piecewise differentiable and

$$g_1, g_2 \in \left\{\tilde{g} \in \mathscr{C}^1([0,t_f])|\ \tilde{g}(0) = 0,\ \tilde{g}'(t) > 0,\ t \in (0,t_f)\right\}$$

such that $g_i(t) = T(0,t;f_i,\omega)$, for $t \in [0,t_f]$, $i = 1,2$.

Then it follows that:

a) if $f_1(T) = f_2(T)$ for $0 \leq T \leq T^*$, then $g_1(t) = g_2(t)$ for $0 \leq t \leq t^*$ and $g_i(t^*) = T^*$, $i = 1,2$;

b) if f_1 and f_2 are distinct in $\mathcal{L}_2([0,T^{\#}])$ for some $T^{\#} > 0$, then $g_1(t)$ and $g_2(t)$ are distinct in $\mathscr{C}([0,t^{\#}])$ for some $t^{\#} > 0$.

Remark that for the solution $P_f(T) \geq 0$ to exist, the data (6.3) and (6.5) must satisfy

$$0 \geq \int_0^t \omega(\tau) g(\tau) d\tau, \qquad t \in [0, t_f]. \tag{6.34}$$

This inequality can be deduced immediately by remarking that in equation (6.1), after preforming a multiplication with T and integrate the result with respect to x from 0 to 1, and with respect to t from 0 to t, we then can employ equations (6.2)-(6.5), and (6.34) follows.

6.3 Numerical Approach

A finite-difference algorithm based on a Crank-Nicolson-type finite-difference scheme, see Dahlquist and Bjorck [34], pp.387-389, is developed in order to solve the direct problem for the parabolic nonlinear equation (6.7), subject to the initial condition (6.2) and the boundary conditions (6.3) and (6.4). This algorithm is then connected with an optimization routine. After choosing a convenient residual functional, a gradient based optimisation procedure is employed in order to minimize this functional over the space of all polygonal lines that approximate the function f.

6.3.1 Polygonal Approximation for $f(T)$

As remarked in Pilant and Rundell [86], in order to be able to recover $f(T)$ over the entire range of values of $T(x,t)$ that appear in equations (6.2)-(6.5) and (6.7), it is necessary to have the temperature $T(x,t)$ take on its maximum range at the

boundary $x = 0$, where the overposed data (6.5) is prescribed. Thus, if we assume that the conditions of Theorem 6.2.2 are satisfied and that

$$0 \leq T(x,t) \leq T(0,t), \qquad (x,t) \in [0,1] \times [0,t_f], \tag{6.35}$$

then, we seek to determine $f(T)$ and subsequently $P_f(T)$ on the interval $I := [0, g(t_f)]$. Let $0 = t_1 < t_2 < ... < t_N = t_f$ be a uniform discretization of the interval $[0,t_f]$ with step $\Delta t = \frac{t_f}{N-1}$. Then, an *a priori* knowledge of a $(N-1)$-dimensional vector of angles, $\Theta := \{\theta_k\}_{k=\overline{1,N-1}}$, provides us with a polygonal approximation $f(\Theta;\cdot) : I \to \mathbb{R}$ for f, which is defined by

$$f(\Theta;T) :=$$

$$\begin{cases} (T - T(0,t_1))\tan\theta_1, & T \in [T(0,t_1), T(0,t_2)], \\ (T - T(0,t_j))\tan\theta_j + \sum_{k=1}^{j-1}(T(0,t_{k+1}) - T(0,t_k))\tan\theta_k, & T \in [T(0,t_j), T(0,t_{j+1})], \\ & 2 \leq j \leq N-1. \end{cases} \tag{6.36}$$

6.3.2 The Direct Solver

In this step, we want to determine the temperature $T(x,t)$, given the assumed knowledge of an approximating polygonal line $f(\Theta;T)$. Let us denote this computed solution by $T^{comp}(\Theta;(x,t))$ and immediately remark that the initial condition (6.2) implies that $T^{comp}(\Theta;(x,0)) = 0$.

According to the so-called method of lines, see Dahlquist and Bjorck [34], p.388, we consider first a uniform space-discretization $0 = x_1 < x_2 < .. < x_{N_0} = 1$, of step $\Delta x = \frac{1}{N_0 - 1}$. Using central finite differences to approximate the Laplacian, we apply this discretization to the equation (6.7) and obtain the following system of ordinary

differential equations:

$$\frac{dT_i}{dt} = \frac{T_{i+1} - 2T_i + T_{i-1}}{(\Delta x)^2} - f_i + \Sigma_i, \qquad i = \overline{2, N_0 - 1}, \tag{6.37}$$

where, for any $i \in \{1, ..., N_0\}$, the functions $T_i, f_i, \Sigma_i : [0, t_f] \to \mathbb{R}$ are defined by: $T_i(\cdot) := T^{comp}(\Theta; x_i, \cdot)$, $f_i(\cdot) := f(T^{comp}(\Theta; x_i, \cdot))$, and $\Sigma_i(\cdot) := \Sigma(x_i, \cdot)$.

Further, we remark that, for any arbitrary $t^* \in [0, t_f - \Delta t]$, by integrating equation (6.37) over the interval $[t^*, t^* + \Delta t]$, we obtain

$$T_i(t^* + \Delta t) - T_i(t^*) = \int_{t^*}^{t^* + \Delta t} \left[\frac{T_{i+1}(\tau) - 2T_i(\tau) + T_{i-1}(\tau)}{(\Delta x)^2} - f_i(\tau) + \Sigma_i(\tau) \right] d\tau, \qquad i = \overline{2, N_0 - 1}. \tag{6.38}$$

Assuming $t^* \in \{t_1, t_2, ..., t_{N-1}\}$, in order to numerically integrate the right-hand side of each of the equations from the system (6.38), we apply a degenerate trapezoidal rule with one subdivision. Thus, by denoting $T_{i,j} := T_i(t_j)$, $f_{i,j} := f_i(t_j)$, $\Sigma_{i,j} := \Sigma_i(t_j)$, for all $i = \overline{1, N_0}$, $j = \overline{1, N}$, we obtain

$$\frac{T_{i,j+1} - T_{i,j}}{\Delta t} = \frac{1}{2} \left[\frac{T_{i+1,j+1} - 2T_{i,j+1} + T_{i-1,j+1}}{(\Delta x)^2} + \frac{T_{i+1,j} - 2T_{i,j} + T_{i-1,j}}{(\Delta x)^2} \right] - \frac{1}{2} \left[f_{i,j+1} + f_{i,j} \right] + \frac{1}{2} \left[\Sigma_{i,j+1} + \Sigma_{i,j} \right], \qquad i = \overline{2, N_0 - 1}, \; j = \overline{1, N - 1}. \tag{6.39}$$

Using the initial condition vector $\{T_{i,1}\}_{i=\overline{1,N_0}} = \{0\}_{i=\overline{1,N_0}}$ as a starting point, the solver proceeds to march forwards in time. For any time index $j \geq 1$, the unknown vectors $\{T_{i,j+1}\}_{i=\overline{1,N_0}}$ and $\{f_{i,j+1}\}_{i=\overline{1,N_0}}$ will be obtained using the knowledge of the vectors $\{T_{i,j}\}_{i=\overline{1,N_0}}$ and $\{f_{i,j}\}_{i=\overline{1,N_0}}$, which have been computed at the time level $j-1$. Given the knowledge of the vectors $\{f_{i,q}\}_{i=\overline{1,N_0}}$, $1 \leq q \leq j$, we extrapolate the

vector $\left\{f_{i,j+1}\right\}_{i=\overline{1,N_0}}$ as follows:

$$f_{i,j+1} = \begin{cases} T_{i,j+1}\tan(\theta_1), & \text{if } j=1, \\ \\ 2f_{i,j} - f_{i,j-1}, & \text{if } j \geq 2, \end{cases} \quad , \qquad i=\overline{1,N_0}. \tag{6.40}$$

For any angles vector Θ and any time level $j \geq 1$, let us define the N_0-dimensional vector $\left\{b(\Theta,j)(p)\right\}_{p=\overline{1,N_0}}$ as

$$b(\Theta,j)(p) := \frac{1}{2}\left[\Sigma_{1,j+1}+\Sigma_{1,j}, \Sigma_{2,j+1}+\Sigma_{2,j}, ..., \Sigma_{N_0,j+1}+\Sigma_{N_0,j}\right]^{tr}$$

$$+ \begin{cases} \frac{T_{p,j}}{\Delta t} + \frac{(T_{p+1,j}-T_{p,j})}{(\Delta x)^2} - \frac{f_{p,j}}{2} - \frac{\omega(t_j)}{\Delta x} - \frac{\omega(t_{j+1})}{\Delta x}, & \text{if } p=1, \\ \\ \frac{T_{p,j}}{\Delta t} + \frac{(T_{p+1,j}-2T_{p,j}+T_{p-1,j})}{2(\Delta x)^2} - \frac{f_{p,j}}{2}, & \text{if } 2 \leq p \leq N_0-1, \\ \\ \frac{T_{p,j}}{\Delta t} + \frac{(T_{p-1,j}-T_{p,j})}{(\Delta x)^2} - \frac{f_{p,j}}{2}, & \text{if } p=N_0 \end{cases} \tag{6.41}$$

Also, let us consider the $N_0 \times N_0$ matrix A given by

$$A_{k,l} := \begin{cases} \frac{1}{(\Delta x)^2} + \frac{1}{\Delta t}, & \text{if } k=l, \qquad l=\overline{1,N_0}, \\ \\ -\frac{1}{2(\Delta x)^2}, & \text{if } k=l+1, \quad l=\overline{1,N_0-1}, \\ \\ -\frac{1}{2(\Delta x)^2}, & \text{if } l=k+1, \quad k=\overline{1,N_0-1}, \\ \\ 0, & \text{otherwise.} \end{cases} \tag{6.42}$$

Then, from the system (6.39) and equations (6.40)-(6.42), the unknown vector $\left\{T_{i,j+1}\right\}_{i=\overline{1,N_0}}$ is obtained as the solution of one of the following linear systems of equations:

a) if $j=1$, then

$$\left(A + (\tan\theta_1) I_{N_0}\right)\left\{T_{i,j+1}\right\}_{i=\overline{1,N_0}} = \left\{b(\Theta,j)(p)\right\}_{p=\overline{1,N_0}}, \tag{6.43}$$

b) if $j \geq 2$, then

$$A\left\{T_{i,j+1}\right\}_{i=\overline{1,N_0}} = \left\{b(\Theta,j)(p)\right\}_{p=\overline{1,N_0}} - \frac{1}{2}\left[2f_{1,j} - f_{1,j-1}, ..., 2f_{N_0,j} - f_{N_0,j-1}\right]^{tr}, \tag{6.44}$$

where I_{N_0} is the $N_0 \times N_0$- identity matrix.

6.3.3 The Optimization Procedure

During the optimization procedure, in order to be able to use a NAG routine that would obtain a minimum of a function defined on the entire $\mathbb{R}^{N-1}$, it is convenient to map bijectively the interval $(0, \frac{\pi}{2})$ into $\mathbb{R}$ via the change of variable $\zeta(\theta) = \tan(2\theta - \frac{\pi}{2})$, $\theta \in (0, \frac{\pi}{2})$. Thus, the angles vector $\Theta := \{\theta_k\}_{k=\overline{1,N-1}}$ defines a corresponding vector $\mathcal{Y} := \{y_k\}_{k=\overline{1,N-1}}$, given by:

$$y_k := \zeta(\theta_k) = \tan\left(2\theta_k - \frac{\pi}{2}\right), \qquad k = \overline{1, N-1}. \tag{6.45}$$

Then, via the transformation (6.45), for any Θ, the computed solution $T^{comp}(\Theta;(x,t))$ induces a corresponding function $T^{comp}(\mathcal{Y};(\cdot,\cdot)) \to \mathbb{R}$, given by

$$T^{comp}(\mathcal{Y};(x,t)) := T^{comp}(\Theta;(x,t)). \tag{6.46}$$

Our aim is to identify an optimal vector of angles Θ such that the corresponding vector $\mathcal{Y}$ is the minimum of the order-one Tikhonov regularization functional $F_1 : \mathscr{C}^1([0,1]) \to \mathbb{R}_+$ defined by

$$F_1(y) := \lambda \parallel y'(t) \parallel^2_{\mathcal{L}_2(0,t_f)} + \parallel T^{comp}(y;(0,t)) - g(t) \parallel^2_{\mathcal{L}_2(0,t_f)} \tag{6.47}$$

where $\lambda > 0$ is a regularization parameter to be prescribed, and $\mathcal{Y}$ is regarded as a discretization of the smooth function y. If one assume continuity of y only, then

the first term $\lambda \parallel y' \parallel^2_{L_2(0,t_f)}$ in the order-one Tikhonov functional (6.47) should be replaced by $\lambda \parallel y \parallel^2_{L_2(0,t_f)}$ giving rise to the order-zero Tikhonov functional, which can also be employed with no major modifications.

Remark that when $\lambda = 0$, expression (6.47) coincides with the classical least-squares functional. However, as could be noticed also in Fatullayev [50, 51] where a similar version of least-squares functional has been used, without using regularization, an unstable solution is obtained.

We start the optimization procedure with the initial guess $\Theta^0 := \{\theta_k^0\}_{k=\overline{1,N-1}} = \{\frac{\pi}{4}\}_{k=\overline{1,N-1}}$, and this is passed to the direct solver, which computes the corresponding numerical solution $T^{comp}(\Theta^0;(x,t))$. This solution is returned to the optimization routine which starts the search for minimizing F_1, given in (6.47). For doing this, we use the NAG routine E04FCF. Once the minimizer $\mathcal{Y}^* := \{y_k^*\}_{k=\overline{1,N-1}}$ for F_1 has been found, the corresponding vector of angles $\Theta^* = \{\theta_k^*\}_{k=\overline{1,N-1}}$ is obtained via the inversion formula

$$\theta_k^* = \frac{\arctan(y_k^*) + \frac{\pi}{2}}{2}, \qquad k = \overline{1,\, N-1}. \tag{6.48}$$

The inverse problem under investigation is solved subject to both exact and noisy measurements

$$g^\alpha(t) = g(t)(1 + \alpha\eta), \qquad t \in (0, t_f), \tag{6.49}$$

where α is the percentage of noise and η are random variables generated from a uniform distribution in the interval $[-1, 1]$, using the NAG routine G05DAF.

Suppose that we know an upper bound $\gamma > 0$ such that

$$\delta_g(\alpha) := \parallel g - g^\alpha \parallel_{L_2(0,t_f)} \leq \varepsilon. \tag{6.50}$$

Then the regularization parameter λ is chosen according to the discrepancy principle as follows. Considering the functional $F : [0, \infty) \to \mathbb{R}_+$, defined by

$$F(\lambda) := \sqrt{F_1(y) - \lambda \parallel y' \parallel^2_{L_2(0,t_f)}}, \tag{6.51}$$

the Morozov discrepancy principle suggests choosing the regularization parameter as being the largest value $\lambda > 0$ for which

$$F(\lambda) \leq \varepsilon. \tag{6.52}$$

6.4 Numerical Results and Discussions

Throughout this section, the space interval $[0, 1]$ is discretized into $N_0 = 90$ uniform cells, while the time interval $[0, t_f]$ is discretized into $N = 100t_f$ uniform time intervals, where, for simplicity, we take $t_f = 1$.

6.4.1 Numerical Example for IP1

Let us consider the Neumann boundary condition (6.3) given by

$$\frac{\partial T}{\partial x}(0, t) = \omega(t) = -2(e^t - 1), \qquad t \in [0, 1], \tag{6.53}$$

and the source Σ given by

$$\Sigma(x, t) = e^t(x-1)^2 - 2(e^t - 1) + (x-1)^2(e^t - 1)\left[(x-1)^4(e^t - 1)^2 + 1\right], \qquad (x, t) \in [0, 1] \times [0, 1]. \tag{6.54}$$

If the temperature measurement (6.5) is given by

$$T(0, t) = g(t) = e^t - 1, \qquad t \in [0, 1], \tag{6.55}$$

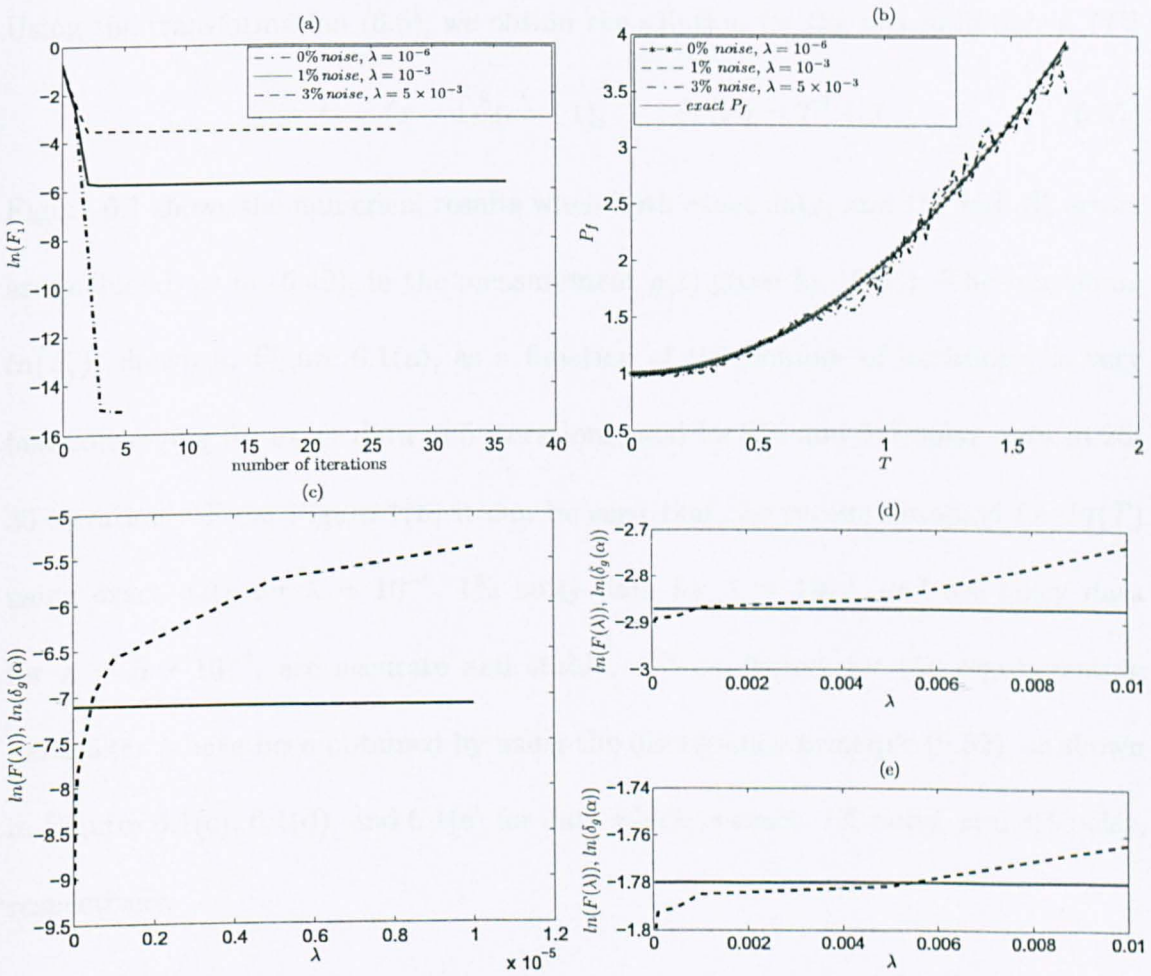

Figure 6.1: Example for IP1. (a) Logarithm of the objective functional F_1, as a function of the number of iterations, (b) the numerically obtained $P_f(T)$, (c) the discrepancy principle for exact data, $\alpha = 0$, (d) the discrepancy principle for $\alpha = 1\%$ noisy data, and (e) the discrepancy principle for $\alpha = 3\%$ noisy data.

then, with the input data (6.53)-(6.55), the inverse problem $\overline{IP1}$, given by equations (6.2)-(6.8), has the analytical solution

$$T(x,t) = (x-1)^2(e^t - 1), \qquad f(T) = T(T^2+1). \tag{6.56}$$

Using the transformation (6.6), we obtain the solution for the inverse problem $IP1$

$$T(x,t) = (x-1)^2(e^t - 1), \qquad P_f(T) = T^2 + 1. \tag{6.57}$$

Figure 6.1 shows the numerical results when both exact data, and 1% and 3% errors are included, as in (6.49), in the measurement $g(t)$ given by (6.55). The functional $ln(F_1)$, shown in Figure 6.1(a), as a function of the number of iterations, is very fast converging for exact data in 5 iterations, and for 1% and 3% noisy data in 25-35 iterations. From Figure 1(b) it can be seen that the results obtained for $P_f(T)$ using exact data for $\lambda = 10^{-6}$, 1% noisy data for $\lambda = 10^{-3}$, and 3% noisy data for $\lambda = 5 \times 10^{-3}$, are accurate and stable. These choices for the regularization parameter λ have been obtained by using the discrepancy principle (6.52), as shown in Figures 6.1(c), 6.1(d), and 6.1(e) for data which is exact, 1% noisy, and 3% noisy, respectively.

6.4.2 Numerical Example for IP2

For the $IP2$, the source term Σ is absent, *i.e.* $\Sigma \equiv 0$. Considering here the same Neumann boundary condition (6.53), we aim to retrieve the perfusion coefficient

$$P_f(T) = T^2 + 1 \tag{6.58}$$

for the inverse problem $IP2$, which, via the transformation (6.6), can equivalently be formulated as the coefficient identification $\overline{IP2}$, seeking to reconstruct

$$f(T) = T(T^2 + 1). \tag{6.59}$$

Since in this case an analytical solution for the direct problem given by (6.1) with $\Sigma \equiv 0$, (6.2), (6.4), (6.53) and (6.58) is not available, the additional Dirichlet boundary temperature data (6.5) was computed numerically, by using the NAG routine C05NCF to solve the resulting system of nonlinear finite-difference equations.

Figure 6.2 shows the numerical results, when $\alpha \in \{0, 1, 3\}\%$ noise is perturbing the data g as in (6.49). In Figure 6.2(a), $ln(F_1)$ is represented as a function of the number of iterations, obtained when the data are assumed exact for $\lambda = 10^{-6}$, 1% noisy data for $\lambda = 5 \times 10^{-4}$, and 3% noisy data for $\lambda = 10^{-3}$. From this figure it can be seen that the convergence of the minimization functional F_1 is immediately achieved in only $5 - 9$ iterations for $\alpha = 0$ and 1% noisy data, and in 49 iterations for $\alpha = 3\%$ noisy data. Figure 6.2(b) shows the plots of the computed solution for $P_f(T)$. From this figure it can be seen that the computed results are an accurate and stable approximation of the exact perfusion coefficient given in equation (6.58). Figures 6.2(c), 6.2(d) and 6.2(e) show the discrepancy principle (6.52) for $\alpha = 0$, $\alpha = 1\%$, and $\alpha = 3\%$, respectively. From these figures it can be seen that the discrepancy principle enables us to effectively locate the regularization parameter λ, when both exact and perturbed noisy measurements are considered.

6.5 Conclusions

Two inverse problems concerning the identification of the temperature-dependent perfusion coefficient in the bio-heat conduction equation (BHCE) have been investigated. In the presence of initial and Neumann boundary conditions, a measurement of the temperature on a part of the boundary is considered as additional informa-

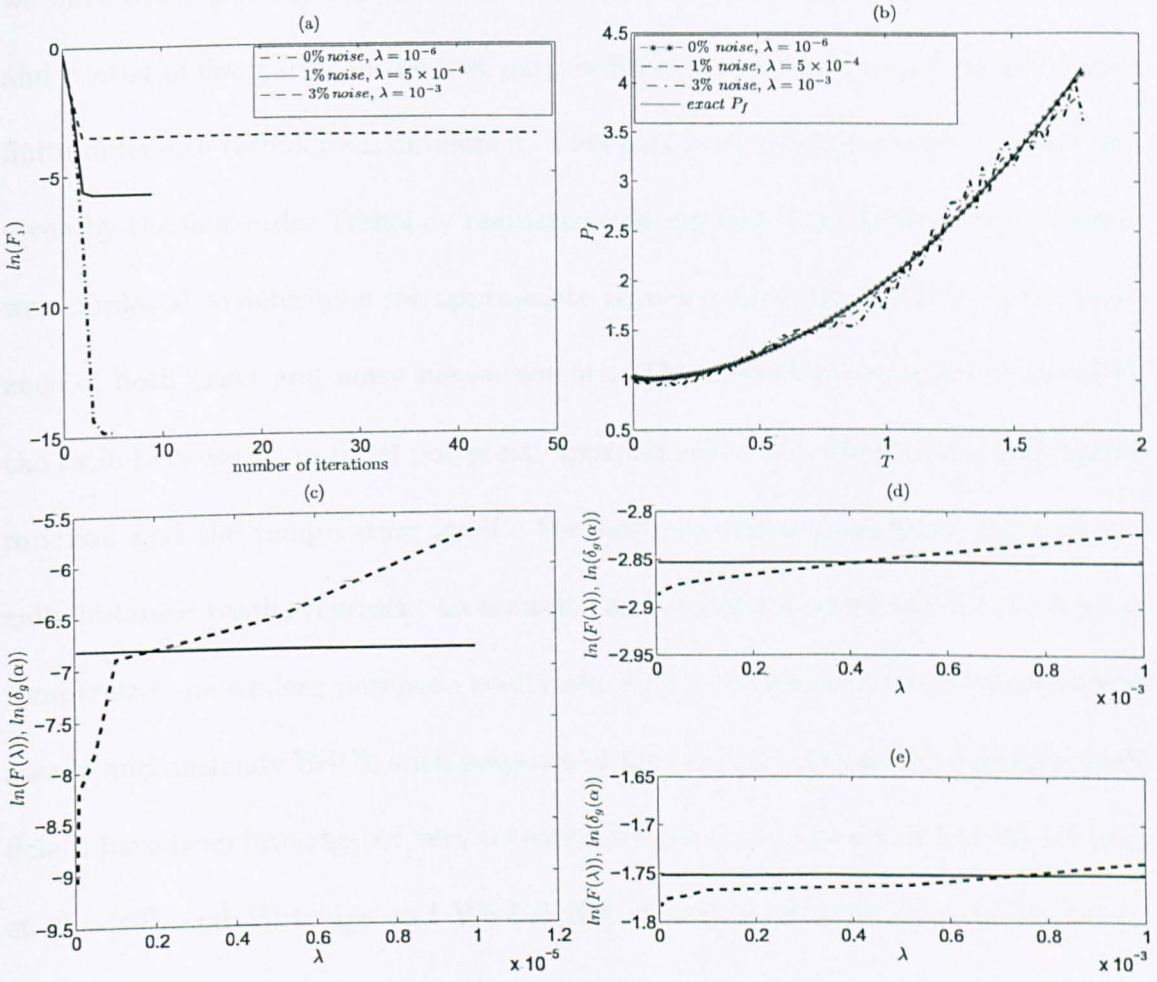

Figure 6.2: Example for IP2. (a) Logarithm of the objective functional F_1, as a function of the number of iterations, (b) the numerically obtained $P_f(T)$, (c) the discrepancy principle for exact data, $\alpha = 0$, (d) the discrepancy principle for $\alpha = 1\%$ noisy data, and (e) the discrepancy principle for $\alpha = 3\%$ noisy data.

tion in the presence of a source, $\Sigma \not\equiv 0$, for IP1, and without a source, *i.e.* $\Sigma \equiv 0$, for IP2. Solvability results for these inverse problems have been provided. These inverse and ill-posed problems have then been solved numerically. For each of them we have developed algorithms that, in essence, are structured in a similar manner and consist of two parts. In the first part, a direct solver based on a Crank-Nicolson finite-difference technique is developed. This part is then coupled with a second one given by the first-order Tikhonov regularization method. The discrepancy principle was employed to determine the appropriate regularization parameter λ, in the presence of both exact and noisy measurements. The perfusion coefficient is found as the ratio between an optimal polygonal approximation of a temperature-dependent function and the temperature itself. For both examples considered, the numerically obtained results represent an accurate and stable approximation of the desired temperature-dependent perfusion coefficient $P_f(T)$. Extensions to two-dimensional steady and unsteady BHCE with polynomial temperature-dependent perfusion coefficient have been investigated very recently elsewhere, see Deng and Liu [45], Erhart et al. [49], and Partridge and Wrobel [79], using the dual reciprocity boundary element method.

Chapter 7

Reconstruction of the Space- and Time-Dependent Blood Perfusion Coefficient in Bio-Heat Transfer

7.1 Introduction

In this chapter, we perform a numerical investigation for the reconstruction of the perfusion coefficient that is considered dependent both of space and time, $P_f(x,t)$, which appears in the bio-heat conduction equation

$$\frac{\partial^2 T}{\partial x^2}(x,t) - P_f(x,t)T(x,t) = \frac{\partial T}{\partial t}(x,t), \quad (x,t) \in (0,1) \times (0,t_f], \qquad (7.1)$$

subject to initial and Dirichlet boundary conditions, when additional information is provided in terms of exact a noisy temperature measurements taken on a certain fixed grid inside the *space*$\times$*time* domain.

Since in the small subregion occupied by a thermocouple contact surface tempera-

ture data are, in effect, recorded both in space, all across the contact region, and in time, during an entire measurement process, this inverse problem essentially refers to the blood perfusion rate which occurs in this small skin-thermocouple contact interface. Also, in a different application, this inverse problem arises in an investigation related to coastal evolution and sediment transport, see Reeve and Spivack [95].

For the numerical approach, at least two methods could be considered. A first method involving a Crank-Nicolson-type scheme combined with the minimization of a first-order Tikhonov regularization functional, gives a global perspective. However, we can immediately observe that even if a very coarse grid is considered, we unavoidably arrive to the situation in which systems with a very large number of equations (of the order of the number of discretization points in the *space*$\times$*time* domain) are to be solved during the optimisation step. This aspect alone can cause a major downgrading effect on the accuracy and stability properties of the numerical results, especially for the case when the measured data are affected by noise. This situation could be improved if a local approach is involved.

In the second strategy, both the first-order time derivative and the second-order space derivative can be obtained by means of first kind Fredholm integral equations. Since numerical solutions of the first kind integral equation have well-known inherited instability issues even for exact measurement data, regularization methods have to be employed in order to obtain stable results.

7.2 Mathematical Formulation

Let us consider a fixed uniform discretization of the *space* × *time* domain $[0,1]\times[0,t_f]$ using N time intervals and N_0 space cells, *i.e.* $t_j = jt_f/N$, $j = \overline{1,N}$, $x_i = i/N_0$, $i = \overline{0,N_0}$. Let us define $y_i := (x_i + x_{i-1})/2$, $i = \overline{1,N_0}$, be the midpoint of the interval $[x_{i-1}, x_i]$ for $i = \overline{1,N_0}$.

We wish to identify the couple $(P_f(x,t), T(x,t))$, satisfying the BHCE (7.1), subject to the initial condition

$$T(x,0) = u(x), \quad x \in [0,1], \tag{7.2}$$

and the Dirichlet boundary conditions

$$T(0,t) = f_1(t), \quad T(1,t) = f_2(t), \qquad t \in (0,t_f], \tag{7.3}$$

when additional information is supplied on either of the following two discretization grids:

a) temperature measurements at $\{(x_i,t_j)\}_{i=\overline{1,(N_0-1)},\, j=\overline{1,N}}$ given by

$$G_1(x_i,t_j) = T(x_i,t_j), \quad i = \overline{1,(N_0-1)},\ j = \overline{1,N}. \tag{7.4}$$

b) temperature measurements at $\{(y_i,t_j)\}_{i=\overline{1,N_0},\, j=\overline{1,N}}$ given by

$$G_2(y_i,t_j) = T(y_i,t_j), \quad i = \overline{1,N_0},\ j = \overline{1,N}. \tag{7.5}$$

Instead of the Dirichlet boundary conditions (7.3), Neumann or mixed boundary conditions can easily be considered.

The measurements (7.4) and (7.5) are set up at slightly different space positions only for the convenience of explanation of Sections 3 and 4. All what one really needs to know is that in principle we wish to determine $P_f(x,t)$ from the noisy measurements of $T(x,t)$.

7.3 Global Least-Squares Minimization Approach

A Crank-Nicolson-type finite-difference algorithm based on the method of lines, see Dahlquist and Bjorck [34], pp.387-389, is developed in order to solve the direct problem for the parabolic equation (7.1), subject to the initial condition (7.2) and the Dirichlet boundary conditions (7.3). This algorithm is then connected with an optimization routine in order to obtain the perfusion coefficient P_f as the minimum point for the least-squares functional $F : \mathscr{C}([0,1] \times (0,t_f]) \rightarrow \mathbb{R}_+$, given by

$$F(q) := \sum_{i=1}^{N_0-1} \sum_{j=1}^{N} \left[T^{comp}(q;(x_i,t_j)) - G_1(x_i,t_j)\right]^2, \qquad q \in \mathscr{C}([0,1] \times (0,t_f]), \quad (7.6)$$

where $\mathscr{C}([0,1] \times (0,t_f])$ is the space of continuous functions and $T^{comp}(q;(\cdot,\cdot))$ is the solution computed via the Crank-Nicolson-type algorithm for the guessed continuous function $q(x,t)$ that is used as a replacement for the currently unknown perfusion coefficient $P_f(x,t)$. In this formulation, uniqueness of the solution cannot in general be assured, because the dependence on P_f and T in equation (7.1) is nonlinear, and also one is typically attempting to reconstruct a continuous function $P_f(x,t)$ from a finite $N \times (N_0 - 2)$ temperature measurements information. Associated with the minimization of (7.6), one could also attach the physical constraint that the sought perfusion coefficient is positive, but the problem is further complicated since the measurements (7.4) or (7.5) are subject to noisy errors, or can be vanishingly small. The optimization procedure is started with an initial guess $\{q^0_{i,j}\}_{i=\overline{1,(N_0-1)},\, j=\overline{1,N}} \equiv 1$, which is transmitted to the direct solver that computes the numerical solution $T^{comp}(q^0;(x,t))$. This solution is returned to the optimization routine which starts the search for minimizing F, given in (7.6). In order to do this, we use the NAG routine E04FCF.

7.3.1 Numerical Example

Let us set, for simplicity, $t_f = 1$ and consider the initial condition (7.2) given by

$$T(x,0) = u(x) = e^{-x}(x^2 + 4), \qquad x \in [0,1], \tag{7.7}$$

the Dirichlet boundary conditions (7.3) given by

$$T(0,t) = f_1(t) = e^{-t}(2t+4), \quad T(1,t) = f_2(t) = e^{-t-1}(2t+5), \qquad t \in (0,1], \tag{7.8}$$

and the temperature measurements (7.4) given by

$$G_i(x_i,t_j) = e^{-x_i-t_j}(2t_j + x_i^2 + 4), \qquad i = \overline{1,(N_0-1)},\ j = \overline{1,N}. \tag{7.9}$$

Then, the inverse problem given by equations (7.1), (7.7)-(7.9), has the analytical solution

$$T(x,t) = e^{-(x+t)}(2t + x^2 + 4), \qquad P_f(x,t) = 2 - \frac{4x}{2t + x^2 + 4}, \tag{7.10}$$

and this can be verified by direct substitution. For this global minimization approach, the time interval $[0,t_f]$ is discretized into $N = 20$ uniform time intervals and the space interval $[0,1]$ is discretized into $N_0 = 20$ uniform cells. However, because the dimension of the least-squares resulting functional (7.6) is $(N \times (N_0 - 2))$, with $(N \times (N_0 - 2))$ unknowns, a finer discretization becomes computationally unfeasible.

Figure 7.1 shows the contour plots of the numerical results for $P_f(x,t)$ obtained for both exact and 1% noisy data in comparison with the exact solution (7.10), in the *space* $\times$ *time* domain $[0,1] \times [0,1]$. As shown in Figure 7.1(b), using exact data, by minimizing the least-squares functional F given by (7.6), the numerically obtained results represent a very good approximation, with four digits accuracy, to the exact

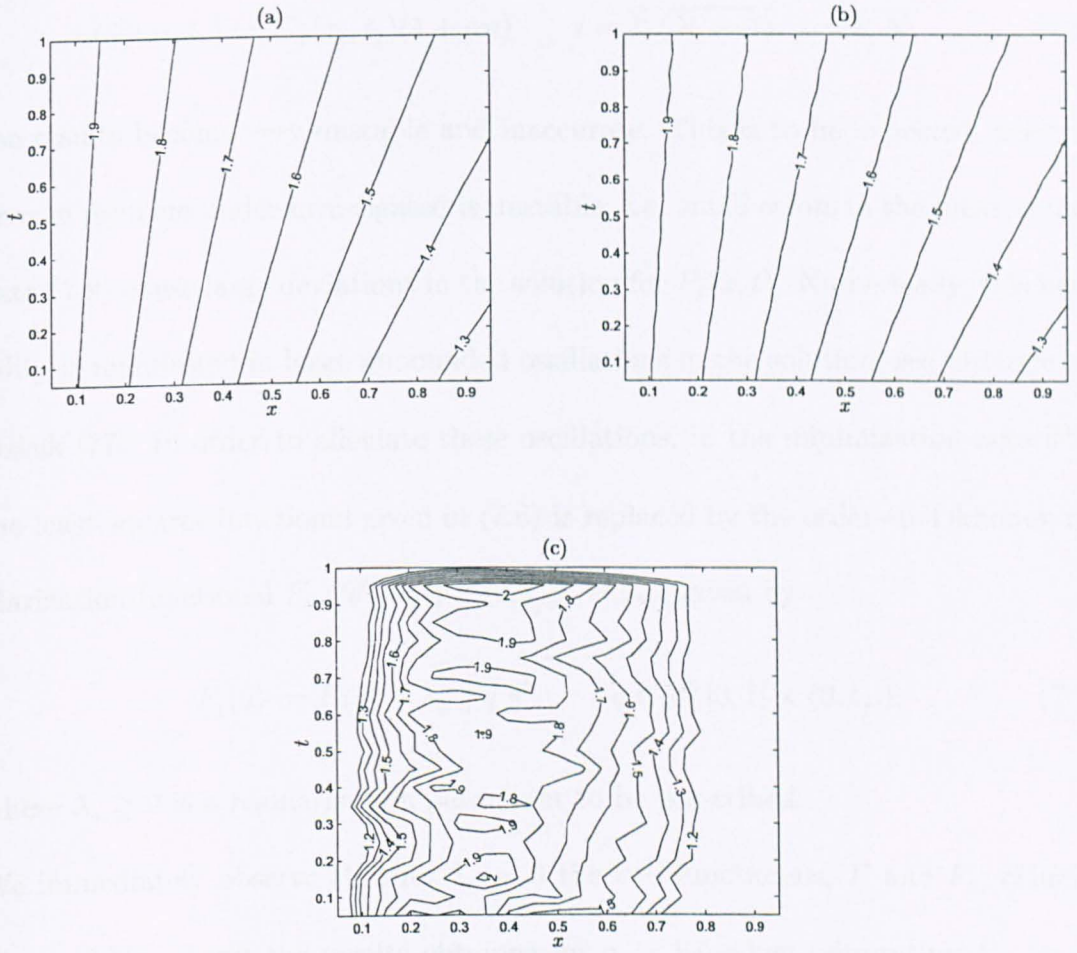

Figure 7.1: Contour plots for $P_f(x,t)$: (a) exact solution, (b) numerical solution obtained with no regularization for exact data, and (c) numerical solution obtained with the order-0 Tikhonov regularization of parameter $\lambda_0 = 10^{-3}$, for 1% noisy data.

solution illustrated in Figure 7.1(a). However, by perturbing the data (7.9) with a percentage $\alpha = 1\%$ of random noise η sampled from a uniform distribution over the interval (-1,1), namely

$$G_1^{\alpha}(x_i, t_j) := G_1(x_i, t_j)(1 + \alpha\eta) \qquad i = \overline{1, (N_0 - 1)},\ j = \overline{1, N}, \tag{7.11}$$

the results become very unstable and inaccurate. This is to be expected, since the inverse problem under investigated is unstable, *i.e.* small errors in the measurement data (7.9) cause large deviations in the solution for $P_f(x, t)$. Numerically, this instability is manifested in large unbounded oscillations in the solution, see Orlande and Özisik [77]. In order to alleviate these oscillations, in the minimization algorithm, the least-squares functional given in (7.6) is replaced by the order−0 Tikhonov regularization functional $F_1 : \mathscr{C}([0, 1] \times (0, t_f]) \to \mathbb{R}_+$, given by

$$F_1(q) := F(q) + \lambda_0 \parallel q \parallel^2, \qquad q \in \mathscr{C}([0, 1] \times (0, t_f]), \tag{7.12}$$

where $\lambda_0 \geq 0$ is a regularization parameter to be prescribed.

We immediately observe that for $\lambda_0 = 0$ the two functionals, F and F_1, coincide. Figure 7.1(c) shows the results obtained for $\alpha = 1\%$ when minimizing F_1, for the regularization parameter $\lambda_0 = 10^{-3}$. From this figure it can be seen that the results obtained, when 1% noise is perturbing the measurements, are not oscillatory anymore (in contrast to the case when $\lambda_0 = 0$, *i.e* no regularization is added, where we have large oscillations), but they are still quite inaccurate. Other values of λ_0, in the range $10^{-4} < \lambda_0 < 10^{-2}$ produced similar results, and, as expected, if λ_0 is too small, the solution in under-smoothed and it becomes unstable, whilst if λ_0 is too large, the solution is over-smoothed and it deviates from the exact solution.

The inaccuracy observed in Figure 7.1(c) led us to propose and investigate a second

approach for the case when noisy measurements are considered.

7.4 Local Approach

In this second approach, we compute locally both the time first-order derivative $\frac{\partial T}{\partial t}$ and the space second-order derivatives $\frac{\partial^2 T}{\partial x^2}$ by means of Fredholm integral equations of the first kind, see Hanke and Scherzer [54] and Murio [73]. Alternative approaches based on the mollification, see Murio [73], or on the finite-difference method, see Ramm and Smirnova [93] and Wang et al. [114], could also be employed.

Everywhere in this section, we consider a discretization in both time and space with $N = N_0 = 100$ and we consider the numerical example of section 7.3.1 with the initial condition (7.7) boundary conditions (7.8) and the temperature measurement (7.5) perturbed by $\alpha\%$ of random noise η given by

$$G_2^{\alpha}(y_i, t_j) := e^{-y_i - t_j}(2t_j + y_i^2 + 4)(1 + \alpha\eta) \qquad i = \overline{1, N_0},\ j = \overline{1, N}. \tag{7.13}$$

7.4.1 Approximating the First-order Time Derivative

For any $i = \overline{1, N_0}$, let us denote $\phi_{y_i}(t) := T(y_i, t) - u(y_i)$. Then from (7.2) we have $\phi_{y_i}(0) = 0$. Also, $\frac{\partial T}{\partial t}(y_i, t) = \phi'_{y_i}(t)$. Then we have

$$\phi_{y_i}(t) = \int_0^t \phi'_{y_i}(\tau)d\tau = \int_0^{t_f} k_1(t, \tau)\phi'_{y_i}(\tau)d\tau, \qquad t \in [0, t_f], \tag{7.14}$$

where the kernel $k_1(\cdot, \cdot) : \mathbb{R}^2 \to \mathbb{R}_+$ is given by

$$k_1(t, \tau) := \begin{cases} 0, & t < \tau, \\ 1, & t \geq \tau. \end{cases} \tag{7.15}$$

Let us consider the uniform grid $\tau_j = t_f/(2N) + jt_f/N$, $j = \overline{0,N}$, such that $t_j = (\tau_{j-1}+\tau_j)/2$ for $j = \overline{1,N}$. Then we approximate the integral in (7.14) as

$$\phi_{y_i}(t) = \int_0^{t_f} k_1(t,\tau)\phi'_{y_i}(\tau)d\tau \cong \sum_{j=1}^{N} \phi'_{y_i}(t_j) \int_{\tau_{j-1}}^{\tau_j} k_1(t,\tau)d\tau, \tag{7.16}$$

where the coefficients $\int_{\tau_{j-1}}^{\tau_j} k_1(t,\tau)d\tau$ have the following analytical expressions:

$$\int_{\tau_{j-1}}^{\tau_j} k_1(t,\tau)d\tau = \begin{cases} 0, & t \le \tau_{j-1}, \\ t - \tau_{j-1}, & \tau_{j-1} < t < \tau_j, \\ \tau_j - \tau_{j-1}, & \tau_j \le t. \end{cases} \tag{7.17}$$

By applying (7.16) at each t_l, $l = \overline{1,N}$, we obtain a system of equations whose $N \times N$-matrix A is given by

$$A_{lj} = \int_{\tau_{j-1}}^{\tau_j} k_1(t_l,\tau)d\tau, \qquad l,j = \overline{1,N}, \tag{7.18}$$

and the N-dimensional right-hand side measurements vector $\{\widetilde{G}_2^{\alpha}(y_i,t_j)\}_{j=\overline{1,N}}$ given by

$$\widetilde{G}_2^{\alpha}(y_i,t_j) := e^{-y_i-t_j}(2t_j + y_i^2 + 4)(1+\alpha\eta) - e^{-y_i}(y_i^2+4), \qquad j = \overline{1,N}. \tag{7.19}$$

Given the well-known instability of the solution of a first-kind integral equation, and the fact that in the resulting linear ill-conditioned system of equations

$$A[\phi'_{y_i}(t_1),...,\phi'_{y_i}(t_N)]^{tr} = [\widetilde{G}_2^{\alpha}(y_i,t_1),...,\widetilde{G}_2^{\alpha}(y_i,t_N)]^{tr}, \tag{7.20}$$

the right-hand side vector contains errors, the solution of (7.20) is sought by using order$-k \in \{0,1,2\}$ Tikhonov regularizations, see e.g. Phillips [82], namely

$$[A^{tr}A + \lambda_k D_k(N)^{tr} D_k(N)]\,[\phi'_{y_i}(t_1),...,\phi'_{y_i}(t_N)]^{tr} = A^{tr}[\widetilde{G}_2^{\alpha}(y_i,t_1),...,\widetilde{G}_2^{\alpha}(y_i,t_N)]^{tr},$$
$$k \in \{0,1,2\}, \tag{7.21}$$

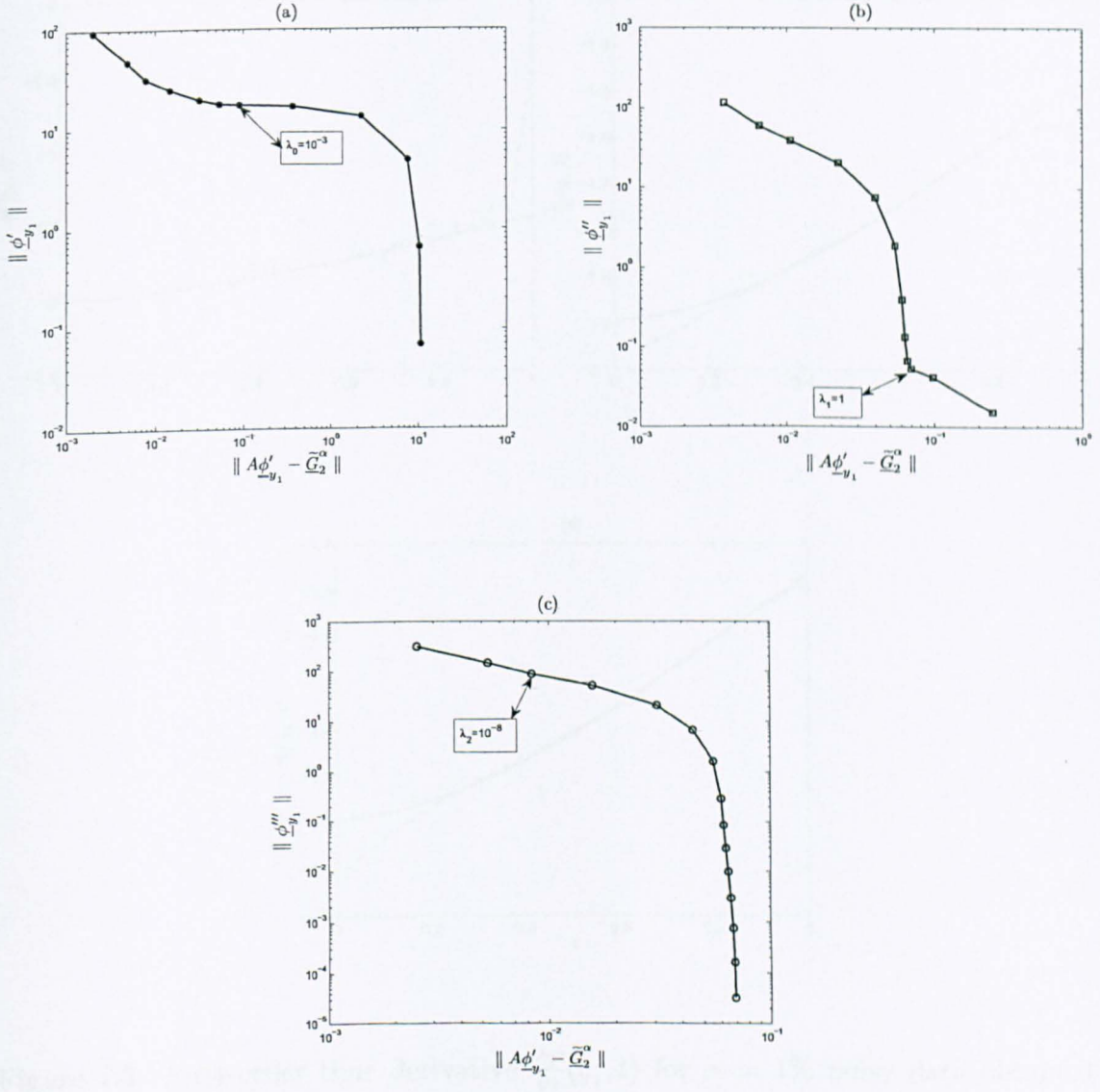

Figure 7.2: L-curves for the first-order time derivative approximation with $\alpha =$ 1% noisy temperature measurements for: (a) order-0, (b) order-1, and (c) order-2, Tikhonov regularizations.

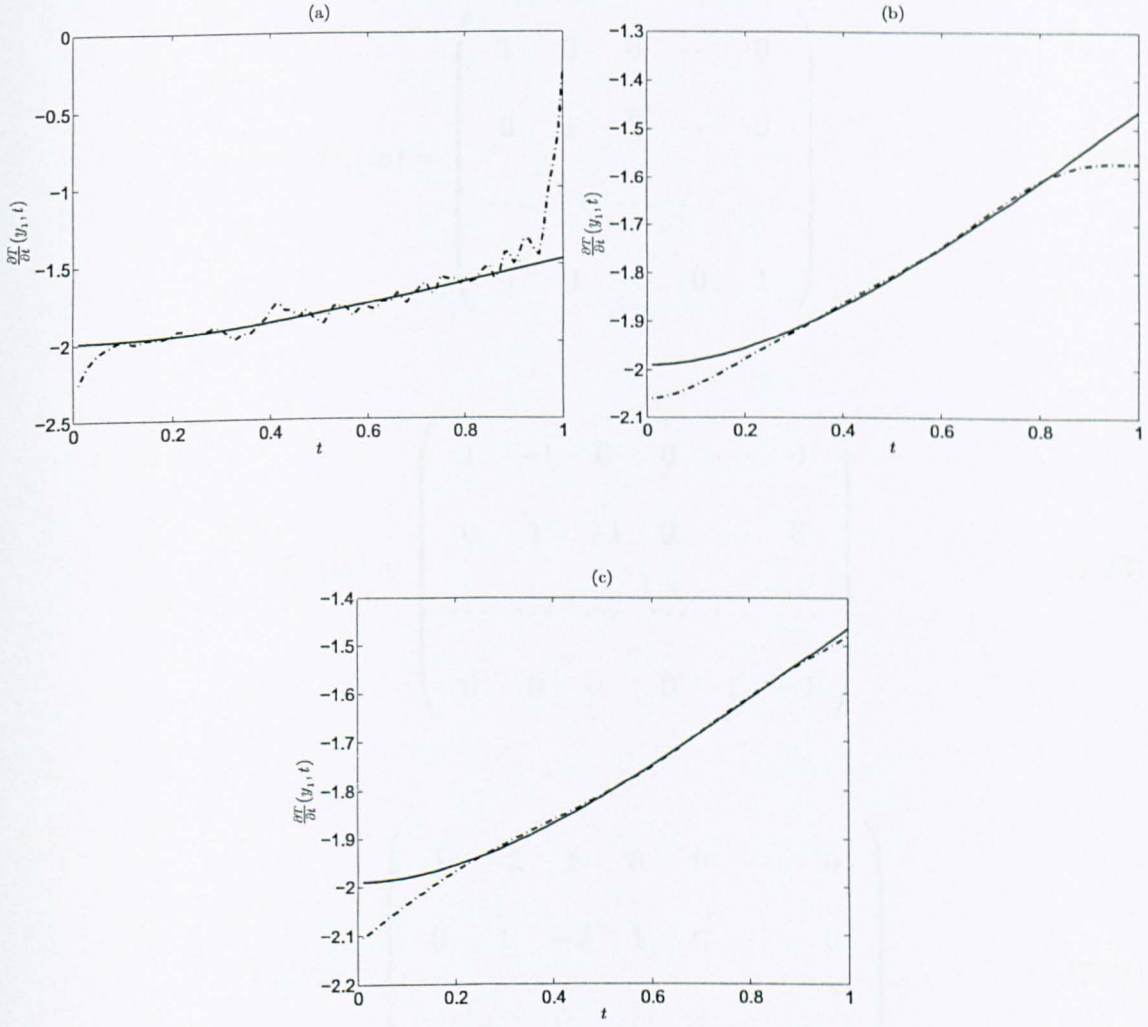

Figure 7.3: First-order time derivative $\frac{\partial T}{\partial t}(y_1, t)$ for $\alpha = 1\%$ noisy data obtained using: (a) order-0 Tikhonov regularization with $\lambda_0 = 10^{-3}$, (b) order-1 Tikhonov regularization with $\lambda_1 = 1$, and (c) order-2 Tikhonov regularization with $\lambda_2 = 100$. Dash-dot line represents the computed results, while the solid line stands for the analytical solution.

where, for any natural number $m \geq 3$, the $(m-k) \times m$ dimensional order$-k$ smoothness matrices $D_k(m)$, $k \in \{0,1,2\}$, are defined by

$$D_0(m) = \begin{pmatrix} 1 & 0 & 0 & \cdots & 0 \\ 0 & 1 & 0 & \cdots & 0 \\ \cdots & \cdots & \cdots & \cdots & \cdots \\ 0 & 0 & \cdots & 0 & 1 \end{pmatrix}, \tag{7.22}$$

$$D_1(m) = \begin{pmatrix} 1 & -1 & 0 & 0 & \cdots & 0 \\ 0 & 1 & -1 & 0 & \cdots & 0 \\ \cdots & \cdots & \cdots & \cdots & \cdots & \cdots \\ 0 & 0 & \cdots & 0 & 1 & -1 \end{pmatrix}, \tag{7.23}$$

$$D_2(m) = \begin{pmatrix} 1 & -2 & 1 & 0 & 0 & \cdots & 0 \\ 0 & 1 & -2 & 1 & 0 & \cdots & 0 \\ \cdots & \cdots & \cdots & \cdots & \cdots & \cdots & \cdots \\ 0 & 0 & \cdots & 0 & 1 & -2 & 1 \end{pmatrix}. \tag{7.24}$$

We solve the system of equations (7.21) using a Gaussian elimination method to obtain the first-order time derivatives for the temperature, $\frac{\partial T}{\partial t}(y_i, t)$, at every space point y_i, $i = \overline{1, N_0}$. For the choice of the regularization parameter λ_k we employ the L-curve method, see Hansen [56].

Figure 7.2 presents the L-curves, for order$-k \in \{0,1,2\}$ Tikhonov regularization

linear systems of equations, defined in (7.21), that are used to determine the time derivative $\frac{\partial T}{\partial t}(y_1, t)$ at the fixed space point y_1. As it can be seen from Figure 7.2, the L-curve method does apply for choosing the Tikhonov regularization parameter in the cases of order-0 and order-1 regularizations, but it does not apply for the order-2 regularization, although the results obtained with order-2 regularization, for values of λ_2 larger than 10^{-1}, are actually very good, and even better that the ones obtained with the order-1 regularization, see Figures 7.3(b) and 7.3(c). Regarding the order-0 regularization, one may observe that although the L-curve method does apply for choosing the parameter λ_0, see Figure 7.2(a), the results obtained are relatively poor in comparison to the one obtained with the order-1 and -2 Tikhonov regularization approaches.

The situation is very similar when computing the first-order time derivative $\frac{\partial T}{\partial t}(y_i, t)$ at all the other y_i, $i = \overline{2, N_0}$, so that values for the parameter λ_k for the order$-k \in \{0, 1, 2\}$ Tikhonov regularizations, that were chosen for the approximation of $\frac{\partial T}{\partial t}(y_1, t)$, are kept unchanged and applied also for these cases.

7.4.2 Approximating the Second-order Space Derivative

For any $j = \overline{1, N}$, let us denote $\phi_{t_j}(x) := T(x, t_j) - (1-x)f_1(t_j) - xf_2(t_j)$. Then from (7.3) we have $\phi_{t_j}(0) = \phi_{t_j}(1) = 0$. Also, $\phi''_{t_j}(x) = \frac{\partial^2 T}{\partial x^2}(x, t_j)$. Then, as described in Collins et al. [32], $\phi''_{t_j}(x)$ can be regarded as the solution of the following Fredholm first-kind integral equation:

$$\phi_{t_j}(x) = \int_0^1 k_2(x, s)\phi''_{t_j}(s)ds, \qquad x \in [0, 1] \tag{7.25}$$

where the Green's function $k_2(x,s)$ is given by

$$k_2(x,s) = \begin{cases} s(x-1), & s < x \\ x(s-1), & x \le s. \end{cases} \tag{7.26}$$

We approximate the right hand side of the integral equation (7.25) as

$$\phi_{t_j}(x) = \int_0^1 k_2(x,s)\phi''_{t_j}(s)ds \approxeq \sum_{i=1}^{N_0} \phi''_{t_j}(y_i) \int_{x_{i-1}}^{x_i} k_2(x,s)ds, \tag{7.27}$$

where the coefficients $\int_{x_{i-1}}^{x_i} k_2(x,s)ds$ have the following analytical expressions:

$$\int_{x_{i-1}}^{x_i} k_2(x,s)ds = \begin{cases} x\left(\frac{x_i^2}{2} - x_i - \frac{x_{i-1}^2}{2} + x_{i-1}\right), & x \le x_{i-1} \\ (x-1)\left(\frac{x^2 - x_{i-1}^2}{2}\right) + x\left(\frac{x_i^2 - 2x_i}{2} - \frac{x^2 - 2x}{2}\right), & x_{i-1} < x < x_i \\ (x-1)\left(\frac{x_i^2 - x_{i-1}^2}{2}\right), & x_i \le x. \end{cases} \tag{7.28}$$

By applying the equation (7.27) for each y_l, $l = \overline{1, N_0}$, we obtain system of equations whose $N_0 \times N_0$-matrix B is given by

$$B_{li} = \int_{x_{i-1}}^{x_i} k_2(y_l, s)ds, \qquad l, i = \overline{1, N_0}, \tag{7.29}$$

and the N_0-dimensional right-hand side measurement vector $\{\overline{G}_2^{\alpha}(y_l, t_j)\}_{l=\overline{1,N_0}}$ given by

$$\overline{G}_2^{\alpha}(y_l, t_j) := e^{-y_l - t_j}(2t_j + y_l^2 + 4)(1 + \alpha\eta) - (1 - y_l)e^{-t_j}(2t_j + 4) - y_l e^{-t_j - 1}(2t_j + 5),$$
$$l = \overline{1, N_0}. \tag{7.30}$$

For the induced ill-conditioned linear system of equations, given the inherited instability of the Fredholm first-kind integral equation, and because the right-hand side vector is affected by noise, a solution is sought using order-$k \in \{0, 1, 2\}$ Tikhonov regularization, namely

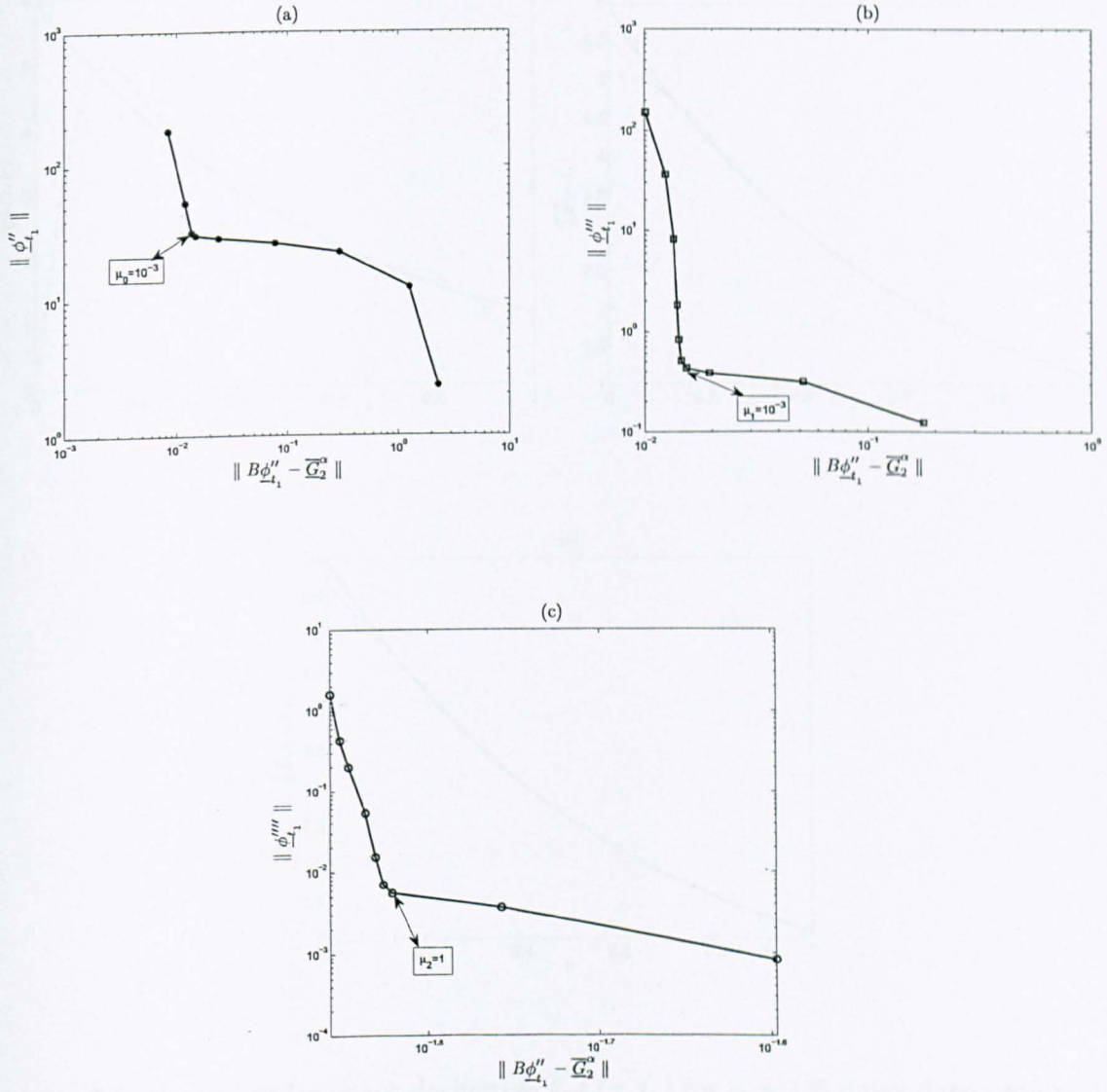

Figure 7.4: L-curves for the second-order space derivative approximation with $\alpha =$ 1% noisy temperature measurements for: (a) order-0, (b) order-1, and (c) order-2, Tikhonov regularizations.

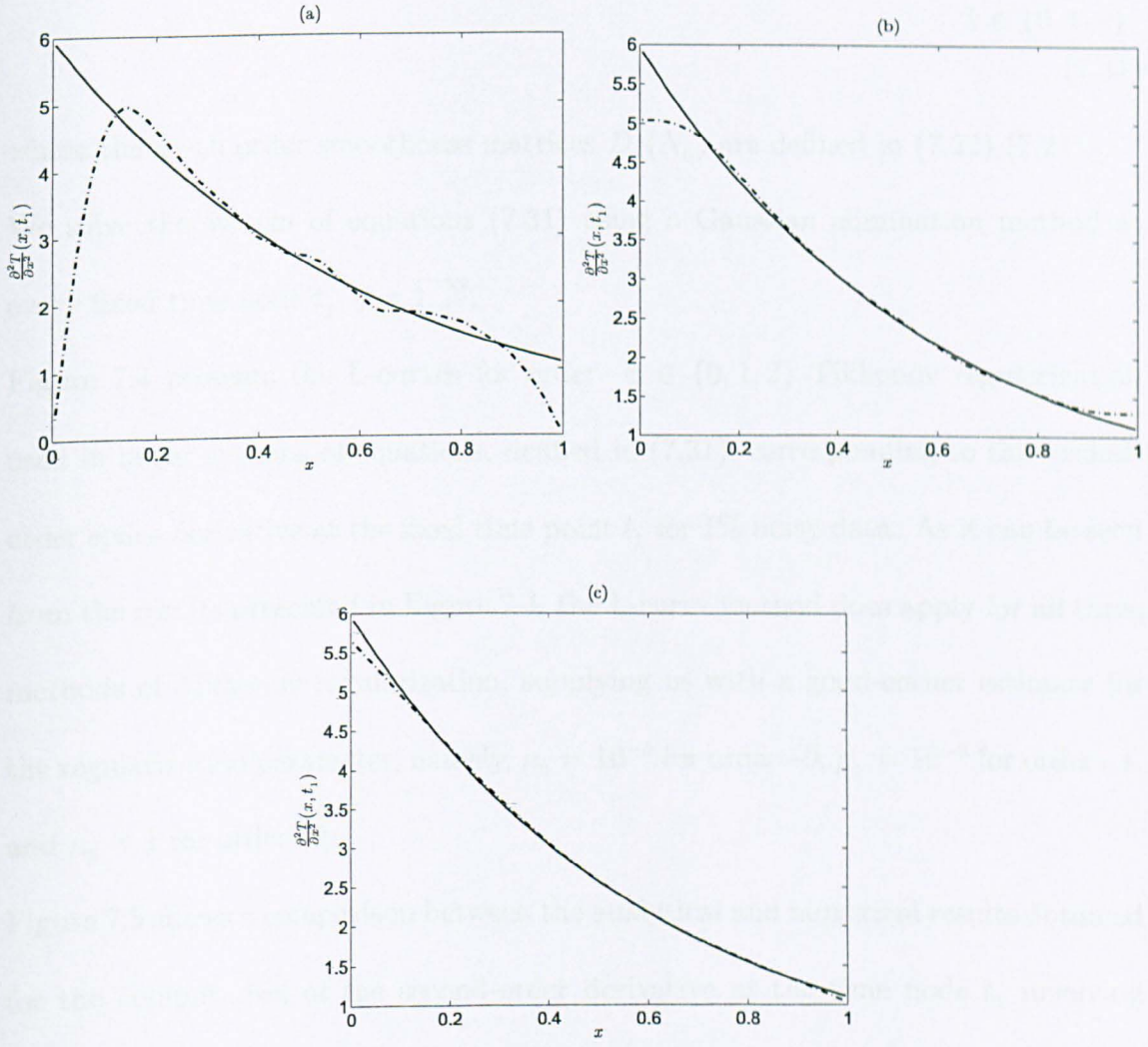

Figure 7.5: Second-order space derivative $\frac{\partial^2 T}{\partial x^2}(x, t_1)$ for $\alpha = 1\%$ noisy data obtained using: (a) order-0 Tikhonov regularization with $\mu_0 = 10^{-3}$, (b) order-1 Tikhonov regularization with $\mu_1 = 10^{-3}$, and (c) order-2 Tikhonov regularization with $\mu_2 = 1$. Dash-dot line represents the computed results, while the solid line stands for the analytical solution.

$$\left[B^{tr}B+\mu_k D_k(N_0)^{tr}D_k(N_0)\right]\left[\phi''_{y_1}(t_j),...,\phi''_{y_{N_0}}(t_j)\right]^{tr}=B^{tr}\left[\overline{G}^{\alpha}_2(y_1,t_j),...,\overline{G}^{\alpha}_2(y_{N_0},t_j)\right]^{tr},$$

$$k\in\{0,1,2\},\tag{7.31}$$

where the $k-$th order smoothness matrices $D_k(N_0)$ are defined in (7.22)-(7.24). We solve the system of equations (7.31) using a Gaussian elimination method at every fixed time node t_j, $j=\overline{1,N}$.

Figure 7.4 presents the L-curves for order$-k\in\{0,1,2\}$ Tikhonov regularization used in linear systems of equations, defined in (7.31), corresponding to the second-order space derivative at the fixed time point t_1 for 1% noisy data. As it can be seen from the results presented in Figure 7.4, the L-curve method does apply for all three methods of Tikhonov regularization, supplying us with a good-corner estimate for the regularization parameter, namely, $\mu_0=10^{-3}$ for order-0, $\mu_1=10^{-3}$ for order-1, and $\mu_2=1$ for order-2.

Figure 7.5 shows a comparison between the analytical and numerical results obtained for the computation of the second-order derivative at the time node t_1 involving order-0, order-1, and order-2 Tikhonov regularization that use the parameters identified by the L-curve method shown in Figure 7.4, when 1% noise is added in the measured data. Although satisfying the L-curve criterion, the results obtained for order-0 regularization, as shown in Figure 7.5(a) are poorer than the results obtained both with order-1 and -2 regularizations, illustrated in Figures 7.5(b) and 7.5(c), respectively. As we may note, out of the three Tikhonov regularization approaches, the best results are obtained using order-2, shown in Figure 7.5(c), with the L-curve chosen parameter $\mu_2=1$.

7.4.3 Perfusion Reconstruction Results

In this subsection we compute the perfusion coefficient, for the inverse problem given by equations (7.1), (7.7), (7.8) and (7.13) using the techniques developed in subsections 7.4.1 and 7.4.2 for computing the first-order time derivative and the second-order space derivative, respectively.

For the computation of the first-order time derivatives, $\frac{\partial T}{\partial t}(y_i, t)$, $i = \overline{1, N_0}$, we use the order-1 Tikhonov regularization with the parameter $\lambda_1 = 1$ that was chosen from Figure 7.2(b). The second-order space derivatives, $\frac{\partial^2 T}{\partial x^2}(x, t_j)$, $j = \overline{1, N}$ are computed using order-2 Tikhonov regularization with the parameter $\mu_2 = 1$ that was chosen from Figure 7.4(c). Then, the values of the space- and time-dependent perfusion coefficient P_f, at the grid points $\{(y_i, t_j)\}_{i=\overline{1,N_0}, j=\overline{1,N}}$, are given by the formula

$$P_f(y_i, t_j) = \frac{\frac{\partial^2 T}{\partial x^2}(y_i, t_j) - \frac{\partial T}{\partial t}(y_i, t_j)}{G_2^{\alpha}(y_i, t_j)}, \qquad i = \overline{1, N_0},\ j = \overline{1, N}, \tag{7.32}$$

provided that G_2^{α} stays away from zero. From (7.10) we have that this is the case in our numerical example. However, if, in a different example, zero points for G_2^{α} do occur, then (7.32) should be understood in the limit sense by applying the l'Hospital rule.

Figure 7.6 presents the contour plots for the numerical results for $P_f(x, t)$ in comparison with the exact solution (7.10), when using the $\alpha = 1\%$ noisy measurements (7.19). While Figure 7.6(a) illustrates the exact solution, in Figure 7.6(b) we show the results obtained numerically via the local method described in subsections 7.4.1-7.4.3 that represents a good and reasonably stable approximation of the space- and time- dependent perfusion coefficient $P_f(x, t)$. The numerical approxi-

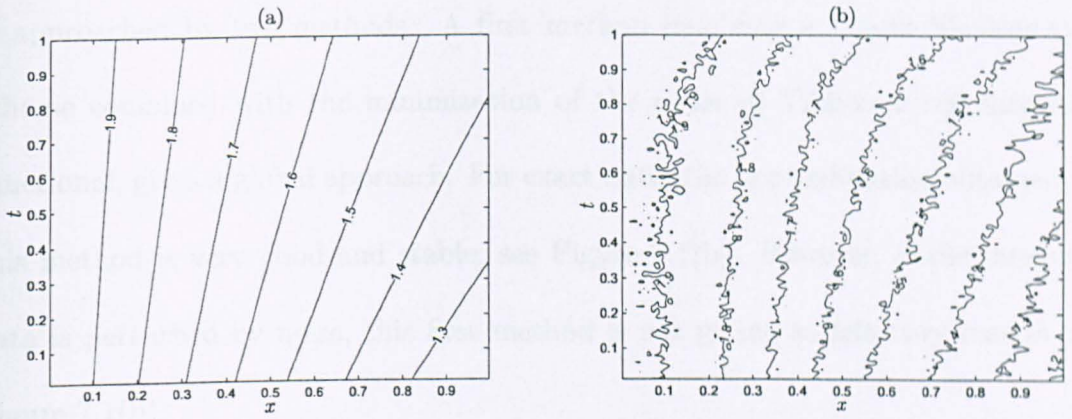

Figure 7.6: Contour plots for $P_f(x,t)$: (a) exact solution (7.10), and (b) numerical solution (7.32) for 1% noise.

mation of $P_f(x,t)$ carried out in subsections 7.4.1-7.4.3 is also placed in a favourable contrast when compared to the numerical approximation obtained in Section 7.3 that is shown in Figure 7.1(c). We immediately observe that the numerical approximation obtained via the local method, using Fredholm integral equations, that was developed in subsections 7.4.1-7.4.3, is more accurate than the one obtained via the global Tikhonov regularization in Section 3.

7.5 Conclusions

This chapter has investigated the reconstruction of the space- and time- dependent perfusion coefficient $P_f(x,t)$ in the bio-heat conduction equation, under supplied initial and boundary temperature conditions, when additional information is provided in terms of exact and noisy temperature measurements in the $x \times t-$region at a resolution imposed by the discretization chosen on the boundary. The problem

is approached by two methods. A first method involving a Crank-Nicolson-type scheme combined with the minimization of the order-0 Tikhonov regularization functional, gives a global approach. For exact data, the approximation obtained via this method is very good and stable, see Figure 7.1(b). However, if the measured data is perturbed by noise, this first method is not giving satisfactory results, see Figure 7.1(b).

For the case with noise, we design a second and local approach, in which two first-kind Fredholm integral equations are used to compute the first-order time derivative and the second-order space derivative, at every fixed space point and in every fixed time node, respectively. In the process of solving these first-kind integral equations, we use order$-k \in \{0, 1, 2\}$ Tikhonov regularization and apply the L-curve criterion to choose the regularization parameter. The numerical results obtained via the local method are better that the ones obtained using the global method and represent a good and stable approximation of the perfusion coefficient.

Chapter 8

Conclusions and Future Work

8.1 Conclusions

The central focus of this work consists of finding new ways in which the blood perfusion can be identified and characterized. Since the perfusion information is encapsulated in the coefficient P_f of the linear term in the transient bio-heat conduction equation (BHCE), the entire investigation is mathematically formulated and placed in the class of inverse problems regarding the retrieval of this parameter. While initial and boundary conditions are prescribed, additional information given in terms of temperature, mass, or heat flux measurements, is supplied at minimally physically damaging locations within the region of interest or on its boundary. All these measurements are assumed to be both exact and noisy.

We have organized our investigation on five major cases, namely for P_f considered as being: constant, time-dependent, space-dependent, temperature-dependent, and time- and space- dependent.

In the constant coefficient case, we started our investigation by developing a new

direct Boundary Element Method (BEM) solver for the forward problem. Unlike the standard approach, which, via a change of variable, transforms first the bio-heat equation in the standard heat equation and then apply BEM, in the proposed approach the BEM is constructed directly for the BHCE. The numerical tests considered reveal quadratic convergence for the new method, as well as a good agreement with the results obtained via the standard method.

The analysis for the inverse problem related to the determination of the constant perfusion coefficient is started by developing a theoretical framework that discusses the existence and uniqueness of the solution. For this inverse problem, the additional information is supplied either as a measurement of the flux, or of the internal temperature taken at one single space point and one single instance in time, or as a time mass measurement considered at a fixed time. The existence of the unique solution associated to the inverse problem is proved to be equivalent to finding P_f as the unique positive solution of an induced nonlinear algebraic equation. Once the perfusion coefficient is identified, the temperature solution is found analytically by using the fundamental solution of the heat equation.

When homogeneous boundary conditions are assumed, the stability is proved to be of logarithmic type.

Assuming arbitrary initial and boundary conditions, the BEM is used to compute the constant P_f, for each of the three types of additional information considered. We have found that the numerical results are accurate and stable under noisy input data.

In the time-dependent case, the perfusion coefficient $P_f(t)$ is sought under the presence of initial and both Dirichlet and mixed boundary conditions, when measure-

ments for either the flux on parts of the boundary, or the temperature at a fixed or moving internal point, or total or partial mass data, are considered.

When the Dirichlet boundary conditions are assumed, and either internal temperature data at a fixed point or total mass measurements are supplied, the existing uniqueness conditions are satisfied. However, since in the flux measurement case there were no uniqueness results previously proved, we formulated and proved an uniqueness criterion which equivalently expresses the uniqueness for the solution of the time-dependent inverse problem in terms of a unique zero for an analytically induced functional.

On the computational side, we have developed a numerical method for the identification of $P_f(t)$ that approaches globally all the types of boundary conditions and measurements considered. In the first stage, the BEM is implemented for this time-dependent inverse problem. Since the measurements are affected by random noise, we used Gaussian mollification to obtain the derivatives of the induced noisy functions. For exact measurements, the numerical tests show an almost exact match between the computed and analytical values. Also, a reasonable approximation of the analytical values is obtained in the case when the measurements are affected by random noise. From the way this numerical method has been built, we immediately notice that it can easily be extended and applied to higher dimensional cases of this time-dependent inverse identification problem.

For the space-dependent perfusion coefficient case, the identification of $P_f(x)$ is carried out in the presence of either Neumann or Dirichlet boundary conditions.

When Neumann boundary conditions are assumed, exact and noisy boundary temperature measurements are considered. The numerical method developed for the

retrieval of $P_f(x)$ consists of two parts. In the first stage, a Crank-Nicolson type finite difference method is developed. This forward solver is then coupled in the second stage with an optimization routine, which performs a search over the class of $\mathscr{C}^k$ functions in order to minimize the nonlinear order$-k$ Tikhonov regularization functional, $k = \overline{0,1}$. The numerical tests performed with both exact and noisy data show that order-1 regularization, where the results obtained are stable and accurate, behaves better than order-0 regularization, for all the values of the regularization parameter λ. Moreover, since the numerical tests were performed with temperature measurements taken on each of three types of time intervals $[0, t_f]$, for $t_f \in \{1, 2, 4\}$, we remark, as expected, that better results are obtained for larger values of t_f.

For the case when Dirichlet boundary conditions are involved, two inverse problems are defined by the two types of additional information considered, namely the measurements available are either the flux over the boundary or the time-averaged temperature data across the region of interest. For the numerical approximation of $P_f(x)$, the methods developed for the two inverse problems are very similar and follow the structural path pursued in the case of Neumann boundary conditions case. Thus, once an appropriate Crank-Nicolson-type solver is developed for the direct problem, then this is linked to a gradient based optimization routine which finds $P_f(x)$ as the minimum point of the order-1 Tikhonov regularization functional, by carrying out a search over all the positive functions from $\mathscr{C}^1([0, 1])$. The discrepancy principle was applied for choosing the regularization parameter λ. The numerical results obtained represent a good and stable approximation of the space-dependent coefficient $P_f(x)$.

In the temperature-dependent case, subject to initial and Neumann boundary conditions, the retrieval of the perfusion coefficient $P_f(T)$ is performed under the presence of a source term $\Sigma(x,t)$, when the additional information is provided in terms of both exact and noisy temperature measurements on a part of the boundary. The investigation is carried out on two major inverse problems, IP1 and IP2, that are defined by the cases when $\Sigma \not\equiv 0$ and $\Sigma \equiv 0$, respectively. Analytical results concerning the solution of the inverse problems IP1 and IP2 are presented and discussed. A new theoretical result concerning the direct problem associated to IP1 is stated and proved. This result, not only that gives a structural characterization of the solution for the direct problem associated to IP1 by proving that, for any arbitrary instance in time $t \in (0, t_f]$, $T(\cdot, t)$ monotonically decreases with respect to space, but also ensures that the maximum range of the function T is achieved along the measurement path, *i.e.* at the left boundary, which is of key importance in the development of the direct solver within the computational approach.

The two inverse problem are solved via two methods, which are very similar, that, in essence, consist of two parts. In the first routine, a direct solver incorporating a Crank-Nicolson-type finite difference scheme, which is combined with an extrapolation technique, is developed. This routine is then linked with an gradient based optimization subroutine where an order-1 Tikhonov regularization functional is minimized, which provides us with an optimal polygonal approximation of $f(T)$ and its corresponding temperature values. The regularization parameter λ is chosen via the discrepancy principle. The ratio between this optimal approximation of $f(T)$ and the corresponding temperature values provides us with an accurate and stable approximation of the temperature-dependent perfusion coefficient $P_f(T)$, when both

exact and noisy measurements are considered.

Finally, the investigation concerning the retrieval of the space- and time- dependent perfusion coefficient $P_f(x,t)$ is carried out under specified initial and boundary conditions, when exact and noisy temperature measurements are provided at a fixed grid inside the $x \times t-$region. The problem is investigated via both a global and a local method. In the first approach, the global method, which combines a Crank-Nicolson-type scheme with a minimization procedure for a order-0 Tikhonov regularization functional, provides results that are very good and stable for exact measurements. However, if the measured data are affected by noise, then the results are not satisfactory. This situation led us to pursue a second approach for the noisy case. In this approach we compute locally the first-order time derivative at every fixed space point, and the second-order space derivative at every fixed time node, by using two first-kind integral equations. In order to solve these integral equations we use order$-k \in \{0,1,2\}$ Tikhonov regularization. The regularization parameters are chosen via the L-curve criterion. The numerical results obtained via this local method are a good and stable approximation of the perfusion coefficient $P_f(x,t)$.

The backward medical importance effect offered by the inverse investigation of perfusion identification problem is underlined by a variety of aspects and clinical situations. In order to illustrate a few of these cases, where the inverse problems investigations produce valuable assistance, let us discuss some clinical situation when a certain part of the human body tissue has to be heated above the average body temperature of $37°C$. This is a situation that occurs in various medical instances, e.g. in certain types of cancer, such as the skin cancer. In these cases, medical devices are used to heat up the tissue. However, since, in the medical practice,

it is well known that temperatures higher that $42°C$ cause necrosis of the living cells, the heat should be applied only on the tumor, while the destruction of the surrounding healthy tissue should be avoided as much as possible. Therefore, a calibration of the device only on the cancer tumor becomes an absolute necessity. An answer to this problem can be given via perfusion identification. Given the fact that the blood perfusion within the inside of the cancer tumor is abruptly different from that in the surroundings, a retrieval of this information becomes of a significant importance in helping to gradually adjust the device to precisely only on the affected region. For doing this, a preliminary iterative procedure can be designed to position the device. In the first step, in relatively bigger region Ω_2, an arbitrarily chosen subregion Ω_1, with $\Omega_1 \subset \Omega_1^\varepsilon \subset \Omega_2$, is heated up to a safe temperature $<< 42°C$ during a time period t_f, where, for a small $\varepsilon > 0$, Ω_1^ε is the $\varepsilon-$bundle of Ω_1, namely $\Omega_1^\varepsilon := \{y \in \Omega_2 | (\exists) x \in \Omega_1$ such that $|x-y| \leq \varepsilon\}$. Then we can immediately distinguish that in the larger region Ω_2 at least the following three type of inverse problems appear, namely: (a) on $\Omega_2 \setminus \Omega_1^\varepsilon$ a time-dependent inverse problem, (b) on $\Omega_1^\varepsilon \setminus \Omega_1$ a space- and time- dependent inverse problem, and (c) on Ω_1 a temperature-dependent inverse problem. Using the analytical and computational techniques developed in this thesis, we solve the three inverse problems and identify the perfusion. If a large disruption in the perfusion occurs in the space- and time-dependent zone, Ω_1^ε, then we record that position. Then the region Ω_1 will be varied in size and moved around in Ω_2 so that we cover all positions in Ω_2. Each time when a disruption occurs in the corresponding Ω_1^ε, then this is recorded. In this way we manage to map the perfusion of the entire area and moreover, to have a complete picture containing all the perfusion disruptions, which allow us to localize the cancer

cells and to calibrate the device that will be used after this preliminary strategy is complete. In this preliminary procedure, the advantage of the process of heating of the moving variable size region Ω_1, over the time period t_f, is that the disruptions in the perfusion that occur between the cancer and non-cancer areas become more visible than in the normal state when the tissue is at the normal body temperature and when many parts of these tumors may even not be visible at all. This allows the procedure to localize these areas with a better precision so that all of them would receive appropriate treatment, while minimal damage would have been produced in the healthy region.

Another very frequent medical situation where the knowledge of the perfusion information is of ultimate importance occur when transplant organs needs to be transported or stored between the moment when they are donated up to the time when they are inserted in the new transplant receiver patient. Further, the blood perfusion monitoring remains important even after the transplant is made, and should continue up until the body fully accepts the implant. During all the storage time the physiological properties of the organ are dependent on a appropriate perfusion rate that allows the nutrients to keep the tissue alive. Depending on the shape of the storage container and also on the type of the organ, the perfusion monitoring problem can be expressed as a combination of time, space, space and time, and temperature dependent inverse problems. The computational techniques developed for solving these inverse problems are used to monitor and maintain the physiological balance of the transplant organ during its storage.

Finally, it is worth mentioning that the measuring instruments design and methodology are benefiting as well from the inverse problems investigation of the blood

perfusion. The ability of the developed techniques to extract valuable perfusion information from noisy data offers the design engineers the possibility of creating simpler shapes and yet more minimally invasive instruments, which would be able to learn, adapt their measurements, and adjust their output along the way, by either performing yet fewer and less invasive measurements than the existing minimally invasive instruments, or obtaining a better accuracy than the level achieved with the existing ones.

8.2 Future Work

A first priority is represented by the following inverse problem:

In the presence of Neumann boundary and initial data, from temperature measurements taken on the entire boundary, we aim to reconstruct the space- and temperature- dependent perfusion coefficient $P_f(x,T)$, see Nanda and Das [74], where, initially, we will only consider an affine dependence on space, namely

$$P_f(x,T) = (1-x)f_1(T) + xf_2(T), \tag{8.1}$$

which satisfies the BHCE

$$\frac{\partial T}{\partial t}(x,t) = \frac{\partial^2 T}{\partial x^2}(x,t) - P_f(x,t)T(x,t) + \Sigma(x,t), \qquad (x,t) \in (0,1) \times (0,t_f). \tag{8.2}$$

Then, this problem will be continued with an analytical and computational investigation of the case when $P_f(x,T)$ is of separable form, namely

$$P_f(x,T) = f_1(x)f_2(T). \tag{8.3}$$

After that, the investigation will move to two- and three-dimensional cases for inverse coefficient identification problems where P_f will be considered as either space

dependent, or space and time dependent, or temperature dependent.

In the temperature-dependent case, the analytical result characterizing the structure of the solution, from Chapter 6, will be sought in the $n-$dimensional case.

All these cases will later be revisited for an ample investigation in random heterogeneous media, in an attempt to answer complex questions arising in the fields of medical imaging, computational biology and material science.

Appendix A

Analytical Expression for a Couple of Special Integrals

A.1 An Important Primitive

We show that for $\alpha \geq 0$ and $\beta > 0$

$$\begin{aligned} I_{\alpha,\beta} &= \int e^{-\frac{\alpha}{t^2}-\beta t^2} dt \\ &= \frac{\sqrt{\pi}}{4\sqrt{\beta}} \left(e^{2\sqrt{\alpha\beta}} erf\left(\sqrt{\beta}t + \frac{\sqrt{\alpha}}{t}\right) + e^{-2\sqrt{\alpha\beta}} erf\left(\sqrt{\beta}t - \frac{\sqrt{\alpha}}{t}\right)\right) + C. \end{aligned} \tag{A.1}$$

Proof: Let us notice first that by using the substitution $\xi(t) = \sqrt{\beta}t + \frac{\sqrt{\alpha}}{t}$ we obtain that $-\beta t^2 - \frac{\alpha}{t^2} = -\xi^2 + 2\sqrt{\alpha\beta}$ and $dt = \frac{d\xi}{\sqrt{\beta}} + \frac{\sqrt{\alpha}}{\sqrt{\beta}t^2} dt$.

Therefore

$$\begin{aligned} I_{\alpha,\beta} &= \int \exp(-\xi + 2\sqrt{\alpha\beta}) \left(\frac{d\xi}{\sqrt{\beta}} + \frac{\sqrt{\alpha}}{\sqrt{\beta}t^2} dt \right) \\ &= \frac{\exp(2\sqrt{\alpha\beta})}{\sqrt{\beta}} \int \exp(-\xi^2) d\xi + \frac{\sqrt{\alpha}}{\sqrt{\beta}} \int \frac{\exp(-\xi^2 + 2\sqrt{\alpha\beta})}{t^2} dt \\ &= \frac{\sqrt{\pi}\exp(2\sqrt{\alpha\beta})}{2\sqrt{\beta}} erf(\xi) + \frac{\sqrt{\alpha}}{\sqrt{\beta}} \int \frac{\exp(-\xi^2 + 2\sqrt{\alpha\beta})}{t^2} dt \\ &= \frac{\sqrt{\pi}\exp(2\sqrt{\alpha\beta})}{2\sqrt{\beta}} erf\left(\sqrt{\beta} + \frac{\sqrt{\alpha}}{t} \right) + \frac{\sqrt{\alpha}\exp(2\sqrt{\alpha\beta})}{\sqrt{\beta}} \int \frac{1}{t^2} \exp\left[-\left(\sqrt{\beta}t + \frac{\sqrt{\alpha}}{t} \right)^2 \right] dt \\ &= \frac{\sqrt{\pi}\exp(2\sqrt{\alpha\beta})}{2\sqrt{\beta}} erf\left(\sqrt{\beta} + \frac{\sqrt{\alpha}}{t} \right) + \frac{\sqrt{\alpha}}{\sqrt{\beta}} \int \frac{1}{t^2} \exp\left(-\beta t^2 - \frac{\alpha}{t^2} \right) dt. \end{aligned} \tag{A.2}$$

On the other hand, if we use the substitution $\eta = \sqrt{\beta}t - \frac{\sqrt{\alpha}}{t}$ we obtain that $-\beta t^2 - \frac{\alpha}{t^2} = -\eta^2 - 2\sqrt{\alpha\beta}$ and $dt = \frac{d\eta}{\sqrt{\beta}} - \frac{\sqrt{\alpha}}{\sqrt{\beta}t^2} dt$.

Therefore,

$$\begin{aligned} I_{\alpha,\beta} &= \int \exp\left(-\eta^2 - 2\sqrt{\alpha\beta} \right) \left(\frac{d\eta}{\sqrt{\beta}} - \frac{\sqrt{\alpha}}{\sqrt{\beta}t^2} dt \right) \\ &= \frac{\exp(-2\sqrt{\alpha\beta})}{\sqrt{\beta}} \int \exp(-\eta^2) d\eta - \frac{\sqrt{\alpha}}{\sqrt{\beta}} \int \frac{\exp(-\eta^2 - 2\sqrt{\alpha\beta})}{t^2} dt \\ &= \frac{\sqrt{\pi}\exp(-2\sqrt{\alpha\beta})}{2\sqrt{\beta}} erf\left(\sqrt{\beta}t - \frac{\sqrt{\alpha}}{t} \right) - \frac{\sqrt{\alpha}}{\beta} \int \frac{1}{t^2} \exp\left(-\beta t^2 - \frac{\alpha}{t^2} \right) dt. \end{aligned} \tag{A.3}$$

By adding up equations (A.2) and (A.3) and then dividing by two, we obtain the claimed identity (A.1).

□

Bibliography

[1] Abramowitz M and Stegun I A 1964 *Handbook of Mathematical Functions with Formulas, Graphs, and Mathematical Tables* **55** (Washington: National Bureau of Standards, Applied Mathematics Series).

[2] Anderson G T and Burnside G 1990 A Noninvasive Technique to Measure Perfusion Using a Focused Ultrasound Heating Source and a Tissue Surface Temperature Measurement, *Advances in Measuring and Computing Temperatures in Biomedicine: Thermal Tomography Techniques, Bioheat Transfer Models*, 31-36, eds. Valvano J W, Hayes J, Roemer R B and Anderson J T (New York: ASME).

[3] Adrian R J and Borgos J A 1990 Laser Doppler Flow Monitor, U.S. patent 4.596.254, 1986, *Laser-Doppler Blood Flowmetry*, eds. Shepherd A P and Oberg P A (Dordrecht: Kluwer Academic).

[4] Azari H 2002 Numerical procedures for the determination of an unknown coefficient in parabolic differential equations, *Dynamics of Continuous, Discrete and Impulsive Systems, Series B: Applications & Algorithms* **9**, 55-573.

[5] Baran E C 2005 Numerical procedures for determining of an unknown parameter in parabolic equation, *Applied Mathematics and Computation* **162**,

1219-1226.

[6] Baran E C and Fatullayev A G 2004 Determination of an unknown source parameter in two-dimensional heat equation, *Applied Mathematics and Computation* **159**, 881-886.

[7] Brebbia C A, Telles J C F and Wrobel L C 1984 *Boundary Element Techniques: Theory and Application in Engineering* (Berlin: Springer-Verlag).

[8] Bowman H F, Cravalho E G and Woods M 1975 Theory, measurement and application of thermal properties of biomaterials, *Annual Review of Biophysics and Bioengineering* **4**, 43-80.

[9] Bowman H F 1985 Estimation of Tissue Blood Flow, *Heat Transfer in Medicine and Biology* **1**, 193-230, eds. Schitzer A and Eberhart R C (New York: Plenum Press).

[10] Cannon J R 1964 Determination of certain parameters in the heat conduction, *Journal of Mathematical Analysis and Applications* **8**, 188-201.

[11] Cannon J R 1984 *The One-Dimensional Heat Equation* (Menlo Park: Addison-Wesley).

[12] Cannon J R and DuChateau P 1980 An inverse problem for an unknown source in a heat equation, *Journal of Mathematical Analysis and Applications* **75**, 465-485.

[13] Cannon J R and DuChateau P 1998 Structural identification of an unknown source term in a heat equation, *Inverse Problems* **14**, 535-551.

[14] Cannon J R and Lin Y 1988 Determination of a parameter $p(t)$ in some quasi-linear parabolic differential equations, *Inverse Problems* **4**, 35-45.

[15] Cannon J R and Lin Y 1988 Determination of parameter $p(t)$ in Holder classes for some semilinear parabolic equations, *Inverse Problems* **4**, 595-606.

[16] Cannon J R and Lin Y 1990 An inverse problem of finding a parameter in a semi-linear heat equation, *Journal of Mathematical Analysis and Applications* **145**, 470-484.

[17] Cannon J R, Lin Y and Wang S 1991 Determination of a control parameter in a parabolic partial differential equation, *Journal of the Australian Mathematical Society, Series B* **33**, 149-163.

[18] Cannon J R, Lin Y and Wang S 1992 Determination of source parameter in parabolic equations, *Meccanica* **27**, 85-94.

[19] Cannon J R, Lin Y and Xu S 1994 Numerical procedures for determination of an unknown coefficient in semi-linear parabolic differential equations, *Inverse Problems* **10**, 227-243.

[20] Cannon J R and Yin H-M 1989 A class of non-linear non-classical parabolic equations, *Journal of Differential Equations* **79**, 266-288.

[21] Cannon J R and Yin H-M 1990 Numerical solutions of some parabolic inverse problems, *Numerical Methods for Partial Differential Equations* **2**, 177-191.

[22] Cardinali A V, Diller T E, Lanz O and Scott E P 2002 Validation of a noninvasive thermal perfusion system using a canine medial saphenous fasciocutaneous

free tissue flap model, *Proc. of IMECE'02, ASME Int. Mechanical Engineering Congress & Exposition*, November 17-22, 2002, New Orleans, Louisiana (Paper No. IMECE2002-32354).

[23] Castellana F S, Skalak R, Cho J M and Case R B 1983 Steady-state analysis and evaluation of a new thermal sensor for surface measurements of tissue perfusion, *Annals of Biomedical Engineering* **11**, 101-115.

[24] Chan C L 1992 Boundary element method analysis for the bioheat transfer equation, *Transactions of the ASME Journal of Biomechanical Engineering* **114**, 358-365.

[25] Chato J C 1990 *Fundamentals of Bioheat Transfer* (Berlin: Springer-Verlag).

[26] Chato J C 1985 Measurements of Thermal Properties of Biological Materials, *Heat Transfer in Medicine and Biology* **1**, 93-122, eds. Schitzer A and Eberhart R C (New York: Plenum Press).

[27] Chen Q and Liu J 2006 Solving an inverse parabolic problem by optimization from final measurement data, *Journal of Computational and Applied Mathematics* **193**, 183-203.

[28] Choulli M 1994 An inverse problem for a semilinear parabolic equation, *Inverse Problems* **10**, 1123-1132.

[29] Choulli M and Yamamoto M 1996 Generic well-posedness of an inverse parabolic problem - the Holder-space approach, *Inverse Problems* **12**, 195-205.

[30] Choulli M and Yamamoto M 1997 An inverse parabolic problem with non-zero initial condition, *Inverse Problems* **13**, 19-27.

[31] Choulli M and Yamamoto M 2004 Stable identification of a semilinear term in a parabolic equation (preprint LMAM 2004-01).

[32] Collins W D, Kanval J, Quegan S, Smith D and Taylor D A W 1997 A regularization method for calculating engineering loads from strain data, *Inverse Problems in Science and Engineering* **4**, 271-294.

[33] Cui Z F and Barbenel J C 1991 The influence of model parameter values on the prediction of skin surface temperature: II Contact problems, *Physics in Medicine and Biology* **36**, 1607-1620.

[34] Dahlquist G and Bjorck A 1974 *Numerical Methods* (New Jersey: Prentice-Hall).

[35] Dehghan M 2001 An inverse problem of finding a source parameter in a semilinear parabolic equation, *Applied Mathematical Modelling* **25**, 743-754.

[36] Dehghan M 2001 Implicit solution of a two-dimensional parabolic inverse problem with temperature overspecification, *Journal of Computational Analysis and Applications* **3**, 383-398.

[37] Dehghan M 2001 New schemes for a two-dimensional inverse problem with temperature overspecification, *Mathematical Problems in Engineering* **7**, 283-297.

[38] Dehghan M 2001 Crank-Nicolson finite difference method for two-dimensional diffusion with an integral condition, *Applied Mathematics and Computation* **124**, 17-27.

[39] Dehghan M 2002 Fourth-order techniques for identifying a control parameter in the parabolic equations, *International Journal of Engineering Science* **40**, 433-447.

[40] Dehghan M 2003 Finding a control parameter in one-dimensional parabolic equations, *Applied Mathematics and Computation* **135**, 491-503.

[41] Dehghan M 2003 Determination of a control function in three-dimensional parabolic equations, *Mathematics and Computers in Simulation* **61**, 89-100.

[42] Dehghan M 2005 Parameter determination in a partial differential equation from the overspecified data, *Mathematical and Computer Modelling* **41**, 197-213.

[43] Dehghan M and Tatari M 2006 Determination of a control parameter in a one-dimensional parabolic equation using the method of radial basis functions, *Mathematical and Computer Modelling* **44**, 1160-1168.

[44] Deng Z-C, Yang L and Yu J-N 2009 Identifying the radiative coefficient of heat conduction equations from discrete measurement data, *Applied Mathematics Letters* **22**, 495-500.

[45] Deng Z-S and Liu J 2000 Parametric studies on the phase shift method to measure the blood perfusion of biological bodies, *Medical Engineering & Physics* **22**, 693-702.

[46] Denisov A M 1999 *Elements of the Theory of Inverse Problems* (Utrecht: VSP).

[47] DuChateau P and Rundell W 1985 Unicity in an inverse problem for an unknown reaction term in a reaction-diffusion equation, *Journal of Differential Equations* **59**, 155-164.

[48] Eberhart R C, Shitzer A and Hernandez E J 1980 Thermal dilution methods: estimation of tissue blood flow and methabolism, *Annals of New York Academy of Sciences, Thermal Characteristics of Tissue: Applications in Detection and Treatment* **335**, 107-132.

[49] Erhart K, Divo E and Kassab A 2008 An evolutionary-based inverse approach for the identification of non-linear heat generation rates in living tissues using a localized meshless method, *International Journal of Numerical Methods for Heat & Fluid Flow* **18**, 401-414.

[50] Fatullayev A G 2002 Numerical solution of the inverse problem of determining an unknown source term in a heat equation, *Mathematics and Computers in Simulation* **58**, 247-253.

[51] Fatullayev A G 2004 Numerical solution of the inverse problem of determining an unknown source term in a two-dimensional heat equation, *Applied Mathematics and Computation* **152**, 659-666.

[52] Fouquet Y, Hager J, Terrell J and Diller T 1993 Blood Perfusion Estimation from Noninvasive Heat Flux Measurements, *Advances in Bioheat and Mass Transfer: Microscale Analysis of Thermal Injury Processes, Instrumentation, Modeling, and Clinical Applications*, 53-60, ed. Roemer R B (New York: ASME).

[53] Friedman A 1964 *Partial Differential Equations of Parabolic Type* (New Jersey: Prentice-Hall).

[54] Hanke M and Scherzer O 2001 Inverse problems light: numerical differentiation, *American Mathematical Monthly* **108**, 512-521.

[55] Hartman P and Wintner A 1950 On the solution of the equations of heat conduction, *American Journal of Mathematics* **72**, 367-395.

[56] Hansen P C 2001 The L-curve and its Use in the Numerical Treatment of Inverse Problems, *Computational Inverse Problems in Electrocardiology*, 119-142, ed. Johnston P (Southampton: WIT Press).

[57] Holti G and Mitchell K W 1979 Estimation of the Nutrient Skin Blood Flow Using a Noninvasive Segmental Thermal Clearance Probe, *Non-Invasive Physiological Measurements*, **1**, 113-123, ed. Rolfe E P (London: Academic Press).

[58] Horvath R 2001 Some integral properties of the heat equation, *Computers and Mathematics with Applications* **42**, 1135-1141.

[59] Isakov V 1991 Inverse parabolic problems with the final overdetermination, *Communications on Pure and Applied Mathematics* **54**, 185-209.

[60] Isakov V 1999 Some inverse problems for the diffusion equation *Inverse Problems* **15**, 3-10.

[61] Isakov V 2006 *Inverse Problems for Partial Differential Equations*, Second Edition (Berlin: Springer).

[62] Kleinman A M and Roemer R B 1983 A direct substitution, equation error technique for solving the thermographic tomography problem, *Transactions of the ASME Journal of Biomedical Engineering* **105**, 237-243.

[63] Klibanov M V, Lucas T R and Frank R M 1997 Fast and accurate imaging algorithm in optical/diffusion tomography, *Inverse Problems* **13**, 1341-1361.

[64] Kress R and Roemer R 1987 A Comparative Analysis of Thermal Blood Perfussion Measurement Techniques, *Journal of Biomechanical Engineering* **109**, 218-225.

[65] Ladyzhenskaya O A, Solonnikov V A and Ural'tseva N N 1968 *Linear and Quasilinear Equations of Parabolic Type* (Providence, RI: American Mathematical Society).

[66] Lesnic D 2006 *Post-Graduate Course on the Boundary Element Method* **CCFD-5070** (University of Leeds: Centre for Computational Fluid Dynamics).

[67] Li G S 2006 Data compatibility and conditional stability for an inverse source problem in the heat equation, *Applied Mathematics and Computation* **173**, 566-581.

[68] Lin Y 1991 An inverse problem for a class of quasilinear parabolic equations, *SIAM Journal on Mathematical Analysis* **22**, 146-156.

[69] Liu J and Xu L S 2000 Boundary information based diagnostic on the thermal states of biological bodies, *Internal Journal of Heat and Mass Transfer* **43**, 2827-2839.

[70] Lorenzi A 1982 An inverse problem for a semilinear parabolic equation, *Annali di Matematica Pura ed Applicata* **131**, 145-166.

[71] Loulou T and Scott E P 2006 An inverse heat conduction problem with heat flux measurements *International Journal for Numerical Methods in Engineering* **67**, 1587-1616.

[72] Michener M, Hager J M, Terrell J P, Veit E and Diller T E 1991 Noninvasive Blood Perfusion Measurement with a Heat Flux Microsensor, *Advances in Biological Heat and Mass Transfer*, HTD-**189**/BED-**18**, 9-14, ed. McGrath J J (New York: ASME).

[73] Murio D A 1993 *The Mollification Method and the Numerical Solution of Ill-Posed Problems* (New York: Wiley-Interscience).

[74] Nanda A and Das P C 1996 Determination of the source term in the heat conduction equation, *Inverse Problems* **12**, 325-339.

[75] Nilsson G E, Tenland T and Oberg P A 1980 A new instrument for continuous measurement of tissue blood flow by light beating spectroscopy, *IEEE Transactions on Biomedical Engineering* **27**, 12-19.

[76] Orlande H R B and Ozisik M N 1994 Determination of the reaction function in a reaction-diffusion parabolic problem, *Journal of Heat Transfer* **116**, 1041-1044.

[77] Orlande H R B and Ozisik M N 1999 Inverse problems computations in heat and mass transfer, *Proceedings of the International Conference on Computational Heat and Mass Transfer (CHMT 99)*, 46-67, eds. Mohamad A A and Sezai I (Turkey: Easter Mediterancan University Printing House).

[78] Partridge P W and Wrobel L C 2007 An inverse geometry problem for the localisation of skin tumours by thermal analysis, *Engineering Analysis with Boundary Elements* **31**, 803-811.

[79] Partridge P W and Wrobel L C 2009 A coupled dual reciprocity BEM/genetic algorithm for identification of blood perfusion parameters, *International Journal of Numerical Methods for Heat & Fluid Flow* **19**, 25-38.

[80] Patel P A, Valvano J W, Pearce J A, Prahl S A and Denham C R 1987 A self-heated thermistor technique to measure effective thermal properties from the tissue surface, *ASME Journal of Biomechanical Engineering* **109**, 330-335.

[81] Pennes H H 1948 Analysis of tissue and arterial blood temperature in the resting human forearm, *Journal of Applied Physiology* **1**, 93-122.

[82] Phillips D L 1962 A technique for the numerical solution of certain integral equations of the first kind, *Journal of the Association for Computing Machinery* **9**, 84-97.

[83] Pierce A 1979 Unique determination of eigenvalues and coefficients in a parabolic problem, *SIAM Journal on Control and Optimization* **17**, 494-499.

[84] Pilant M S and Rundell W 1986 An inverse problem for a nonlinear parabolic equation, *Communications in Partial Differential Equations* **11**, 445-457.

[85] Pilant M S and Rundell W 1986 Undetermined coefficient problems for nonlinear elliptic and parabolic equations, *International Series of Numerical Mathematics* **77**, 139-154.

[86] Pilant M S and Rundell W 1987 Iteration schemes for unknown coefficient problems arising in parabolic equations, *Numerical Methods for Partial Differential Equations* **3**, 313-325.

[87] Pilant M S and Rundell W 1988 Fixed point methods for a parabolic inverse coefficient problem, *Communications in Partial Differential Equations* **13**, 469-493.

[88] Prilepko A I and Sololev V V 1987 Solvability of the inverse boundary-value problem of finding a coefficient of a lower-order derivative in a parabolic equation, *Differential Equations* **23**, 101-107.

[89] Prilepko A I and Kostin A B 1993 On certain inverse problems for parabolic equations with final and integral observations, *Russian Academy of Sciences Sbornik Mathematics* **75**, No. 2, 473-490.

[90] O'Reilly T, Gonzales T and Diller T 1996 Development of a Noninvasive Blood Perfusion Probe, *Advances in Biological Heat and Mass Transfer*, HTD-**337**/BED-**34**, 67-73, eds. Hayes L J and Clegg S (New York: ASME).

[91] Ramm A G 2000 Property C for ODE and applications to inverse problems, *Fields Institute Communications* **25**, 15-75.

[92] Ramm A G 2001 An inverse problem for the heat equation, *Journal of Mathematical Analysis and Applications* **264**, 691-697.

[93] Ramm A G and Smirnova A B 2001 On stable numerical differentiation, *Mathematics of Computation* **70**, 1131-1153.

[94] Ren Z P, Liu J and Wang C C 1995 Boundary element method (BEM) for solving normal and inverse bio-heat transfer problem of biological bodies with complex shape, *Journal of Thermal Science* **4**, 117-124.

[95] Reeve D E and Spivack M 1994 Determination of a source term in the linear diffusion equation, *Inverse Problems* **10**, 1335-1344.

[96] Riva C E, Ross B and Benedek G B 1972 Laser Doppler measurements of blood flow in capillary tubes and retinal arteries, *Investigative Ophthalmology & Visual Science* **11**, 936-944.

[97] Robinson P S, Scott E P and Diller T E 1998 Validation of Methodologies for the Estimation of Blood Perfusion Using a Minimally Invasive Probe, *Advances in Heat and Mass Transfer in Biotechnology* HTD-**362**/BED-**40**, 109-116, ed. Clegg S (New York: ASME).

[98] Scott E P, Robinson P and Diller T E 1997 Estimation of Blood Perfusion Using a Minimally Invasive Perfusion Probe, *Advances in Heat and Mass Transfer in Biotechnology* HTD-**355**/BED-**37**, 205-212, ed. Clegg S (New York: ASME).

[99] Scott E P, Robinson P and Diller T E 1998 Development of methodologies for the estimation of blood perfusion using a minimally invasive thermal probe, *Measurement Science and Technology* **9**, 888-897.

[100] Rodrigues F A, Orlande H R B and Dulikravich G S 2004 Simultaneous estimation of spatially dependent diffusion coefficient and source term in a nonlinear 1D diffusion problem, *Mathematics and Computers in Simulation* **66**, 409-424.

[101] Rundell W 1987 The determination of a parabolic equation from initial and final data, *Proceedings of the American Mathematical Society* **99**, 637-642.

[102] Shepard A P and Oberg P A 1990 *Laser-Doppler Blood Flowmetry* (Dordrecht: Kluwer Academic).

[103] Shiryaev A N 1996 *Probability*, Graduate Texts in Mathematics, Second Edition (New York: Springer-Verlag).

[104] Stern M D 1975 In vivo evaluation of microcirculation by coherent light scattering, *Nature* **254**, 56-58.

[105] M.D. Stern and D.L. Lappe 1990 Method and Apparatus for Measurements of Blood Flow Using Coherent Light, U.S. Patent 4.109.647, 1978, *Laser-Doppler Blood Flowmetry*, eds. Shepherd A P, Oberg P A (Dordrecht: Kluwer Academic).

[106] Stern M D, Lappe D L, Bowen P D, Chimosky J E, Holloway G A, Deiser H R and Bowman R L 1977 Continuous measurement of tissue blood flow by laser-Doppler spectroscopy, *American Journal of Physiology* **232**, H441-H448.

[107] Strohbehn J W and Roemer R B 1984 A survey of computer simulation of hypothermia treatments, *IEEE Transactions of Biomedical Engineering* **31**, 136-149.

[108] Stroock D W 1994 *A Concise Introduction to the Theory of Integration* (Boston: Birkhauser).

[109] Tadi M, Klibanov M V and Cai W 2002 An inverse method for parabolic equations based on quasireversibility *Computers and Mathematics with Applications* **43**, 927-941.

[110] Tikhonov A N and Samarskii A A 1963 *Equations of Mathematical Physics* (New York: Pergamon).

[111] Valvano J W, Badeau A F, Prahl S A, Chan J C and Pearce J A 1988 Thermal Camera Imaging to Measure Tissue Surface Perfusion, *Association for the Advancement of Medical Instrumentation*, 23rd Annual Meeting, May 14-18, Washington DC.

[112] Valvano J W and Nho S 1991 Tissue Thermal Diffusivity Measured with Sinusoidally Heated Thermistors, *Advances in Biological Heat and Mass Transfer* HTD-**189**/BED-**18**, 9-14, ed. McGrath J J (New York: ASME).

[113] Walsh J T and Bowman H F 1984 A Noninvasive Techique for Quantifying Tissue Perfusion, *Advances in Bioengineering*, 5-6, ed. Spilker R L (New York: ASME).

[114] Wang Y B, Hon Y C and Cheng J 2006 Reconstruction of high order derivatives from input data, *Journal of Inverse and Ill-posed Problems* **14**, 205-218.

[115] Wang S and Lin Y 1989 A finite-difference solution to an inverse problem for determining a control function in a parabolic partial differential equation, *Inverse Problems* **5**, 631-640.

[116] Wei D, Saidel G M and Jones S C 1995 Estimation of cerebral blood flow from thermal measurement, *Journal of Biomechanical Engineering* **117**, 74-85.

[117] Yang L, Yu J-N and Deng Z-C 2008 An inverse problem of identifying the coefficient of parabolic equation, *Applied Mathematical Modelling* **32**, 1984-1995.

[118] Yu W 1991 On the existence of an inverse problem, *Journal of Mathematical Analysis and Applications* **157**, 63-74.

[119] Zeghal A 2004 Uniqueness of determination of the unknown source term in some multidimensional parabolic equations, *Proyecciones (Antofagasta)* **23**, 81-90.